

DIFFUSION COEFFICIENTS AND MECHANICAL PROPERTIES OF
POLYMERIZABLE LIPID MEMBRANES

by

Kristina S. Orosz

A Dissertation Submitted to the Faculty of the
DEPARTMENT OF CHEMISTRY AND BIOCHEMISTRY

In Partial Fulfillment of the Requirements
For the Degree of

DOCTOR OF PHILOSOPHY
WITH A MAJOR IN CHEMISTRY

In the Graduate College

The UNIVERSITY OF ARIZONA

2011

THE UNIVERSITY OF ARIZONA
GRADUATE COLLEGE

As members of the Dissertation Committee, we certify that we have read the dissertation
prepared by Kristina S. Orosz

entitled DIFFUSION COEFFICIENTS AND MECHANICAL PROPERTIES OF
POLYMERIZABLE LIPID MEMBRANES

and recommend that it be accepted as fulfilling the dissertation requirement for the
Degree of Doctor of Philosophy

_____ Date: April 18, 2011
Dr. S. Scott Saavedra

_____ Date: April 18, 2011
Dr. Neal R. Armstrong

_____ Date: April 18, 2011
Dr. Jeanne Pemberton

_____ Date: April 18, 2011
Dr. Megan McEvoy

_____ Date:

Final approval and acceptance of this dissertation is contingent upon the candidate's
submission of the final copies of the dissertation to the Graduate College.

I hereby certify that I have read this dissertation prepared under my direction and
recommend that it be accepted as fulfilling the dissertation requirement.

_____ Date: April 18, 2011
Dissertation Director: Dr. S. Scott Saavedra

STATEMENT BY AUTHOR

This dissertation has been submitted in partial fulfillment of requirements for an advanced degree at the University of Arizona and is deposited in the University Library to be made available to borrowers under rules of the Library.

Brief quotations from this dissertation are allowable without special permission, provided that accurate acknowledgment of source is made. Requests for permission for extended quotation from or reproduction of this manuscript in whole or in part may be granted by the head of the major department or the Dean of the Graduate College when in his or her judgment the proposed use of the material is in the interests of scholarship. In all other instances, however, permission must be obtained from the author.

SIGNED: Kristina S. Orosz

TABLE OF CONTENTS

LIST OF FIGURES.....	15
LIST OF TABLES.....	22
ABSTRACT.....	24
CHAPTER 1: INTRODUCTION.....	26
1.1 Cell Membranes.....	26
1.1.1 Lipid Structure and Self-Assembly.....	26
1.1.2 Membrane Proteins.....	28
1.1.3 Model Transmembrane Proteins and Peptides.....	30
1.1.3.1 Rhodopsin.....	30
1.1.3.2 Gramicidin.....	31
1.2 Lipid Membrane Properties.....	33
1.2.1 Phase Transition.....	33
1.2.2 Spontaneous Curvature and Lipid Polymorphism.....	35
1.2.3 Fluidity.....	37
1.2.4 Mechanical Properties.....	39
1.2.4.1 Stretching.....	39
1.2.4.2 Bending.....	39
1.2.4.3 Lysis Tension.....	41
1.3 Lipid Bilayer Platforms for Study.....	42
1.3.1 Vesicles.....	42
1.3.2 Planar Supported Lipid Bilayers.....	42

TABLE OF CONTENTS - Continued

1.3.3 Black Lipid Membranes.....	44
1.4 Bilayer-transmembrane Protein Biosensors.....	46
1.4.1 Biosensor Architectures.....	46
1.4.2 Drawbacks to Artificial Lipid Bilayers.....	46
1.5 Polymerizable Lipids.....	48
1.5.1 Polymerizable Groups.....	48
1.5.2 Polymerization Methods.....	52
1.5.2.1 <i>UV-polymerization</i>	52
1.5.2.2 <i>Redox-polymerization</i>	52
1.5.3 Improvements in Lipid Bilayer Stability with Poly(lipids).....	53
1.5.4 Transmembrane Protein/Peptide Function in Stabilized Poly(lipid) Bilayers.....	55
1.6 Dissertation Overview.....	58
1.6.1 Fluorescence Recovery After Photobleaching Instrumentation and Methods.....	58
1.6.2 Fluidity Measurements of Polymerizable Lipid Bilayers.....	58
1.6.3 Micropipette Aspiration of Giant Unilamellar Vesicles Composed of Polymerizable Lipids.....	62
1.6.4 Conclusions.....	65

TABLE OF CONTENTS - Continued

CHAPTER 2: FLUORESCENCE RECOVERY AFTER

PHOTOBLEACHING.....	66
2.1 PSLB Sample Preparation.....	67
2.1.1 FRAP Sample Chamber and Chamber Heating and Cooling.....	67
2.1.2 PSLB Formation by Vesicle Fusion.....	71
2.2 Qualitative FRAP.....	74
2.2.1 FRAP Instrumentation.....	74
2.2.2 Protocol for Qualitative FRAP.....	76
2.2.2.1 Lamp Photobleaching.....	76
2.2.2.2 Laser Photobleaching.....	79
2.2.3 Qualitative FRAP Data.....	81
2.3 Quantitative FRAP (NBD-PC).....	83
2.3.1 Protocol to Run FRAP (NBD-PC).....	83
2.3.2 Data-processing for FRAP (NBD-PC).....	86
2.3.2.1 Spot Size Determination.....	86
2.3.2.2 Reference Values and Blank Subtraction.....	89
2.3.2.3 Initial Ratio Correction.....	89
2.3.2.4 Bleach Depth (γ_D) Determination.....	91
2.3.2.5 Diffusion Coefficient Determination.....	93
2.3.2.6 Percent Recovery.....	95

TABLE OF CONTENTS - Continued

2.3.2.7 <i>Length of Observation</i>	95
2.3.3 Drawbacks to FRAP (NBD-PC).....	95
2.3.3.1 <i>Photobleaching of NBD-PC</i>	95
2.3.3.2 <i>Hand-timing and Acquisition</i>	98
2.3.3.3 <i>Constant ROI Size</i>	99
2.4 FRAP (rhodamine-PE).....	105
2.4.1 Choice of Fluorophore.....	105
2.4.2 Protocol to Run FRAP (rhodamine-PE).....	107
2.4.3 Data-processing for FRAP (rhodamine-PE).....	109
2.4.3.1 <i>Spot Size and ROI Size Determination</i>	109
2.4.3.2 <i>Blank Subtraction</i>	109
2.4.3.3. <i>Initial Ratio Calculation</i>	109
2.4.3.4 γ_D <i>Determination</i>	110
2.4.3.5 <i>Program for Data Extraction</i>	110
2.4.3.6 <i>Diffusion Coefficient and Percent Recovery Calculations</i>	110
2.5 Possible Improvements to the FRAP System.....	115
2.5.1 Automation with Lamp Monitoring.....	115
2.5.2 Automation with Laser Monitoring.....	116
2.5.3 New Detection System.....	116
2.5.4 Fluorescence Recovery After Pattern Photobleaching.....	117

TABLE OF CONTENTS - Continued

CHAPTER 3: MEASUREMENTS OF POLYMERIZABLE LIPID

DIFFUSION COEFFICIENTS IN PSLBs.....	118
3.1 Introduction.....	118
3.2 Experimental.....	123
3.2.1 Materials.....	123
3.2.2 Phase Transitions of Polymerizable Lipids.....	124
3.2.3 Surface Cleaning.....	124
3.2.4 Polymerization of Lipids.....	126
3.2.4.1 <i>UV-polymerization</i>	126
3.2.4.2 <i>Redox-polymerization</i>	127
3.2.5 FRAP Measurements.....	130
3.3 Results and Discussion.....	131
3.3.1 Diffusion Behavior of Unpolymerized PSLBs.....	131
3.3.2 Diffusion Behavior of UV-polymerized PSLBs.....	135
3.3.3 Diffusion Behavior of Redox-polymerized PSLBs.....	147
3.3.4 Diffusion Behavior of PSLBs UV- and Redox-polymerized at T_m	156
3.3.5 % Recovery as a Function of Diffusion Coefficient.....	159
3.3.6 Data Interpretation with Respect to the Percolation Threshold.....	162
3.4 Conclusions.....	167

TABLE OF CONTENTS – Continued

CHAPTER 4: MEASURING THE MECHANICAL PROPERTIES OF POLYMERIZABLE LIPIDS: MICROPIPETTE ASPIRATION OF GIANT UNILAMELLAR VESICLES.....	168
4.1 Introduction.....	168
4.2 Instrumental Set-up for Micropipette Aspiration Measurements 	171
4.2.1 Imaging.....	171
4.2.2 Positioning.....	171
4.2.3 Pressure Control.....	173
4.3 Experimental Protocol.....	175
4.3.1 Materials.....	175
4.3.2 Forming GUVs.....	175
4.3.3 Pipettes.....	176
4.3.3.1 Pulling Pipettes.....	176
4.3.3.2 Forging Pipettes.....	177
4.3.3.3 Coating Pipettes.....	181
4.3.3.4 Filling Pipettes.....	181
4.3.3.5 Mounting Pipettes.....	183
4.3.4 Sample Chamber.....	185

TABLE OF CONTENTS - Continued

4.3.4.1 Chamber Design.....	185
4.3.4.2 Coverslip/Quartz Coating.....	187
4.3.4.3 Chamber Temperature Control.....	187
4.3.5 Micropipette Aspiration Sample.....	188
4.3.6 Manometer Calibration.....	191
4.3.7 Obtaining a Run.....	191
4.3.7.1 <i>GUV Selection</i>	193
4.3.7.2 <i>GUV Capture and Preparation</i>	195
4.3.7.3 <i>Syringe Pump Program</i>	197
4.3.7.4 <i>Data Set Acquisition</i>	200
4.3.7.5 <i>Changing Sample Osmolarity</i>	201
4.3.8 Polymerization of Lipids in μ PA Geometry.....	201
4.3.8.1 <i>Side-illumination</i>	201
4.3.8.2 <i>Top-illumination Through Quartz</i>	202
4.4 Data-processing.....	206
4.4.1 Determining τ	206
4.4.2 Determining α	208
4.4.3 Determining Elastic Moduli and Lysis Tension (Strength).....	210
4.4.3.1 <i>Linear Subtraction Method</i>	212
4.4.3.2 <i>Two-component Fitting</i>	212
4.4.3.2.1 <i>Two-component Equation and Fitting</i>	212

TABLE OF CONTENTS - Continued

4.4.3.2.2 <i>Comparing Linear Subtraction and Two-component Fitting Outcomes</i>	
.....	213
4.4.3.2.3 <i>Criteria for Acceptable GUVs</i>	215
4.4.3.2 <i>Lysis Tension</i>	216
4.5 Results and Discussion.....	217
4.5.1 Observed Geometries of “GUV”s.....	217
4.5.1.1 <i>Typical GUVs</i>	217
4.5.1.2 <i>“Leaky” GUVs</i>	217
4.5.1.3 <i>Multilamellar Giant Vesicles</i>	218
4.5.1.4 <i>Continuous Collapse</i>	218
4.5.1.5 <i>Crumpling</i>	222
4.5.2 Lysis Tension	222
4.5.3 Elastic Area Expansion Moduli.....	229
4.5.4 Cohesive Energy Density.....	230
4.5.5 Elastic Bending Moduli.....	232
4.5.6 Calculated Membrane Thickness.....	233
4.6 Conclusions.....	237
CHAPTER 5: CONCLUSIONS.....	238
5.1 Summary.....	238
5.1.1 Fluidity of Unpolymerized and Polymerized PSLBs.....	238

TABLE OF CONTENTS - Continued

5.1.2 Mechanical Properties of Polymerized Lipid Bilayers.....	241
5.2 Future Directions.....	245
5.2.1 Future Work with Fluidity Measurements.....	245
5.2.1.1 Diffusion of PSLBs Polymerized at T_m	245
5.2.1.2 Diffusion of Polymerized PSLBs at Room Temperature.....	246
5.2.1.3 Diffusion of PSLBs Composed of Mixtures of Polymerizable/Non- Polymerizable Lipids.....	247
5.2.1.4 Measuring Diffusion in a BLM Geometry.....	247
5.2.2 Measuring Obstacle Fraction to Determine the Percolation Threshold	248
5.2.3 Mechanical Properties of Immobile Bilayers.....	252
APPENDIX A: SPREADSHEETS FOR FRAP CALCULATIONS...	253
A.1 Spreadsheets for Calculating w	253
A.2 Spreadsheet for ROIs and w Conversion.....	256
A.3 Initial Ratio and γ_D Calculation Spreadsheets.....	259
A.4 Single-exponential Data-fitting Spreadsheet.....	262
A.5 Double-exponential Data-fitting Spreadsheet.....	267
APPENDIX B: ATTEMPTED LIGHT-INDUCED PROTON- PUMPING ACROSS A PSLB.....	272
B.1 Introduction.....	272

TABLE OF CONTENTS - Continued

B.1.1 Biomimetic Proton-pumping.....	272
B.1.2 Review of Previous Work with Proton-Pumping.....	274
B.1.3 Goal.....	274
B.2 Experimental.....	279
B.2.1 Materials and Methods.....	279
<i>B.2.1.1 Materials.....</i>	<i>279</i>
<i>B.2.1.2 ITO Cleaning.....</i>	<i>279</i>
<i>B.2.1.3 Layer-by-layer Deposition.....</i>	<i>281</i>
<i>B.2.1.4 PSLB Formation.....</i>	<i>282</i>
<i>B.2.1.5 Q.....</i>	<i>282</i>
B.2.2 AFM.....	282
B.2.3 UV-vis Absorbance.....	282
B.2.4 Electrochemical Cells.....	282
B.2.5 Potentiometry.....	284
<i>B.2.5.1 pH-response.....</i>	<i>284</i>
<i>B.2.5.2 pH-Response Blocking Experiments.....</i>	<i>285</i>
B.2.6 Cyclic Voltammetry.....	285
B.2.7 Fluorescence Microscopy and FRAP.....	285
B.3 Results and Discussion.....	286
B.3.1 ITO Characterization.....	286
<i>B.3.1.1 Roughness.....</i>	<i>286</i>

TABLE OF CONTENTS - Continued

<i>B.3.1.2 UV-vis Absorbance Spectra</i>	286
B.3.2 Polymer Film Characterization	286
<i>B.3.2.1 Cyclic Voltammetry of Polymer Films on ITO</i>	286
<i>B.3.2.2 pH Reponse of Polymer Films on ITO</i>	290
B.3.3 PSLBs on Polymer	294
<i>B.3.3.1 Quantitative FRAP</i>	294
<i>B.3.3.2 Attempted Proton-blocking</i>	296
<i>B.3.3.3 Qualitative FRAP and Fluorescence Microscopy</i>	296
B.3.4 Attempted Incorporation of C-P-Q into PSLBs on ITO/(PANI/PAA)₂	303
B.4 Conclusions	308
B.4.1 ITO Effects.....	308
B.4.2 Mixing Difficulties.....	308
B.4.3 Presence of a Lipid Bilayer.....	308
B.4.4 Potential Changes Upon Light Activation of Full Architecture.....	309
APPENDIX C: PROOF OF PERMISSION FOR COPYRIGHTED MATERIAL	310
REFERENCES	312

LIST OF FIGURES

Figure 1.1	Space-filling model of an average synaptic vesicle.....	27
Figure 1.2	Categories of lipids based on headgroups.....	27
Figure 1.3	Lipid bilayer.....	29
Figure 1.4	Transmembrane protein in a lipid bilayer.....	29
Figure 1.5	Rhodopsin.....	32
Figure 1.6	Gramicidin.....	32
Figure 1.7	Lipid phases.....	34
Figure 1.8	Non-polymerizable lipid structures.....	34
Figure 1.9	DPPC thermogram.....	34
Figure 1.10	Lipid polymorphs.....	36
Figure 1.11	Spontaneous curvature.....	38
Figure 1.12	Elastic stretching and bending.....	40
Figure 1.13	Planar supported lipid bilayer.....	43
Figure 1.14	Black lipid membrane.....	45
Figure 1.15	Polymerizable groups.....	49
Figure 1.16	Polymerizable group locations.....	49
Figure 1.17	Lipopolymer geometries.....	49
Figure 1.18	Linear or cross-linked polymers.....	51
Figure 1.19	Dienoyl lipids.....	51
Figure 1.20	DienoylPC polymer product.....	54
Figure 1.21	Fluidity hypothesis.....	61

LIST OF FIGURES - Continued

Figure 1.22 Bending hypothesis.....	64
Figure 2.1 Schematic diagram of the FRAP chamber.....	75
Figure 2.2 FRAP chamber heating set-up.....	77
Figure 2.3 FRAP chamber cooling set-up.....	77
Figure 2.4 Fluorescence images of a uniform PSLB.....	80
Figure 2.5 FRAP instrument schematic and photo.....	82
Figure 2.6 Qualitative FRAP images.....	85
Figure 2.7 Chemical structure of NBD-PC.....	91
Figure 2.8 Line scan of first image after photobleaching and Gaussian laser spot fitting	95
Figure 2.9 Example of bleach and reference area locations for FRAP experiments.....	97
Figure 2.10 Plot of κ values as a function of $F_{\kappa}(0)/F_{\kappa}$	99
Figure 2.11 FRAP recovery curve data.....	101
Figure 2.12 Background subtracted fluorescence intensity of varying mol % NBD-PC in a PSLB.....	104
Figure 2.13 FRAP curves generated by using different ROI sizes.....	110
Figure 2.14 Chemical structure of rhodamine-PE.....	113
Figure 2.15 Raw intensity data for a FRAP (rhodamine-PE) recovery curve.....	113
Figure 2.16 FRAP recovery curves, fits, and residuals for single- and double- exponential fits.....	119

LIST OF FIGURES - Continued

Figure 3.1 Absorbance spectra of bis-DenPC SUVs as a function of polymerization time	137
Figure 3.2 Calculated fraction of unreacted monomer as a function of polymerization time.....	137
Figure 3.3 Fluorescence images of PSLBs after UV-polymerization.....	138
Figure 3.4 Example FRAP recovery curves for PSLBs composed of polymerizable lipids.....	142
Figure 3.5 UV-poly(mono-DenPC).....	149
Figure 3.6 D_{un}/D_{poly} vs. X_n for Kölchens' data.....	149
Figure 3.7 UV-poly(mono-SorbPC).....	151
Figure 3.8 UV-poly(bis-DenPC).....	152
Figure 3.9 UV-poly(bis-SorbPC).....	155
Figure 3.10 Redox-poly(mono-DenPC) $poly > T_m$	162
Figure 3.11 Redox-poly(mono-DenPC) $poly < T_m$	163
Figure 3.12 Mobile and immobile percents as a function of D_{avg}	169
Figure 3.13 Mobile percents as a function of D	170
Figure 3.14 Percolation threshold.....	172
Figure 4.1 Block diagram of μ PA system.....	184
Figure 4.2 Photo of the μ PA system.....	184
Figure 4.3 Photos of pressure control system.....	186
Figure 4.4 Image of a pulled pipette.....	190

LIST OF FIGURES - Continued

Figure 4.5	Pipette cutting steps.....	192
Figure 4.6	Photo of pipette storage.....	194
Figure 4.7	Pipette coating set-up.....	194
Figure 4.8	Mounted pipette.....	196
Figure 4.9	μ PA sample chamber.....	198
Figure 4.10	Sample chamber with heating block.....	201
Figure 4.11	Sample chamber temperature response.....	201
Figure 4.12	Mounted pipette in sample chamber with heating block.....	202
Figure 4.13	Manometer calibration set-up.....	204
Figure 4.14	Images of vesicles.....	206
Figure 4.15	Absorbance spectra of bis-SorbPC SVs UV-polymerized in side-illumination geometry.....	215
Figure 4.16	Percent of unreacted bis-SorbPC monomer as a function of UV-polymerization time in side-illumination geometry.....	215
Figure 4.17	Absorbance spectra of bis-SorbPC SVs UV-polymerized in top-illumination geometry through quartz slide.....	217
Figure 4.18	Percent of unreacted bis-SorbPC monomer as a function of UV-polymerization time in top-illumination geometry through quartz slide...	217
Figure 4.19	Spreadsheet used for data-fitting.....	219
Figure 4.20	DIC images of an aspirated GUV undergoing a change in applied tension	221

LIST OF FIGURES - Continued

Figure 4.21	Examples of plots for μ PA data-fitting.....	223
Figure 4.22	Continuation of the spreadsheet used for data-fitting.....	226
Figure 4.23	DIC images of typical GUVs.....	231
Figure 4.24	DIC images of “leaky” GUVs.....	231
Figure 4.25	DIC images of a multilamellar GV undergoing a tension ramp.....	232
Figure 4.26	DIC images of a GV being completely aspirated without lysing.....	233
Figure 4.27	DIC images of a polymerized GV crumpling.....	235
Figure 4.28	DIC images of each type of GUV investigated.....	239
Figure 4.29	Calculated cohesive energy density of GUVs.....	243
Figure 4.30	Calculated bilayers thickness.....	247
Figure 5.1	Future work relating to obstacle fractions of poly/unpoly lipids.....	267
Figure A.1	Example of a Gaussian fit.....	274
Figure A.2	Spreadsheet for w conversion and w determination.....	277
Figure A.3	Initial ratio calculations spreadsheet.....	280
Figure A.4	Spreadsheet for calculation of γ_D	280
Figure A.5	Spreadsheet for creating and fitting single-exponential recovery curves...	283
Figure A.6	Spreadsheet for creating and fitting double-exponential recovery curves	288
Figure B.1	Structures of CPQ and Q.....	294
Figure B.2	Important forms of PANI.....	297
Figure B.3	ITO/(PANI/PAA) ₂ architecture.....	297

LIST OF FIGURED - Continued

Figure B.4 ITO/(PANI/PAA) ₂ with PSLB fused on top that includes Q and C-P-Q...	299
Figure B.5 Photo of echem cell hooked up to pH meter.....	304
Figure B.6 AFM images of ITO from different batches.....	308
Figure B.7 Absorbance spectra of ITO types C and D.....	309
Figure B.8 CVs of ITO/(PANI/PAA) ₂ films.....	310
Figure B.9 Potential as a function of time for ITO/(PANI/PAA) ₂ exposed to different pH solutions.....	312
Figure B.10 Potential vs. pH for different ITO/(PANI/PAA) ₂ films.....	313
Figure B.11 FRAP curves for ITO/(PANI/PAA) ₂ and glass with 5 mol% NBD-PC in EggPC at pH = 7.0.....	316
Figure B.12 Potential vs. time for ITO/(PANI/PAA) ₂ with and without a PSLB of EggPC treated identically.....	318
Figure B.13 Qualitative FRAP images for glass and ITO _C /(PANI/PAA) ₂	320
Figure B.14 Qualitative FRAP images for ITO/(PANI/PAA) comparing ITO _C and ITO _D	320
Figure B.15 Fluorescence image of glass with an EggPC PSLB scratched.....	321
Figure B.16 Fluorescence images of ITO/(PANI/PAA) ₂ before and after PSLB deposition.....	323
Figure B.17 Proton-pumping set-up.....	325

LIST OF FIGURES - Continued

Figure B.18 Potential v. time for ITO/(PANI/PAA) ₂ , ITO/(PANI/PAA) ₂ with PSLB with Q, and ITO/(PANI/PAA) ₂ with PSLB with Q and C-P-Q being exposed to light.....	327
---	------------

LIST OF TABLES

Table 2.1	Diffusion coefficients, percent recoveries, and goodness of fit for a single-exponential recovery as a function of ROI size.....	108
Table 2.2	Diffusion coefficients, percent recoveries, and goodness of fit for a double-exponential recovery as a function of ROI size.....	108
Table 3.1	Phase transition temperatures of polymerizable lipids.....	134
Table 3.2	Temperature, diffusion coefficients, percent recoveries, and adjusted diffusion coefficients of unpolymerized PSLBs.....	141
Table 3.3	Temperatures, diffusion coefficients, percent recoveries, and diffusion coefficient ratios of PSLBs UV-polymerized above their T_m	146
Table 3.4	Temperatures, diffusion coefficients, percent recoveries, and diffusion coefficient ratios of PSLBs UV-polymerized below their T_m	146
Table 3.5	Temperatures, diffusion coefficients, percent recoveries, and diffusion coefficient ratios of PSLBs redox-polymerized above their T_m	158
Table 3.6	Temperatures, diffusion coefficients, percent recoveries, and diffusion coefficient ratios of PSLBs redox-polymerized below their T_m	158
Table 3.7	Temperatures, diffusion coefficients, percent recoveries, and diffusion coefficient ratios of PSLBs polymerized at their T_m	167
Table 3.8	Fluidity categories.....	175
Table 4.1	Syringe pump program used for μ PA experiments.....	210

LIST OF TABLES - Continued

Table 4.2 Experimental temperature, lysis tensions, elastic area expansion moduli, and elastic bending moduli of GUVs composed of dienolyPC lipids unpolymerized and polymerized.....	235
Table B.1 ITO batches.....	301
Table B.2 Roughness measurements for different ITO batches.....	308
Table B.3 Electrochemical parameters for ITO/(PANI/PAA) ₂ determined from CVs	310
Table B.4 Calculation of PSLB % on surfaces.....	323

ABSTRACT

It would be beneficial to incorporate transmembrane proteins (TMPs) into biosensors, because TMPs are important for cell function in healthy and diseased states. These devices would employ an artificial cell membrane to maintain TMP function since cell membranes, which are mostly lipids, are necessary for the TMPs to function. These artificial lipid membranes must be robust for sensor applications. The ruggedness of these artificial membranes can be increased by using polymerizable lipids. Some polymerized lipid membranes exhibit increased stability, while successfully incorporating TMPs.

Some polymerized membranes do not support the activity of certain TMPs, while maintaining the function of others. It is believed the physical properties of the membranes are important for TMP function. Some important physical properties of polymerizable lipid membranes have not yet been measured. Here, fluidity and mechanical properties of polymerizable dienoylPC lipid membranes were investigated.

Fluorescence Recovery After Photobleaching was used to measure the fluidity of polymerizable dienoylPC membranes. Unpolymerized, UV-polymerized, and redox-polymerized membranes were investigated. Three types of membranes were found: fluid, partially fluid, and immobile. Unpolymerized and some polymerized membranes were fluid, while only polymerized membranes were partially fluid or immobile. Polymer size is believed to cause the differences in fluidity. This study highlights how polymerization parameters can influence membrane fluidity.

Micropipette Aspiration was used to measure the mechanical properties of Giant Unilamellar Vesicles (GUVs) composed of dienolylPC lipids. Unpolymerized and UV-polymerized GUVs were investigated. Strength measurements showed that denolylPC GUVs were stronger than sorbylPC GUVs. Area expansion moduli of denolylPCs and mono-SorbPC GUVs were slightly lower than SOPC GUVs, while bis-SorbPC GUVs were substantially easier to stretch. The bending moduli of all GUVs was similar. UV-polymerization had no significant effect on the parameters. The difference in strength between denolylPCs and sorbylPCs is hypothesized to be due to the porous nature of sorbylPCs. It is thought UV-polymerization of these GUVs created polymers too small to significantly alter mechanical properties.

It was demonstrated that some stable membranes are also fluid, which is important for the function of certain TMPs. A correlation cannot be made between the bending and stretching moduli of polymerizable membranes and function of TMPs.

CHAPTER 1: INTRODUCTION

1.1 Cell Membranes

The cell membrane is the barrier between the inside and outside of a cell. These membranes compartmentalize other cell components like organelles as well. They must allow for communication in and out of the cell or organelle while providing a protective barrier.¹ The cell membrane is made mostly of lipids and proteins, as shown in Figure 1.1.^{2,3} In mammalian cells, over 2,000 species of lipids, sphingolipids, and sterols have been identified.^{4,5} Numerous proteins associated with these membranes are found and can be grouped into two major categories, peripheral and integral, based on how tightly they are associated with the cell membrane.⁶ Clearly, the natural membrane environment is quite diverse in terms of both lipids and proteins.

1.1.1 Lipid Structure and Self-assembly

Lipids are part of a broad category of amphiphilic molecules that also include single-chain surfactants. Most membrane-forming lipids are glycerophospholipids, which include phosphatidylethanolamine (PE), phosphatidylcholine (PC), phosphatidylserine (PS), phosphatidylinositol (PI), and phosphatidylglycerol (PG).⁶ The categories are based on the identity of the hydrophilic headgroup of the lipid. Figure 1.2 shows the structures of the listed lipid categories. Within each category, the hydrophobic lipid tail groups can vary greatly by changing the length and degree of unsaturation of each tail independently. These changes in tail and headgroup can alter the physical properties of membranes made from these lipids.

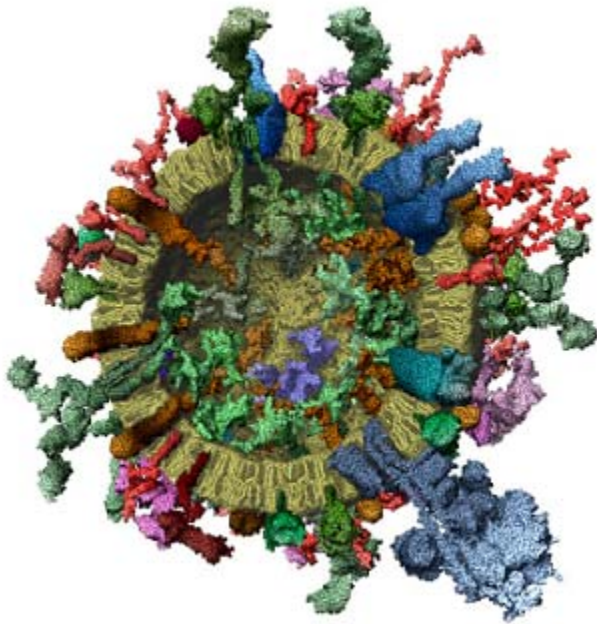


Figure 1.1. Space-filling model of an average synaptic vesicle. Taken from Ref. 2 with permission.

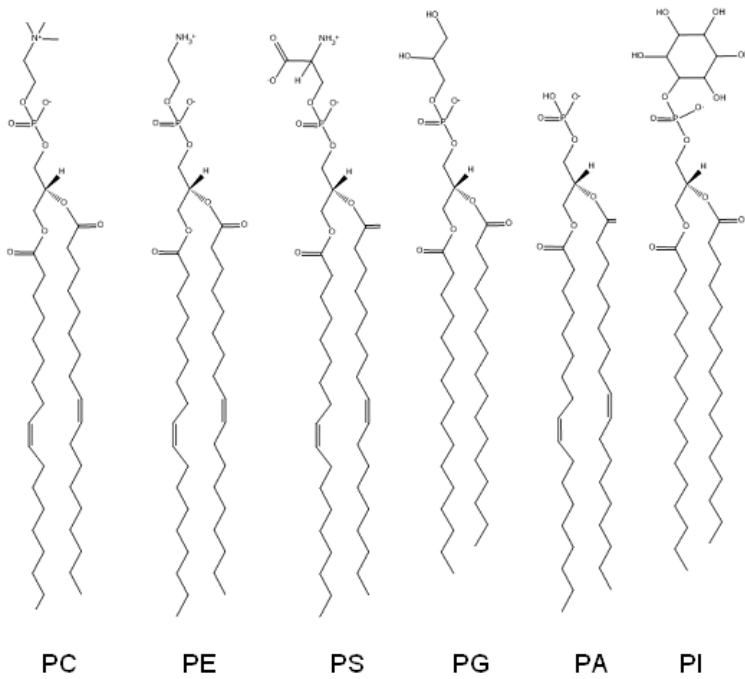


Figure 1.2. Categories of lipids.

Lipids spontaneously self-assemble into various aggregates due to their amphiphilic nature.⁷ The forces holding these aggregates together are weak van der Waals, hydrogen-bonding, and screened electrostatic interactions. Strong covalent and ionic bonds are not naturally present in lipid structures. Although bonds are missing between the molecules, lipid structures are considered ‘soft matter’ since they can resist forces that try to break or bend them.⁸ In the cell membrane architecture, the lipids form a bilayer only a few nanometers thick by burying their hydrophobic tails away from the external aqueous environment as seen in Figure 1.3. Bilayers and other lipid aggregate geometries will be discussed more thoroughly in Section 1.2.2.

1.1.2 Membrane Proteins

As mentioned previously, membrane proteins have varying degrees of association with the cell membrane. Peripheral membrane proteins can bind to lipid membrane surfaces through a variety of mechanisms and are water-soluble.⁶ Other membrane proteins, such as transmembrane proteins (TMPs), are an integral membrane protein subset that span the entire lipid bilayer, as shown in Figure 1.4. Structurally, this means the membrane-spanning portion of the protein must be hydrophobic to match the properties of the hydrocarbon tails of the lipids, while the extramembranous portions of the protein are hydrophilic to match the aqueous environment on either side of the cell membrane. TMPs and other integral proteins need the proper bilayer environment to have the proper structure and thus function correctly.⁹⁻¹¹

In biological membranes, about 50% of the mass is composed of proteins, while certain membranes have about a quarter of the volume taken up by these proteins.^{2, 12}

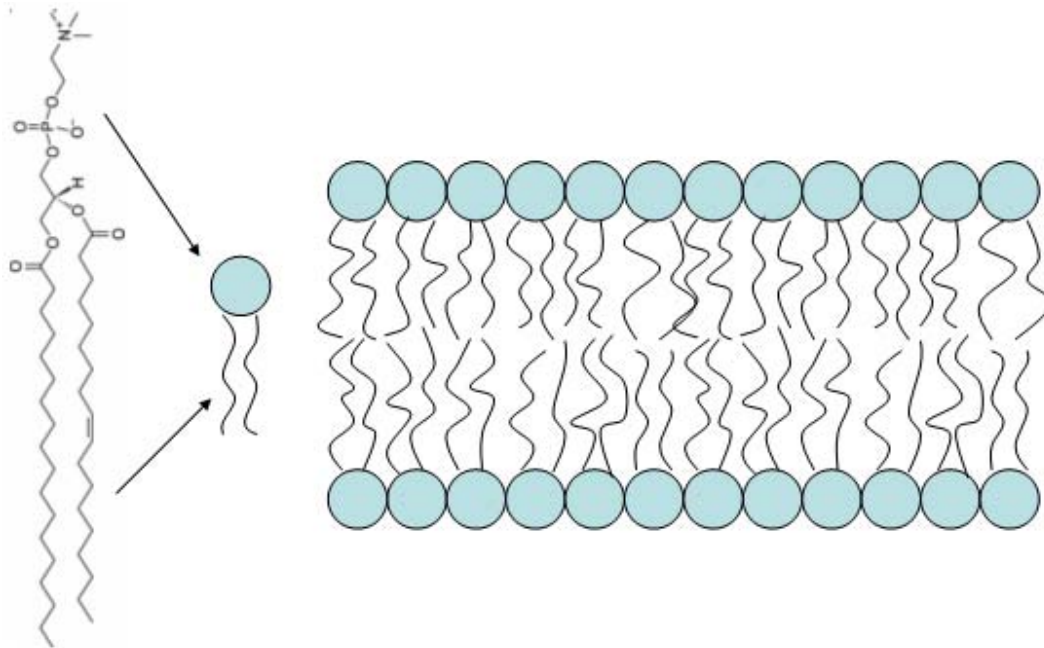


Figure 1.3. Lipid structure and lipid bilayer. Lipid image from www.avantilipids.com. On the left, the shorthand for a lipid molecule is shown, where the circle represents the hydrophilic headgroup and the cartoon tails represent the hydrocarbon tails. On the right is a cartoon of a self-assembled lipid bilayer.

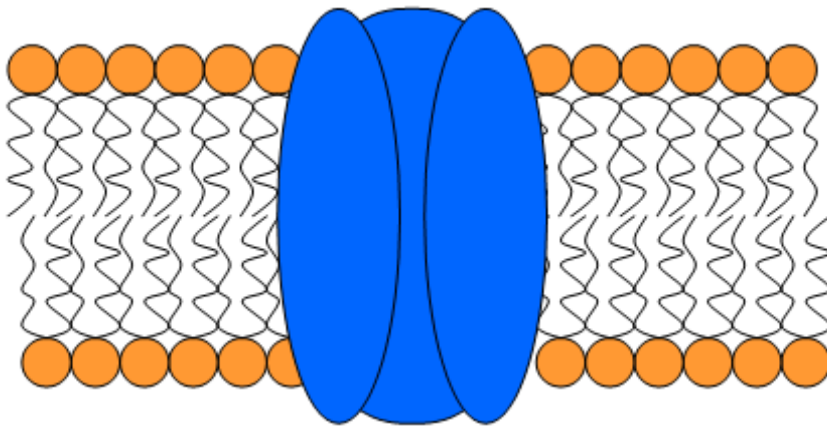


Figure 1.4. A lipid bilayer with an embedded TMP shown in blue.

TMPs are involved in many key biological processes, including signaling, osmoregulation, cell recognition, and changing the membrane potential.^{13, 14} They are believed to be the target of ~50% of marketed drugs.¹⁵ There is a great diversity of membrane proteins: mass spectrometric analysis of synaptic vesicles (which are ~ 40 nm in diameter) discovered over 80 unique integral membrane proteins.²

One large and important family of TMPs are the G-protein-coupled receptors (GPCRs). GPCRs respond to a variety of stimuli, including light, neurotransmitters, and hormones.^{13, 16} As a result, GPCRs are related to a number of disease states such as cardiovascular disorders, psychiatric disorders, asthma, obesity, and more.^{15, 16} Unsurprisingly, this has led to great interest in GPCRs because they are the targets of many pharmaceuticals.¹⁵⁻¹⁹

1.1.3 Model Transmembrane Proteins and Peptides

Two important model TMPs and transmembrane peptides will be discussed in detail: rhodopsin and gramicidin. Previous findings related to these transmembrane entities are important for the understanding of the work in this dissertation

1.1.3.1 Rhodopsin

Rhodopsin is an extremely well-characterized GPCR.^{9, 20, 21} Like all GPCRs it has 7 transmembrane helices. Upon yellow light activation, 11-*cis* retinal, a chromophore buried in the center of rhodopsin, isomerizes to the all-*trans* configuration through a photocycle of many steps. The key event in this photocycle is the metarhodopsin I (MI) to metarhodopsin II (MII) transition. An elongation of the entire TMP normal to the

bilayer plane is associated with the MI/MII transition. Figure 1.5 illustrates this transition.

1.1.3.2 Gramicidin

Gramicidin is a well-studied ion channel formed from two transmembrane peptides.²²⁻²⁴ Each of the peptides individually diffuses in two dimensions within the lipid bilayer, as shown in Figure 1.6. When two peptides in opposing monolayers line up, an ion channel is formed that allows passive transport of monovalent cations.

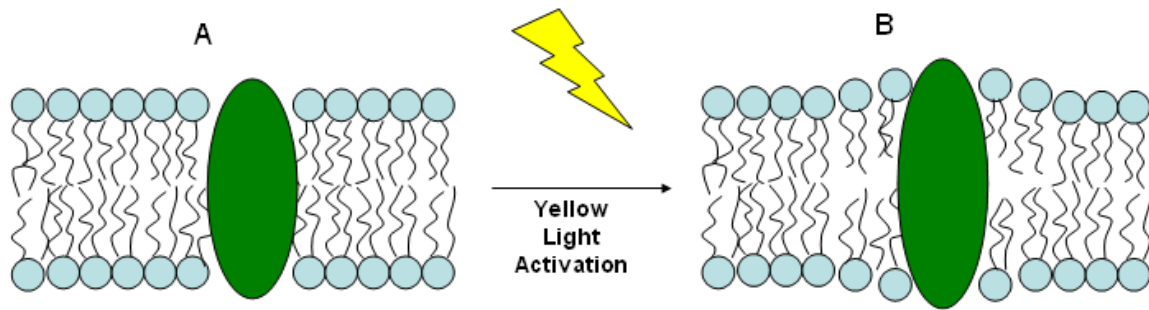


Figure 1.5. Rhodopsin (green) in a lipid bilayer undergoing MI/MII transition upon absorption of yellow light. A) Rhodopsin before being photoactivated. B) After absorbing yellow light, rhodopsin elongates normal to the plane of the lipid bilayer.

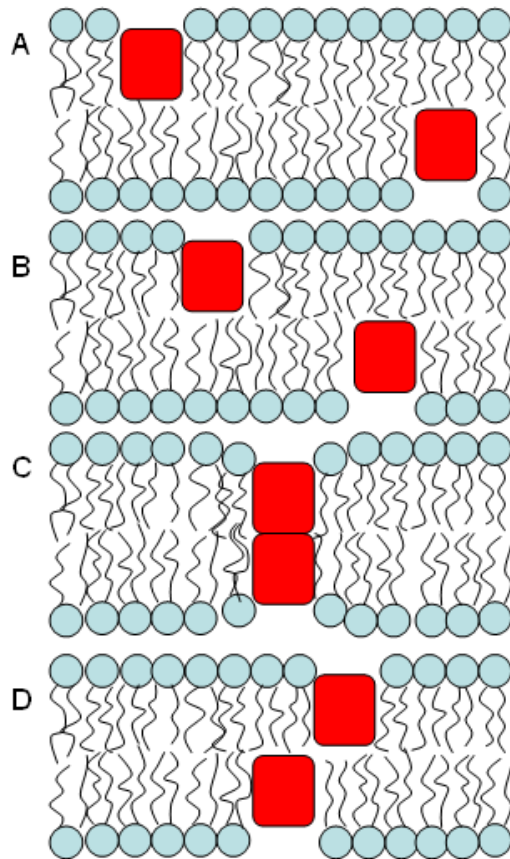


Figure 1.6. Gramicidin (red) diffusing in a lipid bilayer. A) and B) show gramicidin peptides separately diffusing in the bilayer. C) When the peptides line up properly, an ion channel is formed across the membrane. D) Eventually the peptides separate and diffuse away from each other.

1.2 Lipid Membrane Properties

The physical structure and phase of a particular lipid molecule helps dictate the types of lipid aggregates that form.^{7, 25, 26} The aggregate material properties of lipid bilayers influence the function of any associated membrane-bound or TMP/peptide in that membrane.^{9, 10, 27} This Section includes brief descriptions of lipid bilayer properties that are essential to understand the problems being investigated in this dissertation. Phase transition, spontaneous curvature, and lipid polymorphism are known or assumed for the novel lipid systems that were studied. Fluidity and mechanical properties of these systems were measured in this work.

1.2.1 Phase Transition

Lipid bilayers can exist in different phases based on temperature.^{1, 8, 28, 29} Generic structures of the common phases are shown in Figure 1.7. A differential scanning calorimetry (DSC) thermogram performed on DPPC (lipid structure in Figure 1.8) is shown in Figure 1.9. At low temperatures, the “gel” or L_β phase is present in lipid bilayers. The L_β is characterized by a high trans/gauche ratio of the lipid tails and has a high conformational order. Some lipids have an even more ordered “sub-gel” phase, L_C , at lower temperatures. Increasing the temperature from the L_β phase results in a small phase transition on the way to the P_β' phase. The “ripple” phase, or P_β' , is characterized by a periodic ripple in the bilayer and is not present in all lipid types. The largest phase transition for lipids occurs upon heating from the P_β' (or L_β , if no P_β' present) to L_α , the “fluid” or “liquid-crystalline” phase. In the L_α phase, there is a low trans/gauche ratio in the tails and low conformational order.

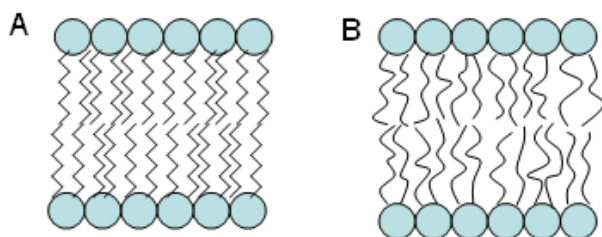


Figure 1.7. Common lipid bilayer phases: A) L_{β} and B) L_{α} .

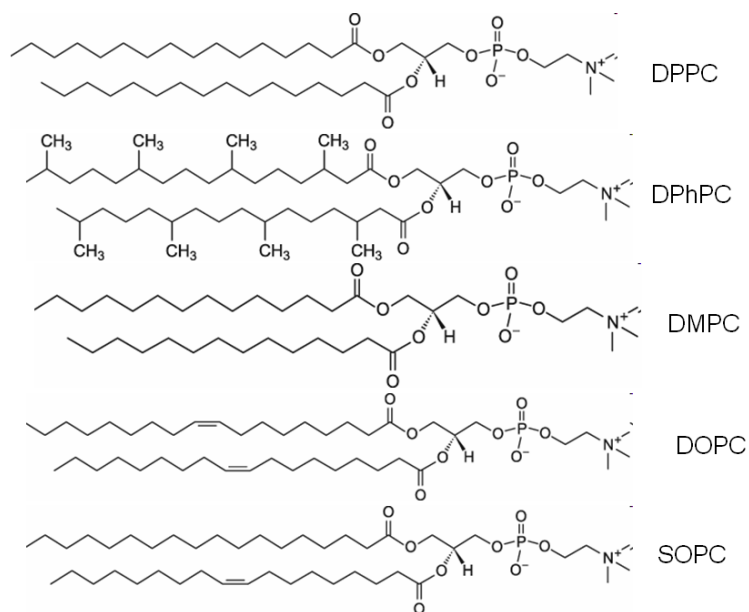


Figure 1.8. Common non-polymerizable lipid structures that will be used throughout this dissertation. Images from www.avantilipids.com.

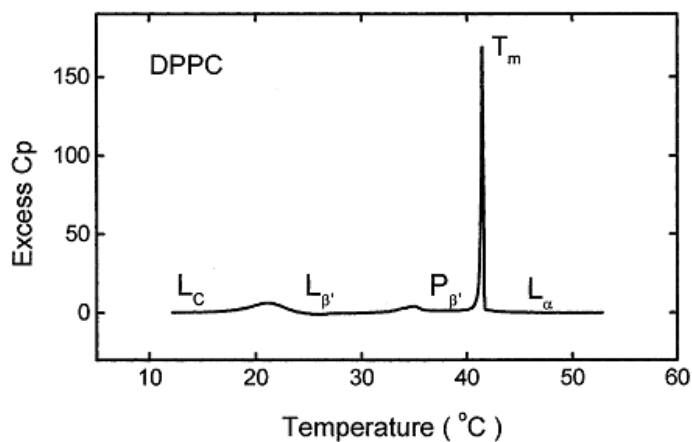


Figure 1.9 DSC thermogram of DPPC. Taken from Ref. 28 with permission.

The large phase transition leading up to the L_α phase (whether it is from P_β' or L_β) is always present in lipid bilayers and is known as the main phase transition temperature, or T_m .^{8, 28, 30} Because the ripple phase is not always present (and has a small change in energy associated with the L_β to P_β' transition even when it is present) the transition associated with T_m is referred to as the gel-to-liquid crystalline or gel-to-fluid phase transition.

1.2.2 Spontaneous Curvature and Lipid Polymorphism

The geometry a lipid aggregate adopts is related to the shape parameter, S , of the lipid or lipids the aggregate is composed of.^{7, 25, 26} S is equal to v/a_0l_c , where v is the hydrocarbon chain volume of a lipid, a_0 is the optimal surface area per molecule, and l_c is the maximum effective length of the hydrocarbon chain. Single-chain surfactants tend to have large headgroups with respect to the volume of the hydrocarbon chain, resulting in shape parameters that are less than $\sim 1/2$. The structures formed from these single-chained lipids tend to be spherical or cylindrical micelles, as shown in Fig. 10. The center of the micelle is hydrophobic in character due to the oily hydrocarbon chains. Double-chain phosphatidylcholine lipids can have shape parameters of $1/2$ -1, which result in spherical vesicles and planar bilayers, as shown in Figures 1.10B-C. The approximately cylindrical packing shape of the lipid is illustrated in Figure 1.10B. Phosphatidylcholines fall into this category. Once the packing parameter is greater than 1, inverted structures, such as the inverted hexagonal phase, will be formed from inverted, truncated cone packing shapes that result from lipids that have small headgroups relative to the hydrocarbon chain volume, as shown in Figure 1.10D.

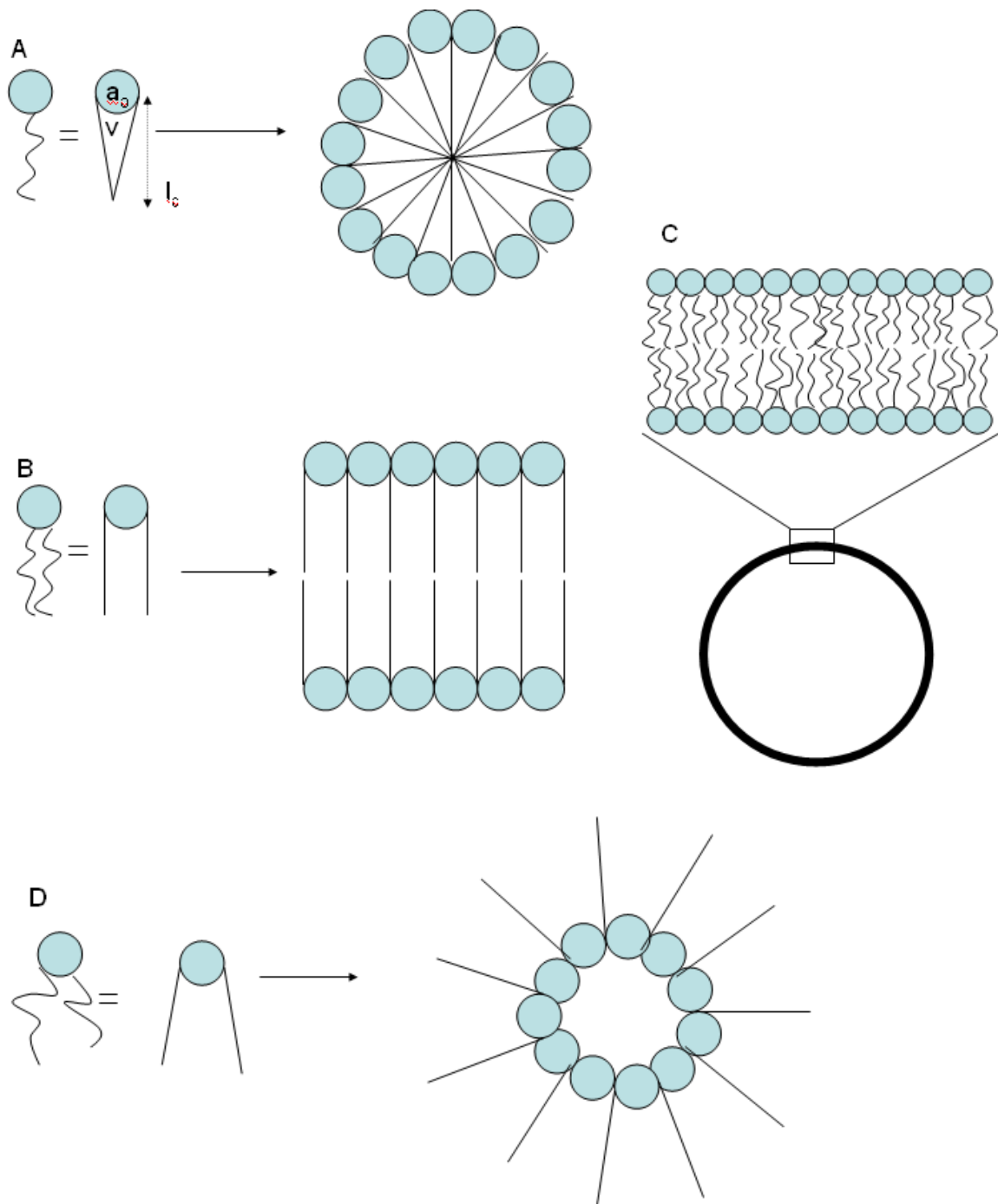


Figure 1.10. Lipid polymorphs. A) A single-chain surfactant and its packing shape resulting from having $S < \frac{1}{2}$. Aggregates of these cone-shaped lipids form micelles. B) A double-chained lipid with a shape factor of $\frac{1}{2}$ -1 will have a near cylindrical shape and form planar bilayer aggregates or C) vesicles. D) When $S > 1$, a truncated, inverted cone shape is formed and the aggregates are in the inverted hexagonal phase.

Unsaturated phosphatidylethanolamines are an example of a lipid with $S > 1$.

Supramolecular structures like those in Figure 1.10A exhibit a positive spontaneous curvature (also known as mean curvature), H_0 , as shown in Figure 1.11.⁹ Negative spontaneous curvatures are found in inverted structures, such as that in Figure 1.10D. A perfectly flat lipid bilayer has $H_0 = 0$.

1.2.3 Fluidity

The ability of lipid molecules in bilayers to laterally diffuse in two dimensions is known as fluidity. As will be described in more detail in Chapter 2, fluidity can be quantified in terms of diffusion coefficients and mobile fractions. The diffusion coefficient quantifies the rate of 2D diffusion in the lipid bilayer, while the mobile fraction measures how much of the membrane is undergoing diffusion. Because membrane fluidity is important for certain membrane proteins to perform their functions, fluidity is a key component of the fluid mosaic model of cell membranes.^{1, 31} Although the concept of the fluid mosaic model has changed since its inception, the importance of the degree of fluidity within specific portions of a membrane is even greater.³² (For a recent review of the fluid mosaic model, see Ref. 32 and references therein.) Diffusion measurements have revealed compartmentalization and dynamic organization of lipid membranes and associated proteins.^{12, 33, 34} This suggests that patches of membrane (that might be diffusing as well) require different diffusion characteristics to properly support the function of the various proteins that they incorporate.

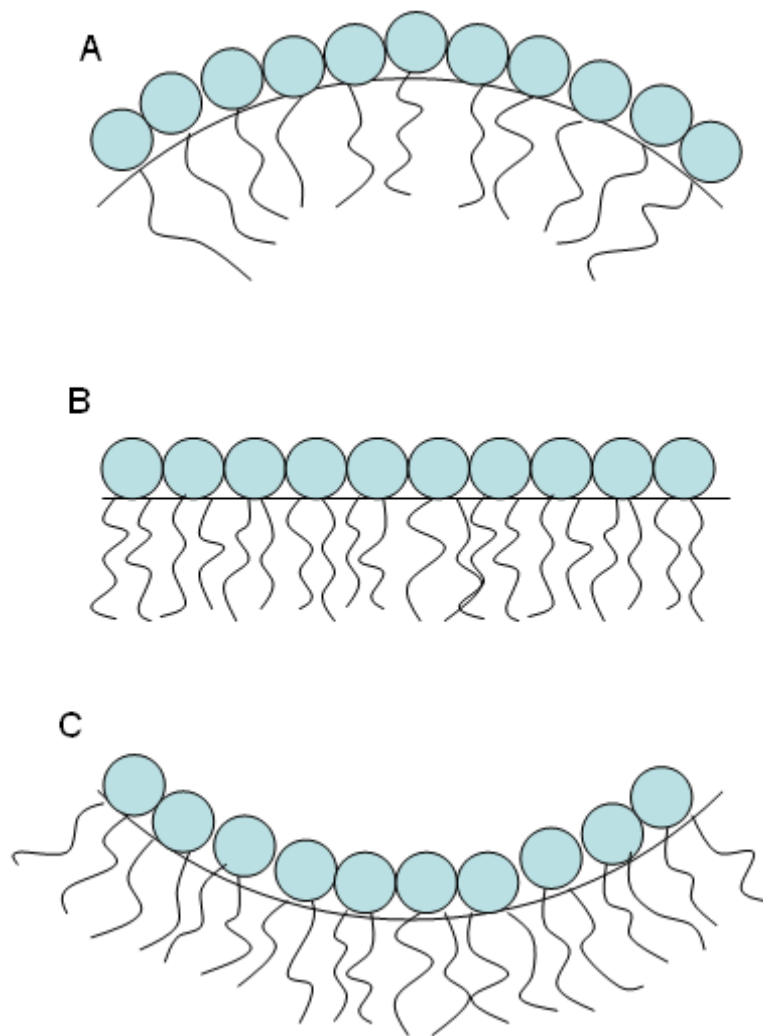


Figure 1.11. Spontaneous curvatures of monolayers: A) positive curvature, B) zero curvature, and C) negative curvature. Redrawn from Ref. 9.

1.2.4 Mechanical Properties

Mechanical properties of membranes are those that quantify the ‘toughness’, or resistance to deformation of the membrane and include the elastic area expansion moduli, elastic bending moduli, and strength.⁸ Figure 1.12 shows the modes of membrane deformation associated with the elastic area expansion modulus and the elastic bending modulus.³⁵ Mechanical properties have been found to vary for different lipid compositions that are found in cell membranes.³⁶

1.2.4.1 Stretching

The elastic area expansion modulus, K_a , is a measure of the tension needed to increase the area per molecule in the plane of the bilayer. It is the resistance to lateral stretching of the bilayer, as illustrated in Figure 1.12A.⁸

1.2.4.2 Bending

The elastic bending modulus, k_c , is a measure of the energy required to bend a bilayer out of plane, as shown in Figure 1.12B. As mentioned above, however, H_0 of the membrane also affects the bending of a membrane. To combine the effects of H_0 and k_c , the curvature free energy per unit interfacial area, g_c , is used as follows from the work of Brown:⁹

$$g_c = k_c(H-H_0)^2 + k_G k \quad (1.1)$$

where H is defined as $(c_1 + c_2)/2$, k_G is the Gaussian curvature, and k is defined as $c_1 c_2$.

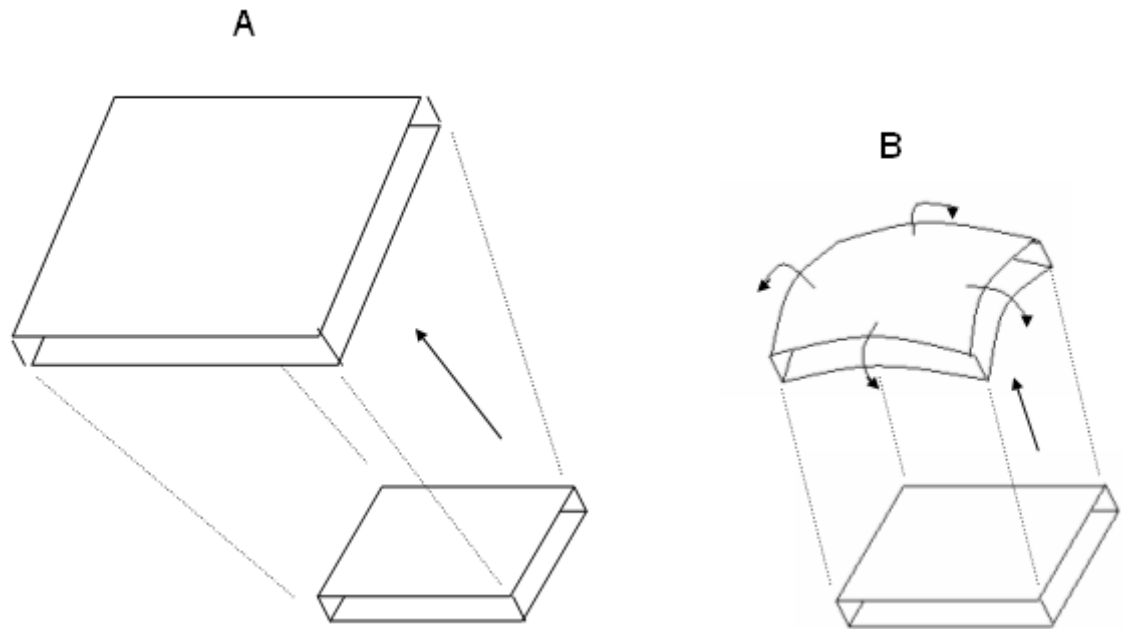


Figure 1.12. Elastic moduli of a lipid bilayer. A) depicts the increase in area per lipid molecule under applied force (tension), which has the area expansion modulus, K_A associated with it. B) shows the deformation of a lipid bilayer related to the elastic bending modulus, k_c .

The curvatures, c_x , where $x = 1$ or 2 , are $1/R_x$, where R_x are the principal radii associated with the lipid/water interface.^{8,9} The Gaussian curvature incorporates the effect of H_o and monolayer bending moduli and is estimated to be $\sim -0.8 k_c$.³⁷

For perfectly flat bilayers, $c_1 = c_2 = H_o = 0$, resulting in $g_c = 0$. Local variations in curvature occur in ‘flat’ bilayers for numerous reasons including thermal fluctuations, which will be the basis of the bending modulus experiments described in Chapter 4, and membrane deformations resulting from TMP activity, like that introduced in Section 1.1.3.1 and further discussed in Section 1.6.3. According to equation (1.1), curvature of a lipid bilayer depends on three material parameters, H_o , k_c , and k_G , which are bilayer composition dependent. While H_o can be assumed based on the shape parameter,⁷ k_c and k_G need to be measured. A few techniques are available for quantitatively measuring k_c and have provided numerous comparable values.³⁷ Estimates and measurements of k_G , on the other hand, are more rare.³⁷

1.2.4.3 Lysis Tension

The resistance of a lipid bilayer to breaking is its strength. This can be determined using the lysis tension of giant unilamellar vesicles, as will be described in detail in Chapter 4. Basically, it is the measure of how much tension needs to be applied to rupture a vesicle of a given composition.

1.3 Lipid Bilayer Platforms for Study

Lipids can be made to form artificial bilayer membranes in many different geometries. The term ‘artificial’ refers to the fact that the architecture is manmade. The lipids in artificial membranes can be and usually are naturally occurring lipids. Three common architectures will be described: vesicles, planar supported lipid bilayers, and black lipid membranes.

1.3.1 Vesicles

A lipid bilayer that forms a spherical structure that separates an internal aqueous compartment from the external aqueous solution is a vesicle, illustrated in Figure 1.10C. Vesicles are grouped into categories based on their size and their lamellarity.^{1, 38} Vesicles composed of more than one lipid bilayer are multilamellar vesicles (MVs) while those made of only one bilayer are unilamellar vesicles. Small unilamellar vesicles (SUVs) are those with diameters less than about 100 nm. Large unilamellar vesicles (LUVs) can range between ~ 100 nm and ~500 nm. Finally, micron-sized vesicles are named giant unilamellar vesicles (GUVs) and can be used as artificial cell analogues.³⁹

1.3.2 Planar Supported Lipid Bilayers

A planar lipid bilayer can be formed on a flat, hydrophilic substrate as shown in Figure 1.13. In these planar supported lipid bilayers (PSLBs), the lipid headgroups of the lower leaflet are separated from the substrate by a 1-2 nm water layer.⁴⁰ The benefit of this geometry is the wide-variety of surface-sensitive methods, which can be used to investigate events at the bilayer/surface interface.^{41, 42}

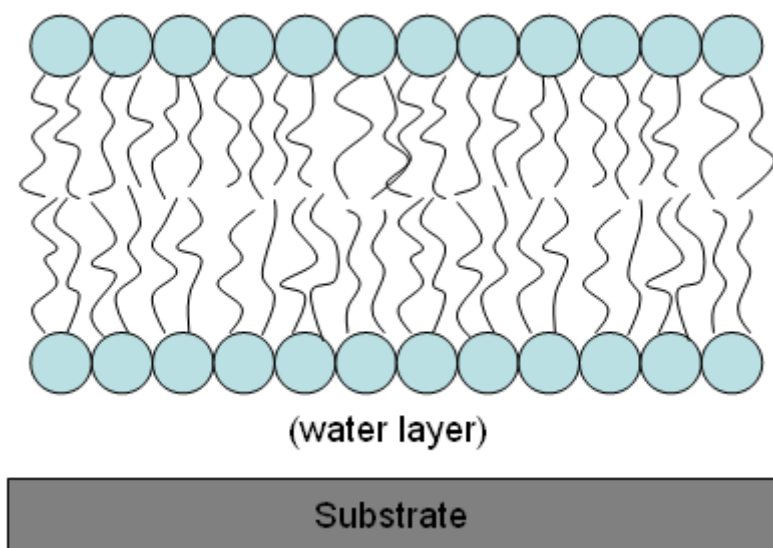


Figure 1.13. Depiction of a PSLB on a substrate surface.

1.3.3 Black Lipid Membranes

Another commonly used lipid bilayer geometry is the black lipid membrane (BLM). Here, a lipid membrane is suspended across an aperture that has aqueous solution on either side.⁴³⁻⁴⁶ Electrodes on either side of the membrane can be used to perform electrophysiological measurements on the membranes themselves and any membrane proteins. Figure 1.14 illustrates a BLM geometry.

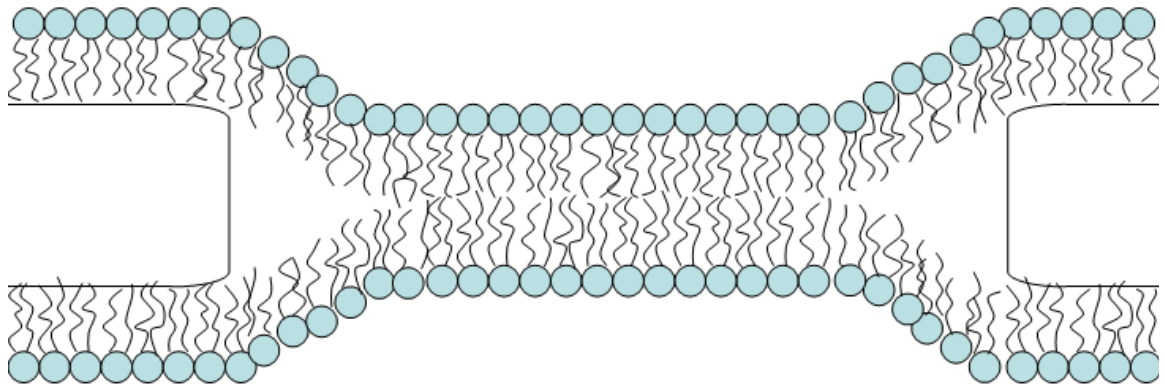


Figure 1.14. Illustration of a BLM spanning a pore formed in a hydrophobic substrate.

1.4 Bilayer-transmembrane Protein Biosensors

A very important reason for studying lipid bilayers is their necessity in the function of TMPs. As described in Section 1.1.2, TMPs are important in cell signaling and disease states. In order for TMPs to function properly, a lipid bilayer environment is necessary. As a result of this, much research has been dedicated to creating novel lipid matrices for biosensors that can incorporate functional TMPs.^{13, 47-54}

1.4.1 Biosensor Architectures

In general, a biosensor that would harness the specificity of actual TMPs requires a bilayer capable of supporting the TMP, as shown in Figure 1.4. This TMP-bilayer can be in PSLB form, sitting either directly on top of glass or some type of hydrophilic sensing substrate.^{48, 49} The PSLB could be tethered to the surface of an electrode.^{47, 48, 52, 54} A BLM could also contain the TMP, spanning the opening of a micro- or nanopore.^{13, 51, 53} Electrochemistry, electrophysiology, or spectroscopy could potentially be used to probe the function of the TMP after creation of these architectures.

1.4.2 Drawbacks to Artificial Lipid Bilayers

One difficult aspect of creating these sensors, however, is the fact that artificial lipid bilayers are not particularly stable.⁵⁵⁻⁵⁷ Exposure to surfactants, air, and organics can damage artificial lipid membranes as can mechanical disruptions and long term storage, because lipid membranes are held together by only non-covalent intermolecular forces. Although there are several ways to address the problem of lipid bilayer instability

in biosensors, this dissertation will expand upon one of them: the polymerizable lipid approach.⁵⁸⁻⁶²

1.5 Polymerizable Lipids

The basic idea behind using polymerizable lipids is that by introducing covalent bonds between the lipid monomers, a more robust lipopolymer membrane will be formed. The hope is that the chemical characteristics required to support the function of inserted TMPs will be maintained, because the monomer structures will be similar to natural lipid structures.

1.5.1 Polymerizable Groups

Numerous polymerizable groups have been introduced into the tails and headgroups of lipids throughout the 30 year history of synthesizing polymerizable lipids.⁶³⁻⁶⁵ A few common polymerizable groups are shown in Figure 1.15. These polymerizable groups can be introduced into numerous places in a lipid molecule, as depicted in Figure 1.16.⁶⁶ Lipids can have polymerizable groups in their tails or attached to the headgroup. In the tails, the polymerizable groups can be nearer or further from the headgroup. A polymerizable group can be in one or both hydrocarbon chains in the same or different positions. Figure 1.17 illustrates some possible polymer geometries, which depend on the location of the polymerizable group. For instance, a lipid with a polymerizable group located in the tail can form polymers similar to those in Figures 1.17A and 1.17B. The difference between the bilayers would be whether or not the lipid monolayers interdigitate enough to have polymerization between the two monolayers, as in Figure 1.17B, or if only intramonolayer polymerization takes place, as in Figure 1.17A. Figure 1.17C is an example of a polymer geometry formed when the

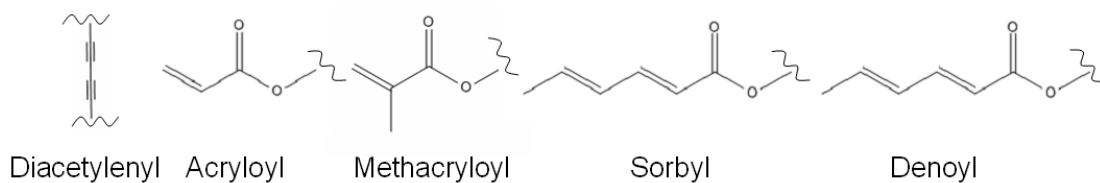


Figure 1.15. Common polymerizable groups.

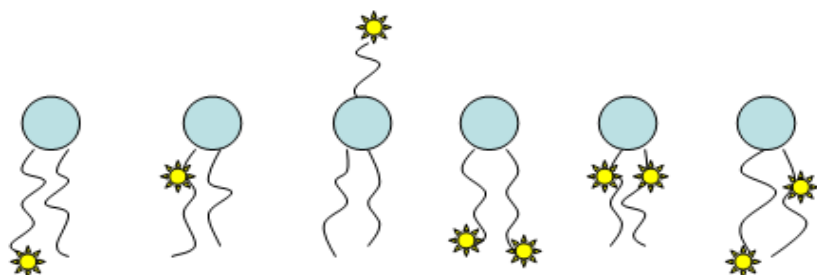


Figure 1.16. Examples of lipid polymerizable group locations. Stars indicate polymerizable groups.

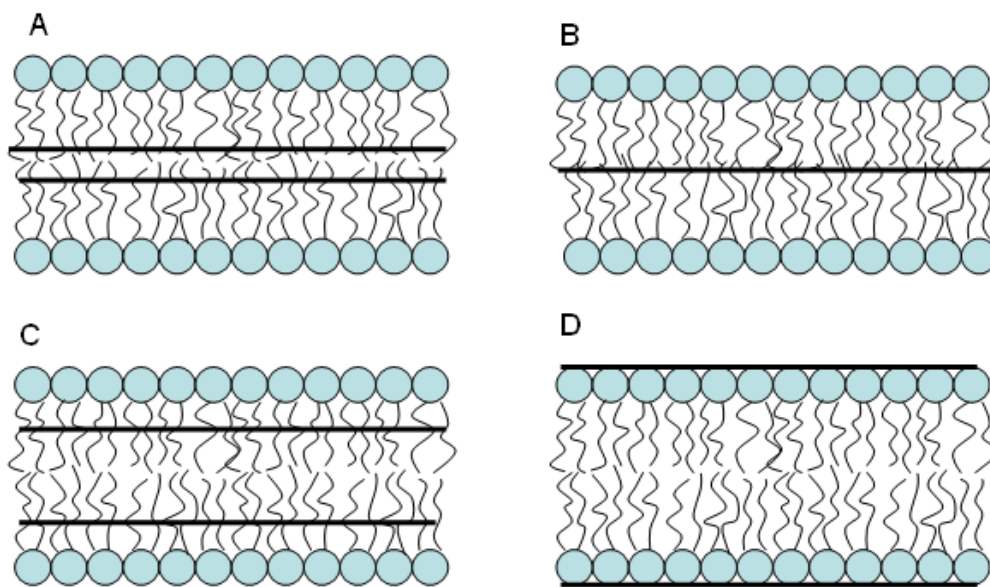


Figure 1.17. Potential lipopolymer geometries. A) and B) show polymer geometries that can form from having polymerizable groups at the distal ends of the tails, where A) exhibits no interdigitation of the tails between the monolayers, while B) shows interdigitation between the tails of different monolayers. C) Lipids with polymerizable moieties attached at the proximal ends of the tails form two distinct polymer networks in different leaflets. D) Headgroup polymerization also shows two separate polymer networks. This image is based on Ref. 66.

polymerizable group is located nearer to the headgroup. In this case, two separate polymer networks will form. Figure 1.17D, illustrates polymerization of a headgroup polymerizable lipid bilayer.

The number of polymerizable groups per lipid monomer is also important. If there is only one group per monomer, only linear polymers are formed, as shown in Figure 1.18A. Two polymerizable groups per monomer results in cross-linking as in Figure 1.18B.

Two of the earliest researched polymerizable lipid types were those containing methacryloyl and diacetylene moieties in the tails.⁶⁷⁻⁶⁹ One potential drawback to using methacrylates is their stiffness at room temperature,⁶³ which might affect how well they can incorporate TMPs. Also, diacetylenes could only be polymerized in the gel phase, limiting their utility.⁷⁰ A potential solution to both of these problems is the use of the more rubber-like dienoyl lipids shown in Figure 1.19, which are capable of being polymerized in multiple phases. The denoylPCs (mono-denPC and bis-DenPC) have polymerizable groups near the PC headgroup in one or both tails. The sorbylPCs (mono-SorbPC and bis-SorbPC) have polymerizable moieties in the distal ends of one or both tails. In addition, these dienoyl lipids retain the PC headgroup that is believed to be a factor in imparting resistance to nonspecific adsorption⁷¹⁻⁷³ and has a shape factor conducive to bilayer formation.

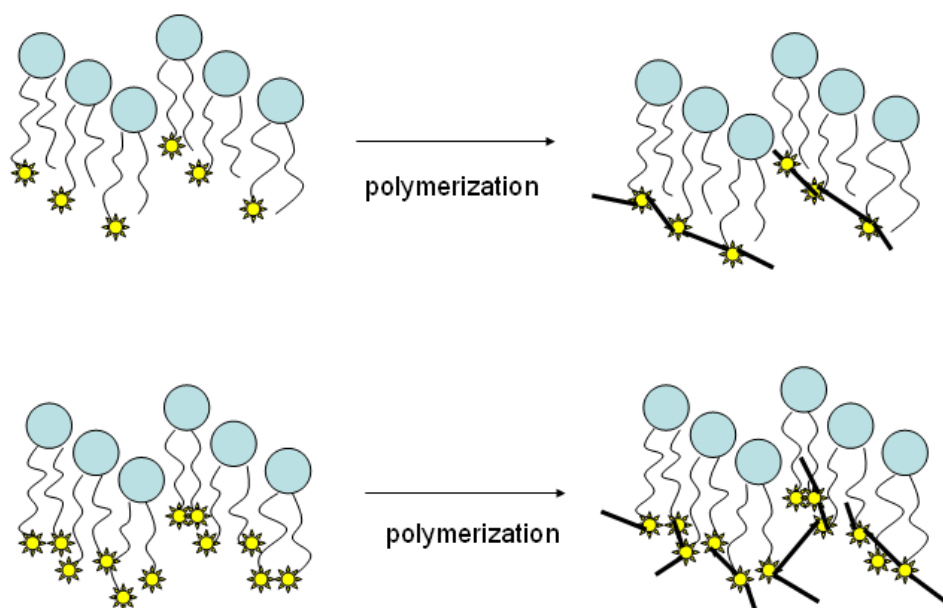


Figure 1.18. Linear and crosslinked polymers formed from mono- and bis-substituted lipids. A) illustrates how polymerization of mono-substituted lipids creates linear polymers, while B) shows how polymerization of bis-substituted lipids makes cross-linked polymers. This image is based on Ref. 63.

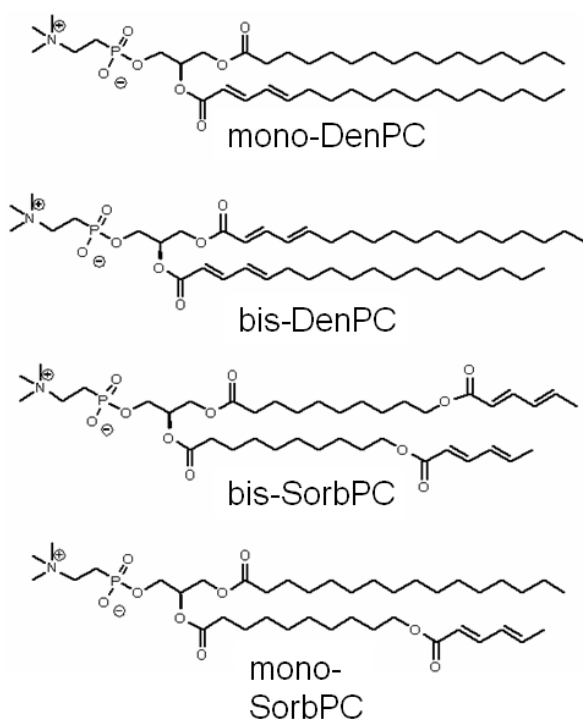


Figure 1.19. Structures of polymerizable dienoylethanolphosphatidylcholine lipids.

1.5.2 Polymerization Methods

Three common ways to polymerize dienoylPCs are: UV-photopolymerization (referred to as UV-polymerization hereafter), redox radical initiated polymerization (redox-polymerization), and γ -irradiation.⁷⁴⁻⁷⁶ However, only UV-polymerization and redox-polymerization will be discussed in this dissertation.

1.5.1.1 UV-polymerization

The dienoyl moieties in polymerizable lipids absorb light in the 250-260 nm region. Irradiation of these lipids with a low pressure mercury lamp (~ 254 nm) causes disappearance of the monomer band and an increase in absorbance at ~ 195 nm.⁷⁵ Usually, oligomers of the 1,4 product are formed, as shown in Figure 1.20.^{63, 75, 76}

1.5.1.2 Redox-polymerization

Depending on the polymerization conditions (monomer/initiator ratio, temperature, initiator identity), various polymer sizes could be produced using redox-polymerization.^{75, 76} Again, the 1,4-product was usually formed by redox-polymerization.⁷⁵ In this work, NaHSO₃/K₂S₂O₈ was used to initiate polymerization at a given monomer/initiator ratio at varying temperatures. Tsuchida et al.⁷⁶ listed the radical producing reactions involved in polymerization using NaHSO₃/K₂S₂O₈:



The radicals are quenched by the following reactions:

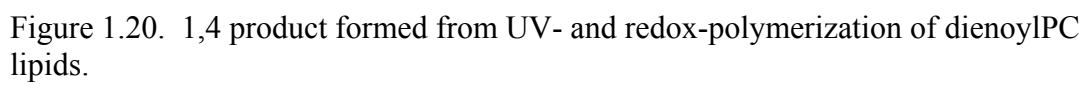




Polymerization of mono-DenPC using UV- and redox-polymerization showed that redox-polymerization resulted in larger polymers.⁷⁵

1.5.3 Improved Lipid Bilayer Stability with Poly(lipids)

As was mentioned earlier in this Section, it is important to create stable membranes for biosensor applications. Here, improvements in the stability of artificial polymerizable dienoylPC membranes will be discussed. The stability of lipopolymer films formed from dienoylPCs was investigated using atomic force microscopy (AFM), contact angle, ellipsometry, fluorescence, solubility studies, and x-ray photoelectron spectroscopy.^{57, 71, 72} These revealed that redox-polymerization of bis-SorbPC and bis-DenPC created films that were capable of surviving a rinsing and drying process. Redox-polymerized mono-SorbPC films were partially damaged after rinsing and drying. UV-polymerized bis-SorbPC film results were contradictory, showing that entire films or partial films survived crossing the air/water interface. UV-polymerized bis-DenPC films were damaged after crossing the air/water interface. Additionally, redox-polymerized bis-SorbPC films were not damaged after 10 minutes of sonication in 1% Triton X-100 detergent or even immersion into common organic solvents. UV-polymerized bis-SorbPC films were analyzed by XPS and were found to have a C/N element ratio indicative of undamaged films, suggesting that these films are stable even in high vacuum.



More recent work by Heitz et al. measured the stability of the polymerizable lipids shown in Figure 1.19 in BLMs.^{43, 77, 78} In this BLM geometry, a bilayer was suspended across a micron-sized aperture at the end of a modified micropipette with buffer in contact with both sides of the bilayer. UV-polymerization increased the lifetimes of BLMs, as measured by electrophysiology experiments, from 1-4 hours to 2-3 days for mono-SorbPC, mono-DenPC, and bis-SorbPC, while increasing the lifetime of bis-DenPC BLMs from ~ 4 hours to ~ 3 weeks. UV-polymerization also increased the number of times the air/water interface could be crossed. The most drastic increase in stability was found for bis-DenPC BLMs, which could cross the air/water interface only ~ 3 times before polymerization, but could cross it ~ 70 times after polymerization. Also, BLMs formed from mixtures of bis-DenPC and a non-polymerizable lipid, DPhPC (shown in Figure 1.8), exhibited increased stabilization, but less dramatically than pure bis-DenPC BLMs.

These improvements in the stability and longevity of lipid membranes using dienoylPCs are important for advancing the technology of creating functional TMP-bilayer biosensor platforms.

1.5.4 Transmembrane Protein/Peptide Function in Stabilized Poly(lipid) Bilayers

Several papers in the last decade have addressed whether it is possible to incorporate functional transmembrane proteins/peptides into polymerizable lipid bilayers. Feng et al. inserted thrombomodulin into PSLBs made from monoacrylatePCs on a polyelectrolyte cushion.⁷⁹ Protein function was detected after lipid polymerization and

the films were still intact for up to 28 days (the time period included several crossings of the air/water interface). The ion channel α -hemolysin was found to retain activity in polymerized BLMs composed of mono-substituted diacetylinicPCs by Shenoy and coworkers.⁸⁰ Gramicidin was inserted into BLMs made of mixtures of diacetylinicPC and DPhPC.⁸¹ The polymerized mixed bilayers were able to sustain ion channel activity; however, the lifetime of the BLM was less than an hour. Seuring et al. recently synthesized a new polymerizable single chain lipid analogue with a methacryloyl group in the tail.⁸² Mixtures of DPhPC and the polymerizable lipid were able to sustain gramicidin activity for over an hour when unpolymerized, but polymerization results with the ion channel were not reported.

Work by Subramaniam et al., which focused on the incorporation of rhodopsin into polymerizable membranes, highlights the effectiveness of dienoylPCs.^{83, 84} Unpolymerized PSLBs composed of bis-SorbPC and mono-SorbPC, both with incorporated rhodopsin, exhibited TMP function when unpolymerized and when UV-polymerized. PSLBs formed from bis-DenPC with rhodopsin showed reduced protein function when unpolymerized and no function when UV-polymerized. UV-polymerized bis-SorbPC PSLBs with rhodopsin withstood high vacuum for angle-resolved XPS analysis and revealed that the protein was indeed inserted into the bilayers instead of being adsorbed to the PSLB surface.⁸⁵

Further experimentation with the dienoylPCs revealed that other geometries and transmembrane proteins/peptides worked best with different lipid environments than rhodopsin. Heitz et al. showed that the function of gramicidin was maintained in BLMs

of DPhPC, unpolymerized bis-DenPC, and unpolymerized mixtures of DPhPC/bis-DenPC.⁸⁶ Upon UV-polymerization of the bis-DenPC containing BLMs, function was seen in all BLMs, except those entirely composed of bis-DenPC. Similar results were found for alamethicin, an ion channel forming peptide.⁷⁷ Alamethicin requires aggregates of 3-11 peptides to form a functional ion channel.^{87, 88} Like gramicidin, alamethicin peptides diffuse within the lipid bilayer to form these aggregates. A more recent publication by Heitz et al. investigated the function of α -Hemolysin in BLMs made from each of the lipids shown in Figure 1.19.⁴³ All of the dienoylPCs studied showed functional α -Hemolysin insertion into the membranes. However, after UV-polymerization, bis-SorbPC membranes ruptured. BLMs from polymerized mono-DenPC and mono-SorbPC remained functional for ~2 days, while BLMs from bis-DenPC were functional for ~1 week.

As was shown above, it is important to investigate multiple types of polymerizable lipids, because not all of them will be compatible with the function of all proteins or even the geometry of the lipid bilayers used. For example, Subramaniam and Heitz had investigated some of the same lipids, but Subramaniam et al. had the most success with bis-SorbPC membranes,^{83, 84} while Heitz et al. had more success with bis-DenPC membranes.^{43, 77}

1.6 Dissertation Overview

The overarching topic of this dissertation is the measurement of the physical properties of novel lipid membranes composed of polymerizable lipids, specifically those lipids shown in Figure 1.19. By investigating this series of lipids, the location of the polymerizable group and the number of polymerizable groups per lipid can be varied. Because both mono-substituted and bis-substituted lipids are included, a comparison can be made between linear and cross-linked polymers as well. Sections 1.5.3 and 1.5.4 have shown that lipid membranes can be stabilized and these stabilized membranes can have functional TMPs or transmembrane peptides reconstituted into them; however, not all polymerizable membranes are compatible with all integral membrane proteins/peptides. It is the hope that the physical properties of these polymerizable membranes can be correlated with the functionality of incorporated proteins.

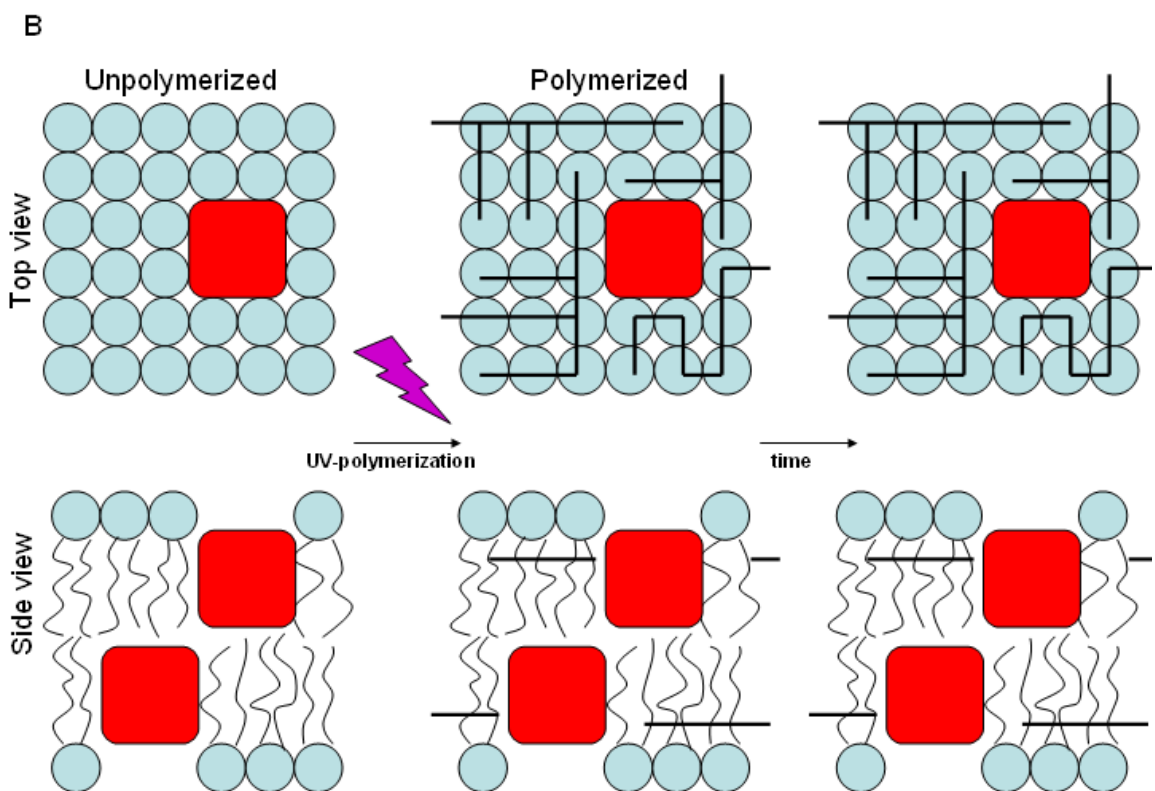
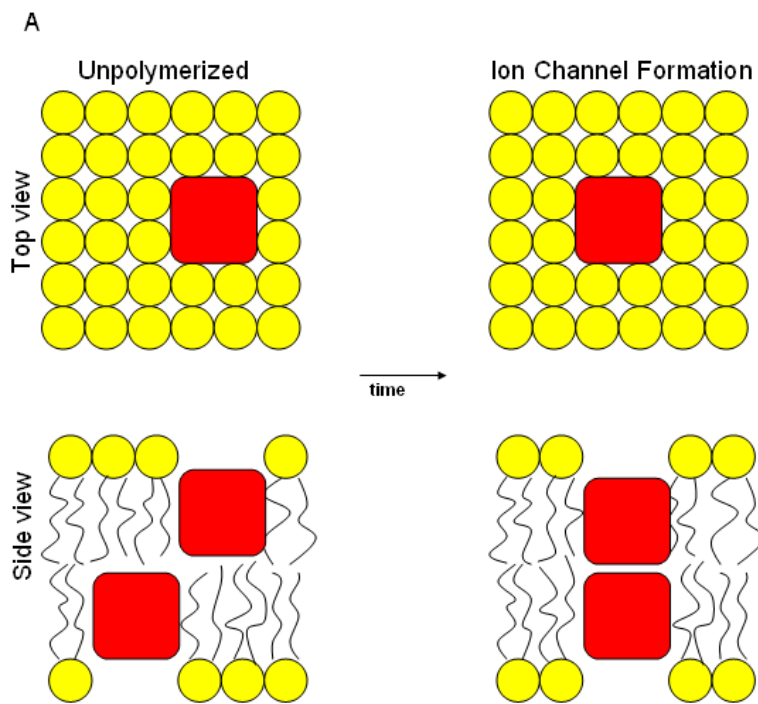
1.6.1 Fluorescence Recovery After Photobleaching Instrumentation and Methods

Chapter 2 describes in detail how the diffusion coefficients of PSLBs composed of polymerizable lipids were determined using the popular fluorescence recovery after photobleaching technique. The methods used for creating PSLBs will be given. The instrumentation used to carry out the experiments will be described. The three ways of running the instrument will also be explained (qualitative and quantitative methods) as will the data-processing used for each method. Possible future improvements to the measurement methods are also included.

1.6.2 Fluidity Measurements of Polymerizable Lipid Bilayers

It has been mentioned that the degree to which proteins/peptides can diffuse in a membrane is related to the proper function of those proteins.^{27, 89-94} As had been described Section 1.5.4, Heitz et al.^{43, 77} had discovered that gramicidin and alamethecin maintained function in DPhPC and unpolymerized bis-DenPC in a BLM architecture. When bis-DenPC was UV-polymerized, neither ion channel was functional. Polymerized mixtures of bis-DenPC/DPhPC retained function, though. It is known that both peptides need a 'fluid' membrane to function, because the individual peptide units in the membrane must diffuse to line up properly.

Figure 1.21 illustrates what is hypothesized to be happening in the completely unpolymerized, fully polymerized, and partially polymerized cases. In the unpolymerized case (for either DPhPC or bis-DenPC), Figure 1.21A shows that two gramicidin peptides are free to diffuse throughout the entire bilayer. With time, two peptides can line up to form an ion channel. Figure 1.21B shows that when a pure bis-DenPC bilayer is polymerized completely, the peptides are now trapped in different portions of the bilayer and unable to come together to form an ion channel. This could be because the diffusion coefficient of the lipid bilayer has decreased so much that the peptides cannot diffuse within the membrane during the observation time. Alternatively, portions of the membrane can still be diffusing, but the peptides are trapped in immobile regions. For the mixed DPhPC/bis-DenPC case, Figure 1.21C shows that although there are polymerized regions of the bilayer, there are still enough unpolymerized portions to allow movement of the peptides around these either slowly diffusing or immobile polymers.



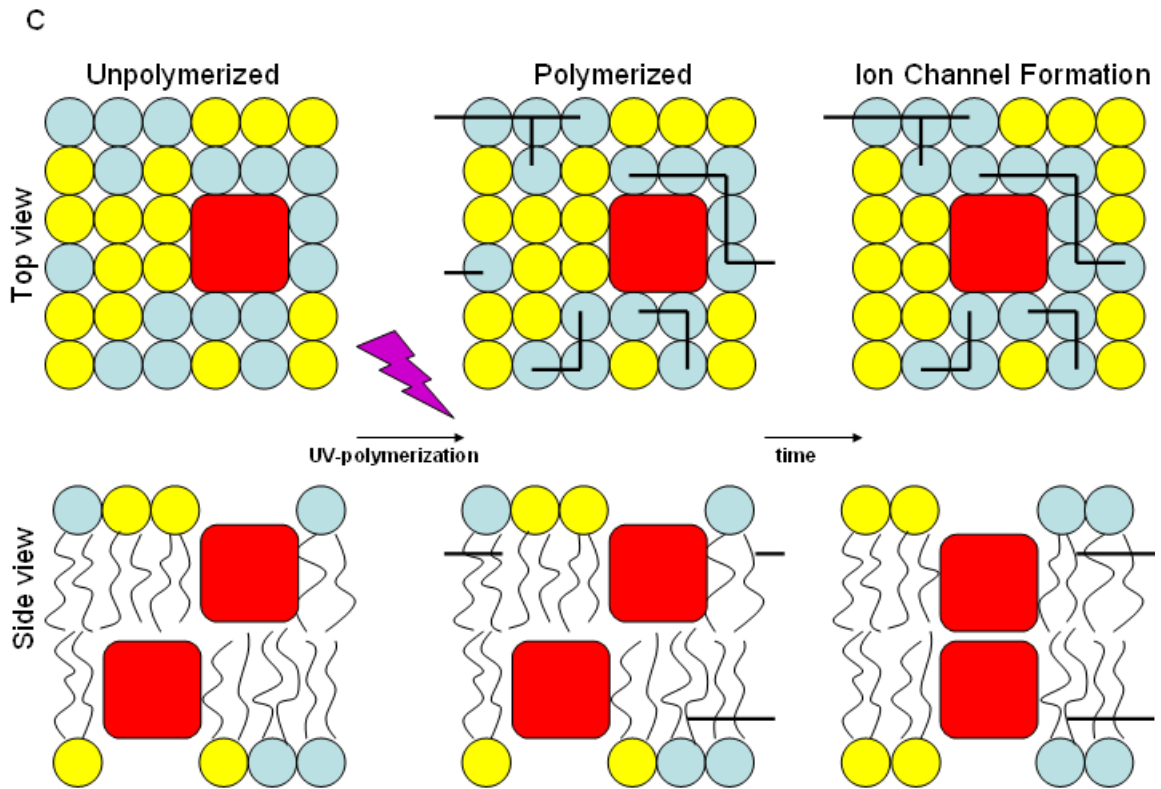


Figure 1.21. Lipid bilayer fluidity is responsible for the function of gramicidin incorporated into an artificial membrane. A) In pure DPhPC (yellow) or unpolymerized bis-DenPC (blue), the gramicidin peptides (red) are free to diffuse throughout the bilayer. In the right column, the peptides line up to form a functional ion channel. B) When a pure bis-DenPC bilayer is UV-polymerized, the entire bilayer is no longer accessible to all peptides, potentially corralling the peptides into separate compartments and not allowing ion channel formation. C) In a partially polymerized bilayer formed from a mixture of DPhPC and bis-DenPC, there is enough fluidity for the gramicidin peptides to diffuse and find each other to form ion channels. The peptides are not completely corralled like in B).

It is hypothesized that a UV-polymerized bis-DenPC bilayer is no longer fluid enough to accommodate the function of alamethicin or gramicidin, while unpolymerized bis-DenPC bilayers and partially polymerized bilayers are fluid enough to support ion channel function. This could be a result of two different occurrences. First, a significant immobile fraction is predicted for UV-polymerized bis-DenPC bilayers compared with unpolymerized, because that would suggest that portions of the bilayer may no longer be accessible for the alamethicin or gramicidin forming peptides to sample. Second, a decrease in diffusion coefficient is also expected since oligomers and polymers are larger in size than lipid monomers and should diffuse more slowly as has been shown for polymerizable acryloyl lipids.⁹⁵ To investigate the fluidity of bis-DenPC and the other polymerizable lipids, Chapter 3 focuses on measuring the diffusion coefficients and percent recoveries of these bilayers using the fluorescence recovery after photobleaching technique described in Chapter 2. The diffusion coefficients for PSLBs above the T_m for unpolymerized, UV-polymerized, and redox-polymerized membranes were measured, varying the polymerization temperature.

1.6.3 Micropipette Aspiration of Giant Unilamellar Vesicles Composed of Polymerizable Lipids

For some TMPs, function includes changing the physical structure of the membrane itself. It has been hypothesized and shown that in order for these proteins to function properly, the mechanical properties of the membrane must be able to tolerate these disturbances.^{11, 96-98} Alternatively, small molecules can alter the physical properties of membranes, which may perturb the function of incorporated proteins.^{22, 99}

Subramaniam et al. showed that sorbylPCs were capable of sustaining rhodopsin function when they were unpolymerized and UV-polymerized, while unpolymerized bis-DenPC bilayers showed attenuated rhodopsin function and poly(bis-DenPC) bilayers were essentially inactive.⁸⁴ The location of the polymerizable groups in sorbylPCs and denoylPCs is different, where denoylPCs have conjugation near the more ordered lipid headgroup and sorbylPCs have conjugation near the more disordered center of the lipid bilayer.¹⁰⁰ Recall that in order for rhodopsin to function, a physical elongation takes place normal to the lipid bilayer plane, as discussed in Section 1.1.3.1. Previous research has shown that increasing the PE content of the lipid bilayer will increase the amount of rhodopsin function in a bilayer.⁹ This is thought to happen because PE lipids have negative H_0 values and are therefore more likely to form the inverted hexagonal phase than PC lipids. As a result, rhodopsin can elongate without (or with less) exposure of its hydrophobic mid-section to the external aqueous solution because the PC/PE bilayer can more easily accommodate the bilayer deformation than just PC lipids. Figure 1.22 shows how the lipid bilayer needs to deform to adapt to the longer hydrophobic transmembrane portion of rhodopsin. In the work of Subramaniam, numerous polymerizable bilayers were compared with each other and it was found that there were distinct differences.⁸⁴ Assuming that bis-DenPC, bis-SorbPC, and mono-SorbPC all have similar shape factors, because they all have PC headgroups, then their H_0 values should be similar. So according to equation (1.1), the difference might lie in k_c or k_G , the bending modulus or Gaussian curvature. Based on what little information is available on k_G ,³⁷ it appears that it scales linearly with k_c and will not be measured.

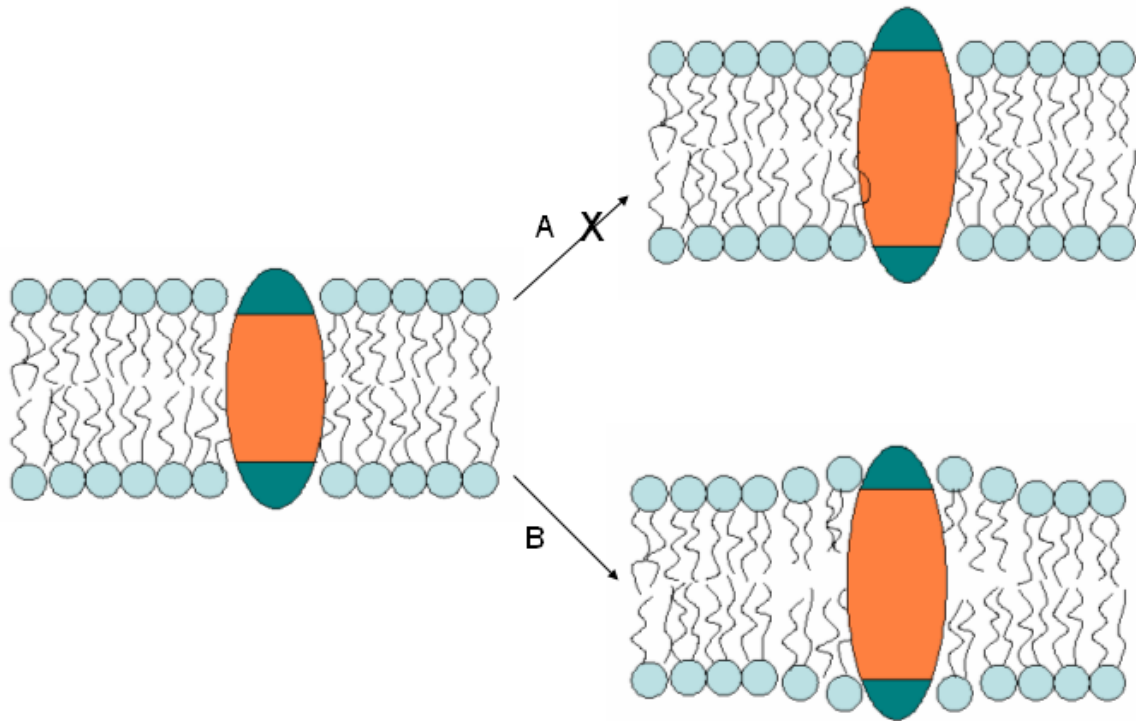


Figure 1.22. Rhodopsin in a lipid bilayer. The blue-green regions of the protein represent the hydrophilic portions and the peach regions represent the hydrophobic sections. Pathway A leads to an elongation of the protein without deformation of the lipid bilayer, which causes an unfavorable interaction of the hydrophobic protein core with the hydrophilic headgroups of the lipids or with water. Due to this unfavorable interaction, there is an X over Pathway A, as this is not expected to happen. Pathway B shows elongation of the protein with deformation of the bilayer that accommodates the lengthening of the hydrophobic protein core.

It is hypothesized that the increase in conjugation in the lipid molecules of bis-DenPC near the headgroup may make it more difficult to bend the bilayer compared to sorbylPCs, which are conjugated in the distal ends of the tails. This means that k_c of bis-DenPC should be greater than for either of the sorbylPCs. This would make it more difficult for the bilayer membrane to allow the elongation of rhodopsin. Also, the absence of function of rhodopsin in polymerized bis-DenPC bilayers suggests that the polymerization might have increased the bending modulus so much that elongation of the protein upon yellow light activation is no longer favorable. To test this hypothesis, Chapter 4 focuses on measuring the mechanical properties of GUVs composed of the polymerizable lipids shown in Figure 1.19. The elastic area expansion moduli, elastic bending moduli, and lysis tensions of these bilayers unpolymerized and UV-polymerized were obtained. In order to accomplish this, a micropipette aspiration system was built and will be described. Instructions on how to make such measurements and analyze the resulting data are included.

1.6.4 Conclusions

Chapter 5 will summarize the diffusion characteristics and mechanical properties findings for the polymerizable lipid bilayers in this dissertation with respect to integral membrane protein/peptide function and lipid bilayer stability. Finally, suggestions will be made for future physical properties measurements for polymerizable lipid systems.

CHAPTER 2: FLUORESCENCE RECOVERY AFTER PHOTOBLEACHING

As mentioned in Sections 1.2.3 and 1.6.2, the fluidity of lipid membranes is believed to be important to many cellular functions.^{91, 93} Three frequently used microscopy techniques to determine the diffusion coefficient of lipids are Fluorescence Correlation Spectroscopy (FCS), Single Particle Tracking (SPT), and Fluorescence Recovery After Photobleaching (FRAP).^{34, 101} (See Refs. 34 and 101 for review and comparison). In FCS, a PSLB sample contains a low concentration of fluorescently-labeled lipids. A small volume spot is illuminated with a confocal microscope and the fluorescence intensity fluctuations are monitored and recorded. Temporal autocorrelation of the signal can yield diffusion coefficients. For SPT, individual lipids are fluorescently-labeled, or labeled with gold colloids in a PSLB. The individual trajectories of these markers are recorded and analyzed to yield the diffusion characteristics of the sample. In the FRAP technique, an area in a fluorescent PSLB is photobleached with intense light from a laser or a lamp. The recovery of fluorescence as a function of time is recorded and analyzed to determine the fluidity of the PSLB.

FRAP was used to carry out the experiments described in Section 1.6.2 for three major reasons. First, processing FRAP data is mathematically more simple than FCS and SPT and does not necessarily require specialized software. Second, the laboratory was already equipped with the necessary major hardware needed to run FRAP experiments. Finally, there is a great wealth of FRAP data in the literature for comparison. FRAP is a decades-old technique (see Ref. 102 for brief historical background of some of the

frequently used FRAP methods) that has been used to measure the diffusion coefficients of various lipids and lipid mixtures on different surfaces and in varying lipid geometries.¹⁰² Diffusion coefficient measurements by the FRAP technique were pioneered by Axelrod et al.¹⁰³ Later, Soumpasis simplified the approach for FRAP accomplished with uniform circular bleach spots.¹⁰⁴ It has also been used to measure protein diffusion and interactions of proteins that are both associated and not associated with the lipid membrane.⁹³

This Chapter describes the construction of a FRAP system used to measure the two-dimensional diffusion of PSLBs, the various modes in which the FRAP system can be used, and the data-processing methods for each mode. Later chapters will refer to the different modes of FRAP described here.

2.1 PSLB Sample Preparation

The FRAP cell used for sample preparation and all FRAP measurements will be described here, along with the basic sample preparation procedure used for all PSLB samples (polymerizable lipid, non-polymerizable lipid, NBD-PC containing, and rhodamine-PE containing).

2.1.1 FRAP Sample Chamber and Sample Heating and Cooling

After a substrate was prepared (described in later sections), it was mounted into the sample chamber, shown in Figure 2.1. An inset within the Teflon wells was the appropriate size to accommodate a rubber o-ring that would seal to the substrate surface. Screws were used to hold the Teflon wells onto the steel mount.

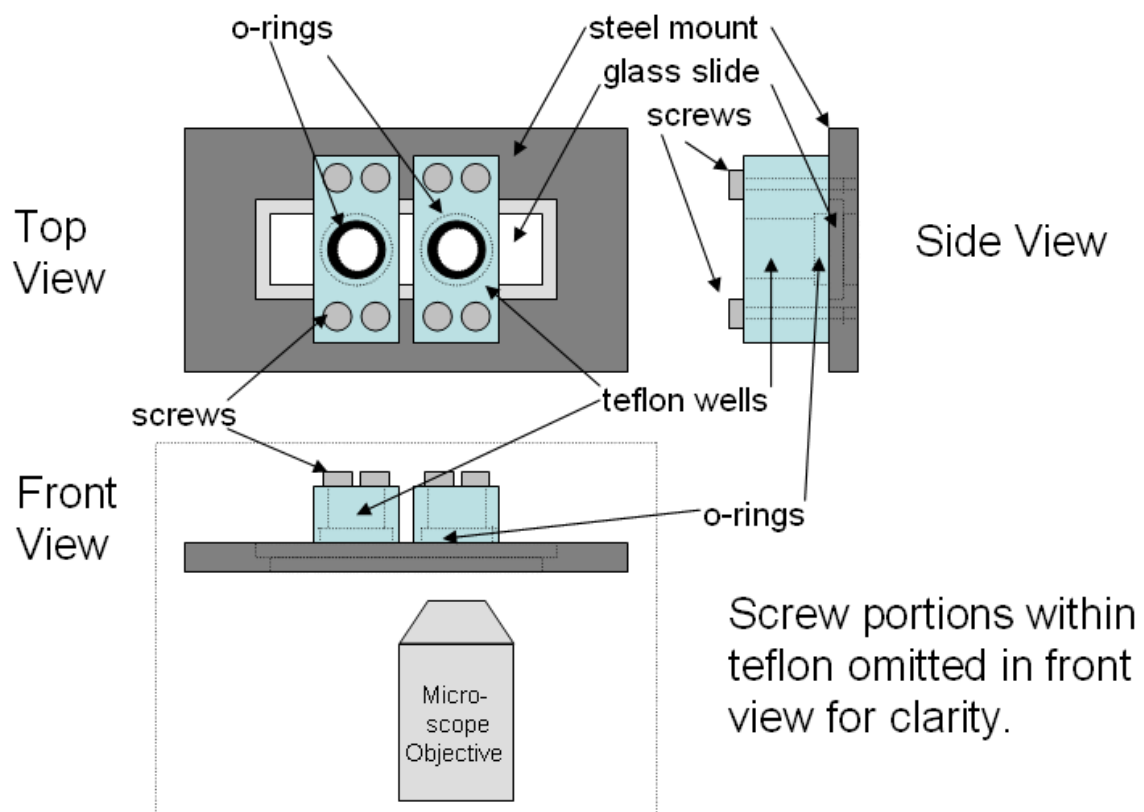


Figure 2.1. Schematic diagram (not to scale) of the FRAP chamber used for all diffusion measurements. A substrate the size of a common microscope slide was sandwiched between the lip of the steel mount and the teflon wells (by an o-ring) to form an open chamber. Vesicles were fused on top of the substrate in the wells to form a PSLB. The chamber was filled with buffer or water after bilayer formation and rinsing to keep the bilayer from being damaged due to solution evaporation.

In order to heat the sample chamber on the microscope stage, a sample heater cover (Bioscience Tools, San Diego, CA) controlled by a temperature controller (TC-1-100 controller, Bioscience Tools, San Diego, CA) in conjunction with heating tape wrapped around the cell (i.e. Cole-Parmer BriskHeat®, Vernon Hills, IL) and controlled by a Powerstat Variac, (Superior Electric Co., Bristol, CT), as shown in Figure 2.2, were used. Both heating elements were not always used. The temperature readout was done by either the temperature controller resistance temperature detectors (RTDs) or a separate RTD (HSRTD-3-100-A-40-E, Omega, Stamford, CT) connected to a 6 ½ digit multimeter (Agilent, Santa Clara, CA). The RTD was placed in between the two FRAP sample chamber Teflon cells as shown in Figure 2.2. Feedback in the heated sample cover was set to “stage” to keep the cover from overheating. As a result, the temperature had to be checked every so often and the settings on the Variac and temperature controller changed if necessary to keep the sample at the appropriate temperature.

In some cases, the sample had to be cooled during polymerization. This was accomplished by placing the FRAP cell on top of the brass temperature control block described in Section 4.3.4.3 and shown in Figure 2.3. An RTD was taped in between the two Teflon chamber holders to measure the temperature and cold water was set to run through the temperature control block.

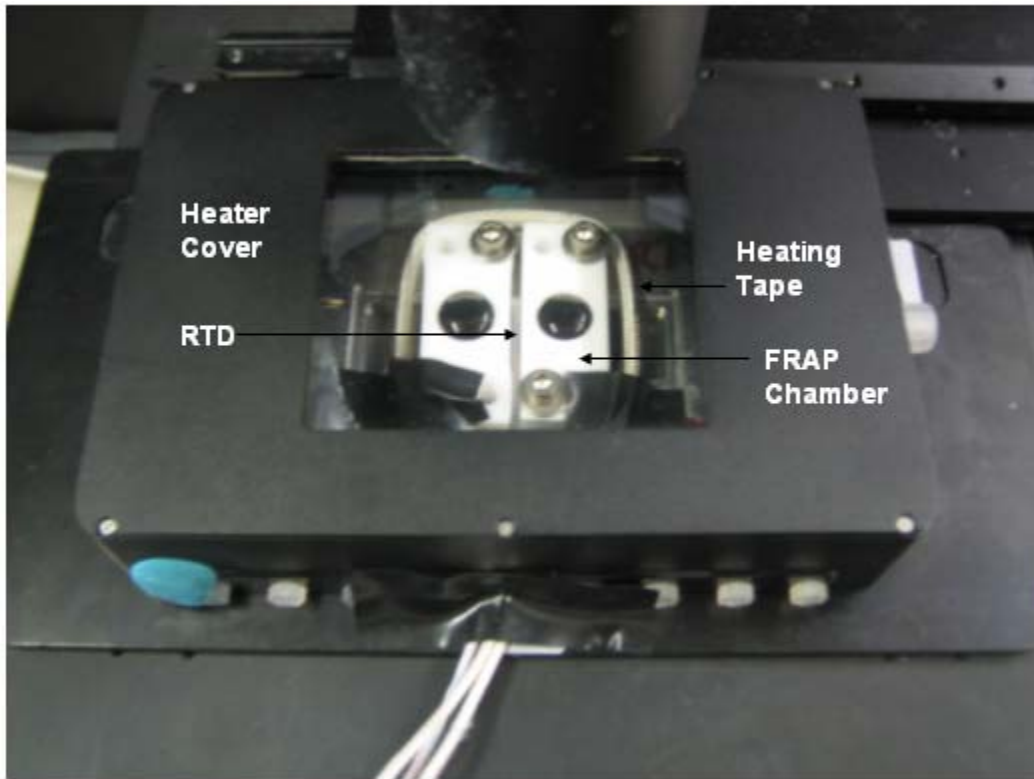


Figure 2.2. FRAP chamber heating set up. A different heating cord is used in this photograph than that listed in the text.

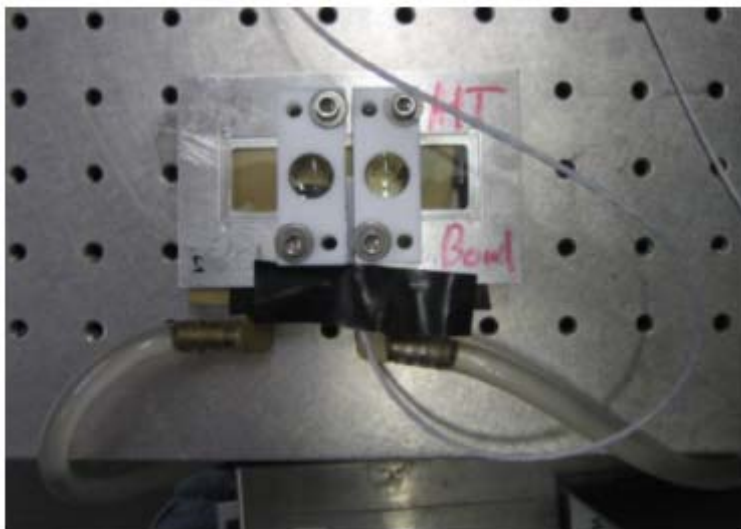


Figure 2.3. FRAP chamber cooling set-up.

2.1.2 PSLB Formation by Vesicle Fusion

A mixture of ~0.6-5 mol % fluorescent lipid and the lipid of interest was prepared in a 4 ml glass vial [amber vials, if polymerizable lipid was being used (Fisher Scientific, Pittsburgh, PA)]. A gentle stream of Ar (g) was used to remove chloroform from the sample. Chloroform was further removed by vacuum drying for 4 hours. If not immediately used, the dried lipid sample was stored at -20 °C. Lipid samples were used within 2 days of drying. Immediately before use, the lipid sample was reconstituted to 0.5-1.0 mg/ml in nanopure water from a Barnstead Nanopure System (Thermolyne Corporation, Dubuque, IA, resistivity of 17.5 Ω-cm or greater) or 10 mM phosphate buffer (EMD, Gibbstown, NJ: sodium phosphate dibasic, anhydrous and sodium phosphate monobasic, monohydrate), pH ~ 7.0. The sample was then sonicated at 25-35 °C (if non-polymerizable) or 5-10 °C above the T_m of the polymerizable lipid in an ultrasonicator fitted with a cuphorn (W-380, Heat Systems Ultrasonics, Inc, Farmingdale, NY or Branson Sonifier 450, Danbury CT with temperature control from VWR Scientific water circulators, Radnor, PA) until the solution became clear and all traces of dried material were visibly gone.^{105, 106} Several drops of sample were then quickly introduced onto the glass surface inside one of the sample chambers depicted in Figure 2.1 in the dark. The sample chamber was heated 5-10 °C above T_m prior to addition of sample drops. Vesicle fusion was allowed to occur for 30 minutes above the T_m .^{42, 107-109} Then, the chamber was rinsed with at least 20 ml of nanopure water or phosphate buffer. Rinsing was accomplished by slowly and carefully adding solution to the sample

chamber wall until the chamber was filled and then carefully withdrawing the solution until only a shallow pool was left on the bottom. This filling and withdrawal were repeated until all 20 ml of solution had been rinsed through the chamber. For observation or measurement, the chamber was completely filled with either water or buffer to keep the sample from dehydrating. The polymerizable lipid samples were reheated to above the T_m after rinsing. Epi-fluorescence microscopy was used to check the condition of the PSLB after rinsing and reheating. A featureless, uniformly fluorescent image was present if a good PSLB had been formed, as in Figure 2.4. After confirmation of a useable PSLB, the sample could be polymerized (when composed of polymerizable lipids), as will be discussed in later chapters.

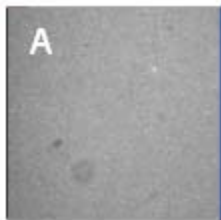


Figure 2.4. Fluorescence image ($125\ \mu\text{m} \times 125\ \mu\text{m}$) taken with a 20x objective of an unpolymerized mono-SorbPC PSLB with 0.6 mol% rhodamine-PE doping. This is an example of a uniformly fluorescent PSLB used for FRAP measurements. The large dark blemishes are spots on the CCD, not flaws in the bilayer, and are present in all images.

2.2 Qualitative FRAP

Qualitative FRAP is a less complex and potentially faster way of determining if a sample is fluid than quantitative FRAP. An actual diffusion coefficient is not calculated in qualitative FRAP. In this Section, the instrumentation used for all FRAP experiments will be described. The protocol for performing qualitative FRAP will be outlined and example data will be presented.

2.2.1 FRAP Instrumentation

A diagram of the instrumentation can be found in Figure 2.5 along with the optical path of the laser beam. The sample was photobleached with an Innova 70 argon ion laser (Coherent, Santa Clara, CA) water-cooled by a liquid/liquid recirculator system (Neslab Coolflow system II, Portsmouth, NH) at 488 nm. A 200-300 mW beam was used, measured after the circular gradient neutral density filter. The beam power was measured using a Coherent 210 power meter (Santa Clara, CA). Five mirrors (3 free-standing and 2 in a beam steerer) were used to direct the bleach beam into the rear port of a Nikon TE2000-U inverted microscope (Nikon Instruments, Inc, Melville, NJ) with Plan Fluor Phase contrast objectives (ELWD 40x/0.60 phase2 DM ∞ .0-2 WD 3.7-2.7, ELWD 20x/0.45 phase1 DM ∞ .0-2 WD 7.4, ELWD 4x/0.13 ∞ /- WD 17.1). A laser line specific filter cube (488 nm, Chroma Technology Corp., Bellows Falls, VT) was used to filter the laser line and direct the beam into the microscope objectives. A mechanical shutter (Uniblitz, Rochester, NY) controlled by a shutter driver (VMM-D3, three-channel, Uniblitz, Rochester, NY) was used to control the laser bleach time.

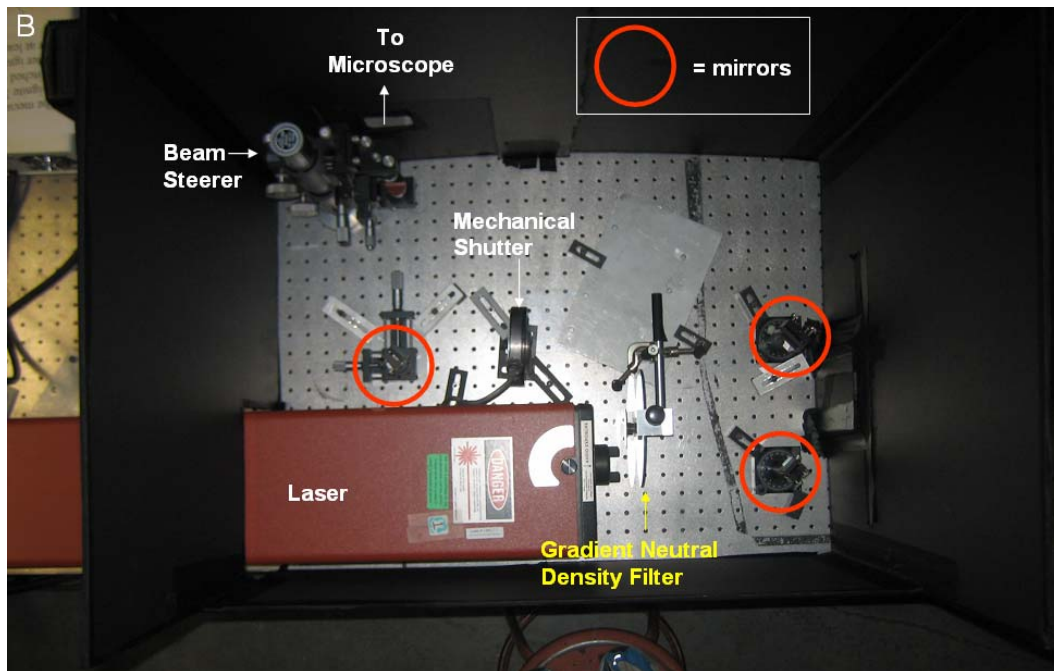
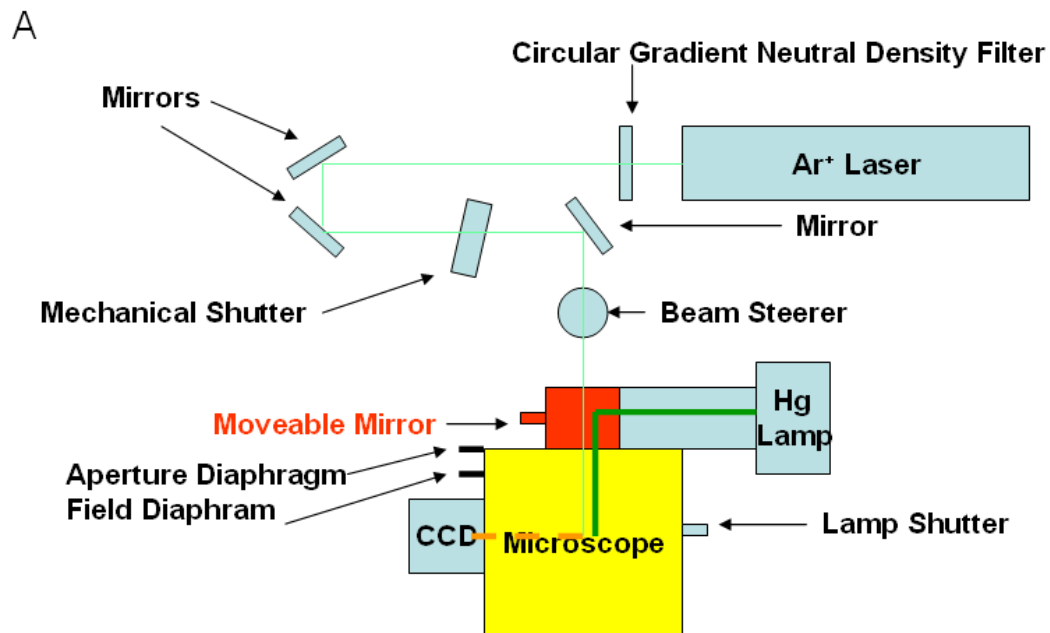


Figure 2.5. FRAP system. A) System schematic. The blue-green line represents the path of the bleach light if the laser is being used to irreversibly photobleach the sample. The thick green line is the excitation from the lamp after the moveable mirror is inserted into the beam path. The dashed orange line is the path of the emitted light during data acquisition. B) Photo of FRAP system.

A 100 W mercury lamp (USH-103S, Ushio, Cypress, CA, with a Chiu Technical Corp. Mercury-100W M-100T power supply, Kings Park, NY) attached to the rear port of the microscope by an epi-fluorescence attachment support pillar was used to monitor the sample after laser or lamp photobleaching. A custom moveable mirror that slid into the rear port of the microscope was used to select either laser or lamp illumination. Either NBD or rhodamine filter cubes (Chroma Technology Corp., Bellows Falls, VT. NBD 460/50x exciter, 500 DCLP dichroic, D535/40m emitter. SPEC TRITC D540/25x exciter, 565 DCLP dichroic, HQ510/75m emitter.) were used for fluorescence imaging. A Princeton Instruments, Inc., 512x512 CCD camera (TE/CCD-512TK/1, Trenton, NJ) was used to record images running Winspec/32 software (Princeton Instruments, Inc, Trenton, NJ). Timing was done with a stopwatch (~ 1 s accuracy).

2.2.2 Protocol for Qualitative FRAP

Two methods of qualitative FRAP were used based on how the sample was photobleached: lamp or laser. These methods are described below.

2.2.2.1 Lamp Photobleaching

The simplest method to perform qualitative FRAP is using lamp photobleaching, because it does not require an aligned laser. After a sample is prepared, as described in Section 2.2, a 512x512 CCD image is acquired using the 4x objective. Next, while the sample is not illuminated (lamp shutter closed), the 40x objective is moved into place and all of the neutral density filters are removed from the lamp light path. Then, the lamp shutter is opened (the shutter immediately below the objectives is most convenient) for a

certain amount of time and closed. Timing starts at the beginning of the bleach period. The 4x objective and the filters are moved back into position as fast as possible and an image or series of images is acquired. Depending on the sample and the fluorophore, shorter or longer bleaching times are needed. Rhodamine is much more difficult to bleach with the lamp than NBD-PC, so 5-30s is sometimes needed to get a noticeably bleached area in the post-bleach images with rhodamine. Because the bleached area is so large with lamp bleaching, an image every minute after photobleaching or longer is generally sufficient to monitor recovery. A typical series of images after bleaching would be taken at: ~ 10 s, 1 minute, 5 minute, 30 minute, and 1 hour. To avoid unnecessary sample photobleaching in between images, the lamp shutter should be closed except when acquiring an image. Usually, diffusion is noticeable by the edges of the bleached spot becoming “fuzzy” and eventual lightening of the entire bleached area as shown in Figure 2.6a.

In order to speed up the ability to observe the “fuzzy” edges, a smaller bleached area is desirable. When photobleaching with the lamp, the various microscope diaphragms (field diaphragm closer to operator and aperture diaphragm further from operator, see Figure 2.5) can be closed down. A polygonal bleached spot will be visible.

If a sample is not fluid, or diffuses very slowly, or has a very low mobile fraction, the edges will not become “fuzzy” within a reasonable (~ 1 hour) amount of time.

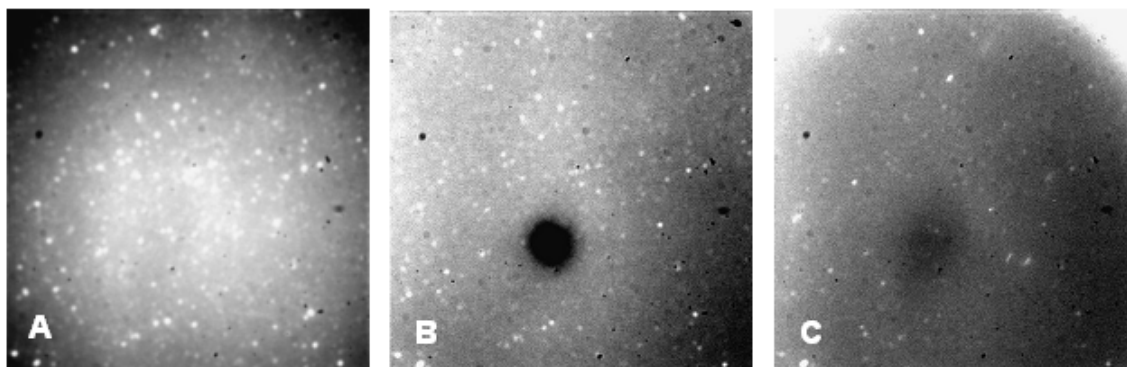


Figure 2.6. Qualitative FRAP results for 5 mol% NBD-PC in EggPC on piranha-cleaned glass. A) A PSLB with numerous vesicles on surface before bleaching with the lamp. B) Image taken 4 s after bleaching the sample. C) Image taken 5 min after bleaching the sample.

2.2.2.2 Laser Photobleaching

A much smaller bleached spot can be created using the laser. This will allow for the recovery to be observed much faster. The downside is that the laser needs to be turned on, which raises the camera temperature about 1-3 °C since the same water is used to cool both the laser and the camera. For all of the experiments described here, the laser aperture was set to the smallest diameter in single wavelength mode (488 nm). Unless the laser has been opened and the aperture changed, it is still currently on this setting. Refer to the laser manual if this setting needs to be changed or checked. For laser photobleaching, any objective can be used for the pre-bleach and post-bleach images because the laser bleach spot is so small, but the 20x and 40x objectives give better resolution. Also, the use of all 512x512 pixels on the CCD is unnecessary and will result in the longest readout times. For instance a 150x150 pixel region of interest (ROI) or a 21x512 pixel ROI around the bleached spot are sufficient if the laser is properly aligned. It is helpful to choose the ROI such that the bleached spot is off-center for referencing purposes that will be discussed later in Section 2.3.2.2.

The laser should be warmed up for at least 30 minutes, set to 200-300 mW after the circular gradient neutral density filter, and be stopped by the mechanical shutter in the beam path. A pre-bleach image of the PSLB is taken with lamp illumination, the corresponding fluorophore filter cube, and mostly like at least one microscope lamp neutral density filter in place. The laser bleached spot will be sharpest and smallest if the sample is in best focus when under **lamp illumination**. Unless aligning and taking appropriate precautions, NEVER look at the laser spot through the eye-piece. The

camera focal point is very near the visual focal point. The shutter to the sample is closed. Then, the laser filter cube is put in position and the moveable mirror is pulled out to select the laser instead of the lamp. (Hint: it is extremely helpful to put the laser filter cube beside the fluorophore filter cube of interest and to note which direction the filter wheel needs to be turned to access each. Also, putting the other filters in the wheel as far from the two filters being used will minimize a possible mix-up.) Then, the microscope shutter is opened. The stopwatch is cleared and ready. The mouse to the computer is moved to an easily accessible spot and the cursor is put on the “acq” button, ready to go. One hand is on the watch and the other is on the mechanical shutter driver open/close switch (make sure that power to the shutter driver is ON at the start of the experiment.). Once this is all done, the following steps need to be done as quickly as possible. The faster these steps are completed, the less “early” time data (see below) will be lost.

- 1) Flick (< 0.5 s) the mechanical shutter open and closed and simultaneously start the stop watch. By looking at the ceiling during this step to make sure the green light pattern of the laser appears momentarily, the operator can be sure the laser illuminated the sample.
- 2) Move the moveable mirror into the beam path to select for the lamp and turn the filter wheel to the fluorophore filter. One hand can do each task nearly simultaneously.
- 3) Click ‘acq’ in Winspec/32. Mentally note the time on the stopwatch when the first camera ‘click’ is heard. Close the camera shutter after the second ‘click’, once the image has been acquired, unless doing a series of images.

- 4) Make sure the image is okay on the screen (should see a nice bleached spot) and record the time.

Steps 1-3 usually take ~ 3 s to complete. This means the first 2 s of data are lost.

Take images at known time intervals after the bleach and first image, such as 1 minute, 5 minute, and 10 minute. As stated above, avoid unnecessary photobleaching by leaving the lamp shutter closed between images. Since the bleached spot is so small, recovery should be easily noticeable by ~ 5 minutes, unless the sample is polymerized, the experiment is being carried out below the phase transition of the lipids, or the sample is immobile. Because the bleached spot edges are “fuzzy” to begin with (the laser beam shape is Gaussian), a spreading and lightening of the spot is the best way to notice a change. If the sample is a fluid phase lipid on a glass substrate, full recovery is expected, so the spot will eventually disappear, usually within ~ 15 minutes, depending on the depth of the bleach and the size of the bleached spot (bleach depth and spot size are described in Section 2.3.2).

2.2.3 Qualitative FRAP Data

As mentioned in the previous sections and implied by the name, numerical data is not expected to be extracted from the qualitative FRAP technique. Examples of “fuzzy” diffusing edges for qualitative FRAP accomplished with lamp bleaching through a smaller objective are shown in Figure 2.6. Unlike the sample “scratching” technique, where a needle or glass pipette tip is used to remove a portion of the PSLB and recovery is watched with time, photobleaching does not damage the substrate. The damage from “scratching” could give false negatives about diffusion. In summary, the qualitative

FRAP technique is an easy way to determine if a sample is fluid, but the degree of fluidity (% recovery) and rate (diffusion coefficient) cannot be extracted accurately.

2.3 Quantitative FRAP (NBD-PC)

To truly compare the rate of diffusion or degree of fluidity between different lipids or different surfaces, quantitative FRAP must be used. A frequently used fluorescent lipid for quantitative FRAP is NBD-PC, because it is extremely easy to photobleach. Its structure, shown in Figure 2.7, reveals that the fluorescent group is part of one of the lipid tails. In this way, any potential interference in the diffusion coefficient determination from the interaction between the fluorescent group and the substrate is expected to be avoided. Section 2.3 describes quantitative FRAP with NBD-PC as the fluorescent dopant, the data-processing required to determine the diffusion coefficients and percent recoveries, and the drawbacks to this method with the given instrumentation and data-processing.

2.3.1 Protocol to Run FRAP (NBD-PC)

Samples were prepared via instructions in Section 2.2 using 5 mol% NBD-PC in the non-fluorescent lipids of interest and finally reconstituted to ~ 0.5 mg/ml in phosphate buffer or water. A sample not containing NBD-PC was also prepared to be used for background subtraction purposes. No heating was ever used in the case of NBD-PC samples investigated because room temperature was above the T_m for all of the lipids measured. Substrates were prepared as described elsewhere (discussed in later sections pertaining to the respective system being studied). Once a good PSLB was formed and rinsed, a pre-bleach image was taken. Due to the low fluorescent quantum yield of NBD-PC, usually at most one lamp neutral density filter (ND8 or ND4) was used.

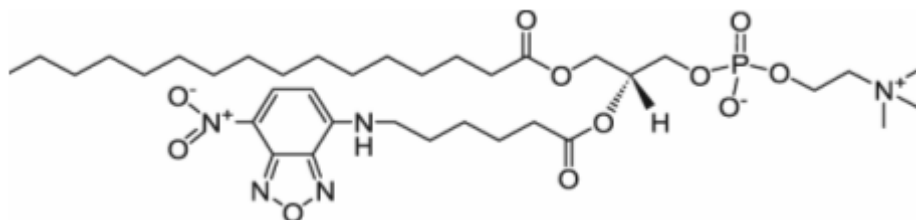


Figure 2.7. Chemical structure of NBD-PC. Image from www.avantilipids.com.

The imaging settings for the pre-bleach image must be carried through for all subsequent images during a run to ensure proper quantitation. This means the same lamp neutral density filters, filter cubes (in this case, always NBD-PC), and acquisition times need to be used. A 1 s acquisition time worked well. Also, the lamp shutter must be closed in between image acquisitions because of how quickly NBD-PC photobleaches. If not careful, the entire PSLB will photobleach to background intensity. It has been found that < 5 mol% NBD-PC was too low to give sufficient fluorescence emission using the detection system described in Section 2.2.1.

Once the pre-bleach image was taken, laser photobleaching was carried out as described in Section 2.2.2.2. The differences between qualitative and quantitative FRAP are that more images are taken, the time intervals between images are shorter, and exact times at which images were acquired were taken (to ~1 s accuracy, because everything was hand-timed). Normally, about 20-30 images were acquired per run over a ~10-40 minute time period (based on whether or not the sample visually appeared to stop changing). Also, more images were taken at early recovery times since that is when the most change occurs. An example of a time series used is as follows: images taken at 0:04, 0:10, 0:20, 0:30, 0:40, 0:50, 1:00, 1:40, 2:00, 2:30, 3:01, 4:00, 5:00, 7:00, 9:00, 11:00, 14:00, 17:00, and 20:00. Again, because NBD-PC photobleaches so quickly, it is imperative to keep the lamp shutter closed whenever an image is not being acquired.

Each run on a particular sample was done on a new spot to obtain an average representation of the entire surface. Also, if the % recovery of fluorescence intensity of a

previous spot was low, it would not then interfere with the FRAP experiment on the next spot. After at least 2 runs, once it was known what time scale was needed to encompass the entire recovery process, a blank was run. In most cases, the blank and sample were prepared in the two separate wells of the FRAP sample chamber at the same time. To run the blank, the same settings and approx. the same time points were used as were done for the sample. In rare instances, depending on the substrate, the blank had a recovery profile of its own that needed to be modeled and taken into consideration for diffusion coefficient and percent recovery calculations.

2.3.2 Data-processing for FRAP (NBD-PC)

In order to calculate the diffusion coefficient and % recovery, the bleach spot size needed to be calculated, the blank subtracted, the data normalized, and the bleach depth determined. These preliminary steps will be explained here along with the creation of recovery curves, the calculation of the diffusion coefficient and the determination of the % recovery. One spreadsheet was used to determine the spot size, another spreadsheet was used to determine the initial ratio and bleach depth, and a third spreadsheet was used to create the recovery curves and calculate the diffusion coefficients and % recoveries.

All of the spreadsheets will be found in Appendix A.

2.3.2.1 Spot Size Determination

From Axelrod's work,¹⁰³ the Gaussian intensity profile as a function of distance, r , from the center of the bleach spot, $I(r)$, can be determined by equation (2.1).

$$I(r) = (2P_0/\pi w^2)\exp(-2r^2/w^2) \quad (2.1)$$

Here, P_0 is the total laser power and w is the radius at $1/e^2$ height. The spreadsheet found in Appendix A.1 was used to fit the data to the above equation using a least squares fit with the Solver function in Microsoft Excel. To determine w , a cross-section of the first image after photobleaching is taken through the center of the bleached spot (similar to the procedure in Ref. 110, except a flat background is assumed).¹¹⁰ The center coordinates of the bleach spot are obtained by eye. Figure 2.8 shows the first image after bleaching an EggPC PSLB doped with 5 mol % NBD-PC on glass. To fit equation (2.1), the cross-section was inverted. This is accomplished by exporting the data as an ASCII file into Excel (convert to ASCII from tool menu using one file per frame, single column, and preserving CCD X/Y/Frame dimension value) and subtracting the value of the baseline from all of the intensity points. The subtracted value was determined by plotting the resultant data after subtraction (Figure. 2.8) and changing the value subtracted until the baseline looked best. A fit to equation (2.1) was done by allowing Solver to change the values of P_0 , w , and the center point of the Gaussian. Refer to Figure 2.8 to see an example of such a fit. Pixel values from the fit needed to be converted to microns based on the calibration of the objective used. Calibration was performed by taking images of a reticle with the objectives.

The first image after photobleaching was used to determine w , although this is a slight overestimate of the actual laser beam spot. Due to changes in laser focus, slight perturbations in laser alignment and power, and bleach time inconsistencies, w had to be calculated for all runs separately from the first image after bleaching.

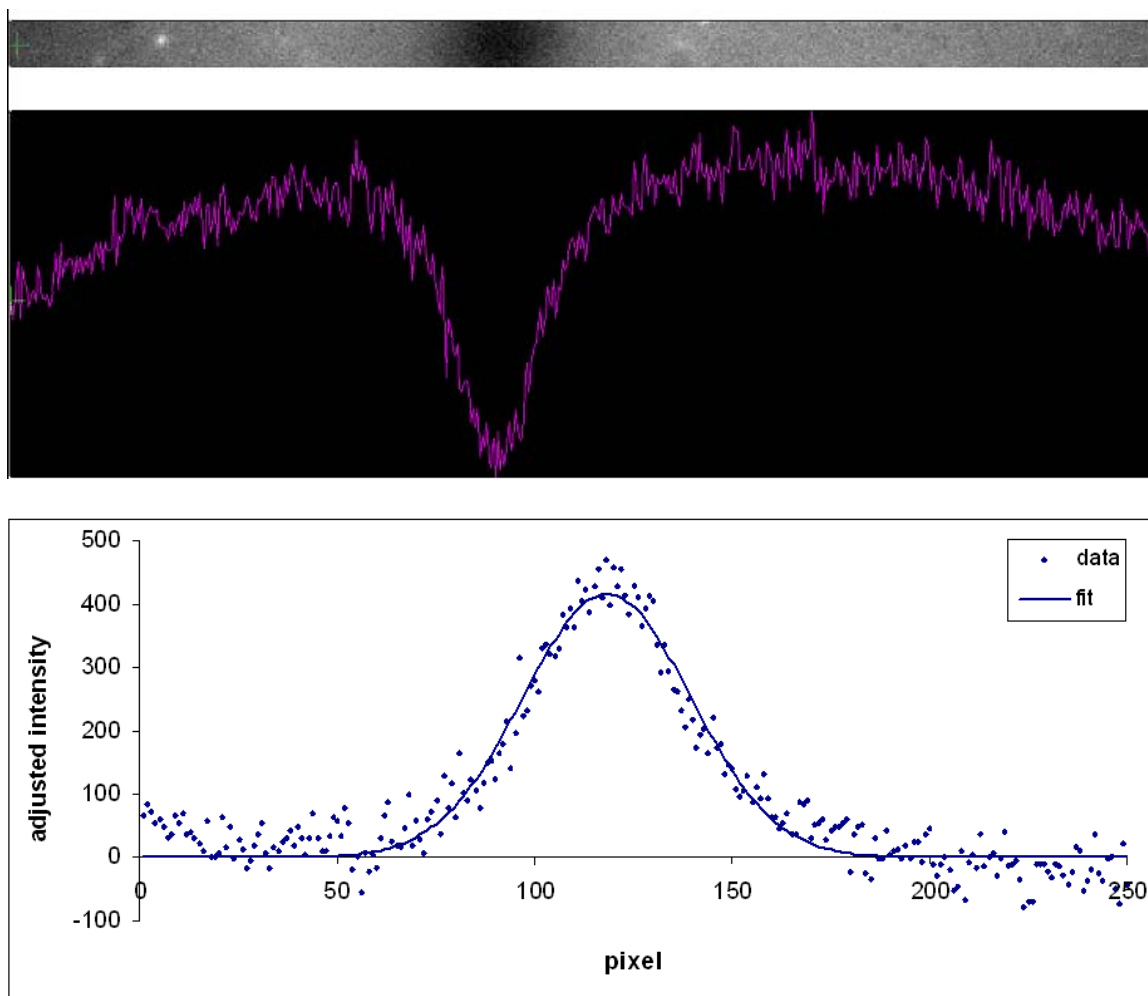


Figure 2.8. Example of the first image after laser photobleaching of a PSLB composed of EggPC with 5 mol % NBD-PC on glass. This image was obtained 4 s after bleaching at room temperature. The top image is the fluorescence image, while the central trace is the cross section going through the center of the bleach spot. The plot at the bottom is the inverted cross-section of the data with the Gaussian fit. It was found that truncating the data to only encompass the Gaussian region by cutting off the rolling edges ensured a better, more reasonable fit. The curvature in the baseline is a result of the lamp profile.

Because diffusion is always happening, the longer the elapsed time after bleaching that the first image is taken, the more the actual w is overestimated, but this is something that cannot be controlled unless bleaching is automated. Also, this leads to some bias in the data, because the very slowly diffusing PSLBs will have more accurate and smaller w values than the faster diffusing ones, which will have artificially larger w values.

2.3.2.2 Reference Values and Blank Subtraction

In order to properly calculate the bleach depth (discussed in Section 2.3.2.4) and the initial ratio for normalization (found in Section 2.3.2.3), the blank values must be subtracted from the data. Two areas of equal ROI are used for determining the intensity ratio: the bleached spot and a reference spot. In the sample data and all data where NBD-PC was the dopant, 15x15 pixel areas were used for both. For the bleached spot, the area was centered on the middle of the bleached region. For the reference spot, an area far enough away from the bleached portion was picked to ensure that the recovery of the bleached area would not affect the reference area. Figure 2.9 shows an example image with the two spots outlined. In nearly every case, the blank intensity was found to not vary with time. The average intensity value for each ROI at all time points was averaged to determine what value needed to be subtracted from the sample FRAP data.

2.3.2.3 Initial Ratio Correction

To determine the % recovery, the pre-bleach intensity ratio of the bleach and reference spots needed to be accounted for. This means that all post-bleach bleach/reference values need to be divided by the pre-bleach intensity ratio of the

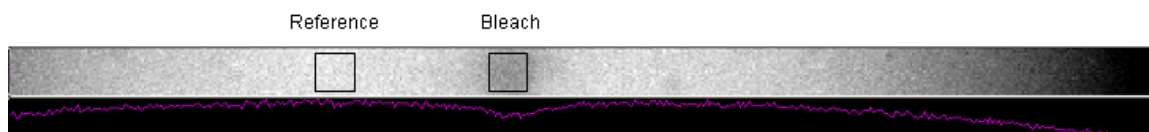


Figure 2.9. An example ROI showing the bleached and reference area locations.

bleached and reference spots. Initial pre-bleach ratios are calculated in spreadsheet A.3.

2.3.2.4 Bleach Depth (γ_D) Determination

The bleach depth, γ_D , is a constant related to how much of the initial background subtracted fluorescence intensity is bleached by the laser and is dependent upon the beam shape. As explained in Axelrod's findings,¹⁰³ γ_D for Gaussian beams changes depending on the amount of decreased fluorescence intensity as a result of bleaching. Figure 7 in Axelrod's paper plots γ_D on a log scale for Gaussians (ignore 'flow' in figure) as a function of a parameter κ . The parameter κ is related to the intensity value, $F_\kappa(0)/F_\kappa$; it is basically the fraction of fluorescence remaining after bleach (background subtracted) and will be the first point on the normalized recovery curve. (Note: Unlike some literature data, which presents recovery curves where the pre-bleach ratio is normalized to one and the first post-bleach point is normalized to zero, in this work only the pre-bleach data was used to normalize to one.) By substituting the expression for F_κ into Axelrod's equation (7), we get:

$$F_\kappa(0)/F_\kappa = \kappa^{-1}(1-e^{-\kappa}) \quad (2.2)$$

Instead of attempting to solve for κ , values of 0.01 to 3.00 were used for κ to solve for $F_\kappa(0)/F_\kappa$ and plotted in Figure 2.10. Based on Axelrod's Figure (7), it looks like κ values of ~ 1.8 and lower give γ_D values of 1.1. The vast majority of the data collected had γ_D values of 1.1. On rare occasions a γ_D of 1.2 needed to be used based on $F_\kappa(0)/F_\kappa$. The spreadsheet used to calculate γ_D can be found in Appendix A.3.

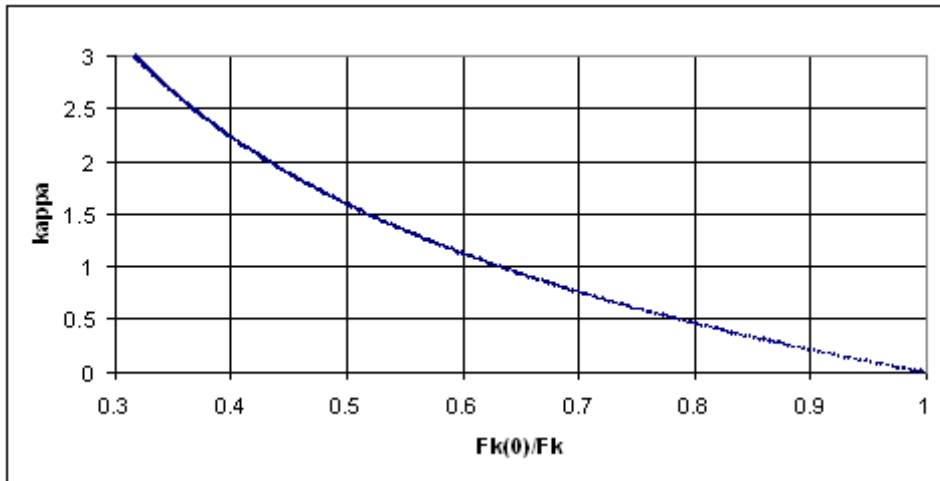


Figure 2.10. Plot of κ values from 0.01 to 3.00 used to solve for $F_\kappa(0)/F_\kappa$ based on Axelrod's equation (7).¹⁰³

According to Endress et al.,¹¹¹ though, bleaching to an $F_k(0)/F_k$ of less than ~ 0.568 leads to distorted Gaussian beam shapes that are more rectangular. Although there will be some $F_k(0)/F_k$ values less than ~ 0.568 in the data presented, the data was used anyway, because there is currently no way of more accurately controlling the laser bleach pulse duration.

2.3.2.5 Diffusion Coefficient Determination

After background subtraction, ratioing the bleached spot average intensity vs. the reference spot average intensity, and normalizing the ratio with regard to the pre-bleach intensity ratio, the recovery curve could be constructed by plotting the fluorescence intensity ratio as a function of time, as in Figure. 2.11a (for spreadsheets and equations used, see Appendix). The curve was fit to a single-exponential recovery of the form:

$$F(\text{bleach})/F(\text{ref}) = A(1 - e^{-t/\tau}) + B \quad (2.3)$$

where $F(\text{bleach})/F(\text{ref})$ is the fluorescence intensity ratio, A is the recovered fraction, τ is the time constant, t is time, and B is the unbleached fraction. The half-time for recovery, $\tau_{1/2}$, is given by

$$\tau_{1/2} = -\ln(1/2)/\tau \quad (2.4)$$

Once $\tau_{1/2}$ is determined, it can be used in Axelrod's equation for diffusion [equation (19) in Ref. 103]:

$$D = \gamma_D w^2 / 4\tau_{1/2} \quad (2.5)$$

In the example shown in Figure 2.11a, the resulting diffusion coefficient for EggPC on glass was found to be $\sim 2.6 \mu\text{m}^2/\text{s}$, which agrees with literature.¹¹²

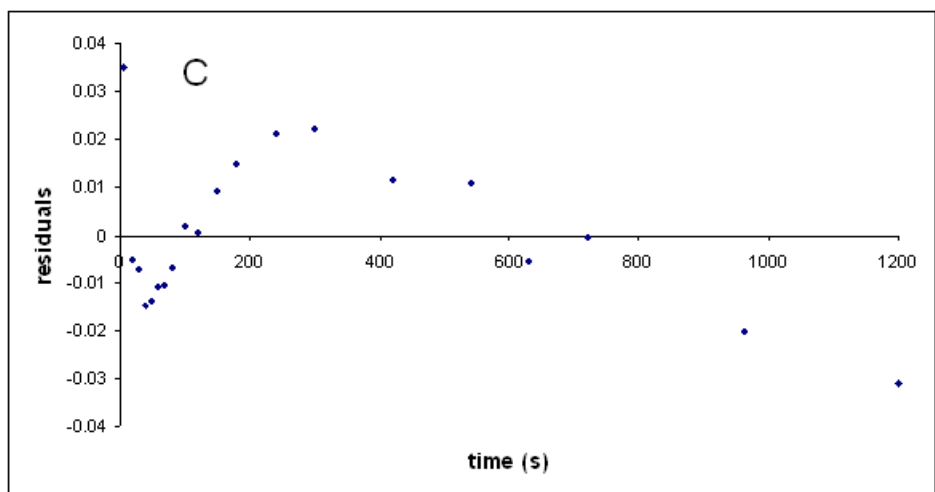
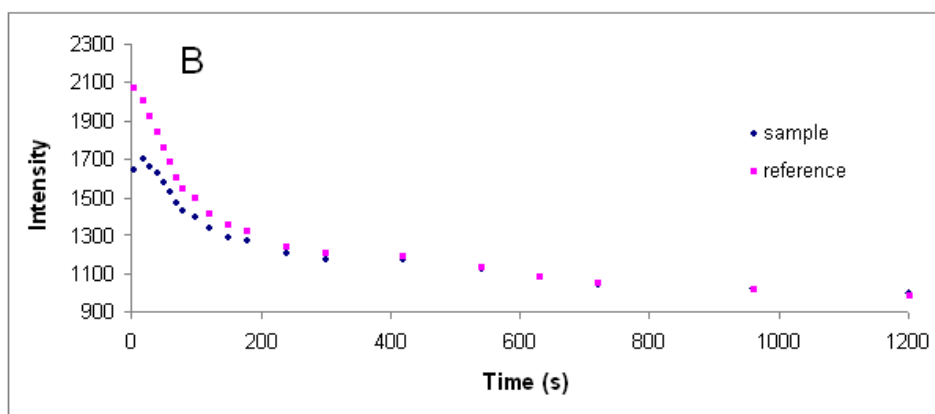
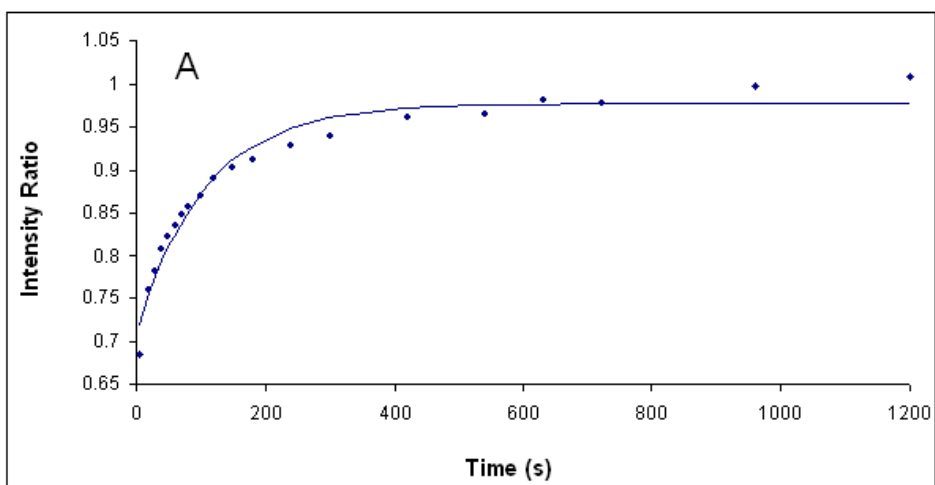


Figure 2.11. FRAP recovery curve data. A) Recovery curve for EggPC with 5 mol% NBD-PC on glass with a single-exponential fit. B) Residuals for data presented in A. C) Raw intensity data.

2.3.2.6 Percent Recovery

Percent recovery refers to the portion of the PSLB that is mobile. It can be found by

$$\% \text{ recovery} = 100\% * (A / (1 - B)) \quad (2.6)$$

In the example in Figure 2.11a, the percent recovery was calculated to be ~ 92% based on the values for A and B taken from the fit to equation (2.3).

2.3.2.7 Length of Observation

In order to properly determine the diffusion coefficient, the length of the experiment needs to be at least ~5 times $1/\tau$. Unfortunately, this cannot be determined ahead of time. In some cases where there were poor fits to the mathematical models, it was because the experiment was terminated too early and not enough of the FRAP recovery curve had been obtained.

2.3.3 Drawbacks to FRAP (NBD-PC)

Although the values for the diffusion coefficient and % recovery of EggPC on glass as well as other systems agree with the broad range of diffusion coefficients and % recoveries in the literature, the residuals in Figure 2.11b demonstrate that there is systematic deviation from the fit. This deviation was found in most of the systems analyzed using this method. This Section addresses some of these problems. Section 2.4 will describe a superior approach to acquiring and fitting FRAP data.

2.3.3.1 Photobleaching of NBD-PC

As can be seen in Figure 2.11c, the raw data for the reference spot in the FRAP recovery curve of EggPC doped with 5 mol% NBD-PC on glass shows a great decrease

in fluorescence intensity (~50%) because of photobleaching by the lamp during image acquisition. This trend is also present in the bleached spot, but at the shortest times the diffusion is fast enough to show an increase in intensity that is later overwhelmed by the lamp photobleaching of the sample. There are other cases where there is no noticeable increase in intensity in the bleached spot, just a slower rate of photobleaching than is observable in the recovery curves. There may be bias in the calculated diffusion coefficient because of the effect of the lamp photobleaching. This has also been suggested by Endress et al.,¹¹¹ where FRAP curves were calculated taking lamp bleaching into consideration. Figure 2 of Endress' work depicts the calculated raw intensity values and is similar to Figure 2.11c.

Another concern with using NBD-PC is that in order to get enough signal throughout the entire experiment, 5 mol % fluorophore had to be used in each PSLB. Figure 2.12 shows the initial intensity of a DOPC PSLB doped with varying amounts of NDB-PC. Although the trend is not linear, suggesting that there might be some self-quenching occurring, the fluorescence intensity still exhibited an increasing trend with concentration. The fluorescence decay profile shown in Fig. 2.11c was acquired with the shutter being closed between each image acquisition. The use of < 5 mol% NBD-PC would result in having very little signal at the end of 10-40 minute FRAP experiments. Because only the fluorescent lipids are monitored during FRAP, the percentage of fluorescent lipid needs to remain low to minimize the affect on the diffusion of the non-fluorescent lipids. Therefore, although more than 5 mol % of NBD-PC might have been beneficial in terms of signal intensity (if self-quenching did not become problem), this

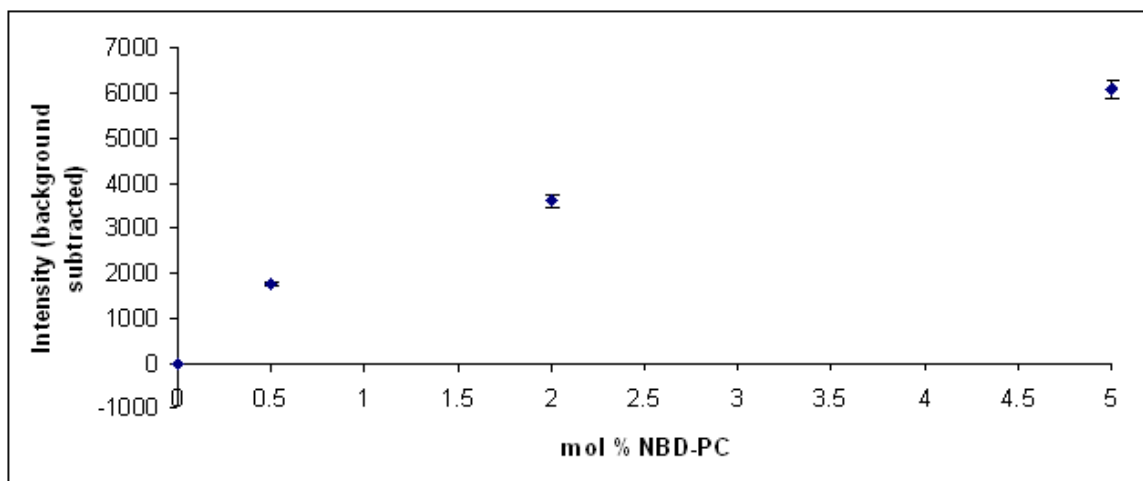


Figure 2.12. PSLBs were formed from DOPC doped with various amounts of NBD-PC formed on detergent- and 30 minute piranha-cleaned glass. Epifluorescence images of the PSLBs were taken with the lamp without any neutral density filters. A 0.5 s acquisition time was used. 9x9 pixel squares in 40x magnification were signal averaged. The background (856 ± 4.3 counts) was subtracted.

was not pursued due to the possible interference of NBD-PC diffusion with the non-fluorescent lipid diffusion. Compared to most FRAP measurements in the literature,^{112, 113} the experiments described here used a higher concentration of fluorophore, although there are other examples of 5 mol % NBD-PC.¹¹⁴

A final drawback to the use of NBD-PC was that a limited number of points could be acquired due to the photobleaching during observation. Acquisition of each image noticeably photobleached the sample. If too many images were taken at the start of the experiment, there would not be enough fluorescence intensity to work with at the end of the experiment, which is why the time points were not evenly spaced. The early time region was important because most of the recovery happened then, so more points were taken early than later, where the change in intensity happened more slowly.

The root cause of the low intensity for NBD-PC is the insensitivity of the camera used to make the measurements. Other researchers can use NBD-PC because they have more sensitive cameras and can cut down the fluorophore concentration and the monitoring beam power enough to avoid photobleaching problems.

To fix the problem outlined above without having to purchase a new CCD camera, a different, more robust, and higher fluorescent quantum efficiency fluorophore was used. This will be discussed in Section 2.4.1.

2.3.3.2 Hand-timing and Acquisition

For each acquired image, the lamp shutter had to be opened, the image taken, the shutter closed and then the time point had to be recorded. The intensities at both the

bleached and reference spots had to be obtained individually, as Winspec/32 does not allow for simultaneous multiple file processing. This allows for the possibility of timing mistakes and data-recording mistakes, and was, honestly, quite tedious and mind-numbing. It would be much more convenient to simply record the experiment as a single file and have a program automatically read out the average intensities in specified ROIs into a text file. Winspec/32 is capable of taking hundreds of images at given intervals as long as the intervals are all the same (which could not be done for NBD-PC FRAP as outlined in Section 2.3.3.1) and the sample does not photobleach to background in the meanwhile.

The fluorophore described in Section 2.3.3.1 would resolve this issue as well. The data could potentially be obtained in one file, if the photobleaching problem was resolved. Unfortunately, the ROI intensity readout method of Winspec/32 was not very convenient even if all of the data were in the same file, so a program to extract all of the user-defined ROI average intensity values into a text file is also needed.

2.3.3.3 Constant ROI Size

In the FRAP (NBD-PC) data processing protocol, a 15x15 pixel ROI was used for both bleached and reference spots regardless of the size of the Gaussian. Axelrod et al.,¹⁰³ used a PMT to measure total fluorescence from the sample and used an attenuated laser beam to excite the bleached area. This monitoring laser beam was the same shape as the bleaching beam, because it was the same laser. The dimensions of a square ROI were not a concern for Axelrod and others because of this.^{103, 112, 115} With the FRAP instrumentation described above, the actual ROI size is always larger than w . To explore

the effect of the ROI sizes on calculated diffusion coefficients and percent recoveries, two data sets were processed using varying ROI sizes.

One data set fit well with the single-exponential approach outlined in Section 2.3.2.5, whereas the second data set fit better to a double-exponential, which will be described in Section 2.4.3.6. The manner of data acquisition will be discussed in later sections, as more data points could be obtained since a more robust fluorophore was used in both cases. The single-exponential dataset, referred to as 1DOPC from now on, was always analyzed with a single-exponential in the following data-processing exercise, while the double-exponential dataset, referred to as 2EPC from now on, was always analyzed with a double-exponential. The w values for 1DOPC and 2EPC were found to be 27 pixels and 15 pixels respectively. For both datasets, entire FRAP recovery curves were fit using ROIs of the following sizes: 5x5 pixels, 11x11 pixels, 15x15 pixels, 27x27 pixels, 35x35 pixels, 51x51 pixels, always centered around the same bleached and reference midpoint. Initial ratios had to be recalculated for each ROI size. In all cases, γ_D was determined to be 1.1. Figure 2.13 shows the resulting recovery curves at each ROI size for both samples. The calculated D values (fast D for 2EPC), % recoveries (total % recovery for 2EPC), and reduced R^2 for all of the fits are in Tables 2.1 and 2.2.

As can be seen in Tables 2.1 and 2.2, the best reduced R^2 value is found for the ROI that is the same width as w . The D values change significantly based on which ROI is used, where the best R^2 corresponds to a D value near the center of the range of recovered values. In cases with larger than w ROIs, the % recoveries are absurdly large ($> 105\%$). For ROIs $\leq w$, the percent recoveries are quite similar.

Table 2.1. Diffusion coefficients, percent recoveries, and R^2 for 1DOPC.

ROI size	D ($\mu\text{m}^2/\text{s}$)	% recovery	R^2
5x5 pixel	3.361	86.64	0.9899
11x11 pixel	3.376	86.94	0.9971
15x15 pixel	3.248	86.56	0.9986
27x27 pixel	2.733	88.80	0.9988
35x35 pixel	2.323	92.56	0.9972
51x51 pixel	1.376	115.10	0.9848

Table 2.2. Diffusion coefficients^{*}, total percent recoveries, and R^2 for 2EPC.

ROI size	D ($\mu\text{m}^2/\text{s}$)	% recovery	$R^{2\dagger}$
5x5 pixel	2.810	102.0	0.9731
11x11 pixel	3.598	98.59	0.9907
15x15 pixel	2.757	103.9	0.9936
27x27 pixel	1.373	238.4	0.9935
35x35 pixel	0.9713	381.4	0.9899
51x51 pixel	17.78	103.8	0.9880

^{*}For 2EPC, two diffusion coefficients were needed for a good fit. The listed diffusion coefficient is the larger of the two obtained values (for more on double-exponential fitting, see Section 2.4.3).

[†] R^2 values for the double exponential were calculated the same way as for the single-exponential (see Section A.4 for R^2 calculation).

The most interesting finding is the apparent decrease in fluorescence intensity ratio at the earliest time points for ROIs $\geq w$ in Figure 2.13. 2EPC did not exhibit this decrease at $w = \text{ROI}$, but 1DOPC did. In both cases, the first couple of seconds of data were lost due to instrumental limitations, resulting in calculated w values that are actually slightly larger than the true w .

This data suggests that the best fits to both single- and double-exponential models are with ROI widths equal to or slightly smaller than w . If the ROI is larger, the bizarre decrease in the recovery curve is present at the start of the data. Endress et al.¹¹¹ theoretically compared the results of FRAP curves with ROI widths equal to w and also equal to the half-width at half-maximum of the Gaussian fit. They suggested that using ROIs with w width would be better since greater overall signal intensity is present and that would be important for the long-term monitoring of slow diffusion coefficients in the presence of monitoring beam photobleaching. Luckily, all data collected and analyzed with the FRAP (NBD-PC) protocol lacked the initial decrease in the recovery curves except in a couple of cases, which were discarded due to bad fits. The diffusion coefficients might have varied somewhat due to the constant ROI widths, but the percent recoveries are correct. Future data analysis will be done with ROI widths equal to or 1-2 pixels smaller than the calculated w to maximize the fit and minimize variation due to ROI size in the calculated D .

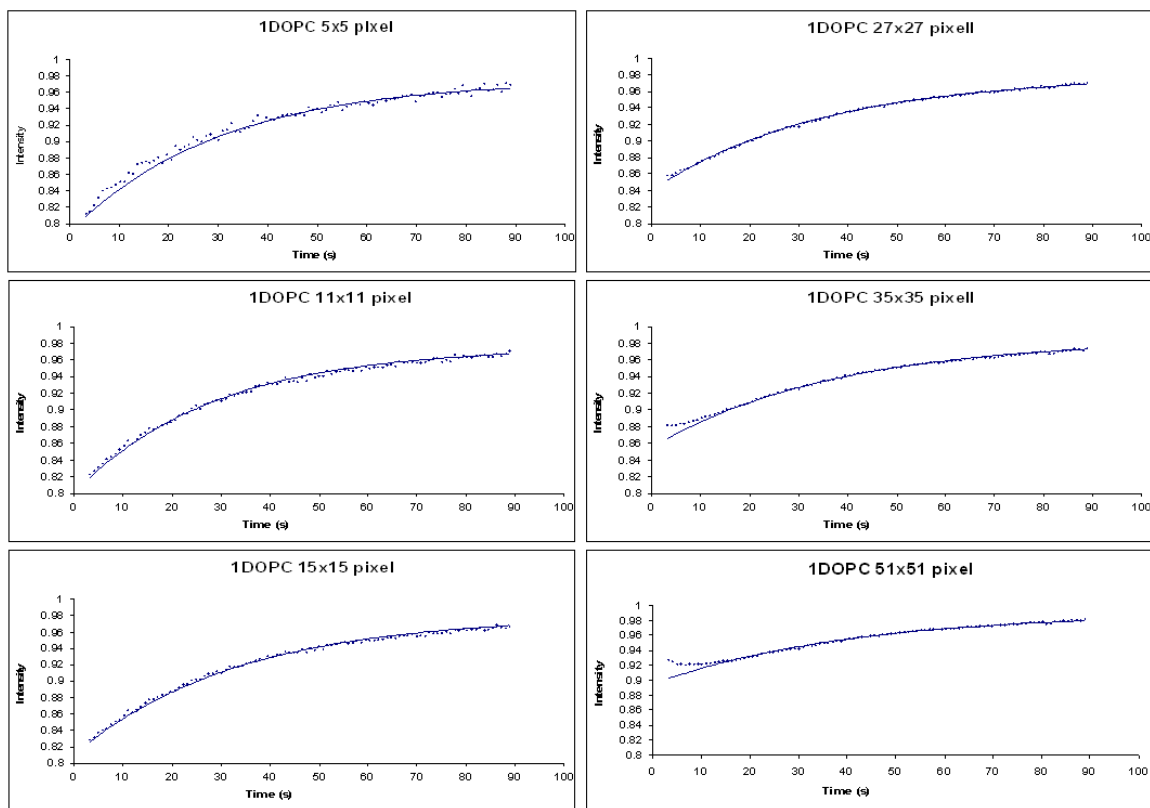


Figure 2.13a. Single-exponential fits to 1DOPC. The plot headings include the ROI size. The ROI was the same width as w in the 27x27 plot.

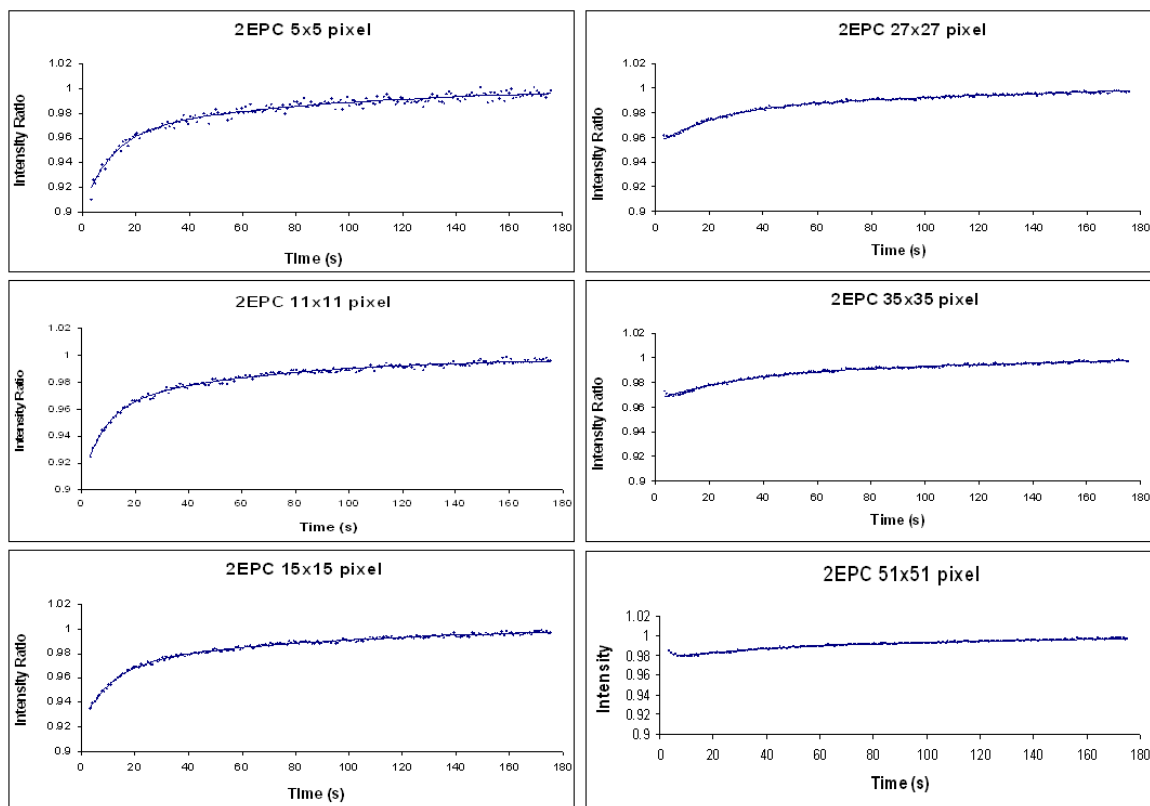


Figure 2.13b. Double-exponential fits to 2DOPC. The plot headings include the ROI size. The ROI was the same width as w in the 15x15 plot.

2.4 FRAP (rhodamine-PE)

As discussed in Section 2.3.3, there were many important drawbacks to the FRAP (NBD-PC) protocol and data analysis. Section 2.4 focuses on an improved method to carry out FRAP that addresses the concerns raised in Section 2.3.3 and more. The choice of a better fluorophore, an improved protocol, and an improved data-processing methodology will be discussed.

2.4.1 Choice of Fluorophore

It was shown in Section 2.3.3.1 that NBD-PC photobleached rapidly and made it difficult to obtain more than ~ 30 data points. A different fluorophore is needed that has a higher fluorescent quantum yield and also photobleaches at a slower rate during lamp illumination, but still photobleaches sufficiently with the 488 nm laser output to make FRAP possible. Rhodamine-PE, shown in Figure 2.14, is a head-labeled phosphatidylethanolamine lipid. Because the headgroup is labeled, there is concern that diffusion measurements of the unlabeled lipids will be convoluted with the interaction of the rhodamine headgroup with the substrate. By using a small fraction of rhodamine-PE in the PSLB (<1 mol %), this interference will be minimized as much as possible. Also, because all of the measurements will be done with this same fluorophore, all of the data will be biased the same way and comparable to each other. Additionally, it has been shown by Derzko and Jacobson that for fluid lipids, the location and identity of the fluorophore does not make a difference in the recovery process.¹¹⁶ Figure 2.15 shows the raw intensity data from the acquisition of a recovery curve measured on bis-SorbPC on glass and illustrates the lack of appreciable fluorescence intensity decay resulting from

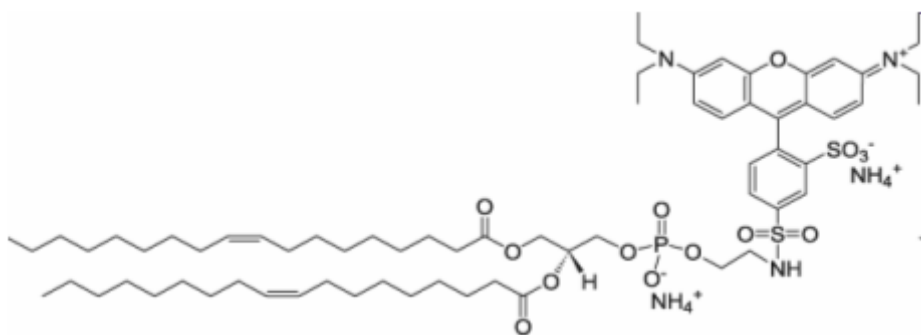


Figure 2.14. Rhodamine-PE structure. Image from www.avantilipids.com.

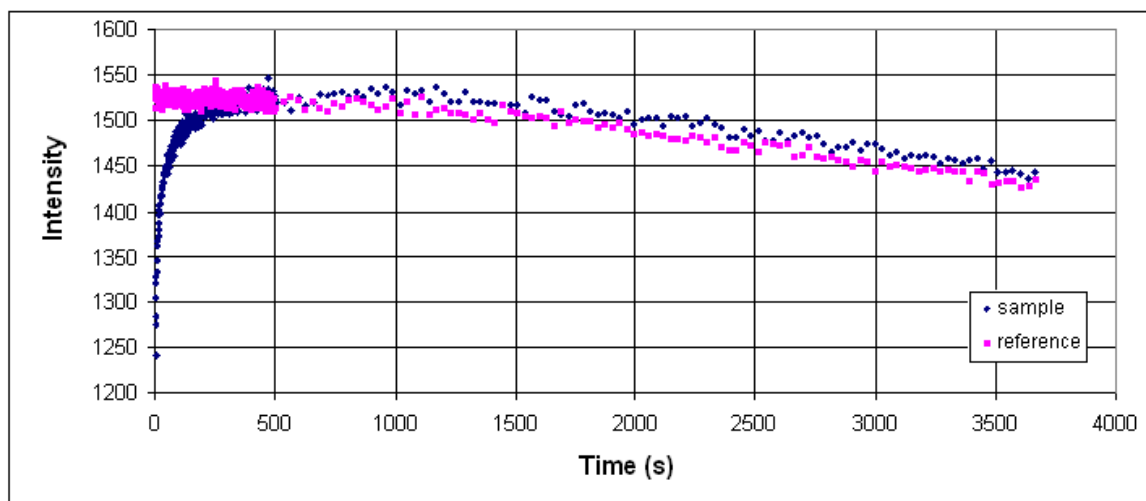


Figure 2.15. FRAP recovery curve raw data for an unpolymerized bis-SorbPC PSLB doped with 0.6 mol % rhodamine-PE on piranha-cleaned glass at $\sim 37^\circ\text{C}$.

lamp photobleaching over the course of an hour under constant lamp illumination with a ND8 neutral density filter. Although there are only ~ 1500 counts per pixel without background subtraction (background fluorescence ~ 634 counts per pixel), the loss of only 100 counts per pixel over the course of an hour leaves sufficient intensity to properly obtain and analyze FRAP data. A clear recovery of fluorescence in the bleached spot is also visible. Also noticeable in Figure 2.15 is the large number of data points obtainable since there is trivial photobleaching under constant lamp illumination during the first hour of observation.

2.4.2 Protocol to Run FRAP (rhodamine-PE)

Refer to Section 2.2.2.2 and follow the set-up described before the 4 steps of laser photobleaching with the following differences in preparation: 1) the PSLB will be composed of 0.6 mol % rhodamine-PE in the PSLB, 2) use a 20x objective and both ND8 and ND4 neutral density filters because that results in the least photobleaching and good resolution, 3) a CCD acquisition time of 0.75 seconds per image was found to be good, and 4) hundreds of sequential images can be taken one after the other without pause (i.e. 400 images with zero second delay will take ~ 8 to 8.5 minutes). After preparation, follow steps 1-4 in Section 2.2.2.2 with only one minor change: in step 3) do not close the shutter after the image is acquired. Then, once the file with multiple images has been collected, record the time of the final image (the time between the opening and closing 'click' of the final image) and close the lamp shutter. A new spot on the substrate is used for each separate experiment.

In most cases, < 10 minutes of acquisition is not enough to fulfill the requirement outlined in Section 2.3.2.7 that the experiment last long enough to encompass ~ 5 times $1/\tau$. Once the first file has run its course and 400 images have been obtained (or another number that was specified), a new file is started to acquire images at a lower frequency since fewer images are required after most of the recovery curve occurs. For example, 105 images with a 0.75 s acquisition time and a 12 s delay starting at ~ 8.5 minutes will finish at about 31 minutes total experiment time. Or 105 images with a 0.75 s acquisition time and a 29 s delay started at ~ 8.5 minutes results in a run that is about 61 minutes long in total. Again, the lamp shutter is left open for the entire experiment. The times were recorded for the first and last image of each separate file.

However, in some instances where the diffusion coefficient was very small (this also depends on the bleach depth and w), even ~ 90 minutes was not long enough to fulfill the requirement in Section 2.3.2.7. If that was the case, individual images with the shutter closed between are taken as described in Section 2.3.1 after 60-90 minutes, and the time is recorded for each image. Some polymerized PSLBs that will be discussed in Chapter 3 had such slow diffusion coefficients paired with high percent recoveries that the films were either damaged from prolonged heating or the sample had physically moved so much (dangling wires from the sample cell were heavy enough to noticeably move the entire microscope stage when left overnight) during data acquisition that unusable data was being collected due to the convolution of the lamp profile with the moving bleached spot. For these extremely slow cases, only the first 8 hours of collection were considered regardless of the magnitude of the time constant, τ .

2.4.3 Data-processing for FRAP (rhodamine-PE)

Some small changes were also made to the way FRAP (rhodamine-PE) data were analyzed. These changes will be outlined in the following Section with some additional data-processing steps.

2.4.3.1 Spot Size and ROI Size Determination

The same steps and spreadsheet were used to calculate w as in Section 2.3.2.1. As described in Section 2.3.3.3, however, it was found that using an ROI for the bleached and reference spot that was larger than w resulted in distorted recovery curves, while the best fit to the mathematical models occurred when the ROI width was approximately equal to or slightly smaller than w . For all data processed with FRAP (rhodamine-PE), the ROI size was selected based on the w found for each bleached spot. As an example, a $w = 14.7$ pixels would lead to an ROI of 13x13 pixels for both the bleached and reference spots.

2.4.3.2 Blank Subtraction

It was found that in the cases of the lipids studied on glass, the background only depended on the acquisition time, the objective, and which neutral density filter was used. Because the acquisition time, objective, and neutral density filter did not vary, after several runs of blanks with different lipids with varying w values, it was determined that the blank was consistently ~634 counts per pixel for both the reference and bleached spots.

2.4.3.3 Initial Ratio Calculation

In addition to making sure that the reference spot was far enough away from the bleached spot to avoid the interference of the bleached lipids diffusing into the reference spot, it was found that choosing a reference spot with a pre-bleach average intensity nearly the same as the pre-bleach bleached spot resulted in better fits to the mathematical models. It was almost always possible to find a reference spot which gave an initial ratio between 0.99-1.01. In the event that the aforementioned was not possible, a reference spot was chosen to give an initial ratio as close as possible to 0.99-1.01.

2.4.3.4 γ_D Determination

The bleach depth was calculated as described in Section 2.3.2.4, but taking into consideration the constant background value and the determined ROI size for each run.

2.4.3.5 Program for Data Extraction

As it would have been extraordinarily tedious to obtain hundreds of average intensities from the increased number of acquired images using only Winspec/32, a simple Java program was written by Troy Comi that would calculate the average intensity in a defined ROI for all images (or defined consecutive images) in a single Winspec/32 file. The data was output as a text file, which could then be used in the Microsoft Excel worksheets found in Appendix A.4.

2.4.3.6 Diffusion Coefficient and Percent Recovery Calculations

The time points at which images were acquired were calculated assuming that the time intervals between each image acquisition in every file were all equal. Because of the time required to read out data from the CCD, the intervals between images were always somewhat larger than the acquisition time added to the delay time. To calculate

when each image was taken, half of the acquisition time was added to the time when the first image was acquired and then the value of the interval was estimated and extrapolated out to the final image in the file. The value of the interval was iterated based on how well it agreed with the recorded acquisition time of the final image. An accuracy of only ~ 1 s was expected because the timing was done by hand.

FRAP curves were generated as described in Section 2.3.2.5. Even though Figure 2.13 shows a set of recovery curves where a single-exponential fit was found to be optimal, in nearly all of the data gathered for polymerizable lipids, a double-exponential fit was clearly better based on the plotted residuals. Figure 2.16 demonstrates just this. In nearly all of the single-exponential fits, there were found to be systematic deviations from the best fit, which were mostly absent from the double-exponential fits of the same data. The double-exponential used is shown in equation (2.7)

$$F(\text{bleach})/F(\text{ref}) = 1 - (C + (De^{-(\tau_1)^{-1}}) + Ee^{-(\tau_2)^{-1}}) \quad (2.7)$$

where $(\tau_1) = \tau_1$ and $(\tau_2) = \tau_2$. Here, τ_1 and τ_2 refer to the fast and slow time constants respectively. This leads to the existence of two distinct diffusion coefficients: D_1 , which is the diffusion coefficient of the more quickly recovering population of fluorescent lipids, and D_2 , which is the diffusion coefficient of the more slowly recovering fluorescent lipid population. The calculation of the diffusion coefficients is the same as explained in Section 2.3.2.5 using equations (2.5) and (2.6).

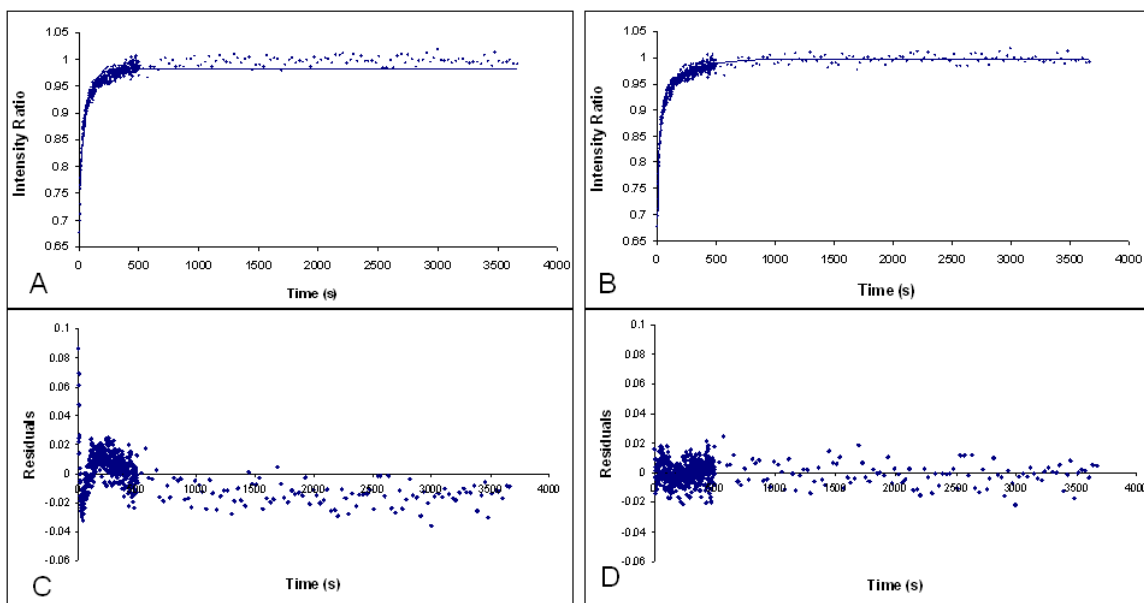


Figure 2.16. Recovery curves, fits, and residuals for single- and double-exponential fits of the same unpolymerized bis-SorbPC data on glass. A) Recovery curve with single-exponential fit. B) Recovery curve with double-exponential fit. C) Residuals for fit in A). D) Residuals for fit in B).

Related to each diffusion coefficient is a population of fluorescent lipids that can be calculated as follows. For the fast diffusion coefficient, the % recovery, %₁, is

$$\%_1 = (D / (C + D + E)) * 100\% \quad (2.8)$$

For the slow diffusion coefficient, the % recovery, %₂, is

$$\%_2 = (E / (C + D + E)) * 100\% \quad (2.9)$$

The total % recovery, %_{tot}, is the sum of %₁ and %₂.

To simplify the comparison of lipids to one another, %_{tot} and D_{avg}, which is the weighted average diffusion coefficient, can be used. D_{avg} is found by

$$D_{avg} = ((\%_1 * D_1) / 100) + ((\%_2 * D_2) / 100) \quad (2.10)$$

The values found for a reference lipid, vesicle-fused DOPC, on 5 minute piranha-cleaned glass at room temperature are $D_1 = 6.2 \pm 0.80 \mu\text{m}^2/\text{s}$, $\%_1 = 69 \pm 2.3 \%$, $D_2 = 0.62 \pm 0.096 \mu\text{m}^2/\text{s}$, $\%_2 = 31 \pm 2.7 \%$, $D_{avg} = 4.4 \pm 0.52 \mu\text{m}^2/\text{s}$, and $\%_{tot} = 99 \pm 1.5 \%$. Seu et al.,¹⁹ found a diffusion coefficient of $\sim 10 \mu\text{m}^2/\text{s}$ with $\sim 100\%$ recovery for the same system, but using a different bleach geometry and mathematical model.¹¹² In the same work, they had found that the diffusion coefficient can be changed by nearly an order of magnitude by changing the glass cleaning method. Although they did not use a double-exponential for fitting, their 2006 publication did a comparison of EggPC on glass fit to a single-exponential or an equation involving Bessel functions.¹¹² The more complex equation fit their data better than the single-exponential, similar to the example in Figure 2.16.

Occasionally, micron-sized, fluorescent objects (assumed to be vesicles which were not rinsed away) floated through the bleached spot or reference spot. If it was clear that an image in the set was compromised due to these objects, as evidenced by a sharp spike or dip in the recovery curve (and could be verified by reviewing the video file) the affected data points were removed from the curve.

2.5 Possible Improvements to the FRAP System

Although a lot of improvement was made going from FRAP (NBD-PC) to FRAP (rhodamine-PE), there are still experimental issues that can be improved involving automation, a better detection system, laser monitoring, and a different bleach geometry. These issues will briefly be discussed here.

2.5.1 Automation with Lamp Monitoring

One of the biggest drawbacks to all of the described FRAP protocols is the loss of the first 2-3 s of data because there is a manual change-over from the bleach beam to the monitoring beam (or the laser to the lamp, with optics changes). Due to this delay in imaging, w is also overestimated and γ_D may be underestimated. The mechanical shutter and driver are capable of interfacing to software such as LabView (National Instruments, Austin, Texas). The moveable mirror could be replaced with a motorized mirror that could also be driven using LabView. If rhodamine-PE continues to be the fluorophore of choice, a program could be written to acquire pre-bleach images, bleach the sample via the shutter that controls laser illumination of the sample, and start acquiring post-bleach images through the end of the experiment with one click of a button. An example of this is found in work by Smith et al.¹¹⁴ Experiments would need to be carried out to verify that the rhodamine-PE filters would not be damaged by use with 488 nm laser light, or a motorized filter system would also need to be implemented.

An additional issue with the current set-up is the unnecessary sample photobleaching that takes place during exposure to the sample to the monitoring lamp.

With the addition of a second shutter in front of the lamp (which is actually there, but not shown in the diagram found in Figure 2.5), the light from the lamp could be blocked whenever images were not actively being taken. This would reduce unnecessary sample photobleaching and could thus be beneficial for samples with slow diffusion coefficients.

Another potential modification to the system could be the use of varying delay times between image acquisitions. The acquisition times of the images must be equal, but progressively longer delays could automatically be built into the program. LabView would have to record the acquisition time of each image, but this would remove the possibility of user error and also save data-processing time by getting all of the information in one file, instead of having to split it into multiple files and process them separately.

2.5.2 Automation with Laser Monitoring

Alternatively, instead of having to obtain or machine a motorized mirror assembly, an automated neutral density filter could be used to cut down the laser power 10^5 -fold, as was done in Seu et al.¹¹² for monitoring purposes before and after photobleaching. Again, the neutral density filter could be controlled by LabView. In this approach, a monitoring lamp would not be needed and no motorized parts would be needed.

2.5.3 New Detection System

In the near future, the issue of a new detector must be addressed because the current CCD is so old that Photometrics no longer supports it. With a more sensitive CCD or photodiode, FRAP could be performed with lower illumination as described in

Section 2.5.2. Also, if NBD-PC matches the spectroscopic needs of a system better than rhodamine-PE, lower illumination powers would be preferable to minimize sample photobleaching during recovery.

2.5.4 Fluorescence Recovery After Pattern Photobleaching

A more versatile way to determine diffusion coefficients is using Fluorescence Recovery After Pattern Photobleaching.^{102, 117-119} In this method, a laser beam is split and then recombined to create constructive and destructive interference in a fringe pattern. The resulting periodic pattern is then used to bleach the sample. This approach allows the determination of diffusion coefficients that vary over many orders of magnitude, which, as will be shown in Chapter 3, would be useful in investigating the fluidity of monomers and varying sizes of polymers.

CHAPTER 3: MEASUREMENTS OF POLYMERIZABLE LIPID DIFFUSION COEFFICIENTS IN PSLBs

3.1 Introduction

The fluidity of the lipid bilayers that membrane proteins are incorporated into can affect the function of the proteins.^{27, 89-94} As was described in Section 1.5, it is necessary to find a balance between the stability of the membrane material with the fluidity needed to maintain the activity of TMPs. This Chapter will describe the measurement of the fluidity of polymerizable lipid membranes.

The fluidity (diffusion coefficients and % recoveries) of a handful of polymerizable lipid types have previously been measured. Both UV- and redox-polymerization have been employed, although not necessarily on the same lipid compositions. These results will briefly be reviewed in this Section.

Cross-linkable diacetylinic lipid diffusion was measured by Sackmann et al. in a GUV geometry by FRAP.¹²⁰ The diffusion coefficient of 100% diacetylinic lipid (not including fluorescent probe) is not reported in the reference, however, a ~6-fold decrease in diffusion coefficient was found for a 1:1 mixture of DPPC/diacetylinic lipid in the fluid phase after UV-polymerization in the solid-analogous phase. Smaller fractions of polymerizable lipid in the GUVs still result in decreased diffusion upon polymerization, but not to the same extent as 1:1 DPPC/diacetylinic lipid. Increasing the percentage of polymerizable lipid from 0% to 100 % in DPPC and polymerizing yields decreasing percent recoveries from 80% to 20% over the range.

Diffusion coefficient measurements on UV-polymerized diacetylinic lipids were also conducted by Okazaki et al. on fluid PSLBs.^{60, 61} In this case, 100% diacetylinic PSLBs were irradiated with varying doses of UV irradiation and the unpolymerized lipids were rinsed away leaving a polymerized partial bilayer. The area fraction obstacle was calculated using ellipsometry and fluorescence microscopy. EggPC vesicles doped with fluorescent probe were then fused into the partial bilayers to create hybrid bilayers. FRAP was used to find D as a function of area fraction obstacle for these hybrid bilayers. For obstacle fractions up to 0.4, the diffusion coefficient decreased to about a quarter of the unobstructed EggPC bilayers. Between 0.4 and 0.7 obstacle fraction, there was a finite D below 10% of the unobstructed bilayer diffusion attributed to channel-like defects in the polymerized bilayers through which probe molecules could still move. The film was essentially immobile above 0.7 obstacle fraction.

Gaub et al. studied the diffusion of dioctadecadienoyl ammonium bromide (DODIAB), a cross-linkable lipid with polymerizable moieties near the headgroup.^{121, 122} FRAP was used to determine D for giant vesicles of DODIAB and DODIAB mixed with DMPC at various temperatures both above and below T_m . UV-polymerization was conducted at an unknown temperature. For purely polymerizable lipid vesicles (not including probe), the value of D above T_m decreased by a factor of ~ 5 after polymerization, whereas at a temperature slightly below T_m , a ~ 3 -fold decrease was measured. For 1:1 mixtures of DODIAB/DMPC, there was $< 30\%$ decrease in D above T_m and a factor of ~ 5 decrease in D at a few degrees below T_m of the mixture.

A PC lipid with a polymerizable methacryl moiety connected to the phosphate group by $(\text{CH}_2\text{CH}_2\text{O})_m$ spacers (POME CY), which could form linear polymers, was also investigated by Sackmann et al.¹²⁰ FRAP was again conducted in a giant vesicle geometry for mixtures of polymerizable lipid POME CY and DMPC above T_m , however, the UV-polymerization temperature was not given. In this case, the percent recovery stayed constant at $\sim 81\%$ for polymerized mixtures in the 0-100 mol% POME CY range. D was determined for mole percents of POME CY up to 50%. As the fraction of POME CY is increased, the diffusion coefficient decreases from $\sim 25\ \mu\text{m}^2/\text{s}$ to $5\text{-}10\ \mu\text{m}^2/\text{s}$.

In general, one would expect the diffusion coefficients of probes in lipid polymers to be slower than in unpolymerized bilayers, because there are larger obstacles to maneuver around. This was demonstrated in the above discussion where the diffusion coefficients were reduced for UV-polymerized PSLBs by about an order of magnitude (or more, as in the case of the immobile diacetylinic films of Okazaki and coworkers). As was mentioned in Section. 1.5.2.2, UV-polymers are expected to be smaller than redox-polymers, therefore, larger reductions in fluidity should be expected for redox-polymerized lipid films since the lipopolymers should be even larger.

Fahmy et al. measured the diffusion properties of a synthetic zwitterionic lipid with a single methacryloyl polymerizable group in the tail capable of forming linear polymers before and after AIBN (2,2'-asobis(2-methylpropionitrile)) polymerization had been carried out at a temperature above T_m .¹²³ The diffusion was measured in the liquid-crystalline phase, though. The diffusion coefficient decreased by a factor of 500 after polymerization. Such a large decrease in D is in good agreement with the expectation of

redox-polymerization creating larger polymers than UV-polymerization, because this is a much larger decrease in D from unpolymerized to polymerized than was found for UV-polymerized bilayers.

Diffusion of acryloyl polymerizable lipids was studied by Kölchens et al. by performing FRAP on fluid-phase PSLBs that were AIBN-polymerized T_m .⁹⁵ The diffusion coefficient was determined as a function of the number-average degree of polymerization, X_n , for a linearly-polymerizable acryloyl lipid (MAPC). Increasing monomer/initiator ratios were used to increase the polymer size from ~ 230 units to ~ 1940 units. For all polymer sizes, the bilayers were found to be $95 \pm 5\%$ mobile. The unpolymerized bilayer had a D of $\sim 3.8 \mu\text{m}^2/\text{s}$. The diffusion coefficient decreases from $\sim 1.4 \mu\text{m}^2/\text{s}$ to $\sim 0.25 \mu\text{m}^2/\text{s}$ as the polymer size increases from ~ 230 units to ~ 700 units. For polymer sizes between 700 units and 1930 units, there were no appreciable changes in diffusion coefficient. The authors also investigated the effect on D of mixing a cross-linkable acryloyl lipid (BAPC) with MAPC. Polymerization conditions were chosen so that 100% MAPC bilayers had polymers that were approximately 250 units in size. The addition of up to ~ 30 mol % BAPC in MAPC resulted in no change in diffusion coefficient. Between 30-50 mol % BAPC in MAPC, the diffusion coefficient was reduced by a factor of ~ 14 . The % mobile was not commented on in these mixed polymerized bilayers. BAPC fractions greater than 50% were not discussed.

Clearly, polymerization of PSLBs leads to noticeable reductions in diffusion coefficient and also % mobility. A number of different polymerizable lipids had been investigated. The diffusion of diacetylinic lipids were studied by multiple groups. Other

polymerizable lipids, such as those in Figure 1.19 have not had their diffusion coefficients measured. Also, none of the previously mentioned studies compared UV-polymerization and redox-polymerization on the same lipid in the same geometry. Additionally, prior research has shown that simply changing the temperature at which polymerization occurs can make a significant difference. Tsuchida et al.⁷⁶ found that redox-polymerization of mono-DenPC employing the same initiators as used in this study yielded number average degrees of polymerization of 27 for polymerization below T_m and 45 for polymerization above T_m . Therefore, polymerization of the PSLBs composed of the lipids pictured in Figure 1.19 will be carried out in different lipid phases as well.

The remainder of this Chapter is devoted to a study of the diffusion coefficients and percent recoveries of PSLBs in the fluid phase of the lipids shown in Figure 1.19 on glass substrates. As discussed in Sections 1.5.3 and 1.5.4, the lipids in Figure 1.19 show varying degrees of bilayer stabilization upon polymerization and some PSLBs are capable of sustaining the activity of various integral membrane proteins. Unpolymerized and polymerized bilayers will be discussed. UV-polymerization and redox-polymerization above and below T_m (and in a few cases, near T_m) were carried out.

3.2 Experimental

3.2.1 Materials

1,2-dioleoyl-*sn*-glycero-3-phosphocholine (DOPC) (refer to Figure 1.7 for chemical structure) and 1,2-dioleoyl-*sn*-glycero-3-phosphoethanolamine-N-(lissamine rhodamine B sulfonyl) (ammonium salt) (rhodamine-PE) were purchased from Avanti Polar Lipids, Inc. (Alabaster, AL, USA). Bis-sorbyl phosphatidylcholine (bis-SorbPC) and mono-sorbyl phosphatidylcholine (mono-SorbPC) were prepared via a modified version of Lamparski et al.¹²⁴ Bis-SorbPC was purified by preparatory scale HPLC on a reverse phase column with a water/methanol solvent system. Bis-denoyl phosphatidylcholine (bis-DenPC) was synthesized using a recent synthesis by Jones and Hall.¹²⁵ Mono-denoyl phosphatidylcholine (mono-DenPC) was prepared via the synthetic route illustrated in Liu et al.¹²⁶ Lipids were kept in -80 °C for longterm storage and -20 °C for shortterm storage. Polymerizable lipids were always handled in yellow light or in darkness during preparation. The structures of mono-SorbPC, bis-SorbPC, mono-DenPC, and bis-DenPC are shown in Fig. 1.19.

All water, referred to as nanopure water, was obtained from a Barnstead Nanopure system (Thermolyne Corporation, Dubuque, IA) with a measured resistivity of greater than 17.5 MΩ-cm. Unless otherwise noted, PSLBs were prepared in pH 7.0, 10 mM phosphate buffer made from sodium phosphate dibasic, anhydrous and sodium phosphate monobasic, monohydrate (EMD, Gibbstown, NJ) using the vesicle fusion procedure described in Section 2.1.2. Redox-polymerization was carried out using

sodium bisulfite (ACS reagent) and 99+% potassium persulfate (Sigma-Aldrich, St. Louis, MO).

3.2.2 Phase Transitions of Polymerizable Lipids

The phase transitions of the polymerizable lipids were previously determined by a variety of methods¹²⁷⁻¹²⁹ and confirmed using the DSC method from Ratnayaka's work.¹³⁰ Briefly, ~2 mg lipid was air dried in an aluminum DSC pan followed by vacuum drying for 4 hours. Once dry, 25 μ l nanopure water was added to the pan, after which the pan was sealed with an aluminum cover. A Mettler-Toledo (Columbus, OH) DSC was used to monitor the change in power as the temperature was raised from 5°C to 50°C and then lowered back to 5°C at a rate of 5°C/min. The results agree with the phase transitions reported in Table 3.1.

3.2.3 Surface Cleaning

All substrates were 25 x 75 mm pre-cleaned microscope slides (Gold Seal, Portsmouth, NH) that were briefly scrubbed with 1% Liquinox (Alconox, Jersey City, NJ) and a cotton pad, followed by rinsing with nanopure water and drying with nitrogen gas. They were then piranha-cleaned for 5 minutes in 70:30 concentrated sulfuric acid /30% hydrogen peroxide (EMD, Gibbstown, NJ). Substrates were then rinsed with copious amounts of nanopure water and blown dry with nitrogen gas. Substrates were used immediately after preparation. As described in Section 2.1.2, the substrates were heated to above T_m before vesicle fusion was done above T_m .

Table 3.1 Phase transition temperatures of polymerizable lipids.

Lipid	Phase Transition Temperatures (°C)*
mono-DenPC	26
mono-SorbPC	34
bis-DenPC	20
bis-SorbPC	29

*Values taken from references 127-129.

3.2.4 Polymerization of Lipids

After vesicle fusion took place and a uniformly fluorescent PSLB was found, the sample could be polymerized. Two methods of polymerization were used: UV-photopolymerization (UV-polymerization) and redox radical initiated polymerization (redox-polymerization). Both will be described.

3.2.4.1 UV-polymerization

UV-polymerization was carried out 5-10 °C above, 5-10 °C below, and, in some cases, at T_m . Heating and cooling above and below room temperature was accomplished using the apparatus shown in Figures 2.2 and 2.3 and described in Section 2.1.1. The temperature was monitored using a resistance temperature detector (RTD) (HSRTD-3-100-A-40-E, Omega, Stamford, CT) connected to a 6 ½ digit multimeter (Agilent, Santa Clara, CA).

The UV-polymerization time for PSLBs was determined by examining the results of illuminating bis-DenPC SUVs in nanopure water in the FRAP chamber for varying amounts of time. The SUVs were prepared as described in Section 2.1.2. Piranha-cleaned glass treated with a silanizing agent, Surfasil Siliconizing Fluid (Thermo Scientific, Dubuque, IA), was used to complete the FRAP cell. The Surfasil was added to keep the vesicles from fusing on the glass and the treatment is described in Section 4.3.4.2. The vesicles were illuminated for 30 minutes by a low pressure Hg pen lamp (rated 4500 $\mu\text{W}/\text{cm}^2$ at 254 nm) held 3 inches above the sample. After polymerization, the sample was placed in a UV-vis spectrometer (Spectral Instruments, Inc., Tucson, AZ)

and absorbance spectra were obtained. Normalized absorbance spectra are shown in Figure 3.1. The disappearance of the band at ~260 nm is the result of monomer to polymer conversion.¹²⁹ Figure 3.2 is a plot of the percentage of monomer unreacted vs. polymerization time assuming that at 1 hour all of the monomers were reacted. After 15 minutes, approximately 95% of the monomers have reacted. To minimize potential damage to the PSLB due to over exposure to UV irradiation and to minimize photobleaching of rhodamine-PE, the polymerization time was limited to 30 minutes for all photopolymerized PSLBs discussed below. No decrease in rhodamine-PE fluorescence intensity in PSLBs was measured after 30 minutes of UV-polymerization. However, PSLBs were frequently found to no longer be uniformly fluorescent after UV-polymerization, as shown in Figure 3.3.

3.2.4.2 Redox-polymerization

Redox-polymerization was also carried out 5-10 °C above, 5-10 °C below, and in some cases, at the T_m . Heating and cooling were performed as explained in Section 2.1.1. Oxygen was excluded from the system by bubbling Ar(g) through the upper portion of the sample cell for 20 minutes prior to addition of the redox initiators. Nearly all of the buffer solution above the PSLB was removed after the 20 minute purge. One ml of 0.0289 M potassium persulfate and 0.0289 M sodium bisulfite in 10 mM phosphate buffer were each vigorously bubbled with Ar(g) for five minutes and then mixed immediately before addition to the PSLB.

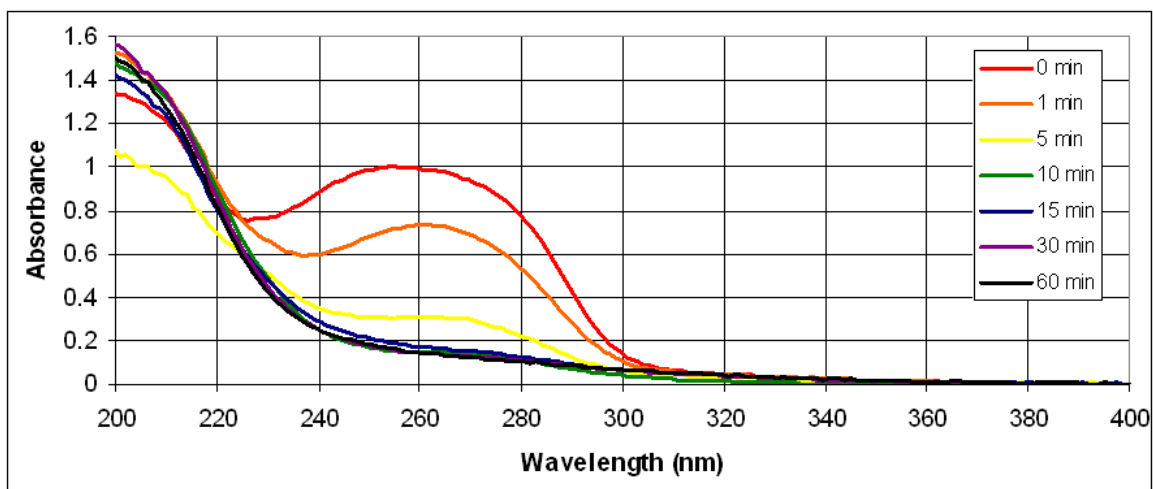


Figure 3.1. Normalized absorbance spectra of bis-DenPC SUVs as a function of UV-polymerization time. All spectra were normalized to an absorbance of 1 at the pre-polymerization ~ 253 nm peak and 0 at 400 nm.

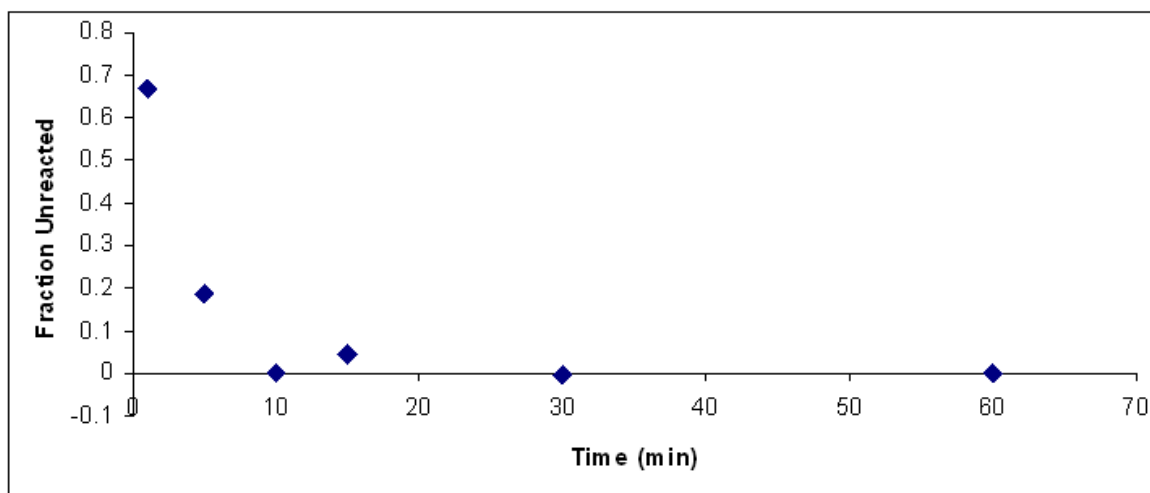


Figure 3.2. Amount of unreacted monomer vs. UV-polymerization time.

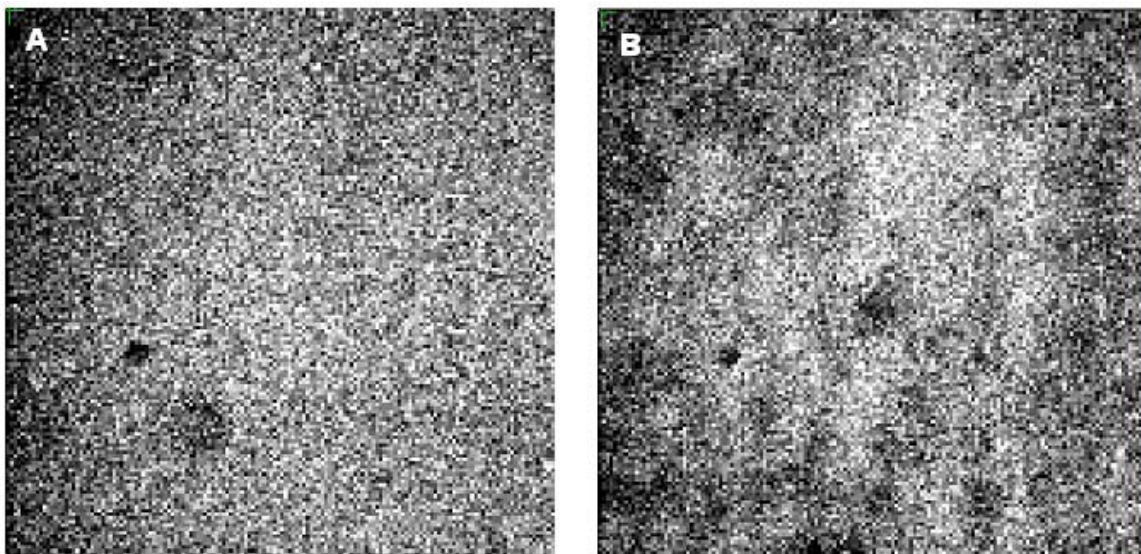


Figure 3.3. Fluorescence images of PSLBs after UV-polymerization ($180\text{ }\mu\text{m} \times 180\text{ }\mu\text{m}$). The uniform PSLB shown in A) is bis-SorbPC polymerized above T_m , while B) is a bis-DenPC PSLB after polymerization above T_m .

The initiators were added gently to the wall of the sample cell in such volumes to give a final concentration of 0.01 M for each initiator in the cell. The polymerization was allowed to take place over the course of 2 hours, as described by Ross et al.,⁵⁷ while continuously bubbling argon gently in the region of solution above the PSLB. After 2 hours, the solution above the PSLB was removed and replaced 1 ml at a time with buffer using a glass pipette until approx. 20 ml of buffer had been rinsed through the cell. The cell was left completely filled with buffer to minimize potential problems with dehydration during the course of the experiment.

3.2.5 FRAP Measurements

FRAP measurements and data analyses were carried out using the FRAP (rhodamine-PE) protocol described in Section 2.4. All measurements were done in the fluid phase, 5-10 °C above T_m for polymerizable lipids. DOPC, a reference lipid, was measured at 25°C, which is significantly above its T_m of -20°C.¹³¹

3.3 Results and Discussion

FRAP was performed on: a) PSLBs that were unpolymerized composed of DOPC, mono-DenPC, mono-SorbPC, bis-DenPC, and bis-SorbPC; b) PSLBs of the polymerizable lipids that were UV-polymerized above and below the T_m ; and c) PSLBs of the polymerizable lipids that were redox-polymerized above and below the T_m . In a few instances, data for lipids polymerized at approximately T_m were also gathered. These findings will be discussed in the following sections. The implications of these findings for integral membrane protein function in polymerizable PSLBs will be discussed in Chapter 5.

3.3.1 Diffusion Behavior of Unpolymerized PSLBs

Table 3.2 tabulates all of the diffusion coefficients (fast, slow, and weighted average) and percent recoveries (fast, slow, and total) of the unpolymerized PSLBs with FRAP performed above the T_m . Two example recovery curves for polymerizable PSLBs are shown in Figure 3.4. In all cases, a single-exponential fit was found to have a systematic deviation from the data, so a double-exponential fit was used instead. This led to two unequal diffusing populations, where $\sim 70\%$ of the probe was diffusing more quickly than the other $\sim 30\%$. Tinland and Scomparin et al. found similar unequal slow and fast population distributions for vesicle-fused DMPC on glass (see Figure 1.8 for lipid structure).^{132, 133} In Scomparin's work, other PSLB formation mechanisms on glass and mica resulted in either a single diffusion coefficient or a fast and a slow diffusion coefficient with equal populations.

Table 3.2 Temperature, diffusion coefficients, and percent recoveries of unpolymersized PSLBs.

Lipid	T (°C)	D ₁ (μm ² /s)	% ₁	D ₂ (μm ² /s)	% ₂	D _{avg} (μm ² /s)	% _{tot}	D' _{avg} (μm ² /s) [*]	n [†]
DOPC	25	6.2 ± 0.80	69 ± 2.3	0.62 ± 0.096	31 ± 2.7	4.4 ± 0.52	99 ± 1.5		5
mono-DenPC	35	7 ± 2.3	74 ± 7.9	0.5 ± 0.12	26 ± 7.5	5 ± 1.6	100 ± 2.2	2.3 ± 0.74	6
mono-SorbPC	43	6 ± 1.5	74 ± 2.1	0.31 ± 0.020	26 ± 2.6	4 ± 1.2	100 ± 1.3	1.0 ± 0.30	5
bis-DenPC	30	2.7 ± 0.30	75 ± 2.3	0.41 ± 0.062	28 ± 3.2	2.2 ± 0.25	103 ± 2.0	1.5 ± 0.17	5
bis-SorbPC	37	1.2 ± 0.21	68 ± 2.5	0.11 ± 0.020	31 ± 2.9	0.9 ± 0.15	99.6 ± 0.89	0.36 ± 0.059	4

^{*}Values normalized to 25 °C.

[†]Number of FRAP recovery curves.

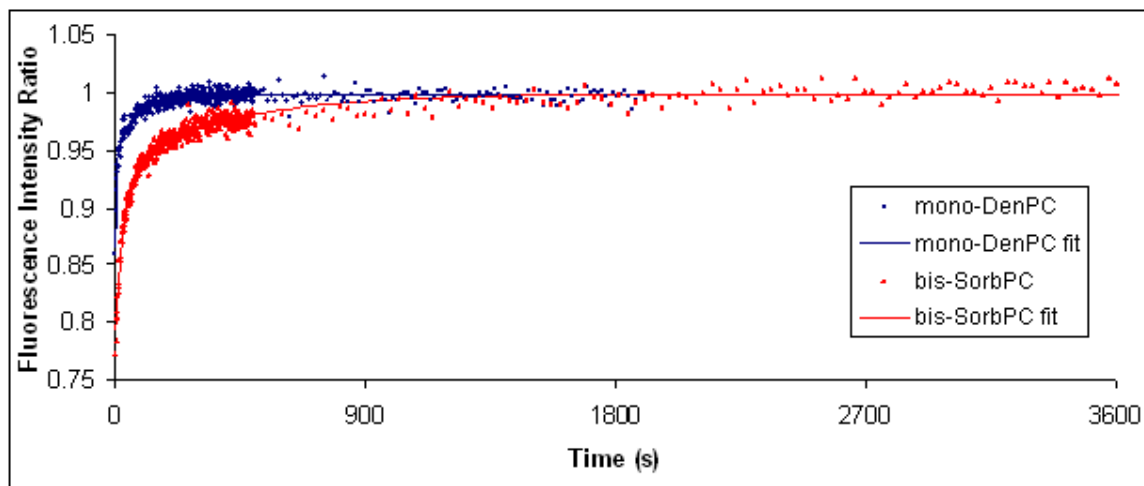


Figure. 3.4. Example FRAP recovery curves. Blue squares show the recovery of an unpolymerized mono-DenPC PSLB, while red triangles show the recovery of an unpolymerized bis-SorbPC PSLB. Lines are double-exponential fits to the data.

It has been suggested that the two equally populated diffusion coefficients could result from proximal and distal leaflet diffusion, because the two leaflets are in contact with different interfaces.^{114, 132} In the case of the unequal diffusing populations, though, if the cause of the biexponential were the separate leaflets, then the probe would have to be partitioning preferentially into one leaflet. Alternatively, the unequal populations could be the result of domains. All unpolymerized PSLBs measured in the study reported herein were ~ 100% mobile. The diffusion coefficients of DOPC fall within the expected range.¹¹²

It is difficult to directly compare the diffusion coefficients of the various lipids, because the FRAP measurements were performed at different temperatures. To enable comparison, the diffusion coefficients were normalized to 25 °C assuming that the lipids were in the fluid phase. This was done by using tabulated diffusion coefficient data from FRAP measurements on vesicle-fused DMPC PSLBs on glass at different temperatures.⁹⁵

The slope of log (D) vs. temperature (in °C) of the literature data above the T_m was found. Both the slow and fast diffusion coefficients in the literature data gave a slope of 0.033. The D_{avg} values in Table 3.2 were then converted to adjusted D_{avg}' by using

$$D_{avg}' = 10^{((\log D_{avg}) - ((T - T_{ref}) * 0.033))} \quad (3.1)$$

where T is the temperature in °C at which the FRAP measurements were performed and T_{ref} is 25 °C, or the temperature to which all of the diffusion coefficients will be normalized. The D_{avg}' values are listed in Table 3.2. Once the data had been normalized,

it could be seen that the diffusion coefficients decrease in the following order: DOPC > mono-DenPC > bis-DenPC > mono-SorbPC > bis-SorbPC. However, DOPC is far above its T_m at 25 °C (unlike the polymerizable lipids, which are only 5-10 °C above T_m), so it might not be fair to suggest that it is ‘faster’ than the polymerizable lipids. In the work of Tinland,^{132, 133} the diffusion coefficients of vesicle-fused DMPC on glass above T_m were measured to be ~ 3 and $0.5 \mu\text{m}^2/\text{s}$ at 27-28 °C, which is in reasonable agreement with values obtained for bis-DenPC measured at 30 °C.¹³² The T_m of DMPC (23°C) is within the range of the values listed in Table 3.1.

When comparing the unpolymerized denoylPCs to the sorbylPCs, it becomes apparent that for both the mono- and bis-substituted lipids, the denoylPCs have faster D_{avg} than sorbylPCs. This may be due to the fact that the sorbyl tail groups have the capability to interact via dipole-induced-dipole and dipole-dipole mechanisms in the center of the hydrophobic tail region, whereas the denoyl tails only interact via van der Waals forces. The stronger the interaction of the tail groups with each other, the slower the microscopic diffusion coefficient should be. If the mono-substituted lipids are compared to the bis-substituted lipids, the mono-substituted lipids are faster. In the case of the sorbylPCs, this could easily be understood, because the bis-substituted lipids have two polymerizable groups that can undergo dipole-dipole and dipole-induced-dipole interactions with each other instead of one. It should be pointed out that the difference in the mono- and bis-substituted denoylPCs is not statistically significant.

3.3.2 Diffusion Behavior of UV-polymerized PSLBs

The results for UV-polymerizing PSLBs above their T_m are shown in Table 3.3. There were no significant differences in any of the measured values between UV-poly(mono-DenPC) and unpolymerized mono-DenPC. The fast diffusion coefficient of mono-SorbPC slowed by a factor of 2 when UV-polymerized, while the slow diffusion coefficient remained unchanged. As a result, D_{avg} did not change for mono-DenPC, while there was a noticeable decrease for mono-SorbPC. For both mono-substituted lipids, the population ratios and total % recovery did not change due to polymerization.

The bis-substituted lipids showed a decrease in all of the measured and calculated diffusion coefficients after UV-polymerization. These lipids also had $< 100\%$ total recovery indicating a third, immobile population as well as a decrease in the quickly diffusing population, denoted as $\%_1$, relative to the respective unpolymerized PSLBs. For bis-DenPC, the slowly diffusing population, denoted as $\%_2$, also increased compared to unpolymerized bis-DenPC.

Table 3.3 also includes the ratio between the weighted average diffusion coefficients of the unpolymerized PSLBs and the polymerized PSLBs ($D_{avg\ un}/D_{avg\ poly}$). The diffusion coefficient ratio shows that there was a slight decrease in mono-SorbPC diffusion and a similar, significant decrease in the diffusion of both bis-substituted lipids upon UV-polymerization. Since the bis-substituted lipids are capable of cross-linking, it seems reasonable that under similar polymerization conditions, the mono-substituted lipids will make smaller polymers that present smaller barriers to diffusion whereas the bis-substituted lipids will make larger polymers, causing slower diffusion in PSLBs simply because there are more polymerizable groups per lipid molecule.

Table 3.3 Temperatures, diffusion coefficients, percent recoveries, and diffusion coefficient ratios of PSLBs UV-polymerized above T_m .

Lipid	T (°C)	D_1 ($\mu\text{m}^2/\text{s}$)	% ₁	D_2 ($\mu\text{m}^2/\text{s}$)	% ₂	D_{avg} ($\mu\text{m}^2/\text{s}$)	% _{tot}	$D_{\text{avg un}}/D_{\text{avg poly}}$	n
mono-DenPC	35	6 ± 1.0	71 ± 2.1	0.65 ± 0.086	28 ± 4.2	4.3 ± 0.85	99 ± 3.6	1.2 ± 0.44	4
mono-SorbPC	43	3.1 ± 0.22	74 ± 4.6	0.37 ± 0.051	25 ± 1.4	2.4 ± 0.30	99 ± 3.3	1.7 ± 0.54	3
bis-DenPC	30	0.7 ± 0.18	55 ± 2.6	0.10 ± 0.034	38 ± 3.6	0.40 ± 0.097	93 ± 3.5	6 ± 1.5	4
bis-SorbPC	37	0.4 ± 0.11	52 ± 4.5	0.06 ± 0.016	34 ± 2.5	0.24 ± 0.061	86 ± 3.0	4 ± 1.1	3

Table 3.4 Temperatures, diffusion coefficients, percent recoveries, and diffusion coefficient ratios of PSLBs UV-polymerized below T_m .

Lipid	T (°C)	D_1 ($\mu\text{m}^2/\text{s}$)	% ₁	D_2 ($\mu\text{m}^2/\text{s}$)	% ₂	D_{avg} ($\mu\text{m}^2/\text{s}$)	% _{tot}	$D_{\text{avg un}}/D_{\text{avg poly}}$	n
mono-DenPC	35	6 ± 1.0	70 ± 11	0.6 ± 0.29	23 ± 8.7	4.5 ± 0.95	96 ± 4.8	1.1 ± 0.43	4
mono-SorbPC	42	1.6 ± 0.21	70 ± 3.6	0.20 ± 0.038	28 ± 2.0	1.2 ± 0.15	98 ± 1.8	3 ± 1.1	5
bis-DenPC	30	1.2 ± 0.27	59 ± 4.9	0.120 ± 0.0091	36 ± 4.9	0.7 ± 0.20	95 ± 1.0	3.1 ± 0.97	3
bis-SorbPC	37	0.2 ± 0.11	40 ± 11	0.022 ± 0.0090	32 ± 5.4	0.09 ± 0.029	70 ± 11	10 ± 3.6	6

In the work by Kölchens et al.,⁹⁵ doping a mono-substituted acrylPC with 40-50% bis-substituted acrylPC and polymerizing under the same conditions as mono-substituted lipids led to slower diffusion than was observed for pure mono-substituted lipid.

In the case of UV-polymerization below the T_m , as shown in Table 3.4, it was again found that mono-DenPC did not display any change in diffusion behavior after UV-polymerization compared to unpolymerized PSLBs. There was a larger decrease in D_1 for mono-SorbPC when UV-polymerized below T_m than when UV-polymerized above T_m . There was also a decrease in D_2 for mono-SorbPC polymerized below T_m , in contrast to polymerization above T_m , which showed no change. For both mono-substituted lipids, there were no changes in percent recovery after UV-polymerization below T_m , similar to the situation above T_m . D_{avg} for mono-SorbPC decreased even more for polymerization below T_m than above T_m .

Similar to UV-polymerization above T_m , there were notable decreases in diffusion coefficients for the bis-substituted lipids compared with the unpolymerized PSLBs. Again, the bis-substituted lipids had $< 100\%$ recovery. Also, the $\%_1$ decreased for both bis-substituted lipids and $\%_2$ increased for bis-SorbPC compared with the unpolymerized PSLBs. In this case, however, the decrease in D_{avg} is largest for bis-SorbPC, yielding a $D_{avg\ un}/D_{avg\ poly}$ of 10, while above T_m , bis-DenPC exhibited the largest decrease in D_{avg} .

In general, for UV-polymerization below T_m , the sorbylPCs seem to create larger polymers compared with their respective denoylPC counterparts. In fact, when UV-polymerizing below T_m , bis-DenPC and mono-SorbPC both have similar decreases in D_{avg} .

The following subsections summarize the UV-polymerization findings.

UV-polymerized Mono-DenPC:

UV-polymerized mono-DenPC PSLBs have the same fluidity as unpolymerized PSLBs. These experiments were carried out under the assumption that all monomers had reacted, although mono-DenPC had not been used to determine the irradiation time. Figure 3.5 shows what might be happening in the case of UV-polymerized mono-DenPC. Assuming that all monomers had reacted to form polymers, then the mono-DenPC polymers must be ‘small’ compared to the other polymers formed by UV-polymerization. Kölchens et al. had investigated the diffusion coefficients of linear polymers formed from acryloyl lipids and had measured X_n of the same polymers.⁹⁵ Data from Ref. 95 is plotted as D_{un}/D_{poly} vs. X_n in Figure 3.6. A value of 2.7 for D_{un}/D_{poly} corresponds to a polymer size of about 230 repeat units, suggesting that there could very well be mono-DenPC oligomers forming on the order of 10-20 units due to UV-polymerization as suggested by Tsuchida et al.⁷⁶

UV-polymerized Mono-SorbPC:

Linear mono-SorbPC UV-polymers did exhibit a decreased D_{avg} compared to unpolymerized PSLBs. As depicted in Figure 3.7, somewhat larger polymers are expected for mono-SorbPC than mono-DenPC, based on the change in diffusion characteristics. Using Kölchens’ data on mono-acryloylPCs to get a rough estimate of polymer size, a $D_{avg\ un}/D_{avg\ poly}$ value of ~ 3 for UV-poly(mono-SorbPC) polymerized below T_m would suggest a polymer that is over 200 monomer units in length.

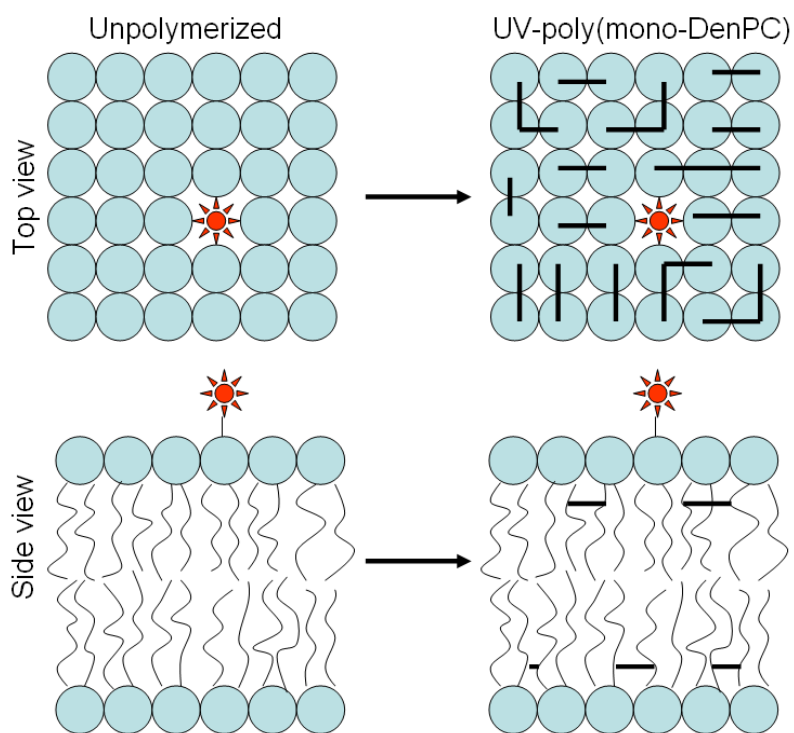


Figure 3.5. Diagram depicting what might be happening in the cases of UV-polymerized mono-DenPC. Red stars represent rhodamine-PE. Small polymers are believed to form, indicated by small numbers of lipids being polymerized together, as shown by the thick lines.

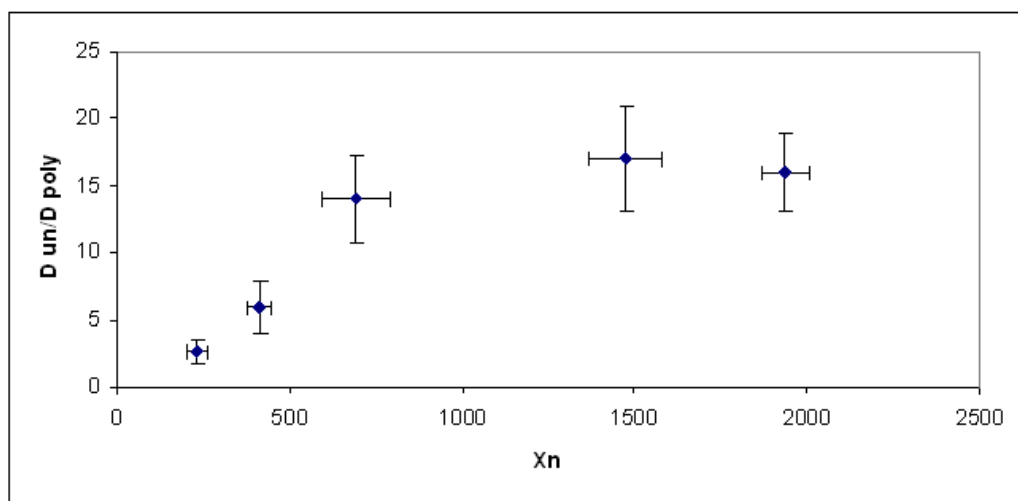


Figure 3.6. Diffusion coefficient ratio vs. number average degree of polymerization for mono-acryloylPCs. Data is from Ref. 95.

That polymer size is much greater than $X_n = 3-10$, as measured by Lamparski and O'Brien for UV-polymerized mono-SorbPC.⁷⁵ Their data, however, was gathered on vesicles polymerized above T_m . Like mono-DenPC, the mono-acryloylPC has the polymerizable group at the distal end of the lipid tail. As shown in Figure 3.7, this could result in the monolayer leaflets of the PSLB being connected. Polymerization above T_m for mono-SorbPC appears to result in smaller polymers than polymerization below T_m , based on the $D_{avg\ un}/D_{avg\ poly}$ value. Perhaps because the sorbylPCs have stronger intermolecular forces between the tails than the denoylPCs, the tails are confined to conformations that are more likely to facilitate polymerization, especially in the gel phase.

UV-polymerized Bis-DenPC:

UV-polymerization of bis-DenPC resulted in an increase in $D_{avg\ un}/D_{avg\ poly}$ both above and below T_m . Figure 3.8 illustrates what might be happening in the case of UV-polymerized bis-DenPC. Since there are two polymerizable groups per lipid molecule, cross-linking can take place. Separate polymers will form in the separate leaflets, because the denoyl group is near the head group of the lipid. UV-polymerization above T_m resulted in a 6-fold decrease in D_{avg} , which would correspond to polymers about 400 units in length according to Kölchens.⁹⁵ However, the data in Figure 3.6 was generated only from redox-polymerized linear polymers, so that estimate is even less reliable than the ones made for the mono-substituted lipids.

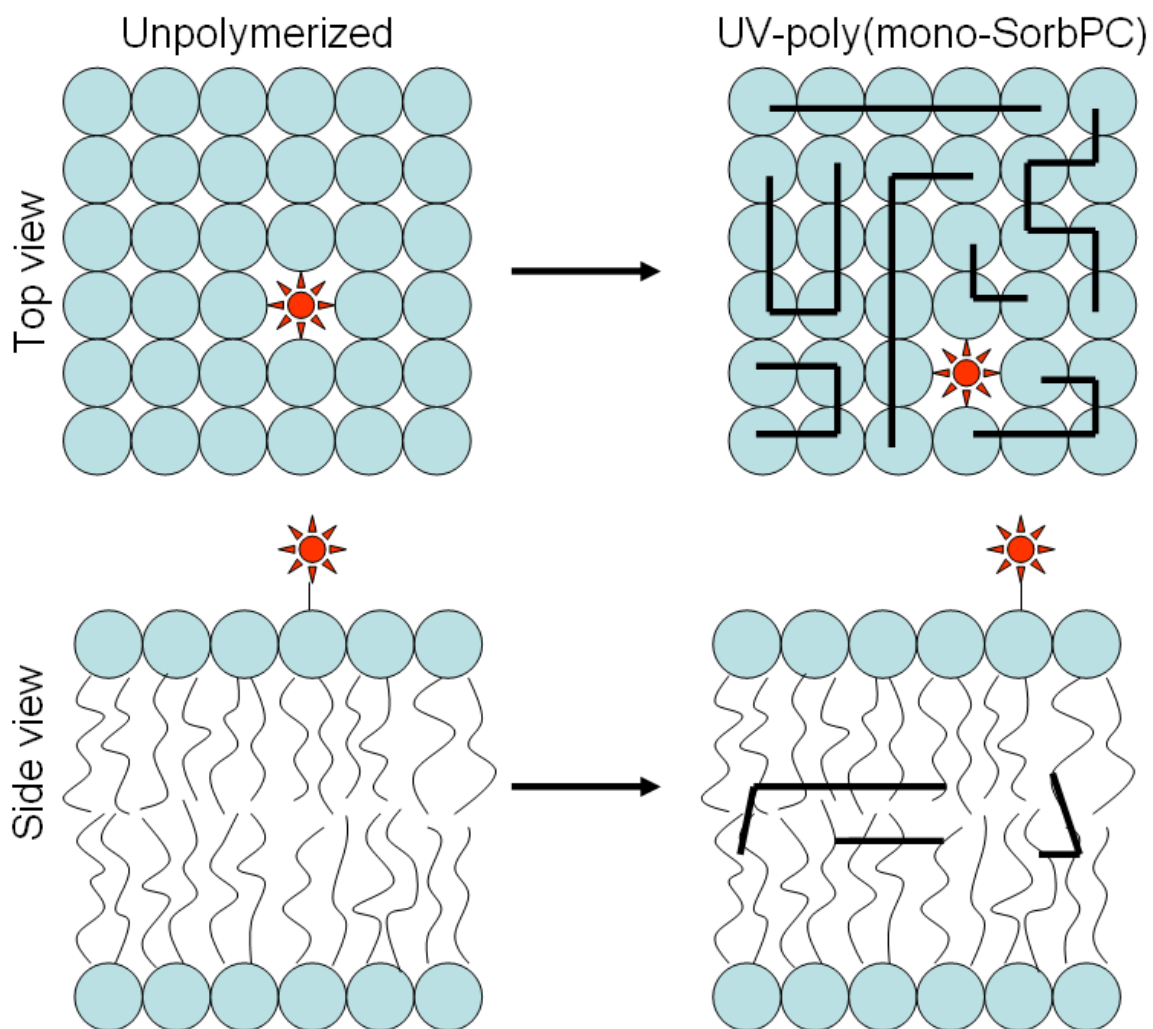


Figure 3.7. Diagram depicting what might be happening in the cases of UV-polymerized mono-SorbPC. Small polymers are believed to form, indicated by small numbers of lipids being polymerized together, as shown by the thick lines. In this case, polymerization is possible between the bilayer leaflets because of the location of the polymerizable group.

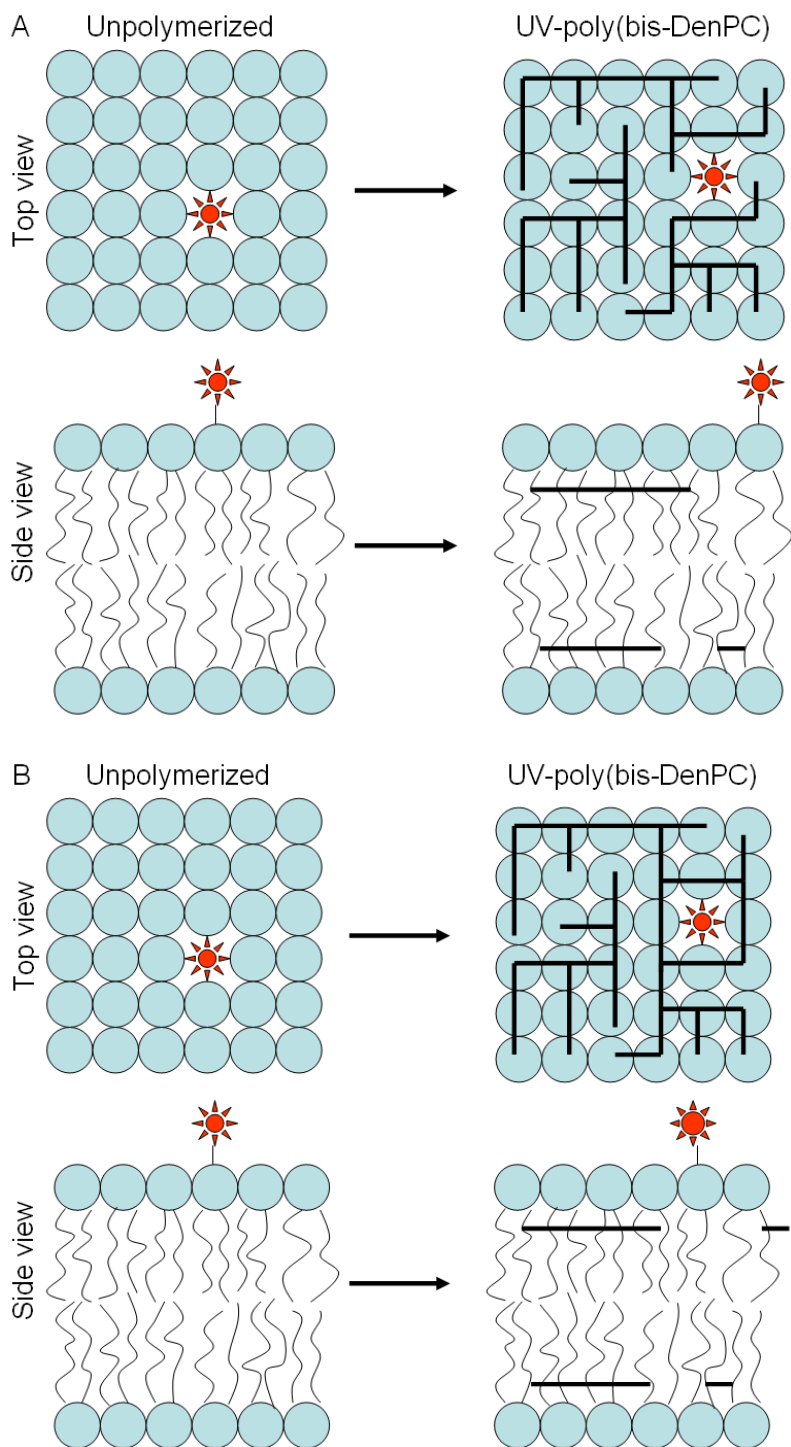


Figure 3.8. Possibilities for the UV-polymerization of bis-DenPC are shown. Cross-linking is now possible because there are two polymerizable units per lipid. In A) the fluorophore is not entirely entrapped by the polymer, while in B) the fluorophore is trapped in a polymer network.

Unfortunately, Kölchens did not report the sizes of polymers composed of both mono- and bis-substituted acrylPCs even though diffusion coefficients were measured. Mixtures of 1:1 mono- and bis-substituted acryloylPCs had a D_{un}/D_{poly} of more than 10 and Okazaki et al. had found similar results for UV-polymerized diynePCs.^{60, 95} There were also a measurable immobile fractions in both polymerized bis-DenPC cases (~ 4% immobile). In 100% fluid cases, the probe lipid is able to diffuse in between the polymers, while in < 100% fluid cases, some of the probe lipids are trapped in immobile regions, which may be a large polymer network, as depicted in Figure 3.8b. Since the mono-substituted lipids were 100% mobile after UV-polymerization and unpolymerized bis-substituted lipids were also, it is not reasonable to attribute < 100% recovery to a chemically heterogeneous substrate. Instead, the results suggest that portions of the lipid film are no longer moving due to the presence of polymers. Polymerization below T_m of bis-DenPC resulted in a faster D_{avg} than polymerization above T_m . This indicates that larger polymers are formed when polymerized above T_m for bis-DenPC, in agreement with the hypothesis by Lamparski and O'Brien that fluid phase lipids, because their chains are more disordered, would be capable of creating larger polymers than gel phase lipids.⁷⁵

UV-polymerized Bis-SorbPC:

Bis-SorbPC, when UV-polymerized, shows the same trends as mono-SorbPC, but amplified. UV-polymerization below T_m results in polymers larger than UV-polymerization above T_m . This is the opposite of the trend that was found for bis-DenPC. As discussed for mono-SorbPC, this may be due to a more fortuitous arrangement of the

polymerizable groups in the gel phase than in the fluid phase. Figure 3.9 depicts what may be happening in UV-polymerized bis-SorbPC films. Substantial immobile fractions were present at both polymerization temperatures, with the lower temperature giving the lowest mobile fraction. Figure 3.9b shows that there may be trapped probe molecules and cross-linking of lipid monolayers. In both UV-polymerized bis-substituted lipid instances, bis-SorbPC had lower mobile fractions than bis-DenPC, indicating that more probes are being corralled in bis-SorbPC films. Because the different bis-substituted polymerizable lipids are measured at different temperatures (due to differences in T_m) and because they did not all have the same unpolymerized diffusion coefficients, it is difficult to hypothesize which polymers between the two different lipid types is larger.

UV-polymerization General Findings:

Overall, the findings presented in Tables 3.2-3.4 are fairly similar to previous findings for UV-polymerized PSLBs.^{60, 120-122} In the literature, there is generally a 3-10 fold decrease in diffusion coefficient after UV-polymerization, as was discussed in Section 3.1. The bis-substituted lipids show this trend, regardless of polymerization temperature, as does mono-SorbPC when polymerized below the T_m . UV-polymerization of mono-DenPC has essentially no effect on its diffusion behavior. This is also the case for mono-SorbPC when polymerized above the T_m . The literature found that UV-polymerization of mono-substituted polymerizable lipids resulted in small polymers.^{75, 76,}

¹³⁴ When comparing D_{avg} of mono- and bis-substituted lipids in this work, it seems reasonable to suggest that mono-substituted lipids form smaller polymers than their bis-substituted counterparts.

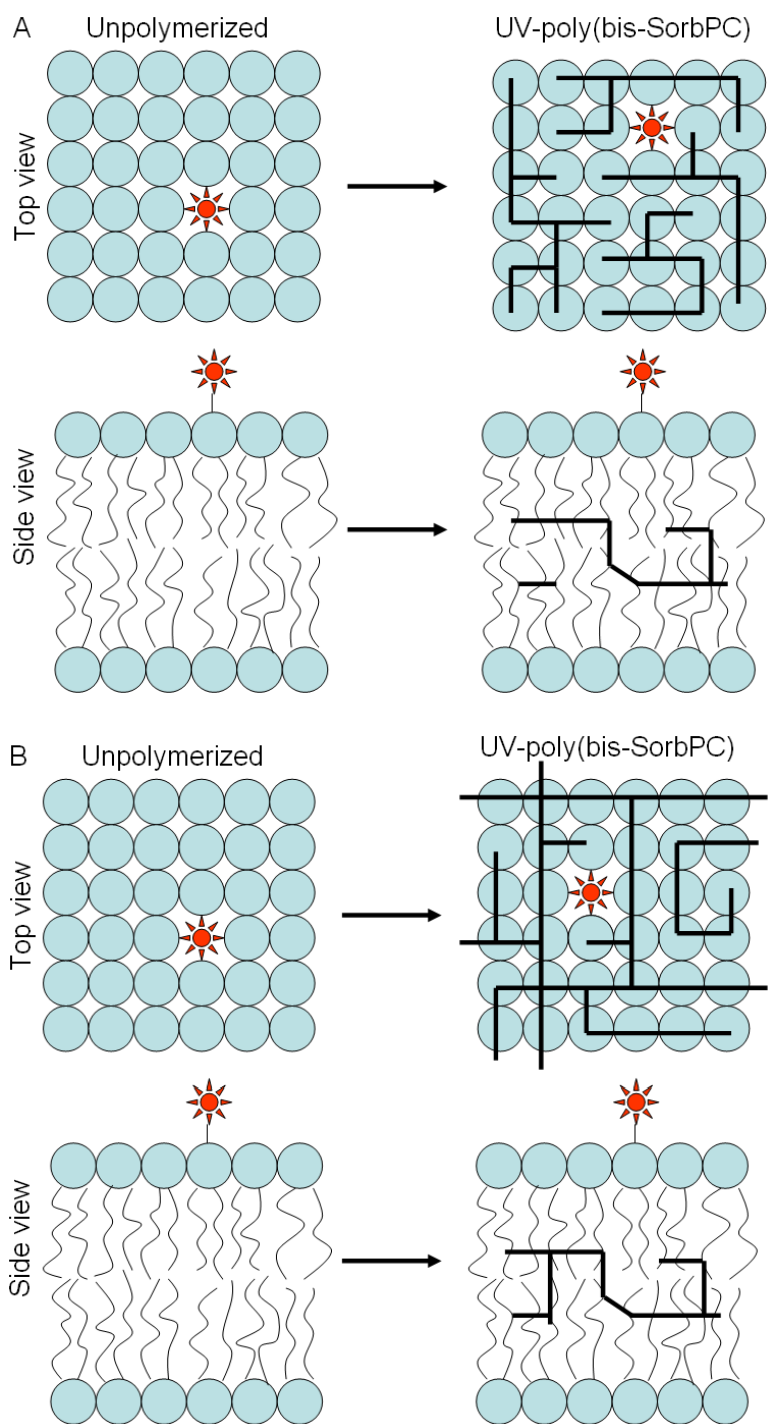


Figure 3.9. Possibilities for the UV-polymerization of bis-SorbPC are shown. Cross-linking and polymerization between leaflets is possible. In A) the fluorophore is not entirely entrapped by the polymer, while in B) the fluorophore is trapped in a polymer network.

3.3.3 Diffusion Behavior of Redox-polymerized PSLBs

Table 3.5 contains the results for redox-polymerization above T_m for all PSLBs. D_{avg} did not significantly change for mono-SorbPC, although there was a significant difference in D_1 compared with unpolymerized mono-SorbPC PSLBs. Mono-DenPC exhibited a 4-fold decrease in D_{avg} upon redox-polymerization above T_m . This is the opposite trend for mono-SorbPC and mono-DenPC than was found for UV-polymerization above T_m . Both PSLB types fully recovered when redox-polymerized above T_m , same as for UV-polymerization.

Bis-substituted lipids redox-polymerized above T_m diffused more slowly than their unpolymerized counterparts. It should be noted that while $D_{avg\ un}/D_{avg\ poly}$ for bis-DenPC suggests that there is overlap with unpolymerized lipids, it is due to the rounding convention (2.4 ± 1.1). Both slow and fast diffusion coefficients of bis-DenPC polymerized above T_m were significantly different than those found for unpolymerized bis-DenPC. Interestingly, redox-polymerized bis-DenPC (polymerized above T_m) diffused at approximately the same rate as films formed from UV-polymerization of bis-DenPC below T_m and was slower than diffusion of bis-DenPC films UV-polymerized above T_m . Full recovery was observed for bis-DenPC films, unlike in the UV-polymerized cases. Bis-SorbPC, on the other hand, showed a very large decrease in diffusion coefficient and a substantial immobile fraction. This was a much larger decrease in diffusion coefficients for redox-polymerized bis-SorbPC compared to UV-

polymerization. Bis-SorbPC was also the only lipid redox-polymerized above T_m that had a larger fraction of its probes diffusing slowly than quickly.

There were no clear trends for mono- vs. bis-substituted lipids or denoylPC v. sorbylPC in the case of redox-polymerization above T_m .

All redox-polymerization data below T_m can be found in Table 3.6. Redox-polymerization below T_m resulted in a very large decrease in mono-DenPC diffusion, while mono-SorbPC diffusion was decreased by a factor of ~ 5 compared to unpolymerized PSLBs. Both mono-substituted lipids had $< 100\%$ recovery, which was found in no other previously described dataset. Based on $D_{\text{avg un}}/D_{\text{avg poly}}$ values, both lipids also formed larger polymers when redox-polymerized below T_m than when polymerized above T_m . Unlike UV-polymerization, mono-DenPC had a noticeable decrease in diffusion. Mono-SorbPC, on the other hand, behaved similarly when UV- and redox-polymerized in terms of diffusion coefficient decreases.

Redox-polymerizing bis-DenPC and bis-SorbPC below T_m resulted in $D_{\text{avg un}}/D_{\text{avg poly}}$ values that are misleading due to the large errors associated with the D_1 and D_2 measurements. In fact, D_1 , D_2 , and D_{avg} for both lipids when unpolymerized and redox-polymerized below T_m are all significantly different. As found in redox-polymerization of bis-DenPC above T_m , there is basically 100% recovery. Bis-SorbPC has $< 100\%$ recovery. As seen in the case of bis-SorbPC redox-polymerized above T_m , $\%_2$ was greater than $\%_1$. Comparing redox-polymerization temperature of bis-substituted lipids, one finds that only D_2 is significantly different for bis-DenPC, while only D_1 is significantly different for bis-sorbPC.

Table 3.5 Temperature, diffusion coefficients, percent recoveries, and diffusion coefficient ratios of PSLBs redox-polymerized above T_m .

Lipid	T (°C)	D_1 ($\mu\text{m}^2/\text{s}$)	% ₁	D_2 ($\mu\text{m}^2/\text{s}$)	% ₂	D_{avg} ($\mu\text{m}^2/\text{s}$)	% _{tot}	$D_{\text{avg un}}/D_{\text{avg poly}}$	n
mono-DenPC	36	1.9 ± 0.66	71 ± 7.7	0.2 ± 0.12	26 ± 7.7	1.4 ± 0.39	97 ± 4.2	4 ± 1.5	3
mono-SorbPC	44	2.7 ± 0.86	79 ± 2.3	0.3 ± 0.12	23 ± 3.7	2.2 ± 0.74	102 ± 1.5	1.8 ± 0.82	3
bis-DenPC	29	1.2 ± 0.47	63 ± 6.4	0.19 ± 0.062	34 ± 4.1	0.9 ± 0.41	97 ± 3.1	2 ± 1.1	9
bis-SorbC	34	0.0067	16	0.0011	56	0.0016	71	~560	1

Table 3.6 Temperatures, diffusion coefficients, percent recoveries, and diffusion coefficient ratios of PSLBs redox-polymerized below T_m .

Lipid	T (°C)	D_1 ($\mu\text{m}^2/\text{s}$)	% ₁	D_2 ($\mu\text{m}^2/\text{s}$)	% ₂	D_{avg} ($\mu\text{m}^2/\text{s}$)	% _{tot}	$D_{\text{avg un}}/D_{\text{avg poly}}$	n
mono-DenPC	35	0.052	21	0.0014	56	0.012	77	~400	1
mono-SorbPC	44	1.1 ± 0.20	68 ± 2.9	0.18 ± 0.033	30 ± 2.1	0.8 ± 0.16	97 ± 1.4	5 ± 1.8	5
bis-DenPC	30	0.5 ± 0.36	65 ± 7.7	0.07 ± 0.050	32 ± 5.5	0.3 ± 0.28	97 ± 2.7	7 ± 6.9	4
bis-SorbPC	36	0.03 ± 0.018	20 ± 14	0.003 ± 0.0030	60 ± 14	0.007 ± 0.0064	74 ± 8.4	100 ± 120	3

As in the case of redox-polymerization above T_m , there are no mono- vs. bis-substituted trends and no denoylPC vs. sorbylPC trends for redox-polymerization below T_m .

The mono-substituted lipids appear to form larger polymers when redox-polymerized below T_m than above T_m , based on the D_{avg} values obtained. The literature shows the opposite trend for mono-DenPC employing redox polymerization using the same redox initiators as this study. Tsuchida et al. had found that mono-DenPC formed larger polymers above T_m ($X_n \sim 45$) than below ($X_n \sim 27$).⁷⁶ The temperatures used for polymerization below T_m were different between that investigation (8°C) and this study (20°C). The enormous drop in D_{avg} found for mono-DenPC suggests that much larger polymers are being formed than those that had been studied by Tsuchida, because an estimate of polymer size from Kölchens'⁹⁵ work on mono-substituted lipids would put the redox-polymers of mono-DenPC polymerized below T_m at significantly larger than $X_n = 2000$. The meaning of this large drop will be discussed later in Section 3.3.6. Meanwhile, similarly estimating the size of mono-SorbPC polymers formed below T_m would put them at ~300-400 units and less than 200 units when polymerized above T_m . These X_n values are in the range of polymer sizes determined for redox-polymers formed from mono-SorbPC and polymerized above T_m .^{75, 135} Srisiri et al. had found that different polymerization temperatures in the same phase will produce different polymer sizes. It was found that mono-DenPC redox-polymerized in the fluid phase using $KBrO_3/L$ -cysteine gave $X_n \sim 185$ at 45°C and $X_n \sim 125$ at 65°C.¹³⁵

The redox-polymerized bis-substituted lipids may have formed larger polymers below T_m , but the large errors associated with the data make these results harder to interpret. In all redox-polymerization cases, bis-SorbPC diffuses about 100 times slower, if not, more than when unpolymerized. Interestingly, Lamparski and O'Brien determined that redox-polymerization of mono-SorbPC and bis-SorbPC at the same monomer/initiator ratios (using AIBN thermal initiation) create similarly sized polymers.⁷⁵ This was not seen in the data gathered by diffusion coefficient measurements. On the other hand, the size of bis-DenPC estimated from Figure 3.6 could have been in the vicinity of 200-700 units, which would put those polymers in the range of sizes found in the work of Lamparski and O'Brien.

Significant differences between UV-polymerization and redox-polymerization were found for mono-DenPC and bis-SorbPC, but not for mono-SorbPC and bis-DenPC. Mono-DenPC did not seem to change its diffusion behavior when UV-polymerized, but did very noticeably when redox-polymerized. This agrees with the findings of others that UV-polymerization does not create polymers as large as redox-polymerization.^{75, 76, 134} Bis-SorbPC shows the same trend, but to a much larger extent. In terms of polymerization temperature, mono-SorbPC appears to polymerize more efficiently below T_m than above in UV- and redox-polymerized cases, while bis-DenPC shows opposite trends for polymerization temperature for UV- and redox-polymerization. Another significant difference in UV- and redox-polymerization behavior for bis-DenPC is that the redox-polymerized PSLBs were all completely fluid, while UV-polymerization resulted in measurable immobile fractions.

The following subsections provide summaries of the redox-polymerized behavior of the PSLBs.

Redox-polymerized Mono-DenPC:

Mono-DenPC redox-polymerized above T_m did have decreased diffusion compared with unpolymerized PSLBs and suggests the formation of larger polymers than those formed by UV-polymerization. Figure 3.10 summarizes what might be happening in the case of redox-polymerization of mono-DenPC above T_m : moderately sized polymers in fluid films. Redox-polymerization below T_m results in enormous linear polymers and a significant immobile fraction, as illustrated in Figure 3.11. Fahmy et al. saw a diffusion coefficient decrease on the order of 500 for a mono-substituted acryloyl lipid, similar to the magnitude of diffusion coefficient decrease in this work.¹²³

Redox-polymerized Mono-SorbPC:

Mono-SorbPC had similar UV- and redox-polymerization behavior as a function of temperature. The same explanation of behavior is also assumed.

Redox-polymerized Bis-DenPC:

Bis-DenPC's redox-polymerization behavior can be summed up in Figure 3.8. There is no measurable immobile fraction and the polymer sizes are most likely similar to what was found for UV-polymerization. Unlike UV-polymerization, though, it appears that larger polymers are capable of forming below T_m than above T_m . As a result, the argument that the fluid phase allows the lipid tails more freedom to properly line up for redox polymerization is not accurate for bis-DenPC.

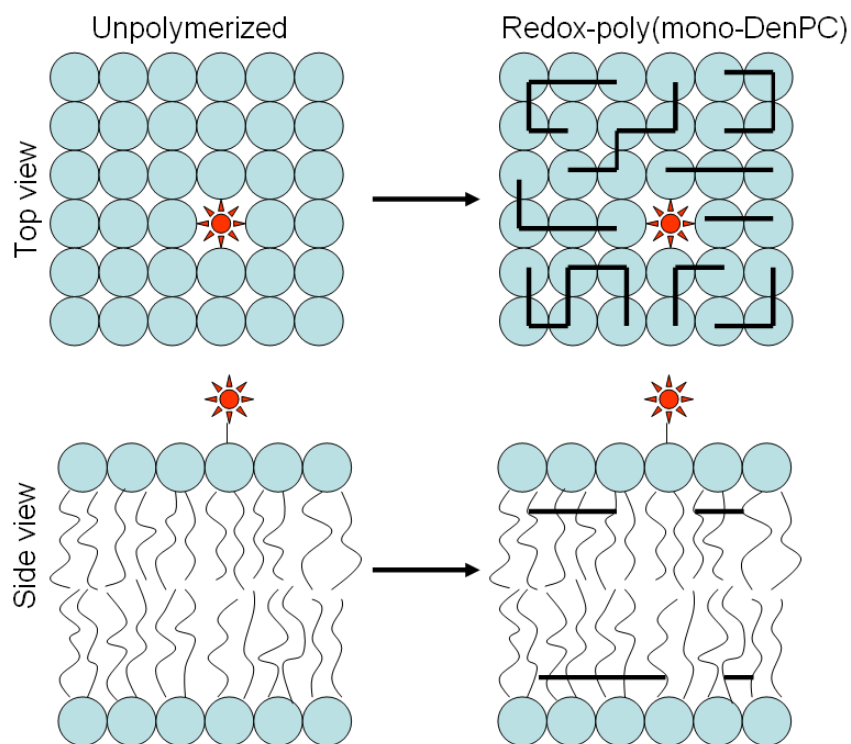


Figure 3.10. Diagram depicting redox-polymerization of mono-DenPC above T_m . Polymers larger than UV-poly(mono-DenPC) are believed to form. Due to the location of the polymerizable group, polymers will not form connecting the two leaflets.

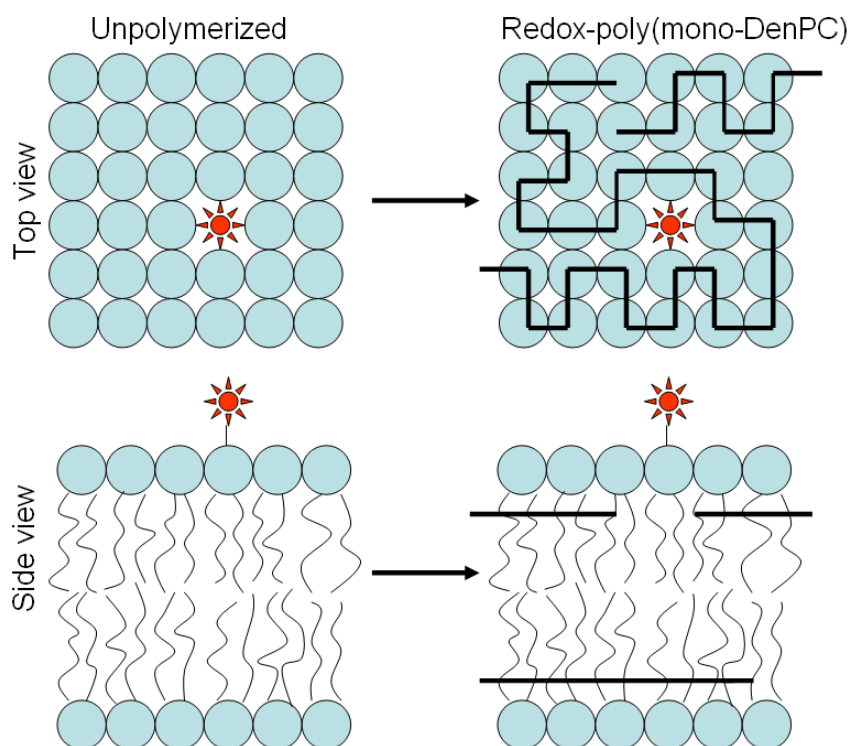


Figure 3.11. The results of redox-polymerization of mono-DenPC below T_m are shown. Based on the diffusion coefficient and % recovery, large polymers in their respective leaflets are expected.

Lamparski had found that larger polymers resulted from acryloylPCs which were mono-substituted than those which were bis-substituted, similar to what was found in the case of mono- and bis-DenPC here.¹³⁶ It had been hypothesized that this was a result of the decrease in monomer diffusion to the propagating end due to cross-linking in the bis-substituted case. Because of the location of the polymerizable group in bis-DenPC, there is a high barrier for the polymer for monomers to cross over.^{75, 136} This effect will be discussed more thoroughly later in this Section (“*General Findings for UV- and Redox-polymerization*”).

Redox-polymerized Bis-SorbPC:

Bis-SorbPC formed large redox-polymers with immobile fractions at both temperatures similar to what is depicted in Figure 3.9b. Based on the magnitude of the diffusion coefficients, redox-polymerization creates larger polymers than UV-polymerization. Also, bis-SorbPC polymers seem to be larger than mono-SorbPC polymers under all polymerization conditions.

Redox-polymerization General Findings:

It is known in the literature that large decreases in diffusion coefficient can happen when a lipid bilayer is redox-polymerized.^{95, 123} This was determined to be true in the cases of bis-SorbPC and mono-DenPC, under certain circumstances. On the other hand, this was not the case for mono-SorbPC and bis-DenPC.

General Findings for UV- and Redox-polymerization:

A variety of conflicting mechanisms that might dictate the size of the polymer or the geometry of the polymer are at play here. In the case of the sorbylPCs, it was found that under all investigated polymerization conditions, bis-SorbPC exhibited a larger decrease in diffusion coefficient than mono-SorbPC. Because the polymerizable group location and identity are the same, this could be attributed to the number of polymerizable groups. There are more possible lipids that can become part of the same polymer molecule per bis-SorbPC lipid than mono-DenPC lipid. Also, as mentioned by Lamparski,^{75, 136} the sorbylPCs have a low barrier to monomer diffusion. In other words, the polymer presents a barrier in the hydrophobic center of the bilayer that can easily be ‘stepped’ over by the hydrophobic monomer tails than if the barrier was at the water/hydrocarbon interface. In contrast, the denoylPCs have a barrier near the water/hydrocarbon interface. It would be hard to envision a monomer ‘ducking under’ the barrier with its hydrophilic headgroup or ‘stepping’ over the barrier with its hydrophobic tails. This means that the formation of polymer could be inhibited by cross-linking, because there would be more possible barriers per molecule for bis-DenPC (2 polymerizable groups) than for mono-DenPC (1 polymerizable group). That may explain why very large polymers (evidenced by a very large decrease in diffusion coefficient) are found for redox-polymerization of mono-DenPC below T_m , while bis-DenPC never exhibits such a large drop in diffusion coefficient.

3.3.4 Diffusion Behavior of PSLBs UV- and Redox-polymerized at T_m

As diffusion coefficients are plotted as a function of temperature for a particular lipid, a discontinuity is frequently noted in the vicinity of T_m .^{120, 122, 132} In the case of

vesicle-fusion on glass, Scomparin found a smoother transition than for Langmuir-Blodgett PSLBs on glass and Langmuir-Blodgett PSLBs on mica.¹³² Additionally, Lamparski noted that UV-polymerization near the T_m resulted in a greater polymerization rate than at other temperatures.⁷⁵ Polymerization at T_m was attempted here for a select few mono-substituted systems. The FRAP measurements for these cases were performed in the fluid phase, so as to be comparable with the measurements described in previous Sections of this chapter.

Table 3.7 shows the raw data for polymerization at T_m . The decrease in D_{avg} for UV-poly(mono-DenPC) is similar to what was found for redox-poly(mono-DenPC) polymerized above T_m . It is unexpected because UV-polymerization of mono-DenPC at temperatures other than T_m did not exhibit a noticeable D_{avg} difference from unpolymerized mono-DenPC PSLBs. The PSLBs were completely fluid, as seen for all UV-poly(mono-DenPC) films and redox-poly(mono-DenPC) polymerized above T_m .

Redox-polymerized mono-SorbPC at T_m is similar to redox-poly(mono-SorbPC) polymerized below T_m in terms of diffusion coefficients and % recoveries.

Redox-poly(mono-DenPC) at T_m resulted in a three orders of magnitude decrease in diffusion compared with unpolymerized films. These films were also 20% immobile. These characteristics are similar to redox-poly(mono-DenPC) polymerized below T_m , but with potentially a larger decrease in D_{avg} , suggesting even larger polymers. The immobile fractions were similar, however.

Table 3.7 Temperatures, diffusion coefficients, percent recoveries, and diffusion coefficient ratios of PSLBs polymerized at T_m .

Lipid	T (°C)	D ₁ ($\mu\text{m}^2/\text{s}$)	% ₁	D ₂ ($\mu\text{m}^2/\text{s}$)	% ₂	D _{avg} ($\mu\text{m}^2/\text{s}$)	% _{tot}	D _{avg un} / D _{avg poly}	n
UV-poly (mono- DenPC)	34	1.7 ± 0.90	63 ± 9.2	0.2 ± 0.17	30 ± 12	1.2 ± 0.55	97 ± 4.2	4 ± 2.3	5
Redox-poly (mono- DenPC)	34	0.012 ± 0.0029	16 ± 4.4	0.0012 ± 0.00019	64 ± 5.2	0.0027 ± 0.00084	80.1 ± 0.83	1,900 ± 830	3
Redox-poly (mono- SorbPC)	44	1.3 ± 0.29	75 ± 1.5	0.09 ± 0.030	24.6 ± 0.64	1.0 ± 0.21	100 ± 1.9	4 ± 1.5	3

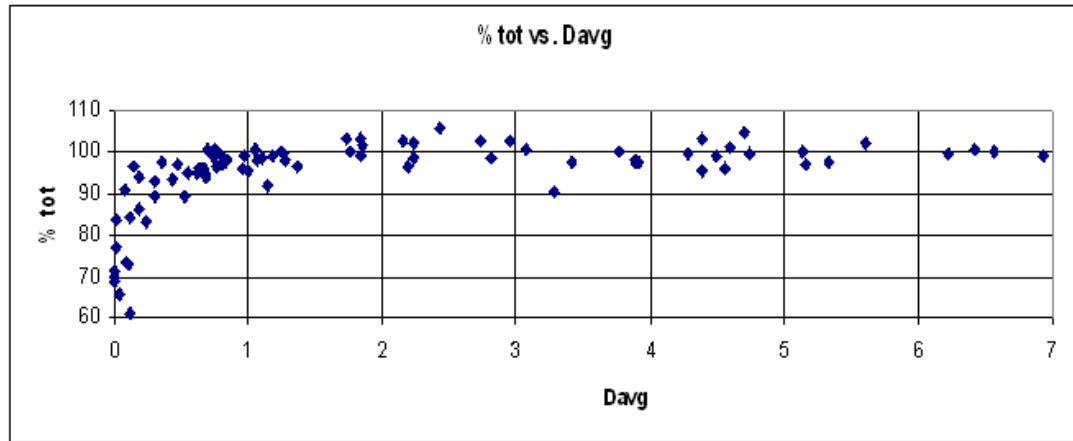
The population distribution between slow and fast moving probes was also similar to redox-poly(mono-DenPC) polymerized below T_m , with approximately 3 times more probes diffusing slowly than quickly, which is nearly the opposite of the population distribution of unpolymerized PSLBs.

3.3.5 % Recovery as a Function of Diffusion Coefficient

It has been noted in previous Sections that as the diffusion coefficients decreased, the $\%_{tot}$ for each species decreased as well. Also, the dominant population switched from the fast diffusing to the slow diffusing with an overall decrease in diffusion coefficient. To further explore this phenomenon, the $\%_{tot}$ of all the previously described data were plotted as a function of D_{avg} , shown in Figure 3.12a. Figure 3.12b shows the percent immobile as a function of D_{avg} . For D_{avg} greater than $\sim 1 - 2 \mu m^2/s$, PSLBs show $\sim 100\%$ recovery. Below that cutoff there is a smooth decrease in mobile fraction (or a smooth increase in immobile fraction). If this data is further broken down into its components, as shown in Figure 3.13, it is notable that the same trend is mirrored in $\%_1$ vs D_1 . When the fast diffusion coefficient is greater than $1-3 \mu m^2/s$, $\%_1$ holds steady at $\sim 70\%$. There is an increase in $\%_2$ once D_2 decreases to less than $0.1 - 0.2 \mu m^2/s$.

The data presented in Figures 3.12 and 3.13 suggest that as polymers get larger, more and more of the probe molecules are trapped in ‘immobile’ regions. The immobile fraction might still retain some mobility, but it is not observable on the timescale of these experiments. These immobile regions are most likely very large polymer networks. Also, the population associated with $\%_2$ begins to dominate once the diffusion becomes slow enough and $\%_1$ approaches zero.

A



B

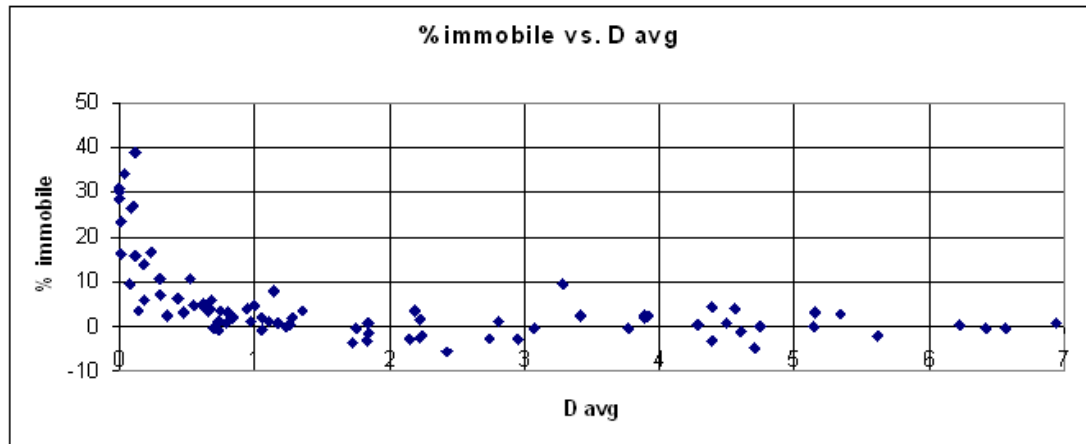


Figure 3.12. Mobile and immobile percents as a function of D_{avg} for all PSLBs included in this work. A) $\%_{tot}$ as a function of D_{avg} . B) $\%_{tot}$ as a function of D_{avg} .

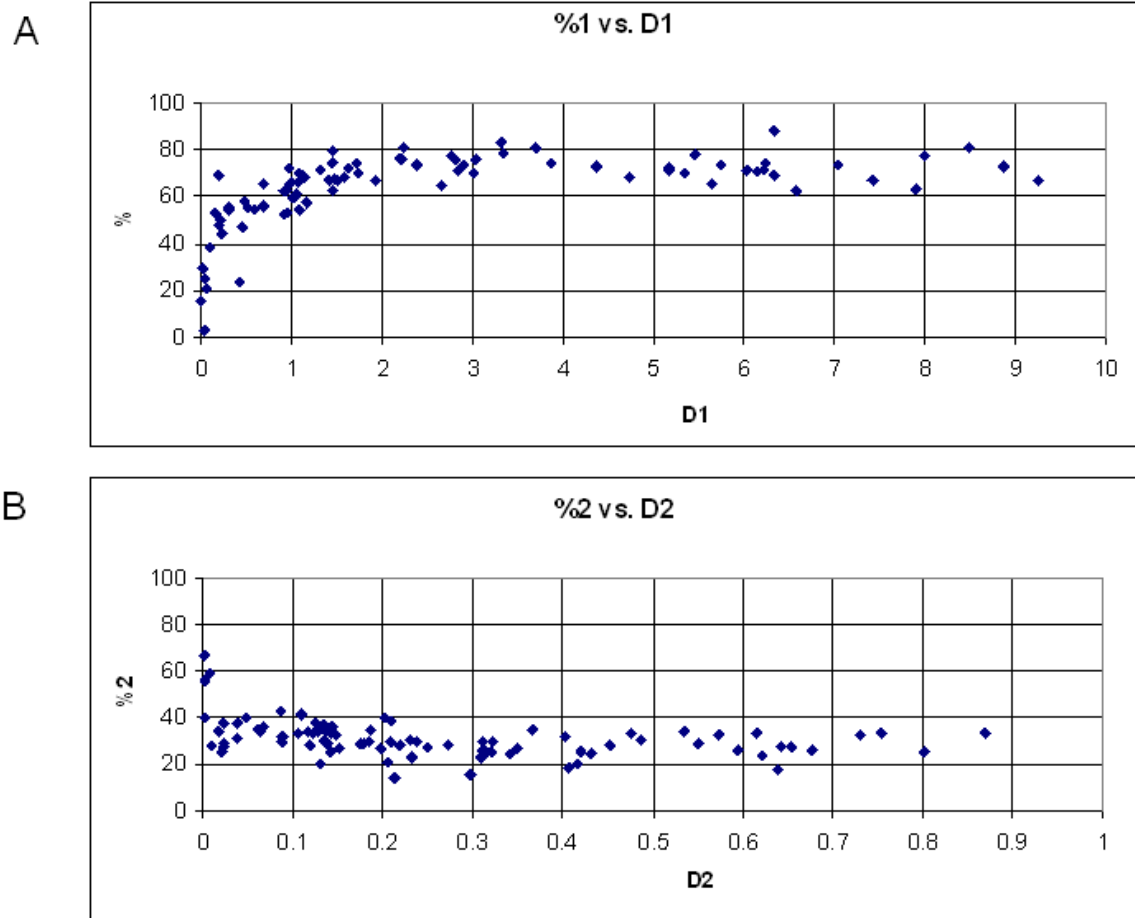


Figure 3.13. Mobile fractions as a function of D. A) %₁ as a function of D₁. B) %₂ as a function of D₂.

This finding implies that as some polymers get larger, there are fewer lipid monomers left to form smaller polymers. The fluorescent probes within the PSLBs are then maneuvering around mostly large obstacles (large polymers) that correspond to %₂.

3.3.6 Data Interpretation with Respect to the Percolation Threshold

As is seen in Kölchens et al.,⁹⁵ the larger the polymer, the slower it will diffuse. However, the $D_{\text{avg un}}/D_{\text{avg poly}}$ of Kölchens' work plateaus around 15 for mono-substituted lipids. Okazaki's work showed a similar response around a $D_{\text{avg un}}/D_{\text{avg poly}}$ value of 10, after which the films were basically immobile.⁶⁰ The data gathered in this work displays a variety of $D_{\text{avg un}}/D_{\text{avg poly}}$ values between 1 and 10. Above 10, there is an enormous jump to 100+. In the specific diffusion coefficient values obtained, there is also an order of magnitude gap below $0.2 \mu\text{m}^2/\text{s}$ for D_1 and below $0.02 \mu\text{m}^2/\text{s}$ for D_2 . That is also the point where the majority of the population switches from diffusing quickly to diffusing slowly based on %₁ and %₂ values.

Saxton had used modeling to investigate the effects of obstacles on lipid diffusion.¹³⁷⁻¹⁴⁰ Almeida et al.¹⁴¹ refined some of Saxton's earlier work based on their findings investigating fluid/gel phase lipid mixtures. They had observed a large drop in recovery time and % recovery above a certain obstacle (gel) fraction in the bilayers, which they interpreted as the percolation threshold. The percolation threshold is where the membrane goes from a continuous fluid phase with islands of obstacles to a continuous obstacle phase with lakes of fluidity, as shown in Figure 3.14.

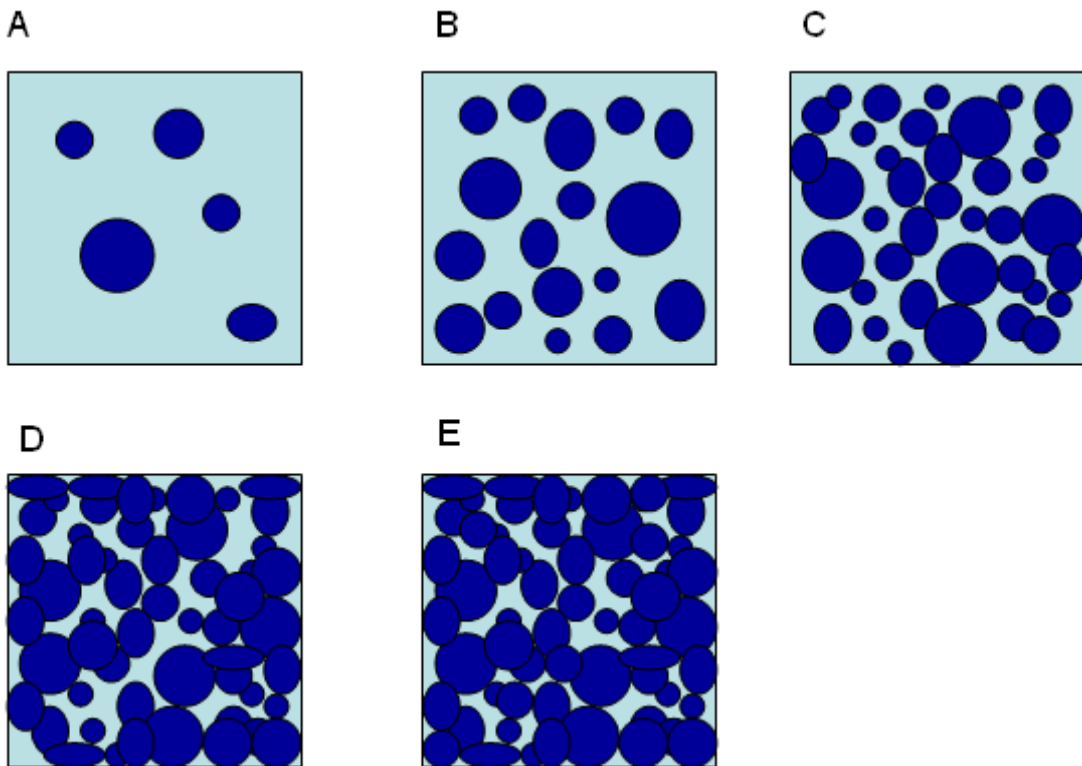


Figure 3.14. Increasing obstacle fraction in a bilayer from A) to E). Light blue areas are fluid, while dark blue are obstacles. In A) there are a few separate, mostly spherical obstacles. B) has an increased number of obstacles. In C) there are more obstacles and they have started to coalesce to form extended shapes. D) shows that the area fraction obstacle has increased so much that all fluid phases are now trapped by obstacles. The percolation threshold was passed from C) to D). In E) the area fraction obstacle has increased again and the fluid regions are even smaller. The bilayer is now mostly obstacle.

Ratto and Longo had also studied gel/fluid mixtures with varying obstacle fractions and obstacle sizes.¹⁴² At obstacle fractions of about 70%, they found an enormous decrease in diffusion coefficient. The films were basically immobile at that point. AFM data gathered on these films showed that the fluid phases were no longer continuous. Both FRAP and AFM data agreed that above 70% obstacle fraction they had crossed the percolation threshold. Interestingly, they noted two types of behavior at < 70% obstacle fraction. Below 50% obstacle fraction, AFM data had indicated isolated circular gel phase islands. Meanwhile, between 50-70% obstacle fraction, they saw these islands coalescing into extended obstacles, which are believed to be more efficient at slowing down diffusion.¹³⁹ Okazaki et al.⁶⁰ had investigated mixed poly/unpoly lipid bilayers and found similar results to Ratto and Longo's findings. Above an obstacle fraction of ~70%, diffusion was found to be nearly zero, indicating the percolation threshold. They also found two regimes below 70% obstacle fraction. Below 40% obstacle fraction, there was a linear $D_{\text{avg un}}/D_{\text{avg poly}}$ v. obstacle fraction regime. For obstacle fractions between 40% and 70% there was finite diffusion, but the linear trend no longer continued. Okazaki interpreted this regime as being where channels between polymers were formed.

Interpreting the data presented in this work with regard to the idea of a percolation threshold, it seems like instances where there was a drop of more than a factor of 10 in $D_{\text{avg un}}/D_{\text{avg poly}}$ would make for a likely place for the percolation threshold. We do not have obstacle fraction data to actually justify this choice, but based on the significant changes in fluidity at that point that were also seen by Ratto, Almeida, Okazaki and their

coworkers,^{60, 141, 142} it seems like a reasonable cutoff. For the PSLBs that did have D_{avg} $D_{\text{un}}/D_{\text{avg poly}}$ values greater than 10 (all redox-polymerized bis-SorbPC, and redox-polymerized mono-DenPC polymerized at or below T_m), they also had greater %₂ values than %₁, which were not found in any other PSLBs. Perhaps it could be argued that like Okazaki et al. and Ratto and Longo,^{60, 142} there are two regimes below the percolation threshold. There appears to be an intermediate region where the %₁ and %₂ populations are changing, as shown in Figure 3.13, but where they have not yet reached a point with a precipitous drop in diffusion coefficient (i.e. all UV-poly bis-substituted lipids and redox-poly(mono-SorbPC) below T_m . These PSLBs do not show complete recovery either.

According to these distinctions, it seems like the data could be broken up into 3 fluidity categories: completely fluid, partially fluid, and immobile (on short time scales). Table 3.8 summarizes the categories.

Table 3.8 Fluidity categories of investigated PSLBs.

Fluid	Partially Fluid	Immobile
unpolymerized lipids	UV-polymerized bis-substituted lipids	Redox-polymerized mono-DenPC at or $< T_m$
UV-polymerized mono-substituted lipids	Redox-polymerized mono-SorbPC $< T$	Redox-polymerized bis-SorbPC
Redox-polymerized mono-substituted lipids $> T_m$		
Redox-polymerized bis-DenPC		

3.4 Conclusions

Diffusion coefficients for PSLBs created from the lipids in Figure 1.19 on glass were measured using the FRAP (rhodamine-PE) technique. Unpolymerized PSLBs as well as UV-polymerized and redox-polymerized PSLBs were investigated.

Polymerization temperatures above and below T_m were investigated for all lipids and polymerization types, while polymerization at T_m was studied in some mono-substituted cases. Although some trends were found, as discussed above, it appears that the polymerizable group identity, polymerization temperature (with respect to T_m) and polymerization method all need to be taken into consideration for elucidating fluidity of PSLBs. In the end, three categories of PSLBs were identified based on their diffusion coefficients and percent recoveries: fluid, partially fluid, and immobile. Unpolymerized and UV-polymerized PSLBs were either fluid or partially fluid, while redox-polymerized PSLBs could fall into any of the 3 categories, depending on the lipid investigated and polymerization temperature. The relationship of these properties to the structure and activity of transmembrane proteins is discussed in Chapter 5.

CHAPTER 4: MEASURING THE MECHANICAL PROPERTIES OF POLYMERIZABLE LIPIDS: MICROPIPETTE ASPIRATION OF GIANT UNILAMELLAR VESICLES

4.1 Introduction

The properties of the lipid membranes into which integral membrane proteins are incorporated can affect the function of the proteins.^{9, 11, 97} Physical deformation of the membranes is sometimes necessary for proper protein function, suggesting that mechanical properties (i.e. elasticity) are important.^{22, 98} As was described in Section 1.5, it is necessary to balance the ruggedness of the membrane material with the flexibility needed to maintain the activity of embedded proteins. The focus of this Chapter will be the measurement of mechanical properties of novel, polymerizable lipid membranes.

Almost no data exists in the literature about the mechanical properties of polymerizable lipids or similar materials. A figure in an Evans and Needham publication comparing the lysis tension and apparent area expansion moduli of GUVs composed of various lipids had two data points labeled “polymerizable lipids”, which exhibited the lowest lysis tensions and lowest apparent area expansion moduli of all lipids measured.³⁵ The identity of the polymerizable lipids was not stated in the text. Correspondence with one of the authors revealed that the polymerizable lipids were unpolymerized diacetylinic lipids.¹⁴³ Polymerization of diacetylinic lipid GUVs was not successful.

Mechanical properties of cross-linkable polymersomes were studied by Discher et al.^{144, 145} Polymersomes are vesicles composed of synthetic diblock copolymers that mimic some of the properties of lipids.¹⁴⁶⁻¹⁴⁸ The cross-linkable polymersomes had more

than 40 polymerizable groups per monomer. It was found that the lysis tension of fully cross-linked polymersomes was on the order of 1,000 mN/m, which is ~100 fold greater than lysis tension found for GUVs consisting of natural lipids.¹⁴⁹ It was also found that non-cross-linkable polymersomes displayed similar bending elastic moduli and area expansion moduli as natural lipids.

A number of methods have been used to measure the mechanical properties of lipid membranes, including photon correlation spectroscopy,^{150, 151} x-ray scattering,¹⁵² and x-ray diffraction coupled with NMR spectroscopy.¹⁵³ Recently, AFM techniques have been employed, which are able to offer more local measurements of membrane deformation.^{44, 154-156} The most popular techniques, however, have been microscopy-based.³⁷ Specifically, micropipette aspiration (μ PA) of GUVs is most common.^{36, 157-163} In general, the μ PA technique involves applying suction to micron-sized GUVs while monitoring the change in GUV area by imaging.^{35, 149, 164} The area and tension data can then be mathematically manipulated to yield mechanical characteristics of the GUV materials. Due to its long history of use, frequency of use in literature, and well-established protocols for carrying out the measurements, the μ PA technique was chosen to investigate the mechanical properties of the polymerizable lipid bilayers.

This Chapter will include a description of a μ PA system constructed specifically to determine the mechanical properties of the polymerizable lipids shown in Figure 1.19 since μ PA systems are not commercially available. Directions for operating the μ PA system and the data-processing require to extract physical parameters will be explained. Finally, the results of performing μ PA on the lipids of interest will be presented.

Implications of the determined mechanical properties of the membranes on the function of transmembrane proteins will be discussed in Chapter 5.

4.2 Instrumental Set-up for Micropipette Aspiration Measurements

A block diagram of the μ PA system is found in Figure 4.1. A photo of the μ PA system is shown in Figure 4.2. The various portions of the measurement system will be discussed in the following Sections.

4.2.1 Imaging

The μ PA system is centered on an inverted Nikon TE 2000-S microscope (Nikon Instruments, Inc., Melville, NJ) equipped with phase contrast and differential interference contrast (DIC) objectives. The 4x phase (4x/0.13 PhL DL, WD 16.4), 10x phase (10x/0.30 Ph1 DL, WD 15.2), and 20x DIC (ELWD 20x/0.45 DIC L, WD 7.4) objectives were used for locating unilamellar vesicles (importance and difficulties will be discussed in depth in Section 4.3.7.1), while the 40x DIC objective (ELWD 40x/0.60 DIC M WD 3.7-2.7) was used for measurement. A CoolSnap_{cf} CCD camera (Photometrics, Tucson, AZ) running WinSpec/32 software (Princeton Instruments, Trenton, NJ) was used for imaging.

4.2.2 Positioning

The position of the pipettes was controlled using a MP-285 micromanipulator operated by a ROE-200 controller (Sutter Instruments, Novato, CA). The pipettes were connected via a pipette mount (World Precision Instruments, Sarasota, FL) and tygon tubing to the pressure control portion of the system. The pipette and tubing were filled with distilled water.

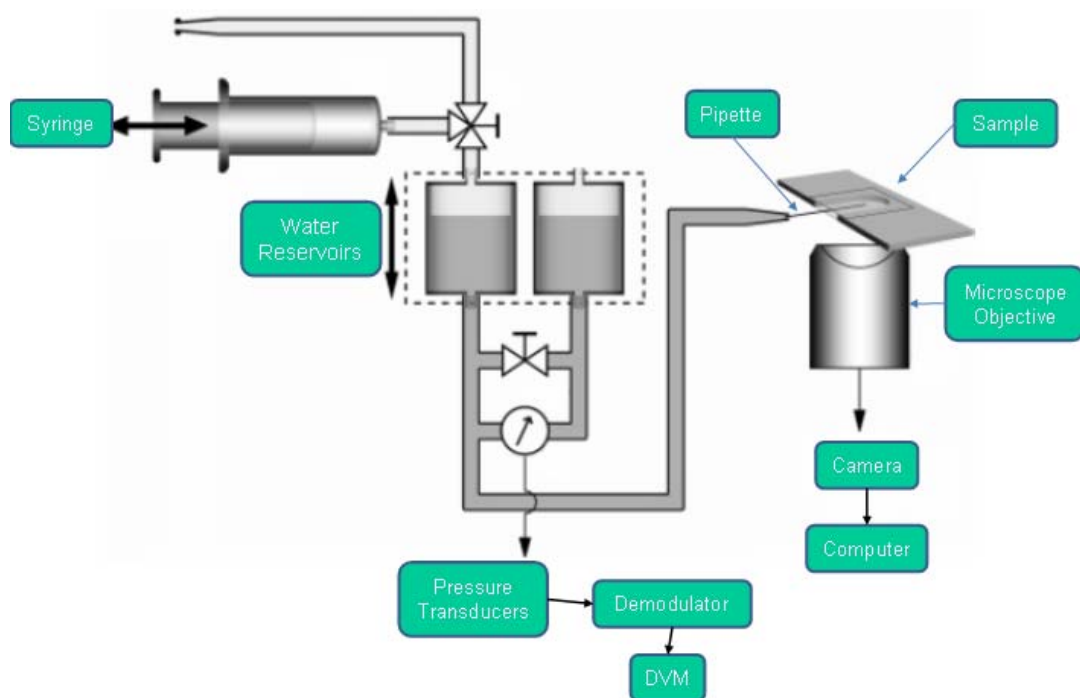


Figure 4.1. Block diagram of μ PA system. Image is modified from Ref. 171.

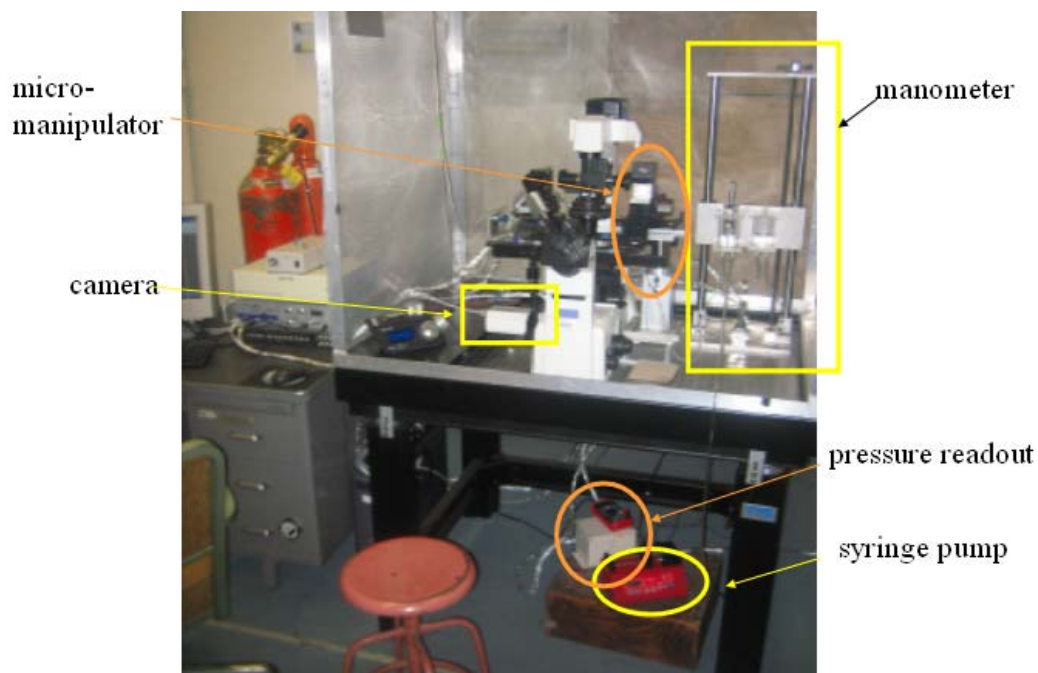


Figure 4.2. Photo of μ PA system. Important features are labeled.

4.2.3 Pressure Control

A home-built manometer, pictured in Figure 4.3, was used to measure the pressure applied to the sample at the end of the pipette. The tubing from the pipette mount is connected to the mobile chamber of the manometer. The mobile chamber is half-filled with water. Between the pipette mount and the mobile chamber, two pressure transducers (DP15 for high tension and DP103 for low tension, Validyne, Northridge, CA) are connected by 3-way valves and more tygon tubing. The mobile chamber is connected to the immobile reference chamber by tubing connected from the bottom of both chambers with a two-way valve in between. Both mobile and reference chambers are mounted on the same piece of steel. The position of the steel rack is controlled by a large course adjustment screw. For fine control of the mobile chamber, a micrometer is positioned between the steel rack and the mobile chamber. The reference chamber is also half-filled with water and connected by tubing and a 3-way valve to both pressure transducers. Both chambers have fill ports at the top, only used during the addition of water or maintenance. Otherwise, those upper ports are kept closed. The two chambers also have two small ports protruding from the front, above the water level. The port of the reference chamber is left open to atmosphere. The port of the mobile chamber is attached by small diameter tygon tubing to a 5 or 10 mL Luer-lock syringe (BD, Franklin Lakes, NJ) mounted into a syringe pump [model # AL1000 (Aladdin), World Precision Instruments, Sarasota, FL]. The signal from the pressure transducers is converted to voltage by a CD280 demodulator (Validyne, Northridge, CA) and read out by a DVM.

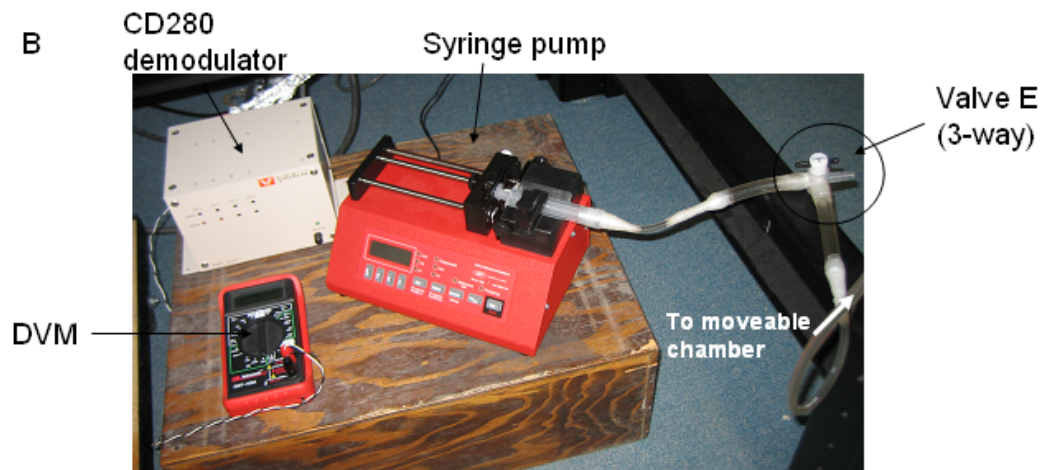
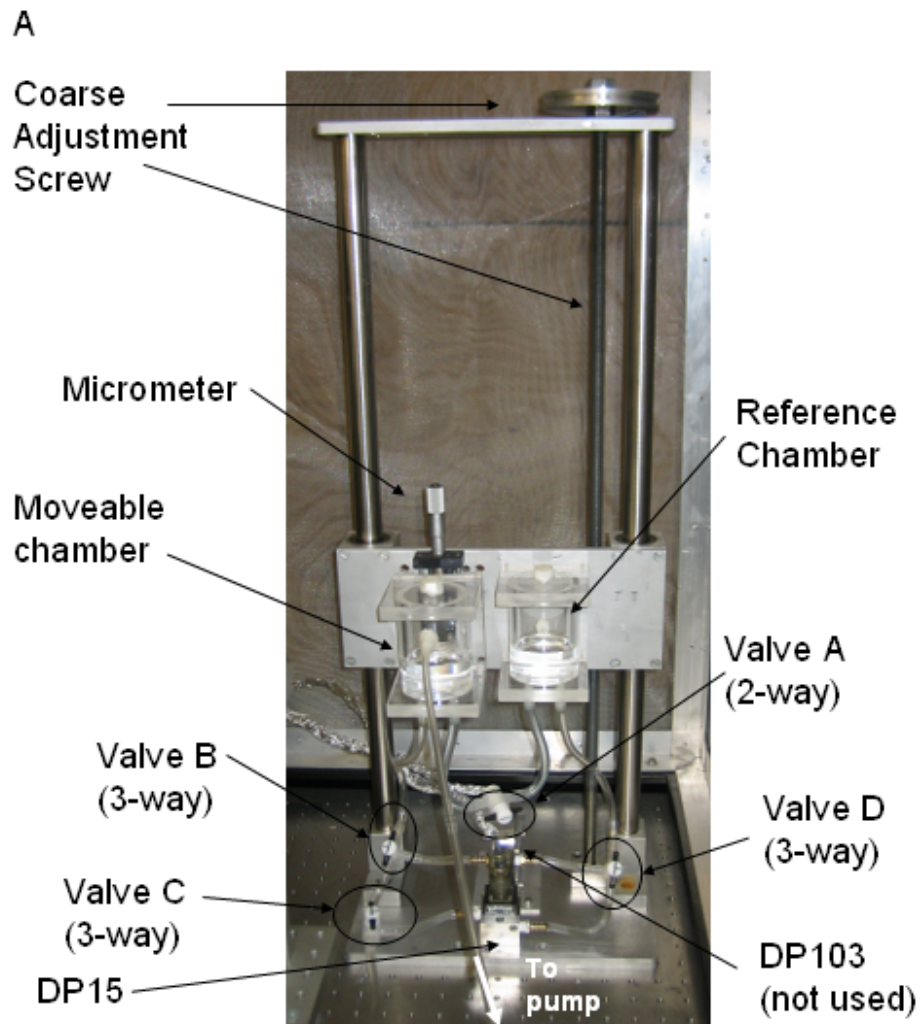


Figure 4.3. Pressure control: A) manometer, B) pressure application and readout devices.

4.3 Experimental Protocol

This Section will describe how the μ PA experiment was carried out. Much of the information in Section 4.3 was based on modifications of directions written by Longo, Ly, Kim, and Duncan.¹⁶⁵⁻¹⁶⁷

4.3.1 Materials

1-stearoyl-2-oleoyl-*sn*-glycero-3-phosphocholine (SOPC) was purchased from Avanti Polar Lipids, Inc. (Alabaster, AL, USA). The source of the polymerizable lipids used in this Chapter are described in Section 3.2.1. Structures of mono-SorbPC, bis-SorbPC, mono-DenPC, and bis-DenPC can be found in Fig. 1.19. Sucrose, HPLC grade chloroform and methanol, sulfuric acid, and hydrogen peroxide from EMD (Gibbstown, NJ) were used. Ethanol (200 proof) was obtained from Decon Labs, Inc (King of Prussia, PA). Glucose and bovine serum albumin ($\geq 96\%$, essentially fatty acid free) (BSA), were obtained from Sigma (St. Louis, MO). All water, referred to as nanopure water, was obtained from a Barnstead Nanopure system (Thermolyne Corporation, Dubuque, IA) with a measured resistivity of greater than $17.5 \text{ M}\Omega\text{-cm}$. Polymerizable lipids in chloroform or benzene were kept at -80°C for long-term storage and -20°C for short-term storage. SOPC was stored at -20°C . Polymerizable lipids were handled under yellow light to avoid unintended polymerization. Surfasil Siliconizing Fluid was from Thermo Scientific (Dubuque, IA). All solution filtration was done with $0.45 \mu\text{m}$ syringe filters (Millex HV, Millipore, Billerica, MA).

4.3.2 Forming GUVs

A variation of the gentle rehydration method was used to create GUVs.^{36, 39, 168-170}

Several 10 ml glass beakers were piranha-cleaned overnight (see Section 3.2.3 for more on piranha-cleaning). Just before GUV rehydration, the piranha solution was discarded and the beakers were rinsed with copious amounts of nanopure water and then blown dry with nitrogen gas. 1 mg/ml stock lipid solution was made in 2:1 (vol/vol) chloroform/methanol. 30 μ L of stock solution was spread in a thin, even layer onto the bottom of each beaker and allowed to air dry under a snorkel. Once the films on the bottoms of the beakers were visibly dry, they were dried under vacuum for an additional 4 hours. Then, 2 mL of filtered 200 mM sucrose solution (warmed to 37°C for SOPC, 30°C for bis-DenPC, 35°C for mono-DenPC and bis-SorbPC, and 42°C for mono-SorbPC) was gently added to the side of each beaker, which was then sealed with Parafilm (Pechiney Plastic Packaging, Menasha, WI). Once the films were covered in solution, the beakers were handled in a way to minimize vibration and moving. Excessively disturbing the solution could lead to more multilamellar vesicles and fewer GUVs.³⁹ The films in the beakers were allowed to hydrate overnight at the temperatures listed previously in an incubator (Thermo Scientific, Dubuque, IA), except SOPC, which was left at room temperature (~ 22 °C). Samples were used the following day.

4.3.3 Pipettes

Pipettes had to be pulled, forged, coated, filled, and mounted before used. This Section describes all of those steps.

4.3.3.1 Pulling Pipettes

A Flaming/Brown micropipette puller (Model: P-97, Sutter Instruments, Novato, CA) was used to pull 10 cm borosilicate glass capillaries (Sutter Instruments, Novato, CA) with O.D. 1.0 mm and I.D. 0.50 mm to a uniform diameter. This was accomplished using the following program (#40 in micropipette puller program list):

Heat: 575 (depends on ramp test result – see manual)

Pull: 150

Velocity: 100

Time: 150

Pressure: 500

This program should produce a very sharp tip on the pipettes. Ideally, in the region of the pipette with 4-9 μm inner diameter, the walls are nearly parallel. Figure 4.4 shows the resulting sharp pipette after pulling. Frequently, two dozen pipettes were pulled in one sitting and stored.

4.3.3.2 Forging Pipettes

A Narshige microforge (Tokyo, Japan) was used to cleanly break the pipette tips open at 4-9 μm diameters using a low melting point glass method similar to the one described in Longo and Ly.¹⁶⁷ This was done by first attaching a low melting point glass bead (leaded soldering glass, CF 7570 VSD #1015477, Ferro Corp., Cleveland, OH) onto the platinum wire electrode of the microforge. The easiest way to attach the bead is to hold a small scoop of glass powder on the end of the spatula and hold it so the platinum wire electrode of the microforge is in the powder. With the electrode in the powder, the microforge is briefly set to heat.

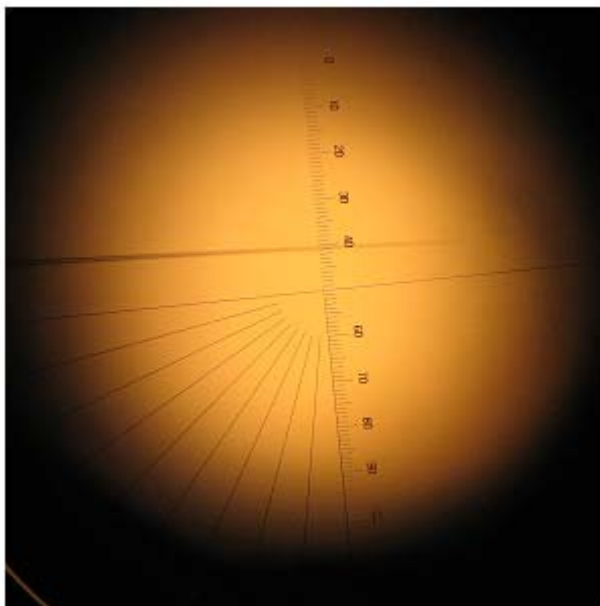


Figure 4.4. Pulled pipette (10x eyepiece and 5x objective of microforge).

The powder will start to solidify into glass on the electrode after the heat is shut off. At first, the bead on the wire is cloudy looking, but with repeated heating and cooling cycles it loses its cloudy appearance and has a smooth, round shape. The bead will occasionally need to be replaced when difficulties start to arise with forging.

To cut the pipette, it is mounted across from the bead in the holder. The pipette tip is maneuvered to point towards the center of the bead. Using the 35x eyepiece is helpful. The pipette cutting process is illustrated in Figure 4.5. The bead is heated to a temperature at which the bead melts, but the borosilicate glass pipette does not. This temperature is easily found by trial and error. The sharp pipette tip is partially inserted into the molten bead. At this point, the heat is shut off. Upon cooling, the pipette usually breaks cleanly at the point where the edge of the bead is. Now, the pipette has a noticeable open end. This end can be reinserted into the molten bead. Once in the bead, the molten glass will start to flow into the pipette. Once the molten glass reaches the desired inner diameter of the pipette, the heat is cut. The cooling glass will start to retract and sometimes the entire system will begin to visibly vibrate. Within a few seconds, the pipette will sever at the point the molten glass reached. Normally, several cutting cycles are needed to finally reach the desired diameter because of the aspect ratio of the pipette. Sometimes, if the glass is not breaking, it helps to tap on the table beside the microforge or translate the pipette holder up/down or left/right a small distance. This method produced cleaner and smoother breaks than the method described in Heitz,⁸⁶ which is the same as the directions found in the microforge manual.

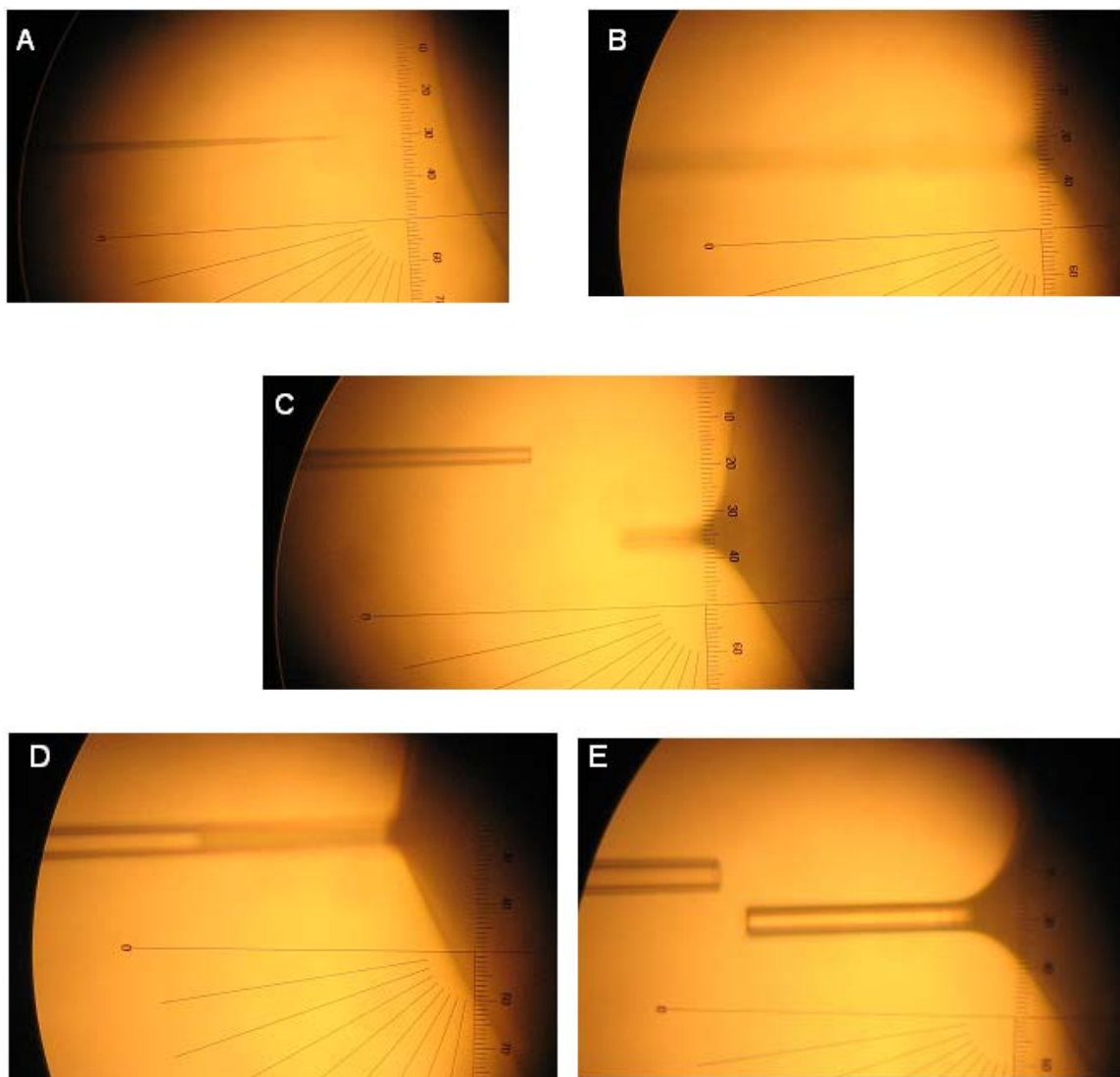


Figure 4.5. Pipette cutting steps. A) Pipette and bead. B) First cut: sharp, closed pipette tip is inserted into the molten bead with heat set below the borosilicate pipette melting temperature. Heat is cut off once the pipette is in the bead. C) After the first cut, the pipette has a noticeable opening at the tip. For following cuts, the open pipette tip is inserted into the molten bead. The molten glass flows into the pipette, as seen in D). Once the molten glass reaches the desired diameter of the pipette, the heat is cut (usually several cuts are needed to reach the proper diameter). E) After a few seconds, the cooling and contracting molten glass will cleanly sever the tip. Sometimes it helps to tap on the surface beside the microforge to encourage this or to translate the pipette holder a small distance. The severed portion of the pipette can be incorporated into the bead with a few seconds of reheating the bead. Images were taken through the 10x eyepiece of the microforge using the 35x objective.

Several pipettes were forged one after the other. The pipettes were stored in a plastic box, mounted in a Plexiglas block (see Figure 4.6).

4.3.3.3 Coating Pipettes

To keep vesicles from adhering to the glass surface, the pipettes need to be coated with a silanizing agent, such as Surfasil. A modified version of the directions by Longo and Ly was used.¹⁶⁷ To do this, the set up in Figure 4.7 is used. A 6-12 inch piece of PTFE tubing (part number: TSI-S20-1100-NAT, SPC Technology) is cut and the back end of the pipette is inserted a few mm into the tubing. A needle (21G1 ½, BD, Franklin Lakes, NJ) attached to a 10 mL luer lock syringe is then CAREFULLY inserted all the way into the other end of the plastic tubing. Before beginning, the syringe should be set so that the plunger is already withdrawn about halfway. The tip of the pipette is dipped into 1% Surfasil in chloroform. The plunger is withdrawn from the syringe enough that solution is drawn up into the pipette visibly. The solution is held for ~ 15 s and then the plunger is pushed in to push the solution out. Once bubbles start coming out, the pipette is removed from the solution. To rinse the pipette, this same process is then repeated for a neat chloroform solution, followed by a neat methanol solution. Afterwards, the pipettes are stored in air.

4.3.3.4 Filling Pipettes

Right before use, the pipettes were backfilled with filtered 200 mM glucose containing 0.05 wt% BSA using Microfil syringe needles (WPI, Sarasota, FL).



Figure 4.6. Plexiglass pipette holder with several pulled pipettes.



Figure 4.7. Set-up used to coat pipettes.

The BSA was added to non-specifically adsorb onto the internal pipette surface to keep lipids from fusing onto the pipette. This was done by drawing ~ 0.5 ml 200 mM glucose/BSA solution into a 1 ml syringe and then attaching the Microfil needle. It is important not to inject air bubbles into the pipette, so the plunger on the needle was pushed in with moderate force until solution drops started forming at the end of the needle. [If too much force is applied, the needle will be launched off the syringe.] Without pushing on the plunger, the end of the needle was then quickly inserted as far as it would go into the pipette. Once sealed against the tapering end, the solution was pushed into the pipette until beads of solution started coming out the end of the pipette tip. Then, while still pressing the syringe plunger, the needle was carefully removed, filling the rest of the pipette with solution. Small bubbles in the body of the pipette could be removed by forcing more solution out the back of the pipette, as long as the needle was placed closer to the pipette tip than the troublesome bubble. The pipette was left with a small amount of solution stuck to the back end of the pipette by surface tension to ensure that when mounted an air bubble would not be trapped between the mount and the pipette.

4.3.3.5 Mounting Pipettes

The pipette mount, as seen in Figure 4.8, is connected by tubing to the manometer. The small tubing from the mount is mated with the larger tubing from the bottom of the moveable chamber by a cut-off 1 ml plastic pipet tip.

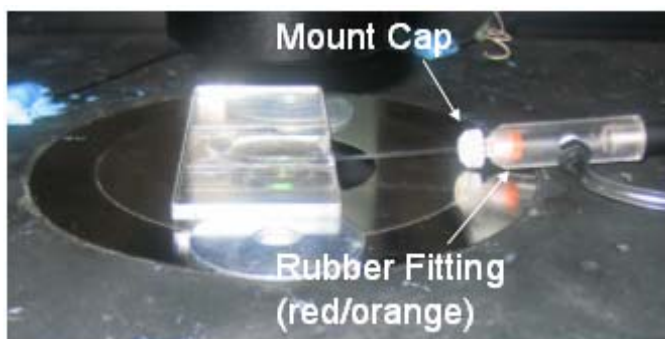


Figure 4.8. Mounted pipette in a sample chamber.

After the manometer is filled and the bubbles removed from the tubing, valves B and C must be open to the moveable chamber, the pipette, DP15, and each other. Valve B is closed to DP103. The pipette was held below the liquid level of the moveable chamber to allow solution to slowly come out of the mount until any trapped bubbles had been flushed out. With solution still flowing out of the mount and the mount cap partially unscrewed, the back end of the pipette was inserted into the mount. To get rid of any visible bubbles in the rubber mount fitting inside the mount, the pipette was repeatedly moved into and out of the fitting with the mount cap unscrewed. Once all of the air was out, the pipette was pushed all the way into the mount and the mount cap was screwed down. The mount was then clamped into the micromanipulator.

4.3.4 Sample Chamber

Samples for μ PA need a chamber that would allow for acquisition of DIC microscopy images of the GUV and the pipette, while maintaining a constant sample temperature. Due to the geometry of the microscope, the pipette needs to enter from the side, meaning that the chamber must be filled with liquid and open to the side. Additionally, to avoid unnecessary damage to the sample, UV-polymerization must take place in the chamber. This Section describes the basic chamber design and how temperature was controlled.

4.3.4.1 Chamber Design

The sample chamber used in these experiments is shown in Figure 4.9. The cutout in the center was 1 cm wide x 2.5 cm long (steel thickness was 3 mm).



Figure 4.9. Sample chamber.

Two glass coverslips (or one glass coverslip and one 1 mm thick piece of quartz, if polymerizing) were cut to be a couple of millimeters larger than the cutout in the steel (coverslips: VWR International, Radnor, PA; fused quartz: Heraeus, Hanau, Germany). The coverslips (or quartz slide) were sealed to the steel using high vacuum grease (Dow Corning, Midland, MI). Prior to sealing the coverslips/quartz to the steel, they had to be coated with Surfasil.

4.3.4.2 Coverslip/Quartz Coating

The same directions were used to coat a quartz slide with Surfasil, although only ‘coverslips’ will be mentioned. The same quartz slide was used repeatedly, while coverslips were only used once. Glass jars with screw caps were filled with solutions of ethanol, methanol, chloroform, and 1% (vol/vol) Surfasil in chloroform. The jars had to be deep enough to accommodate the size of a coverslip.

After cutting coverslips to the appropriate size, they were coated individually. The coverslip was grasped using Teflon tweezers, briefly rinsed with ethanol from a squirt bottle, and then gently swirled in the jar of ethanol for 15 s. The coverslip was allowed to air dry. Once dry, it was swirled in 1% Surfasil in chloroform solution for 15 s, followed by chloroform for 15 s, and finally methanol for 15 s. The coverslip was allowed to air dry and was stored.

4.3.4.3 Chamber Temperature Control

A custom temperature control block was built to fit around the steel chamber and is shown in Figure 4.10. The block is made of brass and connects to a water circulator

(VWR Scientific, Radnor, PA). By changing the temperature of the water in the circulator while the block was on the sample chamber, the temperature of the solution in the chamber was controlled. An RTD (HSRTD-3-100-B-40-E, Omega, Stamford, CT) connected to an Agilent 6 ½ digit multimeter (Santa Clara, CA) was used to verify the response of the chamber solution temperature. A calibration plot used for temperature control can be found in Figure 4.11. The temperature response of the solution in the chamber was linear with respect to the water temperature of the circulator.

4.3.5 Micropipette Aspiration Sample

In order to visualize the GUVs using DIC, the refractive index within and outside of the GUVs must be different. To accomplish this, the GUVs were rehydrated in 200 mM sucrose solution (at a given temperature) and were diluted with filtered ~ 205 mM glucose solution (at the same temperature). The GUV/glucose volume ratio never exceeded 1:3. The reason for the slightly more concentrated glucose solution is that in order to more easily visualize the projection length of the GUV inside the pipette, the osmolarity outside the GUV needs to be slightly higher than the osmolarity inside. This way, the GUV will be somewhat ‘deflated’ and will provide a slightly longer projection length. After filling the sample chamber, it was placed on top of spacers on the microscope stage above the objectives. The purpose of the spacers is to allow clearance of the clamp that holds the micropipette mount. Then the temperature control block was placed onto the sample chamber. The pipette was filled and mounted as described in Sections 4.3.3.4-4.3.3.5 and inserted into the solution in the sample chamber as shown in Figure 4.12.

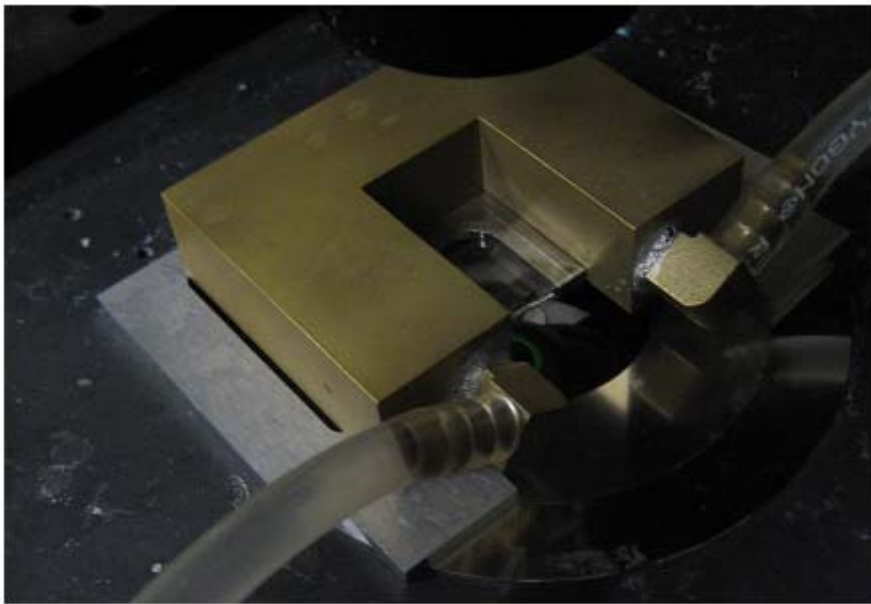


Figure 4.10. Sample chamber with heating block.

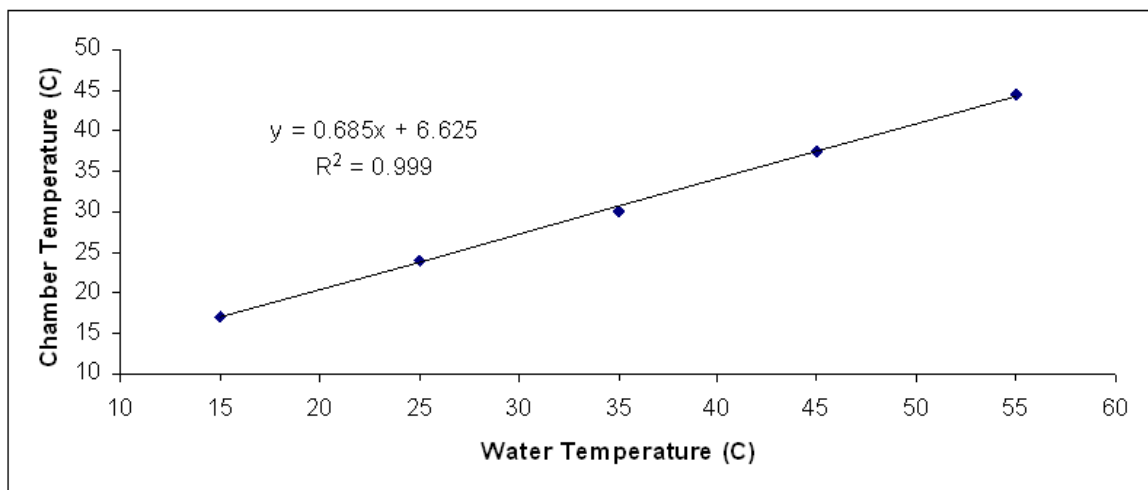


Figure 4.11. Chamber temperature response as a function of water circulator temperature.



Figure 4.12. Pipette mounted and in sample chamber with heating block.

The tip of the pipette was brought into focus to make sure nothing was clogging it. If something was stuck in the pipette or some other defect was visible, a new pipette was mounted. The sample was allowed to settle for 20-30 minutes. This waiting period allowed the GUVs to settle to the bottom of the chamber (because the sucrose inside the GUVs is more dense than the glucose/sucrose mixture outside of the GUVs) and also allowed a constant temperature to be reached in the chamber and pipette.

4.3.6 Manometer Calibration

Before the pressure control system could be used to provide relative pressure measurements, the pressure transducers had to be calibrated. To do this, the set-up shown in Figure 4.13 was used to calibrate the DP15 pressure transducer. The DP103 was not used in this work. The difference in pressure between atmosphere (air) and the tubing between the manometer and the syringe pump could be read off of the meter stick in the U-tube manometer. All of the ports in 3-way valve #1 were always open, and 3-way valve #2 would be set to either 1) open the system to atmosphere or 2) to open a passage between the syringe pump and 3-way valve #1 while not being open to air. The directions in the pressure transducer manuals were then followed.

4.3.7 Obtaining a Run

A lot of operator input is needed to successfully carry out a single μ PA run on a GUV. This section will go into detail about all of the steps involved. There is currently only one automated μ PA system in the world.¹⁷¹

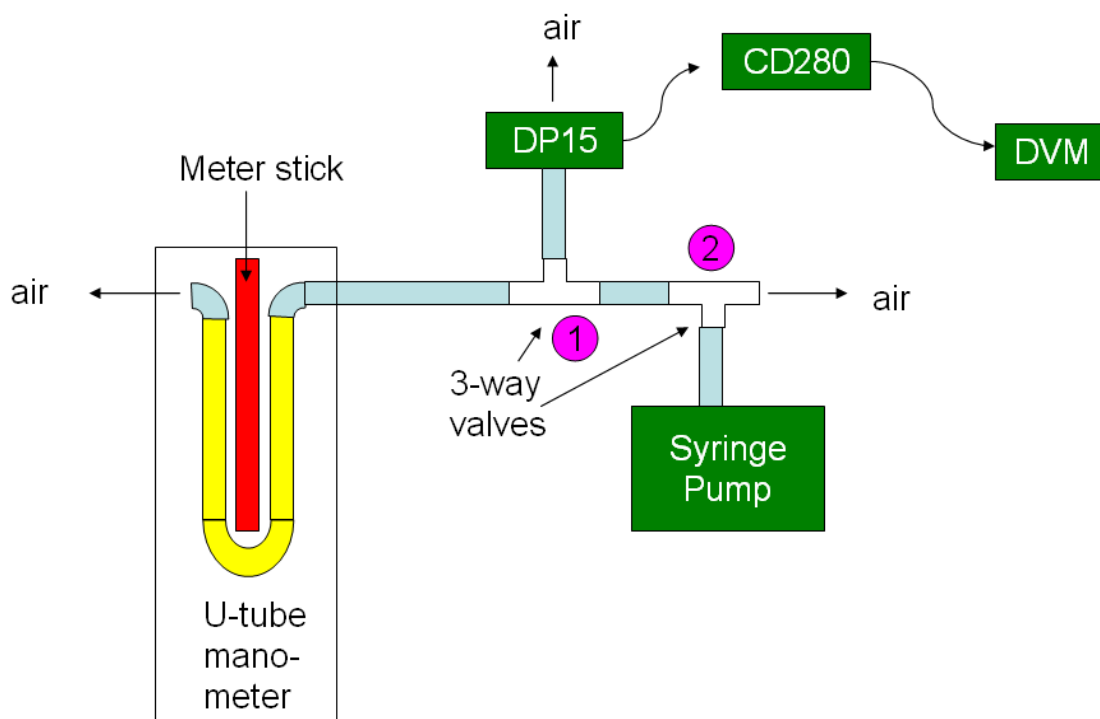


Figure 4.13. Manometer calibration set-up.

4.3.7.1 GUV Selection

Because GUVs have such thin walls, it is nearly impossible to confirm that a true single-bilayer GUV is present based on DIC or phase images. There are indications that suggest a GUV is NOT unilamellar, however. All images were taken with the green interference filter in place, because the author found it easiest to see details using that particular filter. The GUV pictured in Figure 4.14a would be considered a good candidate for aspiration for a number of reasons. The vesicle is circular and the edges do not appear to be very thick. No smaller GUVs are observable inside of it or attached to the outside. The surface looks smooth and homogeneous. The internal and external solutions had not mixed, evidenced by the fact that the image appears to have depth (later examples will show what happens when the solutions mix). There are no strange patterns in the GUV, such as those in the large spherical lipid structure in Figure 4.14b. Another test involves bringing the pipette tip close to the GUV and allowing solution to flow at the GUV by applying pressure to the pipette. If the GUV easily deforms and slides away on the bottom of the chamber, showing that it is flaccid, it will be good for imaging because the projection length will get far enough into the pipette to get beyond the interference fringe region (where the GUV and pipette meet). There can also be tubules attached to the GUV as well that are difficult to see. These are more easily noticed when the GUV is moving, so that is something else to pay attention to when the pipette is used to push the GUV around.

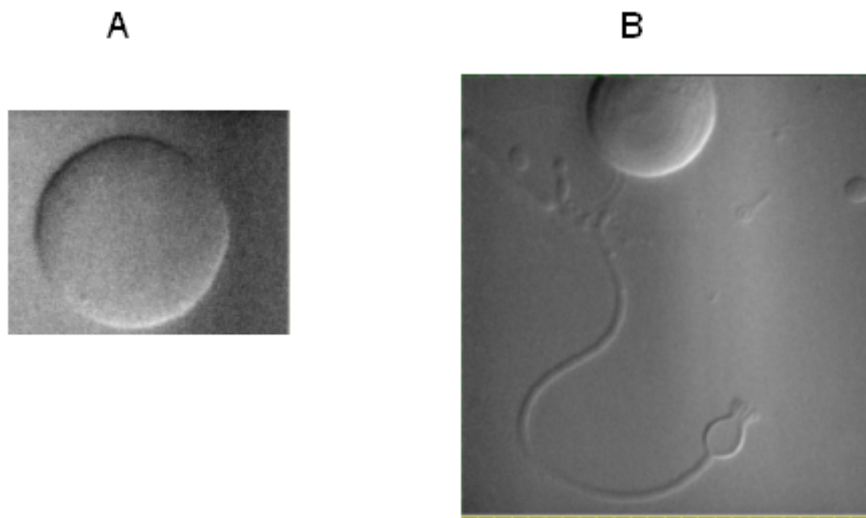


Figure 4.14. Images of vesicles. A) Good GUV and B) other structures under 40x DIC imaging with the green interference filter in place.

Also, switching between DIC and phase objectives can be helpful since some inhomogeneities are more easily noticed in one or the other imaging mode.

The most straight forward way the author found to pick the best GUVs will be briefly described. First, the 10x phase objective is used to find a GUV that appears to have the correct attributes. Then, the 20x DIC objective is used to get a better and different look. If the candidate vesicle still looks good, the pipette is brought beside the GUV and the height of both manometer chambers is adjusted with the course adjustment screw (Valves: A open, B open to moveable chamber and DP15, C open towards all 3 tubes, D open to reference chamber and DP15, and E open in all 3 directions) until the GUV begins to move slowly away from the pipette due to solution flow from the pipette. If the GUV does not look stiff and bends easily without revealing hidden internal vesicles or external tubules, then it is further analyzed with the 40x DIC objective. If inhomogeneities still do not appear, then the GUV is selected for experimentation. Depending on the conditions, sometimes unaspirated GUVs can appear to ‘wobble’. This is a good sign, similar to seeing if the GUV bends under fluid flow from the pipette.

4.3.7.2 GUV Capture and Preparation

Once a GUV is selected, it needs to be gently aspirated into the pipette and removed from the floor of the chamber. The pipette and GUV are maneuvered near each other (by the micromanipulator and microscope stage, respectively), but the pipette is slightly above (in the z-direction) the GUV, with the opening positioned so that once the pipette is brought down, it will aspirate the GUV of interest and not other nearby GUVs.

Since the operator had probably left the course adjustment screw in such a position to be barely pushing fluid out the pipette tip, a half turn or so to lower the manometer chambers will be enough to gently aspirate the GUV of interest into the pipette. The course adjustment screw is set and the pipette is slowly (mode = 5 or 6 on the micromanipulator) brought beside the GUV. If the pipette hits the bottom of the sample chamber and does not quite pick up the GUV, lifting the pipette slightly off the bottom usually does the trick. Once the GUV is aspirated, the pipette with the attached GUV is brought above the surface high enough so that the GUVs still on the bottom are hard to distinguish when the objective is focused on the GUV of interest. The pipette should not be brought up too high, as that will change its position relative to the fluid in the manometer chambers too much. The idea is to hold onto the GUV as lightly as possible without letting it float away and without getting interference from neighboring GUVs.

It is sometimes also helpful to take a good look at the GUV once it is no longer on the sample chamber floor, because other problems may become visible under light aspiration. At this point 40x DIC is used, unless the GUV is monstrous in size. In that case, 20x DIC is used, although that was very rare and frequently resulted in unusable data.

A properly sized and situated ROI (region of interest) is set on the image acquisition program, in this case Winspec/32, and the 'Focus' option is used while the syringe and pressure control valves are set. [The 'Focus' option runs the camera at its highest speed for the chosen exposure time (0.10 s was used in all cases)]. Before changing valves, the syringe is completely pushed in. Then, the valves are set as follows:

E is closed to air, but open to the syringe pump and the moveable chamber and A is closed. All other valves are left as before. Occasionally, the GUV will escape during the resetting of the valves. The image of the GUV in the pipette is optimized by moving the microscope objective to get a good picture of the projection length within the pipette.

Once the captured GUV is in focus, the camera options are checked. About 150-220 images were obtained consecutively. A delay time of 0.2 to ~ 1.6 s was used, depending on the behavior of the GUV (in Winspec/32, 'Safe Mode' needs to be "on" to get the desired delay time). Once camera parameters are set, the data can be obtained. Before discussing the aspiration experiment though, the syringe pump program will be explained. Usually, the pump program is only changed during the first few runs of GUVs of a particular sample type and then left alone.

4.3.7.3 Syringe Pump Program

The syringe pump is capable of storing one program with over 40 steps. The program used for micropipette aspiration experiments is summarized in Table 4.1. The program is more complicated than necessary, because originally there was confusion about how to run the experiment. In the end, it was decided that a tension ramp would be easiest to use, instead of tension steps, so certain portions of the program are set to be ignored. Also, the internal syringe diameter needs to be stored in the pump for the proper volumes and rates to be used.

Phases 1-4 are used for prestressing the GUV. A prestress is a brief application of tension on the GUV, which has been found to help incorporate small attached vesicles into the parent vesicle.

Table 4.1 Syringe pump program used for μ PA experiments.

Phase	Rate (ml/min)	Volume (ml)	Settings	Comment
1	2.0	0.5/0.005	withdraw	0.5 ml: for prestress 0.005 ml: “no” prestress
2			PS:10	10 s delay
3	2.0	0.49/0.004	infuse	0.49 ml: for prestress 0.004 ml: “no” prestress
4			Beep	
5			PS:03	3 s delay
6			LP:st	Start loop if tension steps desired. No steps used in this work.
7	1.0	1.6 to 8.0	withdraw	Tension ramp: Volume depends on lipid being studied. Set through trial and error.
8			PS:03	3 s delay
9			LP:01	Number of loops total for tension steps. Not used in this work, so set to 1.
10			LP:st	Start loop if reverse experiment needed to be run in tension steps. Not used in this work.
11	0.5	0.5	Infuse	Reverse tension ramp. Data not analyzed in this work.
12			PS:03	3 s delay
13			LP:01	Number of loops total for reverse tension ramp. Not used and not analyzed in this work, so set to 1.
14			Beep	
15			Stop	

If these small vesicles are not removed before data is gathered, they can interfere with data collection. Phases 1-4 need to be set in such a way as to prestress or not prestress the sample. If a prestress is desired (in the case of SOPC, for instance), then a value of ~ 0.50 mL is set in phase 1 and a slightly smaller value (~ 0.49 mL) is set in phase 3. This will cause the syringe pump to withdraw 0.50 mL, pause for 10s, and then infuse 0.49 mL. If a prestress is not desired, the volumes of phases 1 and 3 will be set to something low, such as 0.005 and 0.004 mL, respectively. Then, in the case of no prestress, the program will just pause for 10 s. Phase 4 signals the end of the prestress (or pause) with a beep.

Phases 5-9 contain the true experimental portion of the program. Phase 5 is simply a 3 s pause (it gives time for the operator to record values.). Phases 6 and 9 are for tension steps, which were not used in this work. They are part of a loop. To ignore the loop, phase 9 is set to LP:01, meaning that the loop will only be performed one time. After the 3 s pause of phase 5, phase 7 immediately begins. Phase 7 is the tension ramp used for μ PA. The volume is varied, depending on the behavior of the GUVs. Usually, after a few trials at the start of a day of experimenting, the volume is figured out for a particular lipid type. Values between 1.6 mL and ~ 8 mL had been used in this work. The withdraw rate was always set to 1.0 mL/min.

Phases 10-13 are not actually necessary unless a reverse tension ramp or reverse tension steps are desired. They have been set in such a manner as to only go through the inserted loop once. Phase 14 signals the end of the program with a beep and phase 15 ends the program.

4.3.7.4 Data Set Acquisition

After all the camera parameters, syringe pump parameters, and valves have been set as described above, a dataset can be acquired. The directions follow. There are several steps that need to be executed quickly by the operator at the start and end of the tension ramp.

The syringe pump is started. After the first beep (phase 4), the operator has 3 seconds to start the camera image acquisition and record the initial DVM reading (pressure). The frame number is recorded when the syringe pump starts phase 7. The display on the syringe pump will indicate what is happening. Depending on the noise level in the room, the start of phase 7 can also be heard. There is no beep after phase 7 currently, which would have been helpful, so the operator needs to be aware of when phase 7 ends to record the final image frame number and final pressure. Again, if the noise level is low, the end of phase 7 can be heard. There is a 3 s delay in phase 8 when the final DVM reading can be recorded. The syringe pump will then continue through the rest of the phases and beep at the end.

After the run, the system needs to be reset. The tension is released by opening valve E to air, the syringe pump, and the moveable chamber. The syringe can then be pushed all the way forward. Valve A is opened between the manometer chambers. If a GUV is still aspirated into the pipette, the course adjustment screw is used to raise the manometers a small amount. If that does not release the GUV, then quickly translating the microscope stage or the pipette (mode: 0 – fastest setting) usually does the trick. If

even that does not work, removing the pipette from solution almost always takes care of the problem.

When work is complete, the valves were left as follows: A open, B and D open to the manometer chambers and DP15, C was closed to the pipette, but open to DP15 and the manometer chamber, while E was left open in all 3 directions. The pipette holder (without pipette) was stored on top of the chambers to avoid any potential leaks.

4.3.7.5 Changing Sample Osmolarity

On occasion, the GUVs in a sample all display short projection lengths when aspirated. Basically, the GUVs all seem too stiff. This could be due to multilamellarity or the wrong relationship between the osmolarity inside and outside the GUVs. To test for and attempt to alleviate the problem, slightly more concentrated glucose solution is added to the sample cell and allowed to equilibrate for 20-30 minutes. Then aspiration is tried again. Changing the glucose concentration too much can lyse the GUVs as well. On rare occasions, changing the sample osmolarity helped. Most of the time, changing to a sample from a new beaker worked better.

4.3.8 Polymerization of Lipids in μ PA Geometry

UV-photopolymerization of GUVs was carried out above T_m for all polymerizable lipids. Two geometries were used for polymerization. Both geometries will be discussed along with how polymerization time was determined for each.

4.3.8.1 Side-illumination

To determine the amount of time needed for polymerization, small vesicles (SVs) of bis-SorbPC were formed as described in Section 2.1.2. SVs were introduced into the

sample cell and polymerized for varying amounts of time between 1 and 60 minutes while being kept above T_m of bis-SorbPC. A low pressure Hg pen lamp (rated at $4500 \mu\text{W}/\text{cm}^2$ at 254 nm) was held 5 cm from the center of the cell, parallel with the opening of the sample cell for polymerization. Fresh aliquots of SV solution were used for each time investigated. UV-vis absorbance was used to determine the extent of polymerization based on the disappearance of the sorbyl group peak at $\sim 254 \text{ nm}$.¹²⁹ UV-vis spectra were taken with a Spectral Instruments, Inc., UV-vis spectrometer (Tucson, AZ) before and after polymerization. Figure 4.15 shows the normalized absorbance spectra for each polymerization time. Figure 4.16 is a plot of the % unreacted as a function of UV-polymerization time with the assumption that at 60 minutes all of the monomers had reacted. Polymerization for long periods of time was avoided with this sample cell because of solution evaporation. For 15 minute and longer polymerization times, the sample was found to have 95% conversion to polymer. As a result, 15 minutes was used for polymerization in the side-illumination geometry.

4.3.8.2 Top-illumination Through Quartz

Polymerization was also performed with the top coverslip of the chamber replaced with a piece of fused quartz and the Hg pen lamp held above the quartz. Due to the heating block, the closest the pen lamp could be placed to the sample was 5-8 mm. The lamp was parallel with the long axis of the sample chamber opening. The same procedure and data-processing were used to determine the amount of time needed to polymerize using the top-illumination geometry as was used for the side-illumination geometry described in the previous Section.

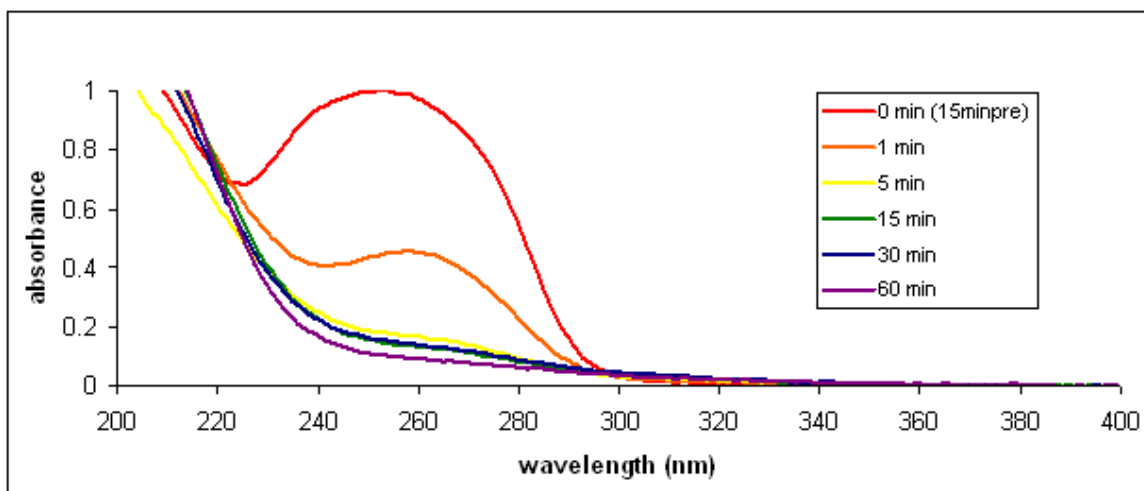


Figure 4.15. Normalized absorbance spectra of bis-SorbPC SVs UV-polymerized in the side-illumination geometry. Normalization was performed by setting the pre-polymerization peak at ~ 254 nm to an absorbance of 1.0 and then setting the pre-polymerization absorbance at 400 nm to 0.0. The same normalization factor was used for the corresponding post-polymerization spectra.

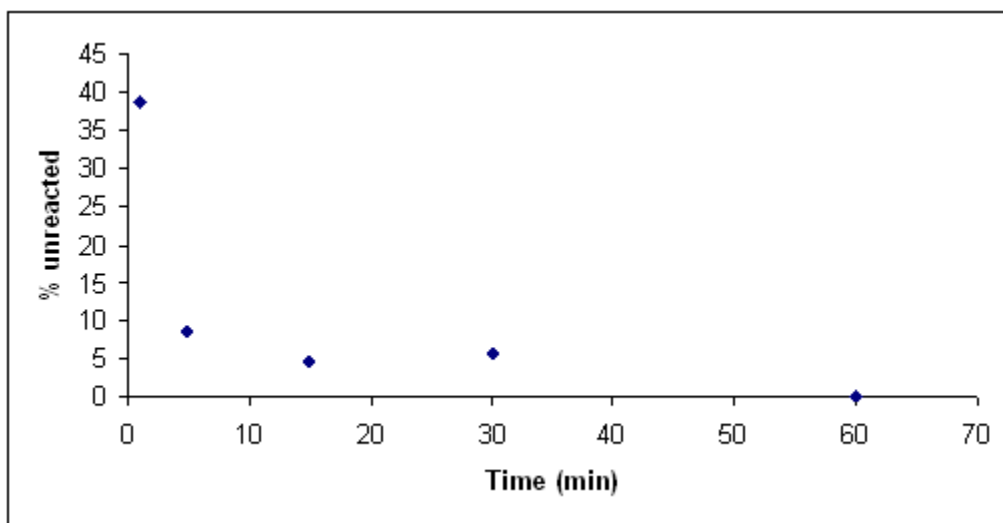


Figure 4.16. Plot of % unreacted bis-SorbPC SVs as a function of UV-polymerization time in the side-polymerization geometry.

Figure 4.17 shows the normalized absorbance spectra for each polymerization time and Figure 4.18 shows the % unreacted as a function of time. Again, it was assumed that after 60 minutes, all the monomers had reacted. In this geometry, polymerization proceeded very rapidly. Based on the data in Figure 4.18, 5 minutes was chosen as the polymerization time.

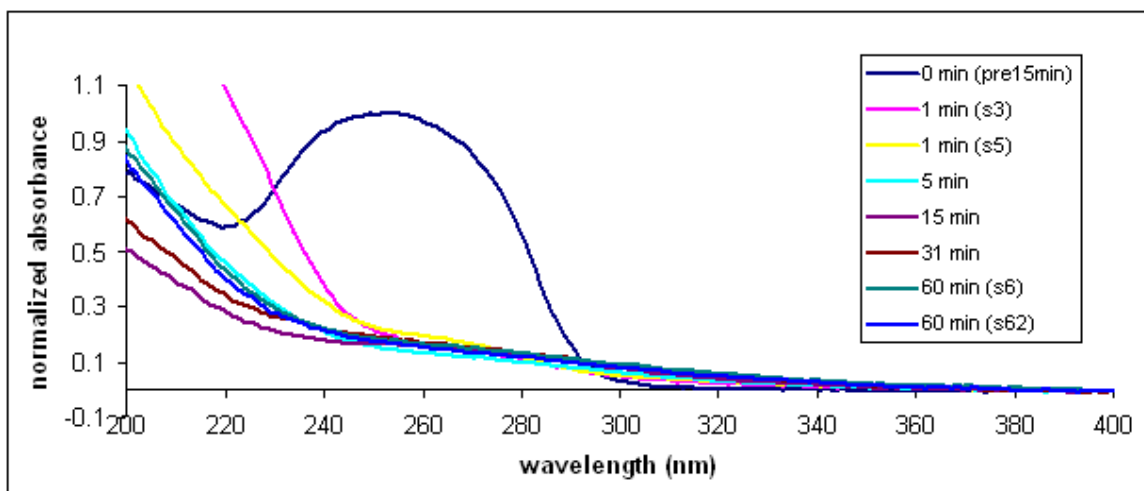


Figure 4.17. Normalized absorbance spectra of bis-SorbPC SVs UV-polymerized in the top-illumination geometry. Normalization was performed by setting the pre-polymerization peak at ~ 254 nm to an absorbance of 1.0 and then setting the pre-polymerization absorbance at 400 nm to 0.0. The same normalization factor was used for the corresponding post-polymerization spectra.

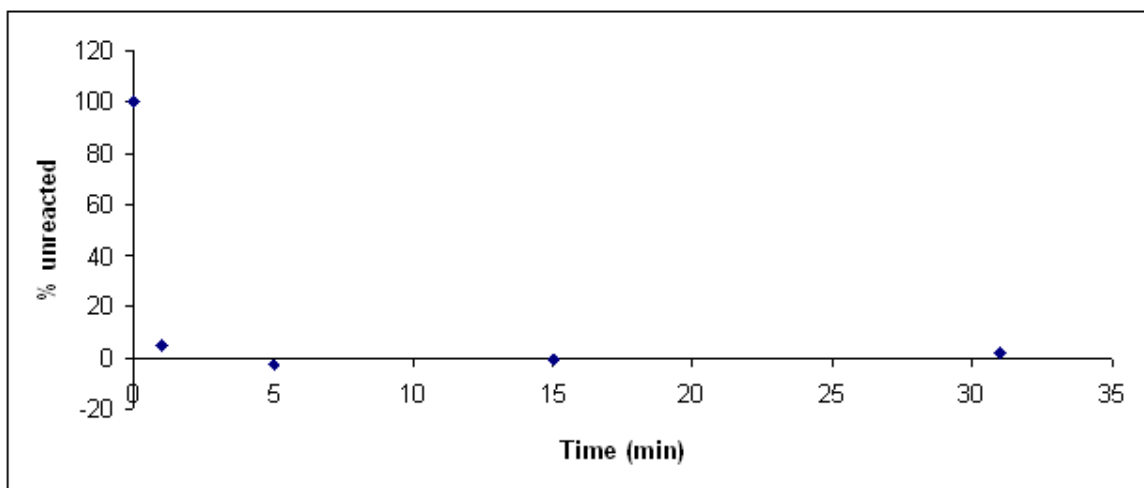


Figure 4.18. Plot of % unreacted as a function of UV-polymerization time in the top-illumination geometry of bis-SorbPC SVs.

4.4 Data-processing

Details of how the mechanical properties were obtained are discussed in this Section.

4.4.1 Determining τ

The tension applied to the GUV can be calculated from the aspiration pressure (ΔP), pipette radius (R_p), and vesicle radius (R_v) using the following equation:^{168, 172}

$$\tau = \Delta P R_p / 2(1 - (R_p / R_v)) \quad (4.1)$$

In practice, ΔP was determined based on the beginning and ending DVM readout recorded as described in Section 4.3.7.4. First, the overall change in voltage was divided by the difference in the number of frames recorded in Section 4.3.7.4. This gave the change in voltage from one frame to the next. The first useable frame in the run was set to 0 V and each following frame was assigned a voltage based on the interval calculated. These voltages were converted to pressure in meters of water in column G of Figure 4.19 by multiplying the voltage by the appropriate factor determined in the calibration of the DP15 pressure transducer (Section 4.3.6). To convert pressure in meters of water to an intermediate labeled “pressure” in column H of Figure 4.19, meters of water in column G are multiplied by the density of water, the gravitational constant, and 1000 (to eventually be converted to mN/m). Finally, tension is found using equation (4.1) in column K by referencing the appropriate cells on the left side of the spreadsheet (columns A and B). R_p was determined from measuring the diameter of the GUV in three different frames of a particular run in at least three separate runs. This average value was converted to a radius in meters using the left most side of the spreadsheet.

	A	B	C	D	E	F	G	H	I	J	K	L	M
1	24MD 010810												
2	pipette diam	48.1	frame	pressure	proj. leng.		pressure	pressure	proj. leng.		tension		In tension
3	(pixels)			(V)	(pixels)		m water		(m)		(mN/m)	alpha	
4			1	0	106		0	0	1.23E-05				
5	pixels/um	8.62	2	0	108		0	0	1.253E-05				
6			3	0.03917	107		0.001369	13385.528	1.241E-05		0.0271543	-0.0013947	-3.60622
7	pipette radius	2.79E-06	4	0.07834	108		0.002738	26771.056	1.253E-05		0.0543085	0	-2.91307
8	(m)		5	0.11751	109		0.004107	40156.584	1.265E-05		0.0814628	0.0013947	-2.50761
9			6	0.15668	108		0.005476	53542.112	1.253E-05		0.1086171	0	-2.21993
10	Vd (pixels)	154	7	0.19585	109		0.006845	66927.64	1.265E-05		0.1357713	0.0013947	-1.99678
11	Vr m	8.933E-06	8	0.23502	110		0.0082139	80313.168	1.276E-05		0.1629256	0.0027894	-1.81446
12			9	0.27419	110		0.0095829	93698.696	1.276E-05		0.1900799	0.0027894	-1.66031
13	HT	HTb	10	0.31336	109		0.0109519	107084.22	1.265E-05		0.2172341	0.0013947	-1.52678
14	Rp/Rv	Rp/Rv	11	0.35253	110		0.0123209	120469.75	1.276E-05		0.2443884	0.0027894	-1.409
15	0.3123377	0.3123377	12	0.3917	110		0.0136899	133855.28	1.276E-05		0.2715427	0.0027894	-1.30364
16			13	0.43087	113		0.0150589	147240.81	1.311E-05		0.2986969	0.0069735	-1.20833
17			14	0.47004	111		0.0164279	160626.34	1.288E-05		0.3258512	0.0041841	-1.12131
18	2(1-Rp/Rv)	2(1-Rp/Rv)	15	0.50921	113		0.0177969	174011.86	1.311E-05		0.3530055	0.0069735	-1.04127
19	1.3753247	1.3753247	16	0.54838	115		0.0191659	187397.39	1.334E-05		0.3801597	0.0097629	-0.96716
20			17	0.58755	115		0.0205349	200782.92	1.334E-05		0.407314	0.0097629	-0.89817
21	(Rp/Rv)^2	(Rp/Rv)^2	18	0.62672	114		0.0219039	214168.45	1.323E-05		0.4344683	0.0083682	-0.83363
22	0.0975548	0.0975548	19	0.66589	113		0.0232729	227553.98	1.311E-05		0.4616225	0.0069735	-0.77301
23			20	0.70506	115		0.0246418	240939.5	1.334E-05		0.4887768	0.0097629	-0.71585
24	(Rp/Rv)^3	(Rp/Rv)^3	21	0.74423	116		0.0260108	254325.03	1.346E-05		0.5159311	0.0111576	-0.66178
25	0.03047	0.03047	22	0.7834	116		0.0273798	267710.56	1.346E-05		0.5430853	0.0111576	-0.61049
26			23	0.82257	115		0.0287488	281096.09	1.334E-05		0.5702396	0.0097629	-0.5617

Figure 4.19. Part of spreadsheet A used to fit μ PA data.

Normally, the GUV diameter changed little during the course of the experiment (< 1 %), so the average diameter was used. The diameter in pixels was converted to radius, R_v , in meters on the left hand side of the spreadsheet.

4.4.2 Determining α

The applied τ ramp caused an increase in the area of the GUV. As mentioned in the previous Section, the change in R_v was considered negligible, but the change in projection length (ΔL) of the GUV was measurable. Figure 4.20 illustrates ΔL . The change in GUV area can be related to relative change in area, α , by the following equation:^{168, 172}

$$A = \Delta A/A_0 \approx \frac{1}{2} [(R_p/R_v)^2 - (R_p/R_v)^3](\Delta L/R_p) \quad (4.2)$$

where ΔA is the change in area and A_0 is the unstressed area of the GUV. To get ΔL , the projection length in pixels was measured by eye in easy to analyze frames of each run and recorded in column E of spreadsheet A as pixels. The brightest portion of the pipette/GUV junction was used as the baseline from which ΔL was measured.

Frequently, there were issues with interference fringes from DIC obscuring the projection length. In those cases, the low tension points were lost. Column I converted the projection length into meters based on the magnification of the image and the number of pixels per meter in the CCD plane. Column L calculated α using equation (4.2) and also factored in the change in projection length by subtracting the first useable length measured from all of the subsequent frames.

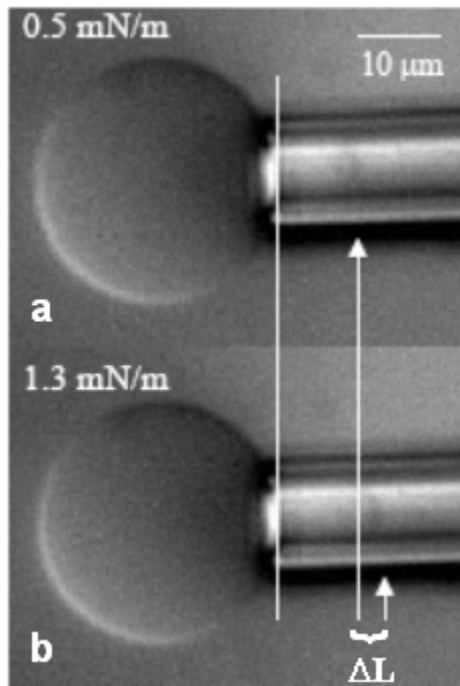


Figure 4.20. DIC of a change in projection length, ΔL , of an aspirated GUV. A) The GUV is pictured under a tension of 0.5 mN/m. The projection length position is highlighted. B) The same GUV is under a tension of 1.3 mN/m and the projection length has moved noticeably. ΔL is marked.

4.4.3 Determining Elastic Moduli and Lysis Tension (Strength)

Plots of τ vs. α were used to determine elastic moduli of GUVs. Example plots are shown in Figure 4.21. The slope of the linear region at high tension is K_{app} , the apparent area expansion modulus, which is related to K_A , the elastic area expansion modulus. K_A is the increase in area per lipid molecule as a function of pressure. K_{app} is the increase in lipid area per molecule plus contributions from thermal fluctuations. Figure 4.21b shows $\ln(\tau)$ vs. α plotted. Here, there is a pseudo linear region in the low tension regime. Column M in spreadsheet A calculated the natural log of tension. The slope of this low tension regime is related to k_c , the elastic bending modulus, by a factor of $8\pi/k_B T$, where k_B is the Boltzmann constant and T is the temperature in Kelvin.¹⁷³ The logarithmic change in α is due to smoothing of thermal undulations under aspiration of the GUV. Once k_c is known, K_{app} can be converted to K_A , as will be described in more detail in the following subsection.

Most literature data has been analyzed by running two separate experiments: one for the low tension regime and one for the high tension regime.^{99, 167, 174} Traditionally, the cross-over tension region has been defined as ~ 0.5 mN/m. The instrumental benefit to determining k_c and K_A/K_{app} separately is that two different pressure transducers can be used: one specific to low tensions and another specific to high tensions. The low pressure transducer is unable to read higher tensions, but can give much better resolution at lower tension than a high pressure transducer.

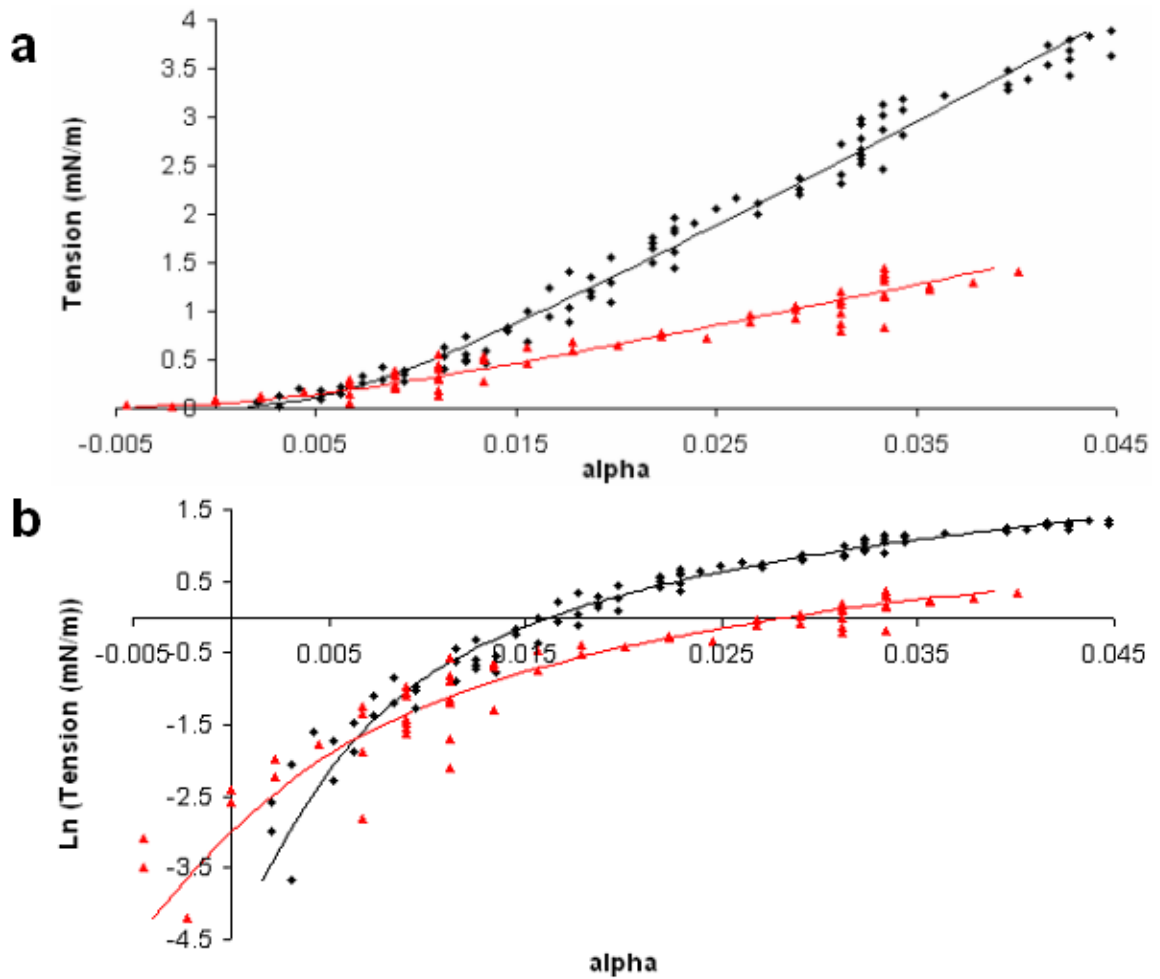


Figure 4.21. Examples of micropipette aspiration experiments for mono-DenPC (black diamonds) and mono-SorbPC (red triangles) GUVs and their respective fits to equation (4.4). a) Tension vs. α results for both lipid types. b) $\ln(\text{Tension})$ vs. α results for both lipid types.

4.4.3.1 Linear Subtraction Method

If two separate experiments are run (or a single run is divided into low/high tension after data acquisition) to get low and high tension data, k_c and K_{app} are obtained separately below and above 0.5-1 mN/m, respectively. The $\ln(\tau)$ vs. α is plotted to obtain k_c from the low tension slope and τ vs. α is plotted to get K_{app} from the high tension slope. Then, the effect of k_c in high tension is removed by calculating the extrapolated effect using

$$\Delta\alpha(i) = -(k_B T / 8\pi k_c) \ln[\tau(i)/\tau(1)] \quad (4.3)$$

where $\Delta\alpha(i)$ is the contribution to α by bending effects (thermal undulations) in the high tension regime, $\tau(i)$ is the tension at point i , and $\tau(1)$ is the initial state of the high tension regime (experimentally set to ~ 1 mN/m).^{167, 174} Once the correction factor, $\Delta\alpha(i)$, is used to readjust the α scale, then τ vs. α_{dir} is plotted, where α_{dir} is the corrected α value. The slope is then K_A .

4.4.3.2 Two-component Fitting

As will be discussed later, many GUV types in this study lysed at low tensions in the transition region between 0.5-1.0 mN/m. To attempt to salvage both K_A and k_c data, a combined equation was used to fit the entire dataset. As seen in Section 4.3.7.4, both low and high regimes were investigated in one run.

4.4.3.2.1 Two-component Equation and Fitting

The following equation, which is simply the sum of the low and high tension trends, was used for data fitting:

$$\alpha = (k_B T / 8 \pi k_c) \ln(\tau) + (\tau / K_A) + b \quad (4.4)$$

The variable b was used to adjust for initial displacements in α for each GUV. This is similar to an equation quoted in the literature,^{173, 175} but never used to fit the data:

$$\alpha = (k_B T / 8 \pi k_c) \ln(1 + c \tau A) + (\tau / K_A) \quad (4.5)$$

where the constant c depends on the mode of expansion being used to describe the phenomenon and A is the area of the GUV. To explain their reasons for not using equation (4.5), researchers often mention that at low tensions, bending is dominant, while at high tensions elastic area expansion dominates,¹⁷⁴ therefore, the two tension regions can be analyzed separately.

4.4.3.2.2 Comparing Linear Subtraction and Two-Component Fitting Outcomes

To see if the two-component method was an appropriate replacement for the linear subtraction method, an entire dataset was processed both ways. As mono-DenPC had the most GUVs from which useable data could be extracted, it was used.

To process the data via the linear subtraction method, ~ 0.5 mN/m was chosen as the cutoff and k_c was calculated from data < 0.5 mN/m. This yielded k_c of 0.310 ± 0.44 ($\times 10^{-19}$ J) ($n = 14$). Using the two-component method, the data was processed in its entirety and k_c was determined to be 0.72 ± 0.25 ($\times 10^{-19}$ J) ($n = 15$). Since the two k_c values were different, both were used in the linear subtraction method to calculate K_A . The goodness of fit for τ vs. α_{dir} was always better for $k_c = 0.72 \times 10^{-19}$ J. This suggested that overall the data fit better when processed using the two-component method. For all k_c and K_A data presented, the two-component method was therefore used for fitting.

K	L	M	N	O	P	Q	R	S
tension		ln tension		fit	chisq	residuals	T (C)	35
(mN/m)	alpha						T (K)	308.15
							kB	1.38066E-23
							pi	3.141593
0.0271543	-0.0013947	-3.60622		-0.002517755	1.26E-06	0.001123		
0.0543085	0	-2.91307		-0.000762975	5.82E-07	0.000763		
0.0814628	0.0013947	-2.50761		0.000387303	1.01E-06	0.001007	kBT/8pi	1.69281E-22
0.1086171	0	-2.21993		0.001290086	1.66E-06	-0.00129		
0.1357713	0.0013947	-1.99678		0.002057255	4.39E-07	-0.00066	kc	0.805609098
0.1629256	0.0027894	-1.81446		0.002738645	2.57E-09	5.07E-05	KA	0.910358466
0.1900799	0.0027894	-1.66031		0.00336084	3.27E-07	-0.00057	A	0.476165681
0.2172341	0.0013947	-1.52678		0.003939709	6.48E-06	-0.00255	chisq	0.000373478
0.2443884	0.0027894	-1.409		0.004485485	2.88E-06	-0.0017		
0.2715427	0.0027894	-1.30364		0.005005158	4.91E-06	-0.00222		
0.2986969	0.0069735	-1.20833		0.005503713	2.16E-06	0.00147		
0.3258512	0.0041841	-1.12131		0.00598483	3.24E-06	-0.0018		
0.3530055	0.0069735	-1.04127		0.006451303	2.73E-07	0.000522		
0.3801597	0.0097629	-0.96716		0.006905306	8.17E-06	0.002858		

Figure 4.22. The rest of spreadsheet A.

Figure 4.22 is the continuation of spreadsheet A and was used to fit the data to equation (4.4). Column O was used to calculate the theoretical α values based on equation (4.4). The fit was optimized using the adjustable parameters in column S and calculating the chisq value in column P. The Solver function in Microsoft Excel was used to minimize the difference between column O and column L by adjusting the k_c , K_A , and A values in column S. “A” is actually the parameter “b” from equation (4.4). The temperature in Celsius also needed to be entered into column S to be used in calculating the effects of bending. Residuals were calculated in column Q by subtracting columns L and O.

4.4.3.2.3 Criteria for Acceptable GUVs

A final aspect of data fitting was determining which data was acceptable to fit. As will be described in Section 4.5.1, there were many vesicle-like structures that could be aspirated, but not all of them qualified as GUVs. If the vesicle exhibited any unusual behavior, such as peeling, having a ‘thick’ edge, or a large jump in its projection length, its data were discarded. If the fit to equation (4.4) returned values more than 10x more than expected for similar systems, the data were discarded. If the run did not have at least one isolated high and low tension point (0.5 mN/m being considered the cutoff between high/low tension), the data was discarded. Finally, once the data was processed, the k_c and K_A values sometimes clustered. If clusters were found, the lowest cluster was assumed to be GUVs (i.e., unilamellar), while the higher value groups were assumed to be multilamellar.¹⁶⁸

In the cases where a GUV was discarded for the previously mentioned reasons for k_c and K_A , it was also not used for lysis tension measurements. There were instances, though, where the suboptimal optical properties of the GUV and pipette did not allow measurement of ΔL . If the GUV did not seem otherwise unusual, it was kept for lysis tension data.

4.4.3.3 Lysis Tension

The lysis tension, τ_c , was the tension of the final frame before lysis of a GUV. If the GUV did not lyse during application of the tension ramp (final tension ramp values varied based on lipid identity and manometer conditions), it was not used for τ_c measurements.

4.5 Results and Discussion

This Section will present and discuss all of the valid results obtained from μ PA experiments. First, the various categories of observed giant vesicles will be discussed. Then, lysis tensions, elastic area expansion moduli, and elastic bending moduli will be presented for both unpolymerized and UV-polymerized GUVs. From the measured quantities, other parameters could be calculated, such as cohesive energy density and peak-to-peak membrane thickness. A discussion of the implications of the measured quantities for integral membrane protein function in polymerized bilayers composed of the lipids of interest will be left for Chapter 5.

4.5.1 Observed Geometries of “GUV”s

Many types of microscopic lipid structures were observed while performing μ PA. Not all of these structures were appropriate for experimentation. This Section categorizes some of the more common GUVs observed based on appearance and behavior. Only GUVs fitting the description of Sections 4.5.1.1 and 4.5.1.2 were used for quantitative measurements.

4.5.1.1 Typical GUVs

Figure 4.23 has three examples of “good” GUVs. The contrast in DIC imaging is good, meaning that there is a relatively impermeable barrier between the internal and external solutions. Also, the GUV walls do not seem overly thick, which would signify multilamellarity. These types of GUVs were rarely observed in sorbylPC samples.

4.5.1.2 “Leaky” GUVs

GUVs which appeared flat and more 2-dimensional than those shown in Section 4.5.1.1 were the result of the mixing of internal and external solutions. This mixing would abolish the refractive index difference that DIC uses to enhance contrast. Several examples are shown in Figure 4.24. All UV-polymerized samples contained “leaky” GUVs as did the unpolymerized sorbylPC samples. In fact, if a sorbyl GUV maintained contrast, it usually turned out to be multilamellar. “Leaky” GUVs were much less common for denoylPC lipids.

4.5.1.3 Multilamellar Giant Vesicles

Figure 4.25 shows a multilamellar giant vesicle (GV) undergoing aspiration. This GV also has a small parasite vesicle attached, which can cause additional problems. However, as the applied tension increases, an outerlayer of the GV peels away to reveal something that looks more like a GUV. The tell tale signs of multilamellarity are easily visible in Figure 4.25A. The edges look sharp and square. Also, there appear to be multiple rings near the edge. Few GVs peel like this example, but this progression shows the difference between a multilamellar and a (most likely) unilamellar GV.

4.5.1.4 Continuous Collapse

Another unusual behavior of GVs is shown in Figure 4.26 with a “leaky” vesicle. In this case, a large, polymerized bis-SorbPC GV is aspirated entirely into the pipette without lysing. The projection length grew extremely quickly at the onset of tension and disappeared out of the frame. Small parasite GVs were polymerized into the surface as well, although not visible in the still frames.

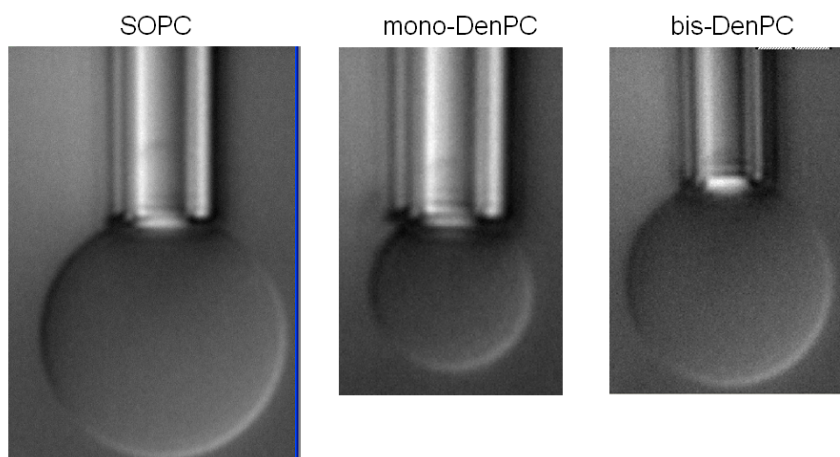


Figure 4.23. GUVs that appear appropriate for experimentation.

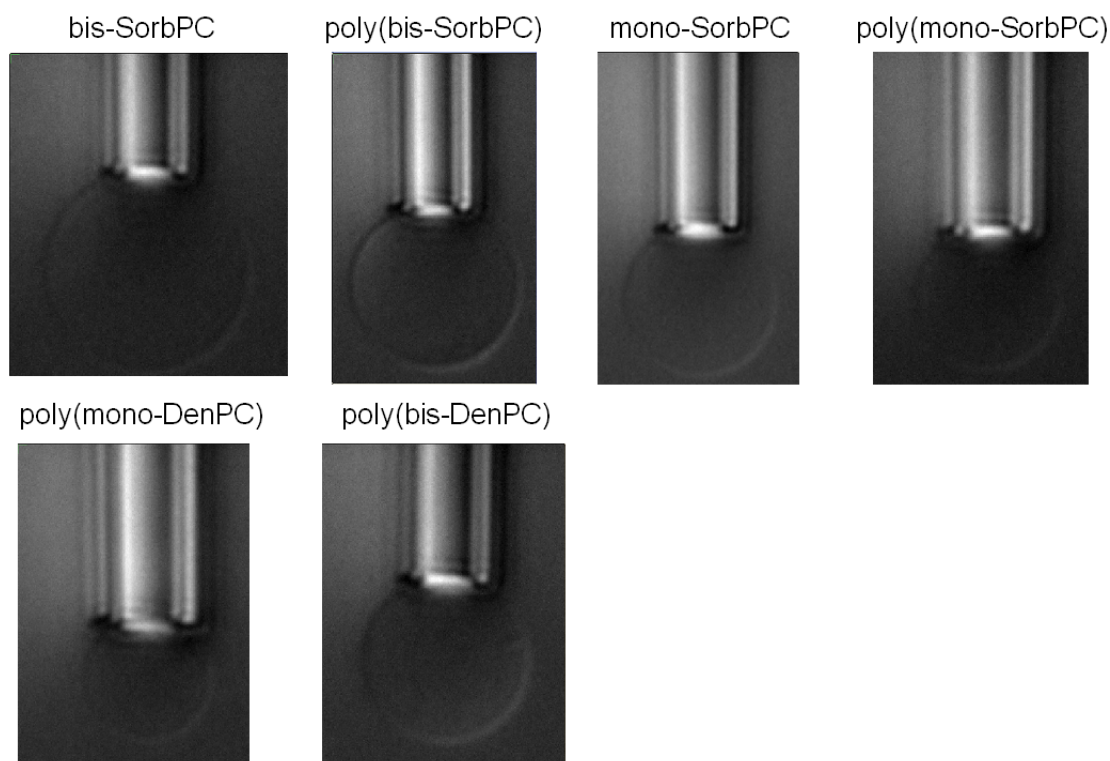


Figure 4.24. All polymerized GUV samples had “leaky” GUVs present (in varying degrees – the bis-DenPC examples is not as extreme as the others). The unpolymerized sorbylPCs also exhibited this behavior. The loss of contrast in DIC images means the internal and external solutions had mixed and there was no longer a difference in refractive index across the membrane.

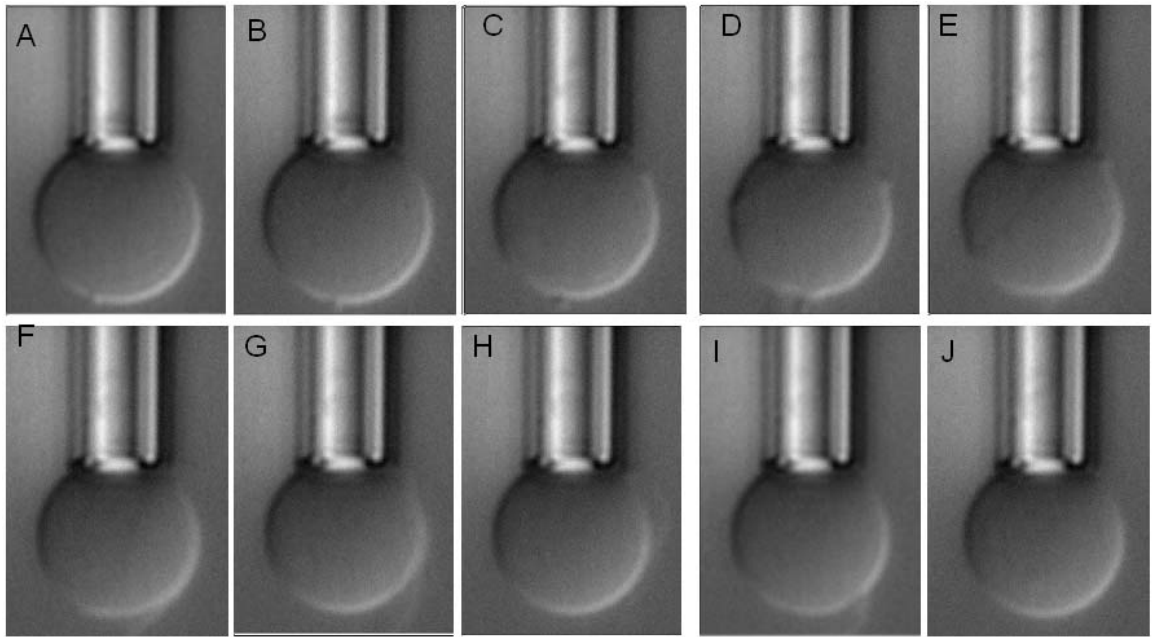


Figure 4.25. A multilamellar GV (mono-DenPC) undergoing aspiration. Applied tension is increasing from A – J. A small parasite vesicle is present in A-C at the lower edge of the GV. Starting at about D, an outer layer of lipids peels off until about H. In I, the extra layer is still hanging onto the parent GV. In J, the edges of the GV look more like a GUV, because they lack the sharpness and rings noticeable in A-C.

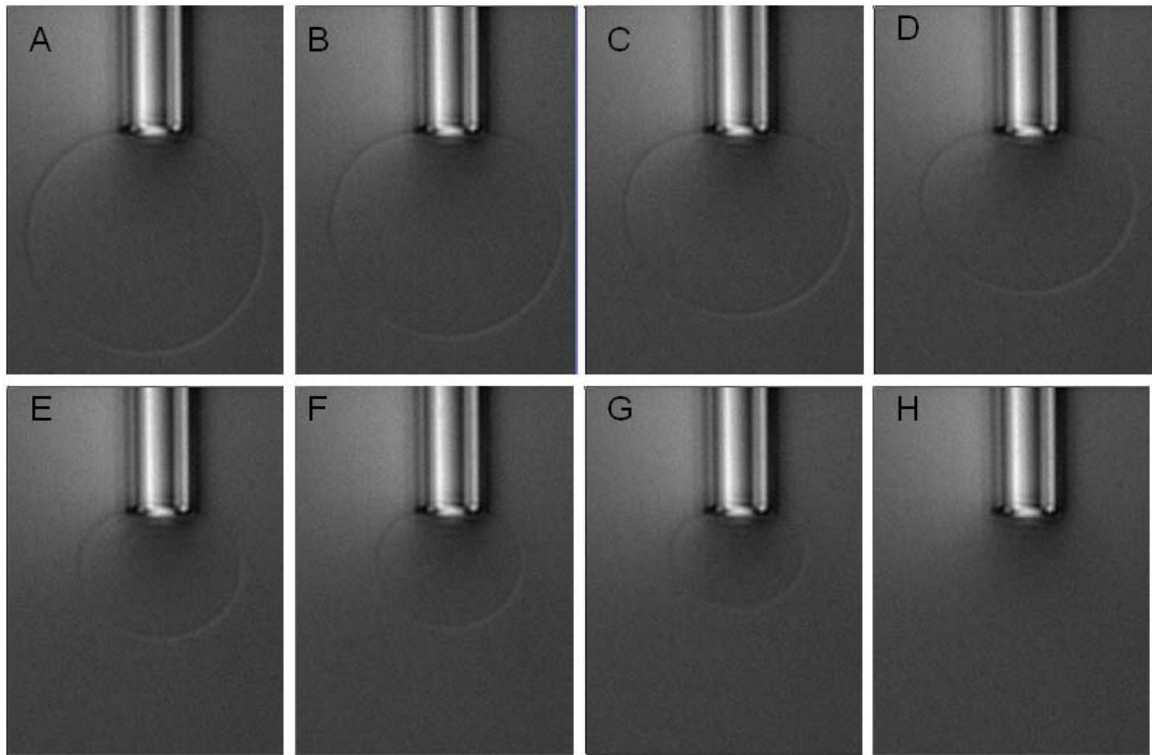


Figure 4.26. A large polymerized bis-SorbPC GV undergoing aspiration. Tension increases from A – H, but the intervals between images are not equal. As is visible in C, the behavior of the GUV is more ‘plastic’ based on the corners appearing. Also, the projection length quickly grew out of the frame. The entire GV was basically aspirated into the pipette without lysing.

It is unlikely that a lipid with only two polymerizable units per molecule could crosslink an entire unilamellar micron-sized structure. This behavior was unlike the majority of the GUVs examined, including polymerized GUVs, and was attributed to a multilamellar structure.

4.5.1.5 Crumpling

The strangest event captured during lysis is shown in Figure 4.27. Again, a large, polymerized bis-SorbPC GV is being aspirated. At first, the behavior seemed similar to what was shown in Figure 4.26, except that the GV began to crumple like a micron-sized plastic bag. This may have been due to the convection happening in the cell due to uneven heating. Despite the fact that this GV was “leaky” based on its appearance under DIC observation, it was clearly polymerized enough to hold its shape until it was eventually aspirated in its entirety into the pipette.

4.5.2 Lysis Tension

Table 4.2 summarizes the τ_c for all measured GUV types. The reference GUVs composed of SOPC lysed in the ~ 5.5 mN/m regime, which is similar to data published by Evans and coworkers.^{35, 176} All of the polymerizable lipids (unpolymerized and UV-polymerized) were found to be weaker than SOPC. When comparing the unpolymerized GUV τ_c results, it becomes apparent that the denoylPCs tend to be stronger than the sorbylPCs. In terms of mono- vs bis-substituted lipids, mono-DenPC is somewhat stronger than bis-DenPC, while the sorbylPCs are similar to each other.

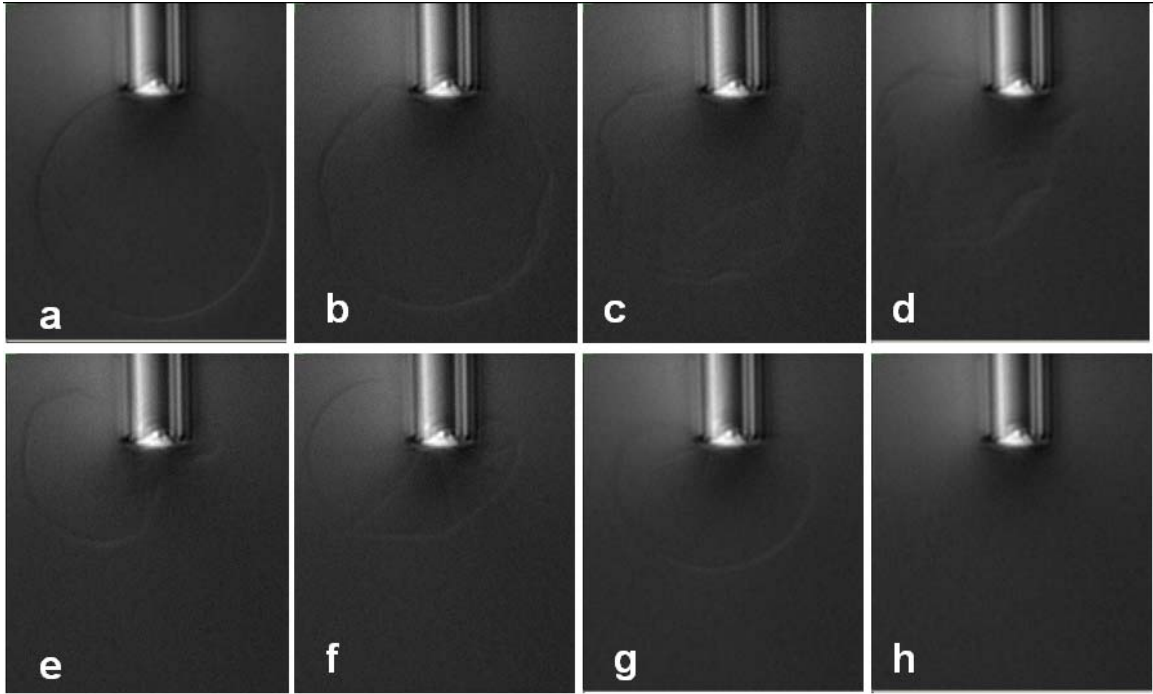


Figure 4.27. DIC images of a UV-polymerized bis-SorbPC vesicle, which is most likely multilamellar, during aspiration. The tension values are 2.47 mN/m (a), 2.51 mN/m (b), 2.56 mN/m (c), 2.61 mN/m (d), 2.65 mN/m (e), 2.70 mN/m (f), 2.79 mN/m (g), and 2.84 mN/m (h). This GV was entirely aspirated into the pipette without rupture.

Table 4.2. Experimental temperature, lysis tensions, elastic area expansion moduli, and elastic bending moduli of GUVs. Numbers in parentheses are the number of GUVs included in the data.

Lipid	Temp (°C)	τ_c (mN/m)	K_A (mN/m)	k_c (10^{-19} J)
SOPC	22	5.5 ± 0.98 (8)	150 ± 13 (16)	0.7 ± 0.34 (16)
mono-DenPC	35	3 ± 1.0 (19)	120 ± 19 (17)	0.7 ± 0.26 (17)
bis-DenPC	30	1.7 ± 0.64 (21)	120 ± 22 (16)	0.7 ± 0.18 (16)
mono-SorbPC	42	0.9 ± 0.56 (43)	100 ± 47 (3)	0.65 ± 0.028 (3)
bis-SorbPC	35	0.8 ± 0.18 (18)	43 ± 7.2 (3)	1.0 ± 0.24 (3)
poly(mono-DenPC)	35	3 ± 1.2 (23)	120 ± 32 (5)	0.4 ± 0.20 (5)
poly(bis-DenPC)	30	1.4 ± 0.65 (22)	90 ± 20 (17)	0.7 ± 0.28 (17)
poly(mono-SorbPC)	42	0.9 ± 0.55 (28)	130 ± 15 (2)	0.7 ± 0.38 (2)
poly(bis-SorbPC)	35	1.1 ± 0.34 (9)	60 ± 28 (2)	0.77 ± 0.057 (2)

The lysis tensions of the sorbylPCs were near the 0.5 mN/m tension cutoff used by other researchers to delineate between high and low tension regimes.^{99, 174} For the data presented in this chapter, only SOPC was prestressed, to be comparable to literature. It was possible to prestress mono-DenPC, because its lysis tension was large enough for the GUV to survive the prestress process. This was not the case for the other lipid types, which would frequently lyse during prestress. The τ_c for both unstressed and prestressed mono-DenPC GUVs were measured and were found to be within error (lysis tension for prestressed mono-DenPC GUVs = 2.0 ± 0.59 , $n = 5$). As a result, it was assumed that prestressing had no effect on polymerizable lipids, and thus no prestress was applied to any of the polymerizable lipid GUVs.

A study by Olbrich et al. found that the addition of two or more cis double bonds in one or both lipid tails resulted in a decrease in lysis tension when compared to GUVs composed of saturated and mono-unsaturated lipids.¹⁷⁷ The difference in τ_c when going from SOPC (a single double bond in one chain) to mono-DenPC to bis-DenPC is proportionally similar to the difference in τ_c when going from SOPC to C18:0/2 (2 double bonds in one tail) to diC18:3 (three double bonds in each tail). This suggests that the unsaturation in the tails of mono-DenPC and bis-DenPC may be the reason they are weaker than SOPC. Because mono-SorbPC is as unsaturated as bis-DenPC, the level of unsaturation cannot explain the further reduction in strength of the sorbylPCs. The study by Olbrich also compared diC18:1_{c9} and diC18:1_{c6} and saw no difference in τ_c for having

the unsaturation in different places in the tails. This suggests that double bond location might not play a role, but other locations in the tails were not investigated.¹⁷⁷

Lysis tensions of GUVs composed of several types of lipid systems were tabulated in Evans et al.³⁵ Figure 7 in Ref. 35 shows the rather weak τ_c of “polymerizable lipids”. Needham, an author of Ref. 35, identified the polymerizable lipids as unpolymerized diacetylinic lipids when he was personally contacted.¹⁴³ Based on the figure in Ref. 35, the τ_c of the diacetylinic lipids was $\sim 0.5 - 1.0$ mN/m, which is in good agreement with the τ_c of the sorbylPCs investigated in this study.

The presence of non-conductive, metastable prepore states during electroporation of DiphyPC was suggested by Melikov and coworkers.¹⁷⁸ Other references¹⁷⁹⁻¹⁸³ also indicate other lysis behaviors during electroporation, implying that the lysis mechanism is dependent on lipid composition. The method of inducing lysis may also affect the lysis mechanism. Evans et al.^{176, 184} investigated the effect of lysis tension ramp rate on PC lipids of varying length and degree of unsaturation. It was hypothesized that a metastable defect state forms prior to unstable catastrophic hole formation (lysis). Depending on the tension ramp rate, however, the rate limiting step in lysis is different. For high tension ramp rates, defect formation was the rate-limiting step. For low tension ramp rates, such as those used in this Chapter, unstable hole formation was the rate-limiting step. Based on the work of Chernomordik and Rawicz,^{176, 178, 184} it can be suggested that there are two types of non-continuous pre-lysis membrane states: non-conductive prepore and metastable pore. Previous studies have shown that bis-SorbPC forms porous bilayers when UV-polymerized with a maximum pore size of 2 nm.¹⁸⁵ Bis-SorbPC was also

found to be conductive in electrophysiology experiments.⁴³ These findings indicate that bis-SorbPC forms the weakest GUVs because those GUVs are already porous.

Additionally, DIC images of GUVs made of different lipids, shown in Figure 4.28, imply ‘leakiness’ of certain membranes. The images of the GUVs highlight the fact that the internal and external solutions are mixing in the cases of some of the sorbylPCs, because the contrast is lost. This implies the presence of longer lived and/or larger metastable pores for sorbylPCs that allow mixing of the internal sucrose and external glucose solutions. It is well established that bis-SorbPC is leaky to low molecular weight molecules.¹⁸⁵ Perhaps the sorbyl moieties of the lipid cause more organized and less densely packed bilayers due to dipole-dipole and dipole-induced-dipole interactions among the polymerizable groups. It was suggested in Chapter 3 that the stronger intermolecular forces present in the sorbylPC tails may align the tails into more favorable geometries for polymerization, because bis-SorbPC (2 polymerizable groups) always exhibited a larger decrease in D_{avg} than mono-SorbPC (1 polymerizable group) under given circumstances.

After polymerization, no statistical difference between unpolymerized and polymerized GUVs were found for τ_c . Discher et al. had studied the mechanical properties of polymerizable polymersomes made from mixtures of poly(ethylene oxide)-polyethyethylene (EO7) and poly(ethylene oxide)-butadiene (OB2) using μPA .¹⁴⁴ In this case, the polymersome bilayers had a core thickness nearly 3 times that of an ordinary lipid bilayer and instead of having 1-2 polymerizable groups in the ‘tails’, like the lipids being investigated in this Chapter, OB2 had 46 polymerizable units per molecule.¹⁴⁵

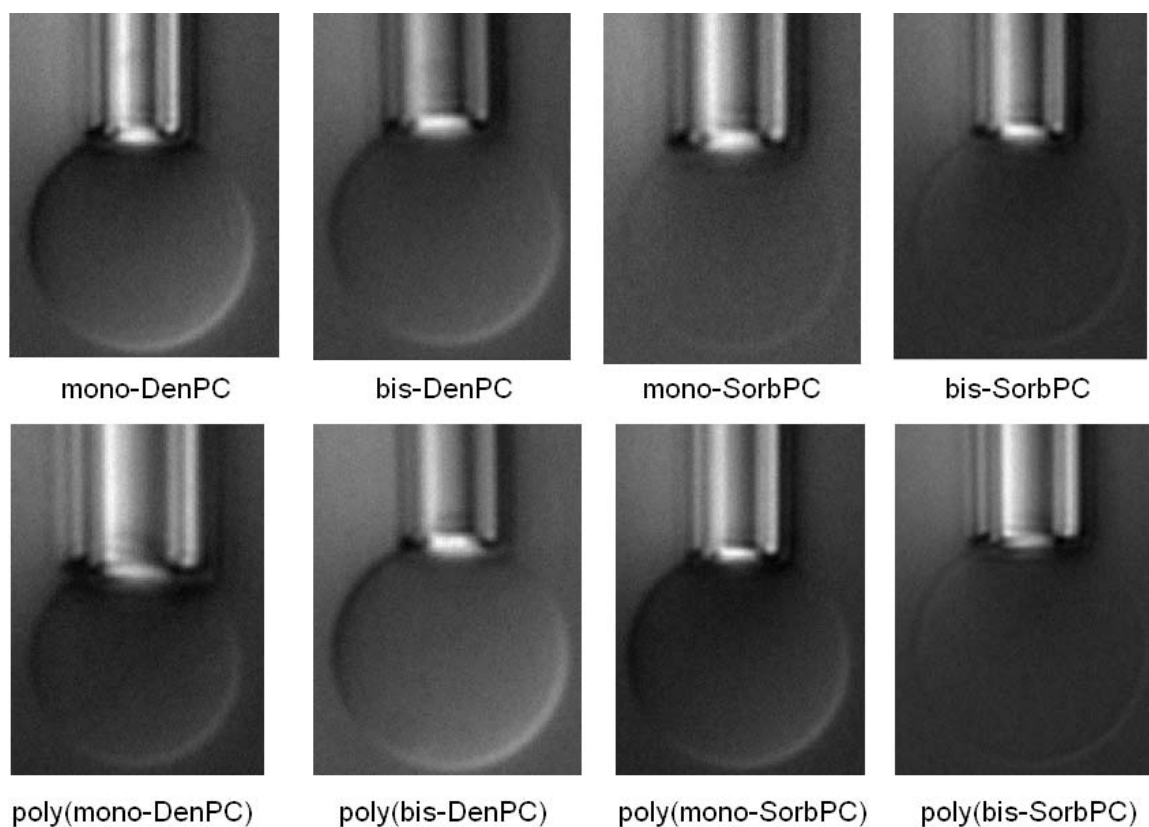


Figure 4.28. DIC images of all of the polymerizable lipid GUVs unpolymerized and UV-polymerized. The lack of contrast between the internal sucrose and external glucose solutions seen in most of the sorbyl-group containing GUVs suggests that there is mixing of the solutions and thus the GUVs are ‘leaky’. Occasionally, UV-polymerized denoyl-containing GUVs exhibited the same behavior.

EO7 was not polymerizable. It was found that for polymerized GUVs made from mixtures of lipids with less than 16 mol % OB2, the τ_c actually decreased compared to pure, unpolymerizable EO7 GUVs. It was hypothesized that the existence of a solid-in-fluid phase causes these weaker structures. According to Table 3.8, UV-polymerized mono-substituted PSLBs were completely fluid, while UV-polymerized bis-substituted PSLBs were partially fluid. Both of those categories are below the percolation threshold, meaning that the membranes still had isolated obstacles in a fluid phase, instead of continuous obstacles with isolated pockets of fluidity in them. When the percent of OB2 is greater than 16 mol %, the strength of polymerized polymersomes increases drastically.¹⁴⁴ It is suspected that above 16 mol %, the polymersomes exhibit a continuous polymer network, which may be above the percolation threshold. Because UV-polymerization had been used to create polymers of the dienoyl lipid GUVs, short polymers are expected based on findings by Tsuchida and Lamparski.^{75, 76} Data in Chapter 3 also suggest that much larger polymers are possible using redox-polymerization than UV-polymerization in some cases. Since there are only 1-2 polymerizable groups in each lipid, cross-linking the entire micron-sized GUV structure is highly unlikely. Based on the finding in Chapter 3 and τ_c results, polymerized GUVs composed of dienoyl lipids would fall into the < 16 mol % OB2 regime. An increase in strength is not expected, because the polymers are so small, but a decrease in strength might be possible due to discontinuities between polymer domains. A decrease was not seen, however. Also, as was shown in Chapter 3, the diffusion coefficient of bilayers

decreases if polymerized, meaning that closing metastable holes or repairing prepore states by diffusing lipids into the defects will be less effective with polymers.

4.5.3 Elastic Area Expansion Moduli

The two-component fitting method [equation (4.4)] was used to analyze all of the K_A and k_c data. Table 4.2 has all of the tabulated results for unpolymerized and polymerized GUVs. The K_A value for the SOPC reference GUVs was somewhat less than expected from literature at ~ 150 mN/m (lit. values range from ~ 190 - 240 mN/m).¹⁷⁴,¹⁸⁶ In general, the unpolymerized lipids had slightly lower elastic area expansion moduli than SOPC with the exception of bis-SorbPC, which exhibited a very low K_A . Based on the study conducted by Rawicz et al.,¹⁷⁴ unsaturation should not play a role in the K_A value of one lipid versus another. That same study also looked at diC18:1_{c9} v. diC18:1_{c6} and found that there were no significant differences in K_A , although as mentioned before, a systematic study of bond location was not carried out. Due to the proximity of the stiff conjugation to the headgroup in the denoylPCs, one might expect greater difficulty (larger K_A) in prying the tails of a single lipid apart compared to the sorbylPCs, where the conjugation is farther from the connection point to the PC moiety. It was found, however, that cis vs trans orientation of the double bonds in the tails does have some effect, suggesting that tail structure could play a role.¹⁷⁴ Needham and Evans³⁵ saw a 4-fold decrease in K_A for diacetylinic lipid GUVs compared to SOPC, similar to the findings in this study for bis-SorbPC. The perturbation to the structure of an alkyl chain tail is much greater with the introduction of a sorbyl group, as in the sorbylPCs, than it is by unsaturation, as in the denoylPCs. Also, caution must be exercised when interpreting

the results from the sorbylPCs, because very few were able to yield enough data to extract K_A values, due to the poor optical properties of those GUVs. Alternatively, the incorporation of two sorbyl groups in the tails may disturb the intermolecular forces holding the lipid tails together more than a single sorbyl group. An estimate of the cohesive energy density will be calculated in Section 4.5.4 to further explore this topic.

UV-polymerization of the GUVs did not significantly change the elastic area expansion moduli compared to the unpolymerized GUV values. As had been discussed in Chapter 3 and Section 4.5.2, UV-polymerization creates small polymers that are perhaps too small to significantly affect the mechanical properties of the GUVs.

4.5.4 Cohesive Energy Density

Another parameter that can be calculated based on K_A and τ_c is the cohesive energy density (E_C) of the membrane.^{99, 145, 186} This is the total elastic energy stored in the membrane at lysis. The references cited used

$$E_C \approx \frac{1}{2} K_A \alpha_c^2 \quad (4.6)$$

where α_c is the lysis area strain, or the α at lysis. Basically, it is the area under the plot of τ vs. α . Since there was more uncertainty involved in measuring α than there was measuring τ in the set-up used for this study, the following equation was used instead:

$$E_C \approx \tau_c^2 / 2K_a \quad (4.7)$$

The calculated E_C values are shown in Figure 4.29. The value found for E_C of SOPC in this work was similar to $\sim 0.1 \text{ mJ/m}^2$ calculated in the work by Needham and Nunn, but was slightly lower than the value of $\sim 0.27 \text{ mJ/m}^2$ found by Ly and coworkers.^{99, 186}

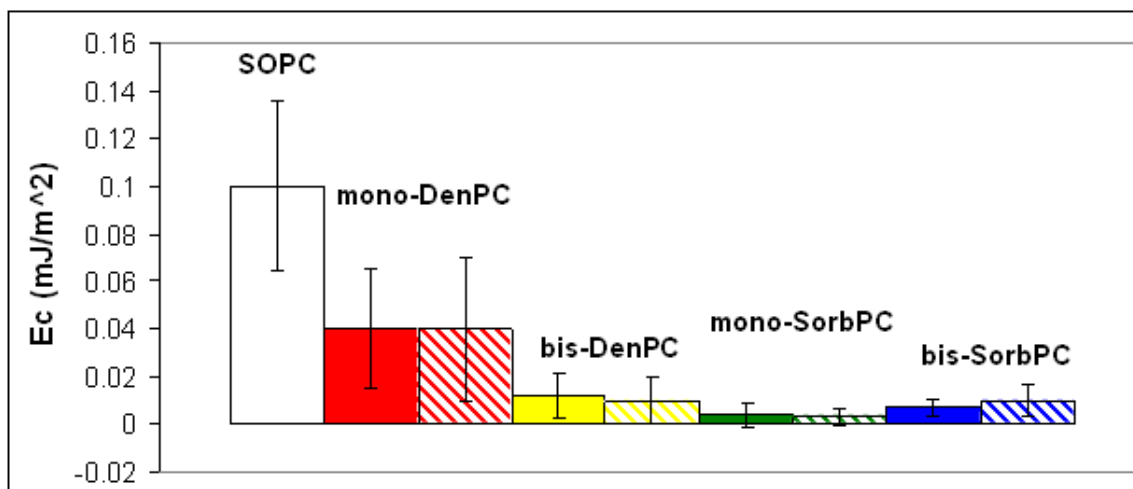


Figure 4.29. Calculated cohesive energy densities for polymerizable lipids using equation (4.7). Solid bars are for unpolymerized GUVs, while striped bars are for polymerized GUVs.

The discrepancy between the values in the literature could be due to the fact that K_{app} was used by Needham and Nunn and K_A was used by Ly et al. Although, based on the small amount K_{app} would be altered by converting to K_A , the data in this Chapter would most likely still be in agreement with Needham and Nunn. As seen in Figure 4.29, in most cases there is a significant difference between SOPC and the polymerizable lipids. Again, polymerization had a negligible effect on E_C . Mono-SorbPC, bis-DenPC, and bis-SorbPC all had similar cohesive energy per unit area, while mono-DenPC seemed to be slightly more energetic. This may be because mono-DenPC is least perturbed from a non-polymerizable lipid, with the least polymerizable groups and the least bulky groups substituted into the tail.

4.5.5 Elastic Bending Moduli

The results for fitting k_c by equation (4.4) are tabulated in Table 4.2. The k_c value determined for SOPC is similar to $\sim 0.90 \times 10^{-19}$ J found in the literature.¹⁷⁴ All unpolymerized lipid GUVs were found to have approximately the same elastic bending modulus as SOPC. As in all previous cases, UV-polymerization did not significantly change the bending modulus, although large standard deviations of the measured values were recorded in most cases. Rawicz et al. had found that increasing unsaturation would cause lower k_c values for PC lipids,¹⁷⁴ which was not the case here. As bending moduli have never been measured for polymerized lipid GUVs or polymerized polymersomes, no comparisons can be made.

As had been mentioned in Section 1.6.3, it was expected that the conjugation near the PC group in the denoylPCs would make k_c larger than for sorbylPCs. That was found not to be the case. It must be stressed, however, that sizable error bars were associated with the low τ measurements and few GUVs were available for sorbylPC measurements. There may be differences in k_c , but the instrument used does not have the resolution to distinguish them. Literature k_c values do have smaller errors, which may be because they could use a more sensitive pressure transducer, while we could not since we were simultaneously investigating low and high τ .

4.5.6 Calculated Membrane Thickness

The peak-to-peak headgroup thickness (h_{pp}) can be estimated from K_A and k_c values and by making some assumptions. Bermúdez et al.¹⁸⁷ had investigated the dependence of k_c as a function of h_{pp} for polymersomes. Theory states that

$$K_c = \beta K_A d^2 \quad (4.8)$$

where β is a scaling factor related to how closely the two leaflets of a bilayers are coupled and d is the hydrophobic thickness of the membrane. The β value can vary from 1/48 for completely uncoupled monolayers to 1/12 for completely coupled, interdigitated monolayers. Rawicz et al.¹⁷⁴ measured h_{pp} using x-ray diffraction for several saturated and unsaturated bilayers of varying tail chain lengths and found that for saturated and mono-unsaturated bilayers, equation (4.8) held and gave a β value of 1/24 and a non-deformable thickness of ~ 1 nm, which corresponds to the difference in mechanical thickness calculated by equation (4.8) and h_{pp} . For more highly unsaturated lipids, this

trend was not followed. It was also found that the measured h_{pp} of highly unsaturated lipids was less than expected based on chain length.

To calculate h_{pp} , β was assumed to be $1/24$, although that would not be appropriate based on the number of double bonds in the polymerizable lipids. This assumption was made because there was not enough data to measure a trend for more highly saturated lipids.¹⁷⁴ Using the K_A and k_c values tabulated in Table 4.2, h_{pp} was calculated using the following equation, which is a modified version of equation (4.8) that accounts for the non-deformable thickness:

$$h_{pp} = 1 + (k_c/K_A)^{1/2}/\beta^2 \quad (4.9)$$

The calculated h_{pp} values can be found in Figure 4.30. Rawicz et al.¹⁷⁴ measured h_{pp} of SOPC as ~ 4 nm, which agrees well with the value calculated for SOPC in this work.

With the exception of bis-SorbPC, all unpolymerized lipids were found to be within one standard deviation of the calculated SOPC h_{pp} thickness. Not surprisingly, since there was no significant difference in K_A and k_c between polymerized and unpolymerized GUVs of the same lipid, there was no difference in h_{pp} after polymerization. Again, there are large errors associated with the calculation since the measured k_c values had large errors.

The calculation for bis-SorbPC yields a very thick value for a single bilayer. One possible explanation for this is that the wrong β was chosen. If β was made smaller, signifying more interdigitation, then the calculated h_{pp} would decrease.

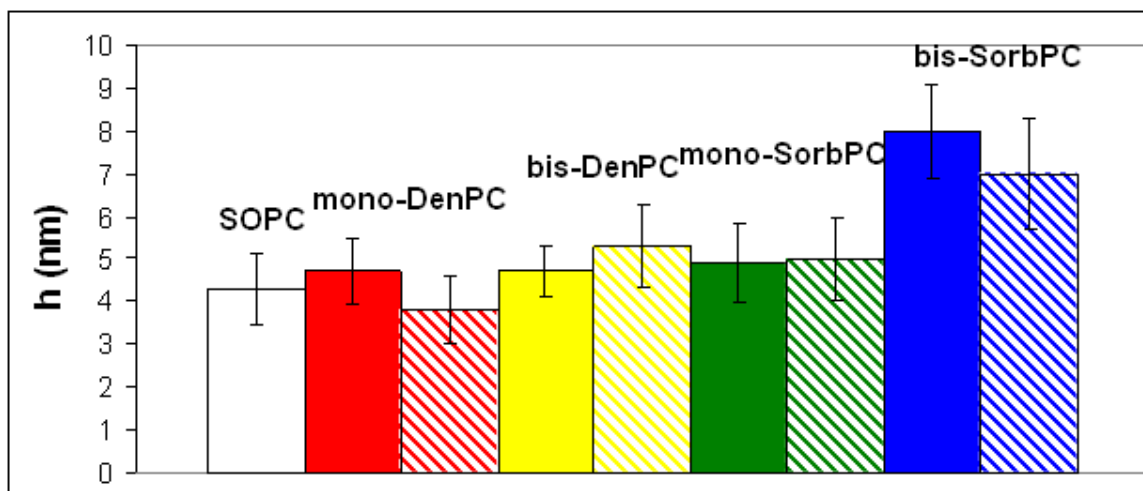


Figure 4.30. Calculated cohesive energy densities for polymerizable lipids using equation (4.7). Solid bars are for unpolymerized GUVs, while striped bars are for polymerized GUVs.

Since the sorbyl moieties in the two leaflets of a bilayer are quite near each other, one could argue that due to the stronger intermolecular forces present in bis-SorbPC, there may be more interdigitation in the tails compared to the other polymerizable lipids investigated.

4.6 Conclusions

The polymerizable lipid GUVs were found to have lower lysis tensions, slightly lower K_A values, and similar k_c values compared to SOPC GUVs. This finding refutes the hypothesis that conjugation at the proximal end of the tail would cause larger elastic moduli than at the distal end. Better instrumental resolution would be needed to further test this hypothesis. UV-polymerization of the GUVs did not significantly change any of the measured properties most likely because small polymers are formed that are still fluid and do not cross the percolation threshold. Implications of these mechanical properties findings will be discussed in Chapter 5.

CHAPTER 5: CONCLUSIONS

5.1 Summary

Because of their importance in cell signaling and disease states, TMPs are attractive sensing materials for biosensors.¹³⁻¹⁶ A significant amount of research has focused on creating suitable membrane matrices for functional TMPs as a result.^{13, 47-54} A critical issue with these artificial membranes, however, is their instability.⁵⁸⁻⁶² Although there are numerous ways to try to stabilize these membranes, polymerizable lipids were focused on in this set of studies since it had been found that TMPs could be incorporated into stabilized polymerized bilayers while maintaining their function.^{43, 77-81, 83-86, 188} The purpose of this work is to investigate some of the material properties of these polymerizable membranes, specifically fluidity and mechanical properties, to see if they are important to maintaining the function of certain TMPs. It is known that lipid bilayer fluidity and mechanical properties can play a role in the function of proteins.^{1, 9, 22-24, 31, 36}

The work presented focused on determining the diffusion characteristics and mechanical properties of polymerizable lipid bilayers formed from mono-DenPC, mono-SorbPC, bis-DenPC, and bis-SorbPC. Unpolymerized, UV-polymerized, and in some cases redox-polymerized bilayers were studied.

5.1.1 Fluidity of Unpolymerized and Polymerized PSLBs

The fluidity of PSLBs on glass created from the lipids in Figure 1.19 were studied using the FRAP (rhodamine-PE) technique outlined in Chapter 2. Unpolymerized, UV-polymerized, and redox-polymerized PSLBs were investigated. The polymerization temperature was also varied (with respect to T_m of the particular lipid). All FRAP

measurements were performed above T_m of the unpolymerized lipid. Diffusion coefficients and percent recoveries for each membrane type were determined. Three basic types of behavior were seen for the PSLBs, as summarized in Table 3.8.

Fluid PSLBs were those that exhibited $\sim 100\%$ recovery, had $\sim 70/30$ or greater $\%_1/\%_2$ population distributions, and had less than $\sim 10 D_{\text{avg un}}/D_{\text{avg poly}}$ values. All unpolymerized PSLBs were in this category, along with UV-polymerized mono-substituted lipids, redox-polymerized bis-DenPC films, and some others (Refer to Table 3.8 for details.).

Partially fluid PSLBs had an immobile fraction between $70/30$ and $50/50$ $\%_1/\%_2$ population distributions, and had $D_{\text{avg un}}/D_{\text{avg poly}}$ values less than or equal to 10. All UV-polymerized bis-substituted lipids and redox-polymerized (below T_m) mono-SorbPC films were partially fluid.

The third category was called ‘immobile’, although there were measurable diffusion coefficients and percent recoveries. These immobile films had an immobile fraction and had a greater slowly diffusing population than quickly diffusing population, i.e. $\%_1/\%_2 < 50/50$. They also exhibited $100+ D_{\text{avg un}}/D_{\text{avg poly}}$ values. These films are basically immobile on short timescales. Redox-polymerized bis-SorbPC and redox-polymerized mono-SorbPC (when polymerized at or below T_m) fall into this category.

There are numerous factors that might influence how fluid each PSLBs is, including polymer size and geometry. For instance, only redox-polymerized films fell into the immobile category, in agreement with the findings of researchers that redox-polymerization can create larger polymers than UV-polymerization.^{75, 76, 134} Interestingly,

bis-DenPC goes against that trend having fully fluid redox-polymerized films and partially fluid UV-polymerized films, suggesting that larger polymer networks can form when UV-polymerization is used. One would also expect bis-substituted lipids to form larger polymers having larger $D_{\text{avg un}}/D_{\text{avg poly}}$ values than their mono-substituted counterparts, because there are more polymerizable groups per lipid molecule. This is generally true for the sorbylPCs, where bis-SorbPC tended to have less fluid PSLBs than mono-SorbPC under similar polymerization circumstances. This was not true in the case of the denoylPCs, where mono-DenPC could form immobile redox-polymerized films under given conditions, while bis-DenPC never formed immobile films. This could be attributed to the ‘barrier height’ argument, made by Lamparski and O’Brien,^{75, 136} where the formation of the polymer network at the water/hydrocarbon interface interferes with the diffusion of the monomers to the propagating polymer more than the formation of the polymer network in the center of the hydrocarbon region does for the sorbylPCs. They argue that more barriers form with bis-substituted lipid cross-linking, which could explain why mono-DenPC could potentially form larger polymers than bis-DenPC.

Lamparski and O’Brien had demonstrated that monomer/initiator ratio could greatly change the size and properties of the formed polymers.⁷⁵ The FRAP data presented here shows that polymerization method and polymerization temperature can greatly affect the properties of a polymer formed from a particular lipid monomer as well.

Data from Heitz et al. showed that gramicidin and alamethecin were functional in DPhPC, unpolymerized bis-DenPC, unpolymerized mixtures of DPhPC and bis-DenPC, and UV-polymerized mixtures of DPhPC and bis-DenPC.^{77, 86} UV-polymerized bis-

DenPC did not maintain gramicidin or alamethicin function. It had been hypothesized that this was because a significant immobile fraction formed, as depicted in Figure 1.21B, or there was a large enough decrease in diffusion coefficient that the peptides could not form ion channels on the time scales of the experiments. Data gathered in this work show a decrease in diffusion coefficient and % recovery for UV-polymerized bis-DenPC PSLBs compared to unpolymerized PSLBs, which led to categorizing UV-poly(bis-DenPC) as partially fluid. Mixtures of DPhPC and bis-DenPC were not investigated by FRAP. Depending on the polymerization temperature, though, at most 10% of the UV-poly(bis-DenPC) films were immobile. Unfortunately, polymerization at T_m was not investigated here, while that is actually where the polymerization and electrophysiology measurements took place in the work of Heitz et al.^{43, 77, 78, 86} As seen in the case of mono-DenPC polymerized at T_m , unexpected things can occur. This work did show that there is a decrease in fluidity of pure bis-DenPC films when UV-polymerized, meaning that either films need to have 100% recovery or faster diffusion is needed for successful incorporation into films of gramicidin, alamethicin, or any TMP requiring fluidity for function. Heitz had used mixtures to get around this problem, but based on the FRAP results, one of the polymerized PSLBs from the “fluid” category might also work.

5.1.2 Mechanical Properties of Polymerizable Lipid Bilayers

A micropipette aspiration system was built and tested. The system was used to measure the elastic area expansion moduli, elastic bending moduli, and lysis tensions of GUVs composed of the polymerizable lipids shown in Figure 1.19. The effect of UV-polymerization of GUVs above T_m on the mechanical properties was also investigated.

The lysis tensions of denoylPCs were in the same vicinity as poly-unsaturated PCs.¹⁷⁷ SorbylPCs were found to be even weaker than expected based simply on unsaturation. Perhaps this is because the sorbylPCs form naturally more porous structures than denoylPCs, as evidenced by their optical properties and measured pore sizes.¹⁸⁵ Pore formation is believed to be a crucial step in lysis and the sorbylPCs readily form pores.^{176, 178, 184} UV-polymerization above T_m did not change the lysis tension of GUVs. This is attributed to the formation of small polymers since UV-polymerization was employed.^{75, 76, 134} Findings in Chapter 3 also indicate that none of the UV-polymerized membranes were above the percolation threshold, meaning that the polymer network was not continuous over the entire membrane. In the case of polymersomes,¹⁴⁴ it was found that until greater than 16 mol% cross-linkable monomer was included in non-polymerizable monomer, GUVs were actually weaker than those made from 100% non-polymerizable monomer. Discher et al. hypothesized a solid-in-fluid phase below 16 mol% cross-linkable monomer for these polymersomes, where the interfaces between solid and fluid phases would nucleate rupture. Above 16 mol% cross-linkable monomer, though, large increases in strength were observed and believed to be the result of a thin, solid-like shell. In the case of dienoylPCs, where at most 2 polymerizable groups are found per lipid (Discher's cross-linkable monomers had 46 polymerizable units each), it is highly unlikely that an entire GUV could have a continuous shell, especially when small polymers are expected based on the fluidity data found in Chapter 3 for UV-polymerization above T_m .

The area expansion moduli for the GUVs was found to be slightly lower than that found for SOPC, with the exception of bis-SorbPC, which was significantly easier to stretch than the other lipid compositions. It had been suspected that conjugation near the PC group of the denoylPCs would make them resist membrane deformation more than the sorbylPCs. That seems to be the case for bis-SorbPC, but not for mono-SorbPC. The sorbyl groups may introduce dipole-dipole and dipole-induced-dipole forces into the tails, but perhaps their bulkiness disrupts the van der Waals forces more, resulting in a net decrease in strength. Why this affects only bis-SorbPC and not mono-SorbPC could be due to the number of sorbyl groups per lipid. Really, we are not sure. UV-polymerization did not significantly change the elastic area expansion modulus for any of the investigated lipids. As discussed for the lysis tension results, this may be due to the formation of small polymers that are not big enough to have a net impact on the elastic area expansion modulus.

The bending moduli for the investigated systems all turned out to be within error of the value for SOPC. This was not expected based on the findings of Rawicz and coworkers,¹⁷⁴ where poly-unsaturation resulted in a decreased bending modulus. Polymerization did not significantly change the bending modulus in any case. This finding would refute the hypothesis that denoylPCs would be more difficult to bend than sorbylPC, because of the location of the conjugation in the tails. It must be noted, though, that the errors of the bending moduli measurements are large. An instrument with better resolution may find differences. Perhaps because the conjugation of the dienoylPCs is not in the glycerol backbone, it does not affect the mechanical properties.

Subramaniam et al. had found that bis-DenPC bilayers did not retain as much rhodopsin function as the sorbylPC bilayers.^{83, 84, 188} It is known that the inclusion of PE lipids into the membrane increases the function of rhodopsin compared to a bilayer of pure PC lipids.⁹ This is because the PE lipids have a negative spontaneous curvature, which could better adjust to rhodopsin elongation perpendicular to the membrane upon light activation. Since denoylPCs and sorbylPCs are both PCs, which are believed to have $H_0 = 0$, it was hypothesized that the bending moduli might be larger for denoylPCs than sorbylPCs, resulting in a larger free energy per unit interfacial area as shown in equation (1.1). The hypothesis was not found to be correct in this case. Mono-SorbPC, bis-SorbPC, and bis-DenPC were all found to have similar unpolymerized and polymerized bending moduli. If the culprit is not k_c as expected, it could be that the sorbylPCs and denoylPCs have different spontaneous curvatures. Since it was found that the sorbylPCs were similar to DOPC in terms of retaining rhodopsin function and inclusion of PEs (with negative curvature) improved rhodopsin function, then this would suggest that denoylPCs would have to have a positive spontaneous curvature.

5.2 Future Directions

5.2.1 Future Work with Fluidity Measurements

Chapter 3 showed that a variety of different diffusion behaviors were observed for polymerized PSLBs depending on the polymerization method and polymerization temperature employed. As had been demonstrated by Heitz et al.,^{43, 78} differences in fluidity may be the deciding factor for whether or not a transmembrane protein or peptide functions in a membrane. Based on the measurement of diffusion coefficients carried out in this work, it seems very likely that the reason alamethicin and gramicidin do not function in UV-poly(bis-DenPC) is that there was not enough fluidity. This type of information is important to know for membrane-TMP biosensor device applications. Although a number of different lipids, temperatures, and polymerization methods were employed in this work, there are still many parameters that need investigation. Also, based on the results of Chapter 3, it is difficult to predict the fluidity of a particular lipid membrane under a given set of polymerization conditions. Lamparski and O'Brien had noted that polymer size could vary greatly depending only on the particular monomer/initiator ratio used for redox-polymerization.^{75, 136} Future work with regard to diffusion coefficient measurements will be outlined below. For future work regarding FRAP instrumentation, please refer to Section 2.5.

5.2.1.1 Diffusion of PSLBs Polymerized at T_m

Heitz's work involved carrying out all measurements and polymerizations at room temperature.^{43, 77, 78, 86} This causes some issues in using the work in Chapter 3 to interpret

the results of his work because of the T_m values listed in Table 3.1. Room temperature is very near the T_m of bis-DenPC, which coincidentally, turned out to be the most successful lipid in all of Heitz's studies with respect to stability. No data was gathered in Chapter 3 where bis-DenPC was polymerized at T_m . Clearly, this is an important missing piece in interpreting Heitz's work. Additionally, since Subramaniam and Ross' work showed that polymerized bis-SorbPC was most stable and capable of maintaining the function of rhodopsin and mono-SorbPC was also capable of maintaining rhodopsin function,^{62, 83-85, 188} it would be an oversight not to investigate all of the lipids in Figure 1.19 when polymerized at T_m . As the findings in Section 3.3.4 for polymerization at T_m show, unexpected and important things can happen in this difficult to understand mixed phase.

5.2.1.2 Diffusion of Polymerized PSLBs at Room Temperature

A second important difference between the work of Heitz and that presented in this dissertation is that the membranes were at room temperature for electrophysiological measurements, while all FRAP data was gathered in the fluid phase of the unpolymerized lipid bilayers.^{43, 77, 78, 86} A lot of literature highlights the differences in diffusion between the fluid phase and gel phase of lipid membranes.^{120-122, 132, 189-191} Scomparin showed that by simply changing the way a PSLB was created on the same surface using the same lipid, the diffusion behavior as a function of temperature could change.¹³² It is therefore difficult to extrapolate with much confidence the results of Chapter 3 to room temperature, although that was done in Table 3.2 based on Scomparin's work, who, luckily, was studying a very similar surface and identical PLSB formation mechanism.

Because of this, it is important to measure diffusion at room temperature since that is where much of the previous work with these polymerizable lipid systems has been carried out. Room temperature would be in the gel phase for the sorbylPCs and mono-DenPC, meaning that a decrease in diffusion for the unpolymerized versions would be expected. Based on Sackman's work, a decrease in the diffusion coefficient for polymerized bilayers is also expected.^{121, 122}

5.2.1.3 Diffusion of PSLBs Composed of Mixtures of Polymerizable/Non-Polymerizable Lipids

A third variable that could be investigated is the mixing of the polymerizable lipids with non-polymerizable lipids. Heitz used this approach to obtain both stability and functionality in his gramicidin and alamethicin experiments, where bis-DenPC was mixed with DPhPC in varying mol fractions and polymerized.^{77, 86} Although polymerized mixed bilayers were not as stable as pure UV-poly(bis-DenPC) bilayers, there was ion channel function. It had been found that incorporating as little as 1/8 DPhPC (mol fraction) into a bis-DenPC bilayer was enough to allow ion channel function. Cataloging the diffusion characteristics of the same bis-DenPC/DPhPC mixtures studied previously (pure bis-DenPC, 7:1, 3:1, 1:1 bis-denPC/DPhPC, and pure DPhPC) could shed some more light on the types of fluidity required to conserve ion channel function.

5.2.1.4 Measuring Diffusion in a BLM Geometry

Finally, the last big difference between the works of Subramaniam and Heitz and that presented here is the geometry of the bilayer.^{43, 77, 78, 83-86, 188} While the other authors

worked with BLMs, essentially, the work here was done on PSLBs. PSLBs are interfaced with solution on one side and glass (with an intermediate solution layer) on the other, whereas BLMs have solution on both sides. It has been noted by others that different bilayer geometries (BLM vs vesicles vs PSLBs) can lead to differences in diffusion coefficient.^{192, 193} As a result, it is proposed that FRAP should be performed on BLMs under the same polymerization and experimental conditions as the studies done by Heitz et al.^{43, 77, 78, 86} Also, mixtures of DPhPC and bis-DenPC were used in some experiments and those same mixtures should be investigated by FRAP.

Pure diffusion and combined diffusion and electrical measurements have been carried out on BLMs ranging in size from 7 μm to 300 μm .¹⁹²⁻¹⁹⁵ The larger diameter BLMs could be compatible with the FRAP system used in Chapters 2 and 3. Pure DPhPC in a BLM format has already been investigated and resulted in a diffusion coefficient value of $14 \pm 1 \mu\text{m}^2/\text{s}$.¹⁹³ The diffusion characteristics of the mixtures that Heitz et al. investigated and pure bis-DenPC have not been quantified yet. All measurements and UV-polymerization were carried out at room temperature, which is very close to the T_m of bis-DenPC. This would be the most accurate way to define the fluidity required to maintain ion channel function.

5.2.2 Measuring Obstacle Fraction to Determine the Percolation Threshold

The concept of the percolation threshold was used to justify the categorization of the lipids shown in Figure 1.19 in Chapter 3. Okazaki et al. measured the obstacle fractions of lipid bilayers made of polymerized diynePC and EggPC using ellipsometry and fluorescence.⁶⁰ Okazaki's bilayers were formed by first creating a pure diynePC

bilayer and UV-polymerizing it at different UV doses and then rinsing away non-polymerized lipid using SDS. Finally, the gaps left in the PSLBs by non-polymerized lipids were filled in with vesicle-fused EggPC.

Ellipsometry was done in air on the polymerized and rinsed diynePC PSLBs (without the addition of non-polymerizable lipids to fill in the gaps) on silicon. This gave an average estimate of the bilayer thickness. Fluorescence samples were prepared by incorporating 1 mol% fluorophore into the EggPC vesicles and then fusing with the polymerized (and rinsed) partial bilayers. The fluorescence intensity was found to scale linearly with the ellipsometric thickness of the diyne bilayer. Based on these two parameters, the authors were able to make an estimate of the obstacle fraction. Interestingly, at maximum polymer coverage, there was a measurable fluorescence, suggesting that the polymer never completely covers the surface. QCM-D was used to verify that this residual fluorescence was not a result of adsorbed fluorophore on the surface.

It would be useful to try a similar set of experiments to investigate lipid mixtures of a non-polymerizable lipid and a polymerizable lipid, similar to the compositions Heitz used,^{77, 86} to try to correlate the diffusion behavior with obstacle fraction. This would help determine if the percolation threshold arguments made in Chapter 3 are valid.

Ellipsometric measurements were performed on a number of UV- and redox-polymerized PSLBs formed from the polymerizable lipids shown in Figure 1.19 by Ross et al.⁶² Not all of the PSLBs in Chapter 3 were investigated by ellipsometry, however, including UV-polymerized bis-DenPC, which formed the most stable membrane in the

electrophysiology experiments. Based on Ross' data and the data in Chapter 3, bis-DenPC did not survive sonication in surfactant and no immobile films were found composed of bis-DenPC. UV-poly(bis-DenPC), however, was not investigated by ellipsometry and was also found to be less fluid than redox-poly(bis-DenPC), meaning that the results of experiments outlined in Section 5.2.1.2 may indicate that bis-DenPC is actually a good system. In the meanwhile though, it has been shown that bis-SorbPC can form immobile PSLBs already and withstand sonication in surfactant, making it a good candidate for this work if bis-DenPC does not meet the requirements.

Performing the same types of ellipsometric, fluorescence, and FRAP measurements as Okazaki on mixtures of bis-SorbPC (or preferably bis-DenPC) and DPhPC to determine if the diffusion behavior of the systems investigated in Chapter 3 are a result of obstacle fractions below or above the percolation threshold would be beneficial. It is predicted that mixtures of polymerized bis-SorbPC and DPhPC will be able to create PSLBs with all three of the fluidity categories outlined in Section 3.3.6, because pure bis-SorbPC redox-polymerized can make immobile films and pure DPhPC is quite fluid. Using these different obstacle fractions then, made as depicted in Figure 5.1 based on Okazaki's work, the diffusion coefficient (or percent recovery) can be plotted as a function of area obstacle fraction to see if three regions of behavior are found (which would hopefully correlate to fluid, partially fluid, and immobile films) as were for Okazaki and Ratto.^{60, 142}

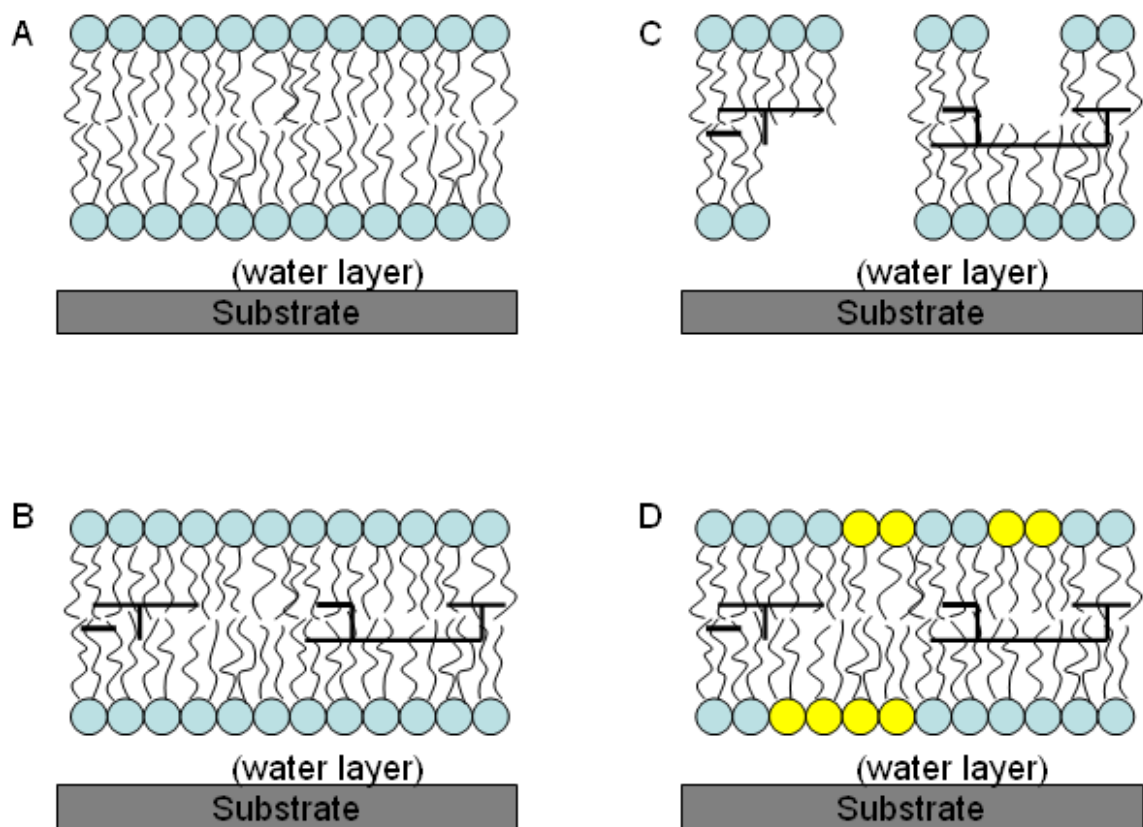


Figure 5.1. Method for preparing mixed bilayers, based on the work of Okazaki et al.⁶⁰

A) A bis-SorbPC PSLB is fused on a substrate by vesicle fusion. Blue lipids are bis-SorbPC. B) Redox-polymerization for different times is used to create partially (or completely) polymerized bis-SorbPC PSLBs. C) The unpolymerized bis-SorbPC monomers are removed by surfactant. D) DPhPC vesicles are fused into the partial bilayer to fill in the gaps. Yellow lipids are DPhPC.

5.2.3 Mechanical Properties of Immobile Bilayers

All of the GUV experiments described in Chapter 4 were performed on fluid or partially fluid bilayers, according to the bilayer designations of Chapter 3. For comparison, it would be useful to measure the mechanical properties of GUVs composed of immobile bilayers. Discher et al. showed that once a critical cross-linking threshold was crossed, the GUVs became much stronger.¹⁴⁴ Below that threshold, however, weaker GUVs were found. These measurements require the use of an osmometer to adjust the osmolarity inside and outside of the GUVs, because redox-polymerization was attempted for mono-DenPC at T_m , but the GUVs all lysed before measurements were able to be taken. It is suspected that these measurements failed because the osmolarity was too imbalanced between the insides and outsides of the GUVs. If GUVs of redox-polymerized lipids could be formed and μ PA measurements performed, it would be helpful to know if an increase in strength could be correlated with the formation of larger polymers, or if one to two polymerizable units per lipid is simply too few to actually create a thin, solid-like shell that is hypothesized in Discher's work.¹⁴⁴

APPENDIX A: SPREADSHEETS FOR FRAP CALCULATIONS

A number of spreadsheets were used for calculating values in FRAP experiments. They are shown in this Appendix and explained.

A.1 Spreadsheets for Calculating w

Figure A.1 is a screen shot of the Microsoft Excel spreadsheet used to calculate the half-width at $1/e^2$ of a Gaussian bleached spot. As described in Section 2.3.2.1, the cross-section through the center of the bleached spot was converted to ASCII and then a text file. The pixel number is in column A, while column B has the intensities. Column C, “radius”, refers to the number of pixels from the defined center of the Gaussian and is calculated for cell C3 as

$$C3=ABS(I\$5-A3) \quad (A.1)$$

where the “center” is cell I\$5. The rest of column C is calculated similarly. With the exception of the top two cells in column D, those values are the “adjusted intensity”. To get “adjusted intensity”, the corresponding value in column B is subtracted from the number in cell D\$1. The number in cell D\$1 is the best guess at the baseline intensity in the vicinity of the bleached spot. The plot in Figure A.1 shows “adjusted intensity” is about zero, as seen in the plot in Figure A.1. Column E, “fit”, is the calculated fit to the Gaussian equation (2.1) as a function of “radius”, column C.

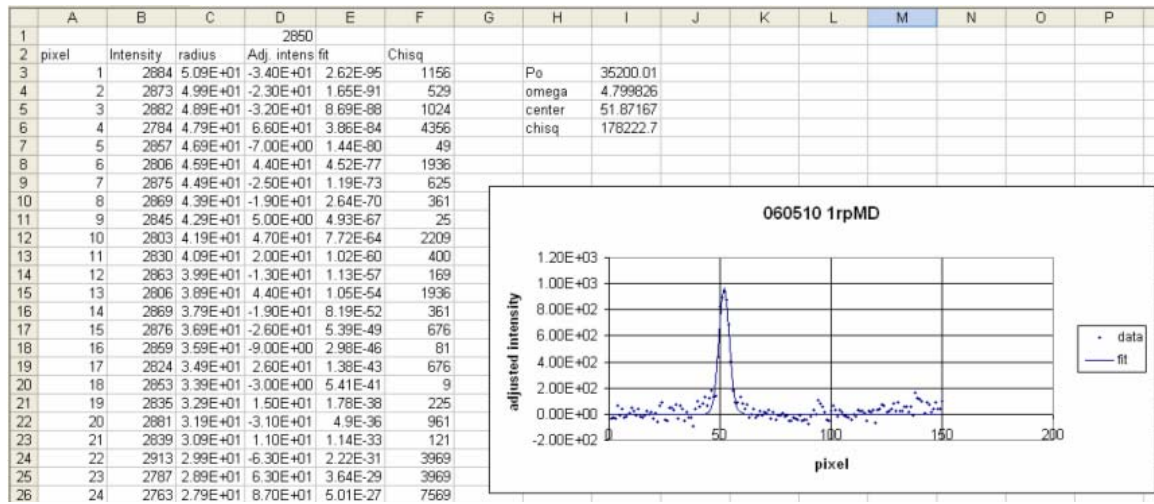


Figure A.1. Example of a Gaussian fit to a bleached spot in FRAP.

The Excel equation is as follows for cell E3:

$$E3=(2*(I\$3(EXP(-2*((C3^2)/(I\$4^2)))))))/(3.14159265*(I\$4^2)) \quad (A.2)$$

where I\$3, “Po”, is the total laser power and I\$4 is w. The remainder of column E is calculated likewise. Column F, “Chisq”, is the square of the difference between the values in columns D and E. Cell I\$6, “chisq” is the sum of the defined values in column F. I\$6 may very well not be all of the values in column F due to the convolution of the lamp profile with the bleached spot. It has been beneficial to restrict the values summed in I\$6 to be only those encompassing the Gaussian. For example, in the plot in Figure A.1, I\$6 is restricted to cells F27:F77. In cases where there is a lot of interference from adsorbed vesicles or the lamp profile, this restriction will give a more reasonable fit than if the entirety of column F were summed. Due to changes in ROI size and the use of different objectives, though, it was found to be easier to simply adjust the cell range in I\$6 than to delete large portions of data in the spreadsheet.

To fit the data, first the value in D\$1 is set by eye to give the best baseline. Then the values of “center”, Po, and w are guessed to try and overlap the fit in the plot to the actual data. Then Solver in Excel is used to improve the fit by changing “center”, Po, and w to minimize “chisq” (I\$6). If a completely ridiculous fit is given, evidenced by the fit and data not overlapping well in the plot, adjusting the cell range summed in I\$6 can help.

A.2 Spreadsheet for ROIs and w Conversion

After w is known, it is handy to keep track of the center point of the bleached spot and also what ROIs will be used for further calculations. Figure A.2 is a screen shot of the spreadsheet used to keep track of these variables. Column A is for the particular sample run. Column B has the coordinates of the bleached spot center. This is useful for remembering what column or row had been used to determine w and also to decide what the ROI area should be. Column C is the calculated w in pixels from the spreadsheet in A.1. Column D is w in microns. In the example shown in Figure A.2, the 20x objective was used. Previously, it had been determined that the distance from the center of one pixel to a neighboring pixel is $\sim 1.2 \mu\text{m}$ for 20x. This scaling factor is employed in column D to obtain w in microns. Columns E and F are the x and y ranges, respectively, for the bleached spot ROI. In the example shown in Figure A.2, w was ~ 10 pixels. Based on the findings in Section 2.3.3.3, the width of the ROI needs to be equal to or slightly less than w . Since fractions of pixels cannot be used, the center coordinates take up the central pixel, meaning that all ROIs have an odd number of pixels for their width. If w is 10 pixels, the ROI width is 9 pixels, centered around the value in column B. Columns G and H are the x and y ranges of the reference ROI, respectively. The reference and bleached ROIs are the same size. Finding the correct reference ROI is more tricky, though. As explained in Section 2.4.3.2, the average intensities of the reference and bleached pre-bleach ROI need to be as close as possible to within 1% of each other to get the best fit to mathematical models.

	A	B	C	D	E	F	G	H	I	J	K
1			radius	radius						sample	reference
2	file	center	(pixels)	(microns)	sample x	sample y	ref x	ref y	comment	avg +/- stdev	avg +/- stdev
3	1pMD	40,52	10.12	12.144	36-44	48-56	50-58	120-128	ND4+8		
4	2pMD	39,52	7.319	8.7828	36-42	49-55	35-41	130-136	ND4+8		
5	3pMD	39,52	7.281	8.7372	36-42	49-55	85-91	130-136	ND4+8		
6	4pMD	39,52	7.393	8.8716	36-42	49-55	35-41	105-111	ND4+8		
7	5pMD	39,52	10.43	12.516	36-42	49-55	30-36	120-126	ND4+8		
8	6MD		10.505	12.606					ND4+8		
9	7MD		8.596	10.3152					blank ND4+8	635.34 +/- 0.91	636.46 +/- 0.88
10	8MD		8.596	10.3152					control ND4+8		
11											

Figure A.2. Spreadsheet for w conversion and ROI determination.

Basically, random, uniformly fluorescent spots far away from the bleached ROI were checked for their pre-bleach average intensities until one was found that was close enough to the value of the pre-bleached spot. The spreadsheet in Figure A.3 automatically calculates the initial ratio. This spreadsheet is explained in Section A.3. Column I, “comment”, was generally used to keep track of which neutral density filters were used and whether the run was a blank or some other type of control. Columns J and K were for tabulating blank or control average intensities for the bleached and reference spots, respectively.

A.3 Initial Ratio and γ_D Calculation and Spreadsheets

The spreadsheet in Figure A.3 is for calculation of the initial ratio used to scale the recovery curve to have 100% recovery equal to a fluorescence intensity ratio of 1. Column A is the sample name. Columns B and C are the pre-bleach average intensity values in the bleached and reference ROI, respectively. Columns D and E are the corresponding background values. Finally, column F is the background subtracted initial intensity ratio found by

$$F3=(B3-D3)/(C3-E3) \quad (A.3)$$

for cell F3.

The spreadsheet in Figure A.4 is for calculation of γ_D . It is part of the same Excel sheet as Figure A.3, which is why the screen shot starts at column H, the sample name. Column I is the first post-bleach average intensity value of the bleached ROI. Column J is the background intensity for the bleached ROI. Column K, “t<0”, is actually

$$K3=B3-D3 \quad (A.4)$$

referring to values in Figure A.3. It is the background subtracted pre-bleach average intensity value of the bleached ROI. Column L, “t(0)”, is

$$L3=I3-J3 \quad (A.5)$$

or the first background subtracted post-bleach average intensity of the bleached ROI.

Column M, “t(0)/t(<0)” is

$$M3=L3/K3 \quad (A.6)$$

the ratio of the first post-bleach average intensity to the pre-bleach average intensity in the bleached ROI, or the y-axis value of the first point on the recovery curve.

	A	B	C	D	E	F
1	Initial Values			Bkgd Values		ratio w/
2		sample	reference	sample	reference	bkgd sub.
3	1pMD	2185.15	2224.43	634	634	0.9753023
4	2pMD	2338.29	2353.65	634	634	0.9910679
5	3pMD	2370.59	2348.57	634	634	1.0128429
6	4pMD	2209.71	2260.73	634	634	0.9686365
7	5pMD	2056.86	2086.1	634	634	0.9798636
8	6MD	2111.72	2116.17	634	634	0.9969976
9	8MD	2170.45	2172.63	634	634	0.9985832
10			avg	634	634	0.989042
11			stdev	0	0	0.015353

Figure A.3. Initial ratio calculation spreadsheet.

H	I	J	K	L	M	N	O
	yD	avg.					
	s(t(0))	bkgd(t(0))	t<0	t(0)	t(0)/t(<0)	K axelrod	yD Axelrod
1pMD	1427.41	634	1551.15	793.41	0.5114979	1.53	1.1
DOPC2	4250.27	841	1704.29	3409.27	2.0004049	1.33	1.1
DOPC5	3619.2	841	1736.59	2778.2	1.5998019	1.41	1.1

Figure A.4. Spreadsheet for the calculation of γ_D .

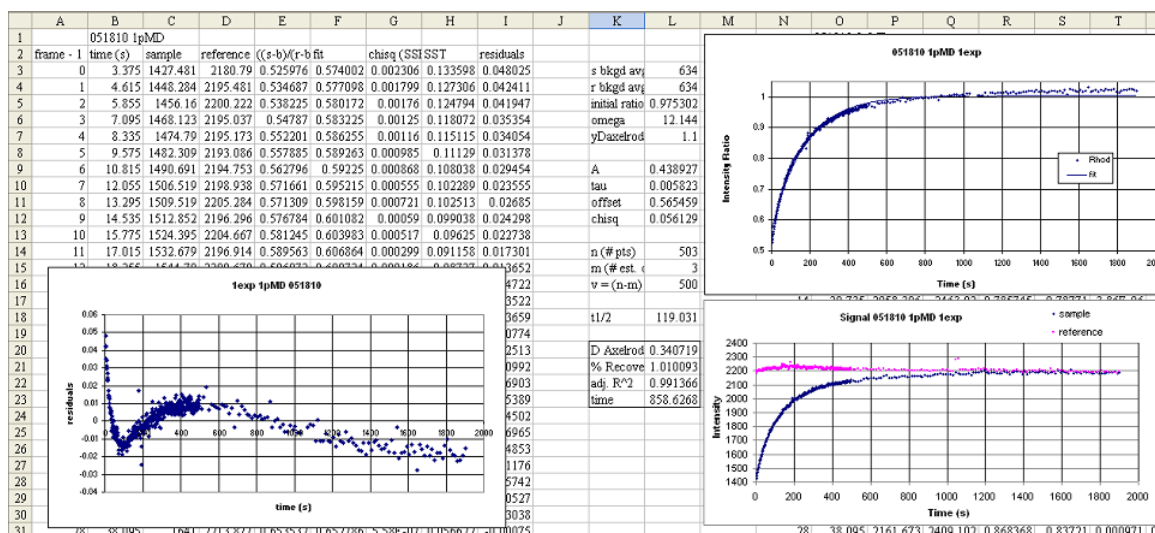
This value is $F_{\kappa}(0)/F_{\kappa}$ from Axelrod's method.¹⁰³ Based on this value, κ , a.k.a. the amount of bleaching, can be determined and entered into column N. Figure 2.9 shows the relationship between κ and $F_{\kappa}(0)/F_{\kappa}$ ("t(0)/t(<0)" in Figure A.4). Those values had been tabulated for easier determination. Once κ is known, then γ_D can be found from Axelrod's Figure 7 and included in column O. The values of γ_D were always found to be 1.1-1.2, with 1.1 (having a $\kappa < \sim 1.8$) being used the vast majority of the time.

A.4 Single-exponential Data-fitting Spreadsheet

Once w , the initial ratio, the background values [constant for FRAP (rhodamine-PE)], and γ_D are determined, the recovery curves can be created and the D and % recovery calculated. Figure A.5 shows the spreadsheet used to find these values. The values found in previously described spreadsheets are entered into cells 3-7 in column L. L\$3 and L\$4 are background values for the bleached and references spots (respectively) and L\$5 is the initial ratio. L\$6 is w in microns. Finally, γ_D is entered into L\$7. Column A is the frame value from the Winspec/32 files minus 1, which is used for calculating the times in column B (described in Section 2.4.3.6). As can be deduced from the frame values at the end of column A and the row numbers seen in the bottom portion of Figure A.5, more than one file was used to construct this recovery curve, as explained in Section 2.4.2. When calculating the time, cell B3 is the first recorded file time in seconds plus half of the acquisition time. The following equation is used for the rest of the column B cells to determine times:

$$B4=B3+(1.265*A4) \quad (A.7)$$

where the number multiplied by A4 is the guessed interval between the frames, which is always larger than the delay time plus the acquisition time, because of the CCD readout time. To check if the correct interval was used, the final time point for the file is compared to the recorded end time. The interval is then changed accordingly. Columns C and D are the bleached and reference values extracted from the files by the Java program using the defined ROIs assigned in the spreadsheet from Figure A.2.



	A	B	C	D	E	F	G	H	I
502	99	1834.61	2191.16	2194.037	1.023433	1.004376	0.000363	0.01741	-0.01906
503	100	1848	2188.926	2191.136	1.023868	1.004377	0.00038	0.017525	-0.01949
504	101	1861.39	2189.272	2187.222	1.026676	1.004377	0.000497	0.018276	-0.0223
505	102	1874.78	2194.148	2192.494	1.026411	1.004378	0.000485	0.018205	-0.02203
506	103	1888.17	2182.198	2184.741	1.023642	1.004379	0.000371	0.017465	-0.01926
507	104	1901.56	2189.519	2198.037	1.019739	1.004379	0.000236	0.016449	-0.01536
508				average da	0.891487	0.565459	sum SST	6.527224	
509					est. t = 0				

Figure A.5. Screen shot of the spreadsheet (top and bottom portions) used to create recovery curves and calculate D, % recovery, and $5 \times 1/\tau$ for a single-exponential fit. The upper right plot is the recovery curve with fit. The lower right plot is the raw data for the bleached and reference spots. The lower left plot shows the residuals to the fit.

The plot in the lower right of the top portion of Figure A.5 presents the raw intensity data as a function of time for both the bleached and reference spots. The numerical values in column E from E\$3 to E\$507, which have the heading “((s-b)/(r-b))/ratio”, are the background subtracted and normalized fluorescence intensity ratios. The equation used is

$$E3=((C3-L$3)/D3-L$4)/L$5 \quad (A.8)$$

for cells E\$3 to E\$507. E\$508 is the average value for column E from E\$3 to E\$507.

The values in column F (F\$3 to F\$508) are the fit values for each time point and are found by

$$F3=(L$9*(1-(EXP(-((L$10*0.001)*B3)))))+L$11 \quad (A.9)$$

where L\$9-L\$11 are part of the fits to equation (2.3). Specifically, L\$9 is the recovered fraction, A. L\$10 is τ , the time constant. L\$11 is labeled “offset” and is the unbleached fraction. The factor of 0.001 in the column F equation is used to adjust for the magnitude difference between the values of τ and A (and “offset”). It was found, through trial and error, that when τ gets very small, Solver has a problem manipulating the values in L\$9-L\$11, because A and “offset” are so much larger. So, by making the value written in L\$10 a thousand times larger and dividing by 10^3 in the actual equation, the values that Solver changes are near each other in terms of absolute value. For fast diffusion, where τ is large, the factor of 0.001 in the equation does not make a difference, but for slow diffusion, better fits are found with the 0.001 factor included. However, if 0.001 is not used, care must be taken to appropriately adjust the later equations used to determine the diffusion coefficient to make sure they are the correct order of magnitude. For the purposes of this Appendix, 0.001 will be left in and all of the subsequent calculations will

be presented appropriately for that scaling factor. The value in cell F\$508 is basically the value of the F column equation if time was equal to zero. The upper right plot in Figure A.5 is the recovery curve and the fit. At first, the values in L\$9-L\$11 are manually changed to try to best fit the data by visually comparing the traces in the recovery curve plot. Column G, “chisq (SSE)”, is the difference between columns F and E squared. The sum of the active cells in column G is found in L\$12 by varying the values in L\$9-L\$11. Column H, “SST”, is used for calculating a reduced R^2 value to help assess the goodness of fit. Values in column H are found using

$$H3=(E3-E\$508)^2 \quad (A.10)$$

except for H\$508, which is the sum of column H. Finally, column I shows the residuals and is column F minus column E. The plot on the lower left of the upper half of Figure A.5 shows the residuals as a function of time. There is a clear, systematic deviation from the best fit in this particular example.

Cells L\$14-L\$16 are also used for determining the R^2 value. L\$14, “n(# pts)”, is the total number of data points in the dataset. If points were deleted due to instrumental errors or in cases where non-PSLB fluorescent material swam past the ROIs, that must be reflected in the value entered into L\$14. L\$15, “m (# est. coeffs)”, in the case of the single-exponential fit is always 3 since Solver is allowed to fit the time constant, A, and “offset”. L\$16, “n-m” is L\$14 minus L\$15. The half-recovery time is calculated in L\$18, “t1/2”. It is found by

$$L\$18=-(\text{LN}(0.5))/(\text{L\$10}*0.001) \quad (A.11)$$

where the 0.001 factor accounts for the scaling used in the fit equation. At long last, the values in L\$20-L\$23 are the results. “D Axelrod”, L\$20, is the diffusion coefficient in $\mu\text{m}^2/\text{s}$ found using

$$\text{L\$20} = ((\text{L\$6}^2) * \text{L\$7}) / (4 * \text{L\$18}) \quad (\text{A.12})$$

“% Recovery”, L\$21, is the percent recovery divided by 100%, so it is actually the fraction of recovery as shown. It is calculated by

$$\text{L\$21} = \text{L\$9} / (1 - \text{L\$11}) \quad (\text{A.13})$$

The value found in L\$22, “adj. R^2 ”, is the determined goodness of fit by

$$\text{L\$22} = 1 - ((\text{L\$12} * (\text{L\$14} - 1)) / (\text{H\$508} * \text{L\$16})) \quad (\text{A.14})$$

In the example given in Figure A.5, R^2 is greater than 0.991, which is good because the best R^2 value is 1.00. The last calculated value in the spreadsheet is L\$23, “time”, which is

$$\text{L\$23} = 5 * (1 / \text{L\$10} * 0.001) \quad (\text{A.15})$$

where 0.001 is again adjusting for the scaling factor used in the single-exponential fit equation for the time constant. This is the length of time in seconds that the experiment had to be run to properly account for the calculated time constant as described in Section 2.3.2.7. The example in Figure A.5 had to run ~ 860 s to truly account for the time constant of 0.0058 s^{-1} used to fit the data.

A.5 Double-exponential Data-fitting Spreadsheet

As evidenced in the residuals plot found in Figure A.5, there was systematic deviation in the single-exponential fit, meaning that the behavior of the PSLB in the sample was not being properly modeled. This was the case in nearly all of the FRAP samples investigated. A way to accommodate for this was by assuming two populations of diffusing species with different diffusion coefficients and using the double-exponential equation (2.7). Figure A.6 is a screen shot of the spreadsheet used to employ the double-exponential model. It is similar to the single-exponential fit, with exceptions that will be discussed. Column F, “fit”, uses the following equation:

$$F3=1(L\$8+(L\$9*(EXP(-((L\$10*0.01)*B3))))+(L\$11*(EXP(-((L\$12*0.001)*B3)))))) \quad (A.16)$$

The terminology for the fit parameters is a little confusing because of the way equation (2.7) is written. L\$8 (titled “A”) is actually C from equation (2.7), the unrecovered fraction. L\$9, “B”, is D from equation (2.7), the fraction of the dye population diffusing with the fast diffusion coefficient. L\$10 (“tau1”) is τ_1 , the time constant of the fast diffusion coefficient. L\$11, “C”, is E from equation (2.7) and is the fraction of the dye population diffusing with the slow diffusion coefficient. The time constant of the slow diffusion coefficient, τ_2 , is L\$12 (“tau2”). Again, L\$10 and L\$12 are multiplied by factors of ten to assist Solver in fitting the equation for column F, as was done in Section A.4. Another difference is L\$16, “m (# est. coeffs)”. L\$16 equals 5 for double-exponential fits because 5 parameters are being changed.

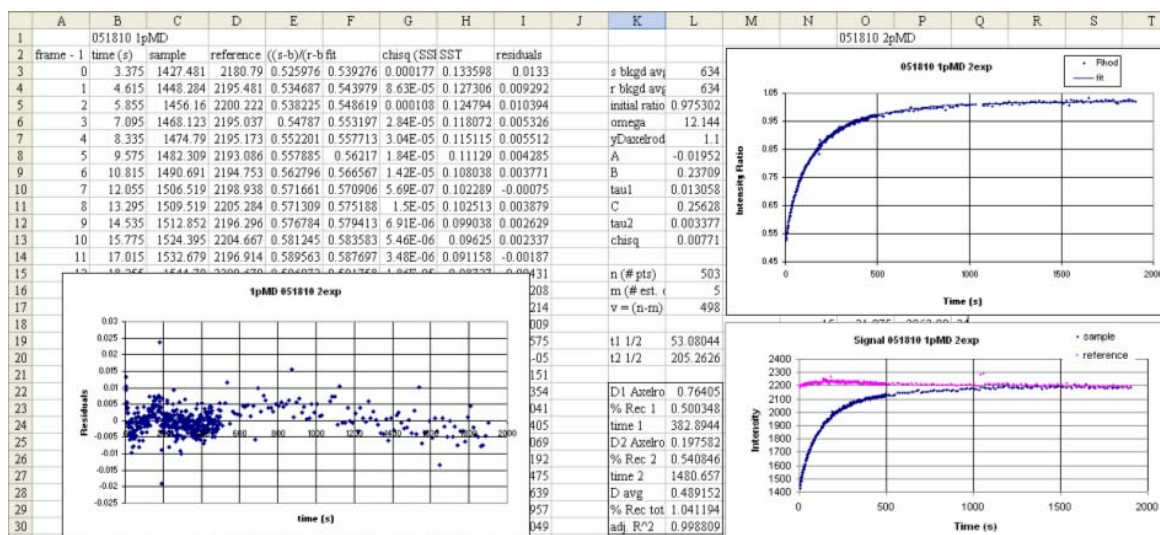


Figure A.6. Screen shot of the spreadsheet used to create recovery curves and calculate diffusion coefficients, percent recoveries, and $5 \times 1/\tau$ values for a double-exponential fit. The upper right plot is the recovery curve with fit. The lower right plot is the raw data for the bleached and reference spots. The lower left data shows the residuals of the fit.

Because there are two diffusion coefficients, there are two half-times for recovery. For the fast and slow diffusion portions, L\$19 (“t1 1/2”) and L\$20 (t2 1/2”), respectively, calculate the half-times for recovery as will be explained next. For the fast recovery, the half-time is

$$L\$19 = -(\ln(0.5)) / (L\$10 * 0.01) \quad (A.17)$$

For the slow recovery, the half-time is

$$L\$20 = -(\ln(0.5)) / (L\$12 * 0.01) \quad (A.18)$$

In both instances, the scaling factors in the fit parameters are adjusted for by multiplying by the appropriate factors of ten.

L\$22-L\$30 are the values of interest. The fast diffusion coefficient, “D1 Axelrod”, is L\$22 and is calculated by

$$L\$22 = ((L\$6^2 * L\$7) / (4 * L\$19)) \quad (A.19)$$

The fraction of the dye population associated with the fast recovery is L\$23, “%Rec 1”, and is found using

$$L\$23 = L\$9 / (L\$8 + L\$9 + L\$11) \quad (A.20)$$

The time needed to observe the entire fast recovery is found in L\$24, “time 1”, as follows:

$$L\$24 = 5 * (1 / (L\$10 * 0.01)) \quad (A.21)$$

The slow diffusion coefficient, “D2 Axelrod”, is L\$25, and is determined by

$$L\$25 = ((L\$6^2) * L\$7) / (4 * L\$20) \quad (A.22)$$

The fraction of the dye population associated with the slow recovery is L\$26, “% Rec 2”, and is calculated with

$$L\$26=L\$11/(L\$8+L\$9+L\$11) \quad (A.23)$$

The time needed to observe the entire slow recovery is L\$27, “time 2”, and can be determined using

$$L\$27=5*(1/(L\$12*0.001)) \quad (A.24)$$

To make comparisons between different double-exponential fits easier, a weighted average diffusion coefficient was employed and calculated in L\$28, “D avg” by

$$L\$28=(L\$22*L\$23)+(L\$25*L\$26) \quad (A.25)$$

The overall recovered fraction is found in L\$29, “% Rec tot”, using

$$L\$29=(L\$9+L411)/(L\$8+L\$9+L\$11) \quad (A.26)$$

Finally, L\$30, “adj. R²”, is a measure of the goodness of fit, using the single-exponential goodness of fit equation. Although it was not certain that this R² value was appropriate for double-exponentials as well as single-exponentials, it was noted that visually better double-exponential fits corresponded to R² values nearer to 1.00. The equation used to get R² is the same as for a single-exponential, but references different cells:

$$L\$30=1-((L\$13*(L\$15-1))/(H\$508*(L\$17)) \quad (A.27)$$

The plots in Figure A.6 are the same as in Figure A.5, including the dataset, except that they are for the double-exponential instead of the single-exponential fit. Figure A.6 shows a better distribution of residuals than those in Figure A.5 for the single-exponential fit. Also, the R² value for the double-exponential was better (0.999 vs 0.991). Additionally, because the single-exponential diffusion coefficient was some sort of average between the slow and fast diffusion coefficients from the double-exponential,

the time required to observe the entire recovery in the double-exponential was longer with a “time 2” of nearly 1500 s (vs ~860 s for a single-exponential).

APPENDIX B: ATTEMPTED LIGHT-INDUCED PROTON-PUMPING ACROSS A PSLB

B.1 Introduction

This project was focused on adapting the biomimetic, transmembrane, proton-pumping architecture developed by Moore, Gust, Moore and coworkers from a vesicle geometry to a planar geometry.^{196, 197} The hope was that solar-powered energy storage devices could be constructed using a biomimetic approach.

B.1.1 Biomimetic Proton-pumping

Moore, Gust, and Moore have worked for decades to develop artificial photosynthetic reaction centers.^{198, 199} One of their most successful attempts was using a carotenoid-porphyrin-quinone molecule, which will be referred to as C-P-Q.¹⁹⁶ Figure B.1 shows the structure of C-P-Q. Upon photoexcitation of the porphyrin in C-P-Q, the molecule will undergo a series of step-wise electron transfers, which will eventually result in the charge-separated species, $C^{+}\text{-P-Q}^{-}$. C-P-Q can be vectorially inserted into vesicles, because of the long, oily carotenoid moiety. The quinone moiety will be near the external aqueous solution, while the carotenoid will be closer to the internal aqueous compartment. A “proton shuttle”, benzoquinone (Q), can also be inserted into the lipid membrane of the same vesicle as C-P-Q. The structure of Q is shown in Figure B.1.

Once both Q and C-P-Q molecules are inserted into the membrane, photo-induced proton-transport across the lipid membrane can take place,¹⁹⁶ as will be described briefly. Light is absorbed by the porphyrin in C-P-Q and charge separation takes place to form the $C^{+}\text{-P-Q}^{-}$ species.

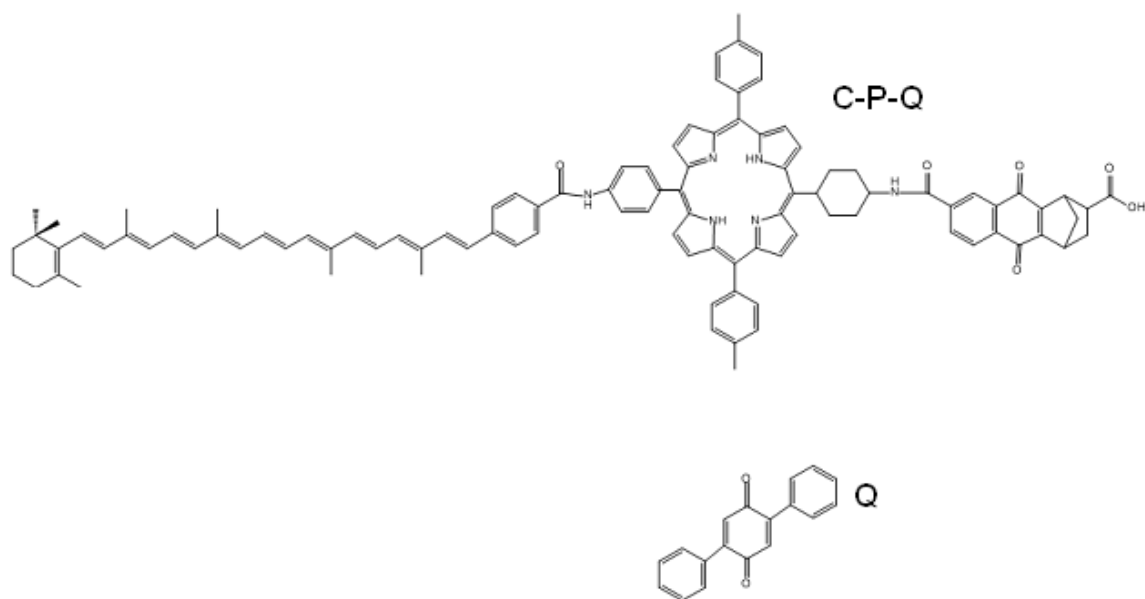


Figure B.1. Chemical structures of C-P-Q and Q.

The quinone molecule is reduced at the outer edge of the lipid membrane by the radical quinone anion moiety of C-P-Q, leading to $C^{\cdot+}$ -P-Q and $Q^{\cdot-}$. $Q^{\cdot-}$ is protonated by the external solution to form Q-H, which can then diffuse through the membrane towards the inner aqueous compartment of the vesicle. Then, Q-H can reduce the carotenoid of $C^{\cdot+}$ -P-Q, leading to C-P-Q and Q^+H . Q^+H can deprotonate into the inner aqueous compartment. The net affect of this series of reactions is the acidification of the internal vesicle solution, which was measured by Steinberg-Yfrach and coworkers.¹⁹⁶ Later, the authors went a step further and used the same architecture to drive the production of ATP by incorporating F_0F_1 -ATP synthase into the vesicles with Q and C-P-Q.^{197, 199} ADP and inorganic phosphate were added to the external vesicle solution. F_0F_1 -ATP synthase requires a proton gradient across the lipid bilayer to drive the production of ATP from ADP and phosphate. By exposing the vesicles to light and generating the pH gradient with C-P-Q and Q, ATP production was observed.

In essence, our role in this project was to adapt the lipid membrane/Q/C-P-Q architecture to a planar surface with the aim of creating biomimetic energy conversion devices. First, to prove that proton-pumping could be carried out in a planar geometry using Q and C-P-Q in a PSLB, a substrate was needed that could both support a PSLB and also detect changes in pH. Towards this end, coupling layers between lipids and indium-tin-oxide (ITO), a transparent electrode, had been investigated.²⁰⁰⁻²⁰² This work will be reviewed in the following Section.

B.1.2 Review of Previous Work with Proton-pumping

Polyaniline (PANI), depicted in Figure B.2, can undergo various protonations and reductions/oxidations. Exposing PANI to different pH solutions changes the equilibrium potential of the ES/EB and LE forms making it an electrochemical pH sensor. The negatively charged surface of ITO can have positively charged PANI (emeraldine base form) deposited onto it, because of electrostatic attraction. PANI, due to its hydrophobic nature, would not couple well to hydrophilic lipid headgroups. As a result, poly(acrylic acid) (PAA), a negatively charged polymer, could be deposited on top of PANI. This was done using layer-by-layer deposition.²⁰³ Optimization of these ITO-PANI-PAA systems was done by previous group members.²⁰⁰⁻²⁰² The most successful geometry is illustrated in Figure B.3 and is denoted ITO/(PANI/PAA)₂. Two different polymer formulations were used (for both PANI and PAA). Linear potential responses were found for the pH 3-9 range.

PSLBs were found to form on ITO/(PANI/PAA)₂ surfaces. After the formation of a PSLB on the ITO/(PANI/PAA)₂ surface, changes in pH did not result in potential changes, suggesting that the PSLB was so uniform and defect-free that protonated species were not able to diffuse through the impermeable membrane. Q was inserted into uniform PSLBs on ITO/(PANI/PAA)₂ films and the PSLBs were still found to be proton-impermeable. To see if Q could shuttle protons across the lipid membrane, ascorbic acid was used to chemically reduce and protonate the Q, which could then diffuse through the lipid membrane towards the ITO/(PANI/PAA)₂ surface and eventually protonate and reduce the PANI. These experiments were successful.

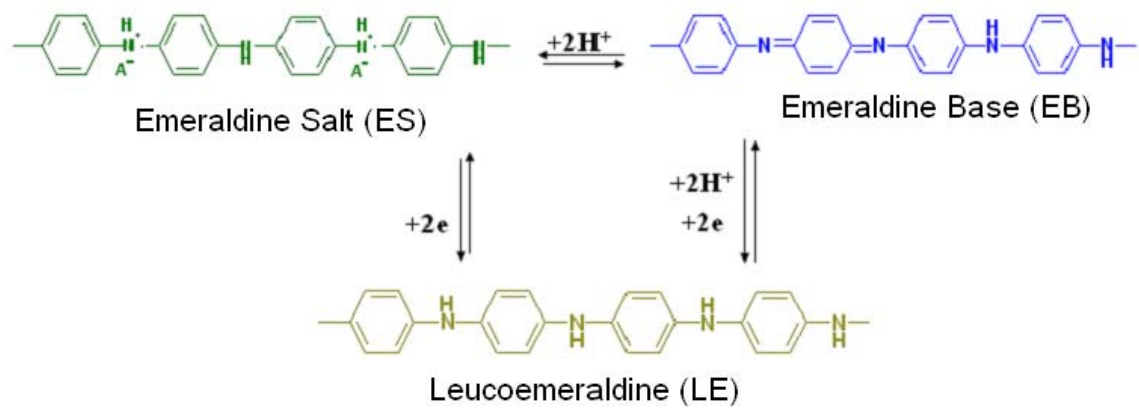


Figure B.2. Important forms of PANI.

PAA
PANI
PAA
PANI
ITO

Figure B.3. ITO/(PANI/PAA)₂ architecture.

The last step in attempting to couple the work of Moore, Gust, and Moore with a planar substrate was repeating the light-induced proton-pumping experiment using the architecture shown in Figure B.4. This was accomplished by McBee,²⁰⁴ who showed that a pH decrease was observed when the films were exposed to light with Q and C-P-Q in the lipid membranes. Unfortunately, this accomplishment was not very repeatable.

B.1.3 Goal

The purpose of the work in this Appendix is to explain attempts to reproduce the work of McBee and Ge.^{200-202, 204, 205} During these experiments, it was determined that the batch of ITO was very important to the success or failure of forming a defect-free PSLB on ITO/(PANI/PAA)₂ films. The data that led to this conclusion will be presented. Sadly, it was found that although ITO can have good electrochemical characteristics and low surface roughness, it did not guarantee successful PSLB fusion onto the surface.

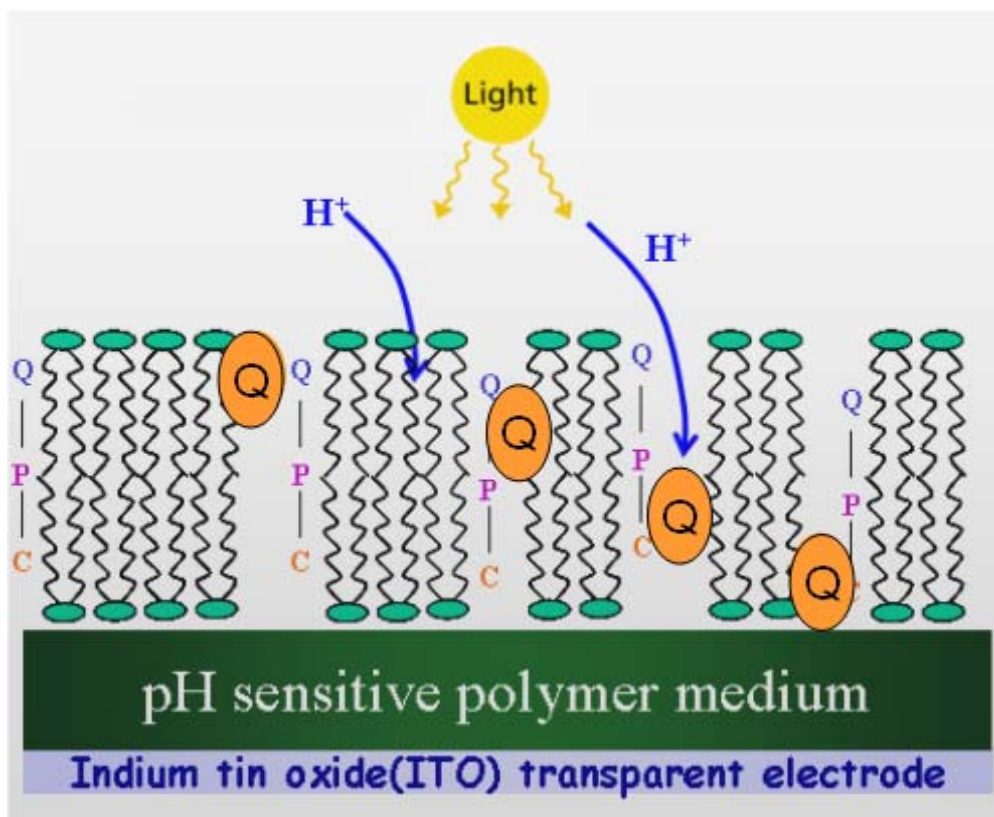


Figure B.4. ITO/(PANI/PAA)₂ with a PSLB fused on top that includes Q and C-P-Q.

B.2 Experimental

B.2.1 Materials and Methods

B.2.1.1 Materials

L- α -phosphatidylcholine (egg, chicken) (EggPC) and NBD-PC (1-palmitoyl-2-{6-[(7-nitro-2-1,3-benzoxadiazol-4-yl)amino]hexanoyl}-*sn*-glycero-3-phosphocholine) were purchased from Avanti Polar Lipids, Inc. (Alabaster, Alabama). 1,4-Benzoquinone from (Aldrich, St. Louis, MO) was used. C-P-Q was provided by our collaborators at Arizona State University. THF and chloroform were purchased from (EMD, Gibbstown, NJ). Polyaniline (PANI), emeraldine base form, M_n 10,000, poly(acrylic acid) (PAA), M_n 2,000, and NMP (1-methyl-2-pyrrolidinone), anhydrous, 99.5% were acquired from Aldrich (St. Louis, MO). Phosphate buffers of varying pH values were made from sodium phosphate monobasic, monohydrate and sodium phosphate dibasic, anhydrous (EMD, Gibbstown, NJ).

Several batches of indium-tin-oxide (ITO) coated glass were used in this work. They are listed in Table B.1.

B.2.1.2 ITO Cleaning

After cutting ITO to 1" x 1" squares, the substrates were briefly sonicated in chloroform to remove the cutting fluid. The substrates were then scrubbed with 1% Liquinox (Alconox, Jersey City, NJ) on a cotton pad, followed by thorough rinsing with nanopure water.

Table B.1. ITO batches.

ITO	Maker	Generation
ITO _A	Colorado Concepts	Earliest
ITO _B	Colorado Concepts	2 nd earliest
ITO _C	Colorado Concepts	Youngest
ITO _D	Delta Technologies	Youngest

The substrates were then sonicated in 1% Triton-X 100 (Sigma-Aldrich, St. Louis, MO), nanopure water, and ethanol for 15 minutes each in a Branson 2210 bath sonicator (Danbury, CT) with nanopure water rinsings between each step. Substrates were stored in ethanol for 1-2 days if needed. Immediately before use, $N_2(g)$ was used to blow the ITO dry. This was followed by air plasma cleaning in a Harrick PDX-3XG sterilizer (Pleasantville, NY) for 15 minutes.

B.2.1.3 Layer-by-layer Deposition

Two general polymer deposition methods were investigated and they will be called ‘aqueous’ and ‘organic’.

The aqueous deposition method used is from Ref. 202. Briefly, 18 mg/ml PANI in 1:9 dimethylacetamide in nanopure water was adjusted to a pH of 2.6 with methylsulfonic acid. PAA was dissolved in water to obtain a final concentration of 0.72 mg/ml. Films were formed by submerging a piece of plasma-cleaned ITO into PANI solution for 15-20 minutes. Then, pH 2.6 methylsulfonic acid was used to rinse the surface, which was then allowed to soak in PAA solution for 15-20 minutes. The surface was rinsed with nanopure water after PAA. One more PANI layer and one more PAA layer were adsorbed to the surface using the same directions for a final film with the following composition: ITO/(PANI/PAA)₂. Films formed by aqueous deposition will be denoted ITO/(PANI/PAA)_{2(aq)}.

The organic deposition method used is from Refs. 201-202. In this case, 1 mg/ml PANI in NMP and 15 mg/ml PAA in nanopure water were used. Rinsing between layers

was always done with nanopure water. Deposition order and times were the same as for the aqueous deposition method. Again, the final film architecture was:

ITO/(PANI/PAA)₂. This architecture will be denoted as ITO/(PANI/PAA)_{2(o)}.

B.2.1.4 PSLB Formation

Vesicles were sonicated and fused, as described in Section 2.1, onto a freshly deposited ITO/(PANI/PAA)₂ surface to form ITO/(PANI/PAA)₂/PSLB. 0.5-1 mg/ml lipid was sonicated in 10 mM phosphate buffer pH 7.0.

B.2.1.5 Q

Benzoquinone (Q) was added into PSLBs by drying 2 mol% Q with EggPC and fusing as described in Section B.2.1.4.

B.2.2 AFM

AFM was done using tapping mode in air on a Digital Instruments Dimension 3100 (Veeco, Plainview, NY) using MikroMasch tips (San Jose, CA) with a resonance frequency of 325 kHz and an average force constant of 40 N/m (product code: NSC15/no Al).

B.2.3 UV-vis Absorbance

UV-vis absorbance was performed on a Spectral Instruments Inc. spectrophotometer (Tucson, AZ) in air.

B.2.4 Electrochemical Cells

Several home-built electrochemical cells were used for experiments. The most commonly used kind is shown in Figure B.5. The window facing the viewer in the photo is the ITO (glass on back side).



Figure B.5. Echem cell hooked up to the pH meter. Red arrow is pointing at flow cell tubing. Photo courtesy of J. Faust.

A brass contact was used to make contact with the working electrode (ITO) surface. A platinum wire counter electrode was used when needed. A Ag/AgCl reference electrode from Bioanalytical Systems (West Lafayette, IN) was also used. Ports had been drilled through the PTFE body to allow for tubing (part number: TSI-S20-1100-NAT, SPC Technology) to be inserted near the glass window to create a flow cell. One of the tubes is clearly visible in Figure B.5. The other tube is indicated with a red arrow. Various peristaltic pumps (PeriStar Pro: World Precision Instruments, Inc., Sarasota, FL and Mini-pump Variable Flow: VWR, Radnor, PA) were used to move solution through the cell as well as using hand injection.

B.2.5 Potentiometry

Potentiometry was performed using a Denver Instrument Model 215 pH meter (Bohemia, NY) connected to the Ag/AgCl aqueous reference electrode and the brass contact electrode, which was in contact with the ITO surface.

B.2.5.1 pH-response

To measure the pH response of the ITO/(PANI/PAA)₂ films, several milliliters of 10 mM phosphate buffer of various pH values were injected and allowed to equilibrate. Potential measurements were recorded by hand as a function of time after injection to verify that equilibrium was reached. Injections were done using a syringe by hand as well as using peristaltic pumps. The orientation of the ITO/(PANI/PAA)₂ film was varied with respect to the inlet and outlet tubing of the echem cell and also with respect to the ground (perpendicular or parallel or upside down).

B.2.5.2 pH-response Blocking Experiments

Blocking experiments were performed the same as pH-response experiments, except that there was a PSLB on the ITO/(PANI/PAA)₂ films. In these cases, a lack of pH-response was considered a success.

B.2.6 Cyclic Voltammetry

The echem cell described in Section B.2.4 was used with working, reference, and counter electrodes using an EG&G potentiostat (Model: 263A, Princeton Applied Research, Oak Ridge, TN). A 50 mV/s scan rate was used for all measurements.

B.2.7 Fluorescence Microscopy and FRAP

Quantitative FRAP experiments were run using the FRAP (NBD-PC) method described in Section 2.3. Qualitative FRAP measurements were also performed as described in Section 2.2.

B.3 Results and Discussion

B.3.1 ITO Characterization

Several batches of ITO (A-D) were used during the course of these experiments. Roughness values and absorbance measurements were used to characterize the ITO.

B.3.1.1 Roughness

Figure B.6 shows examples of AFM height images for the four types of ITO used. The rms roughness for the ITO types are tabulated in Table B.2. Types A and D were similar in roughness and were smoother than types B and C, which were similar to each other.

B.3.1.2 UV-vis Absorbance Spectra

Absorbance spectra of types C and D were taken and are shown in Figure B.7. The difference spectra of C-D is also shown in Figure B.7. The major difference in the absorbance spectra of the two types is the increased absorbance of type C in the vicinity of 300 nm.

B.3.2 Polymer Film Characterization

Cyclic voltammetry (CV) and potentiometry were used to characterize ITO/(PANI/PAA)₂ films.

B.3.2.1 Cyclic Voltammetry of Polymer Films on ITO

Example CVs of ITO/(PANI/PAA)₂ are shown in Figure B.8. Both (o) and (aq) polymer types were investigated. A summary of the peak separation and $E^{0'}$ is in Table B.3.

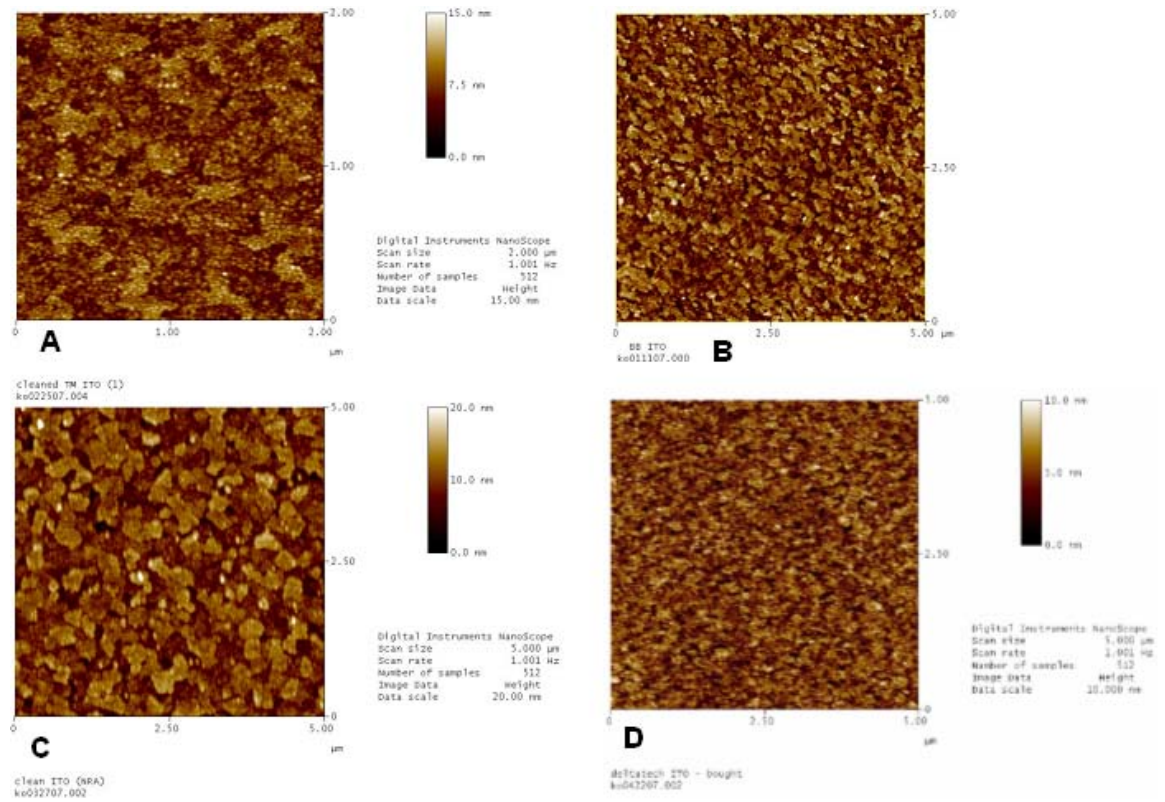


Figure B.6. AFM images of the four ITO batches.

Table B.2. Roughness measurements of different ITO types.

ITO type	rms roughness (nm)
A	1.6 ± 0.22 (7)
B	2.7 ± 0.19 (3)
C	~ 2.52 (2)
D	1.53 ± 0.025 (4)

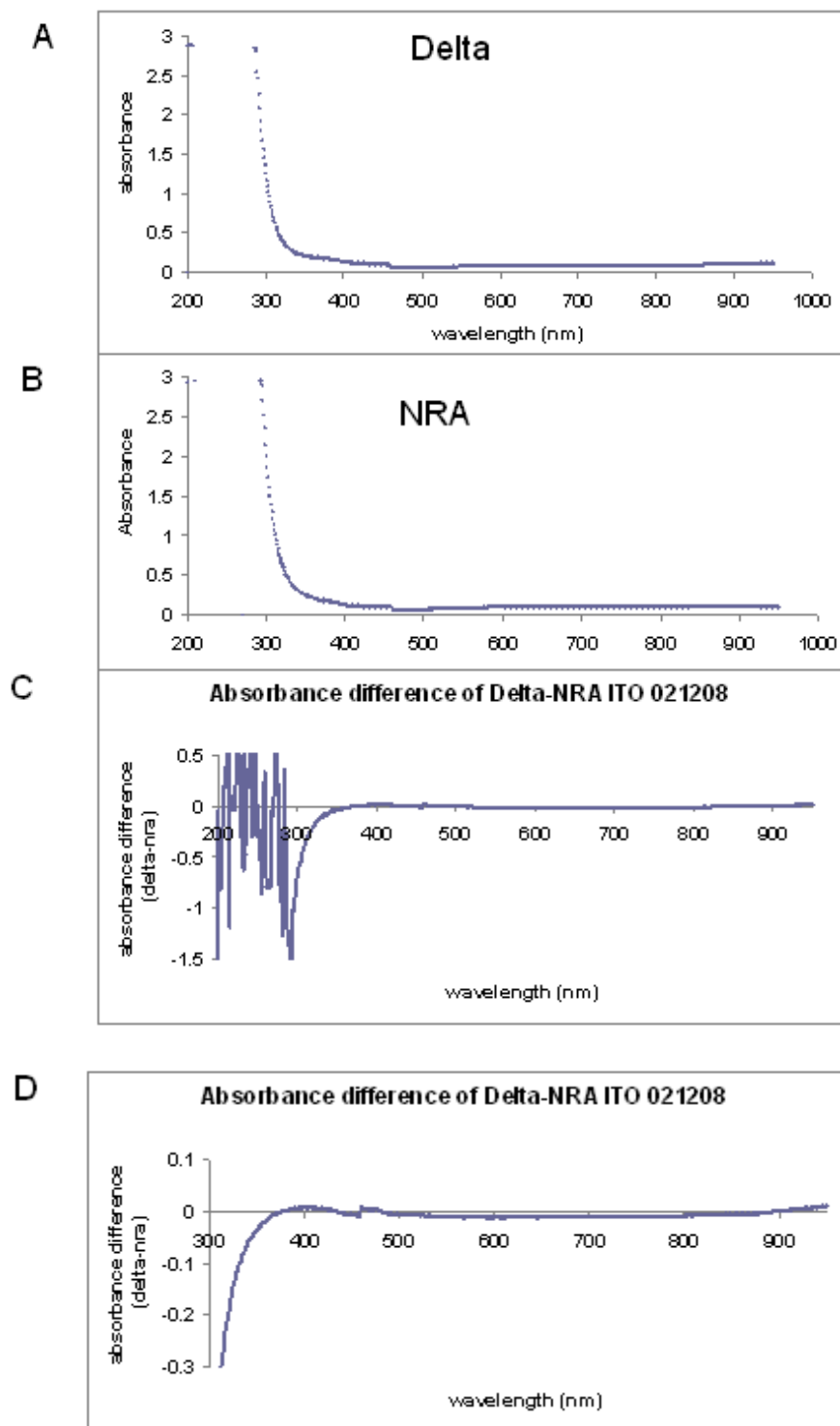


Figure B.7. Absorbance spectra of ITO types C and D. A) Shows type C. B) Shows type D. C) is the full D-C difference spectrum, while D) is a blow up of C).

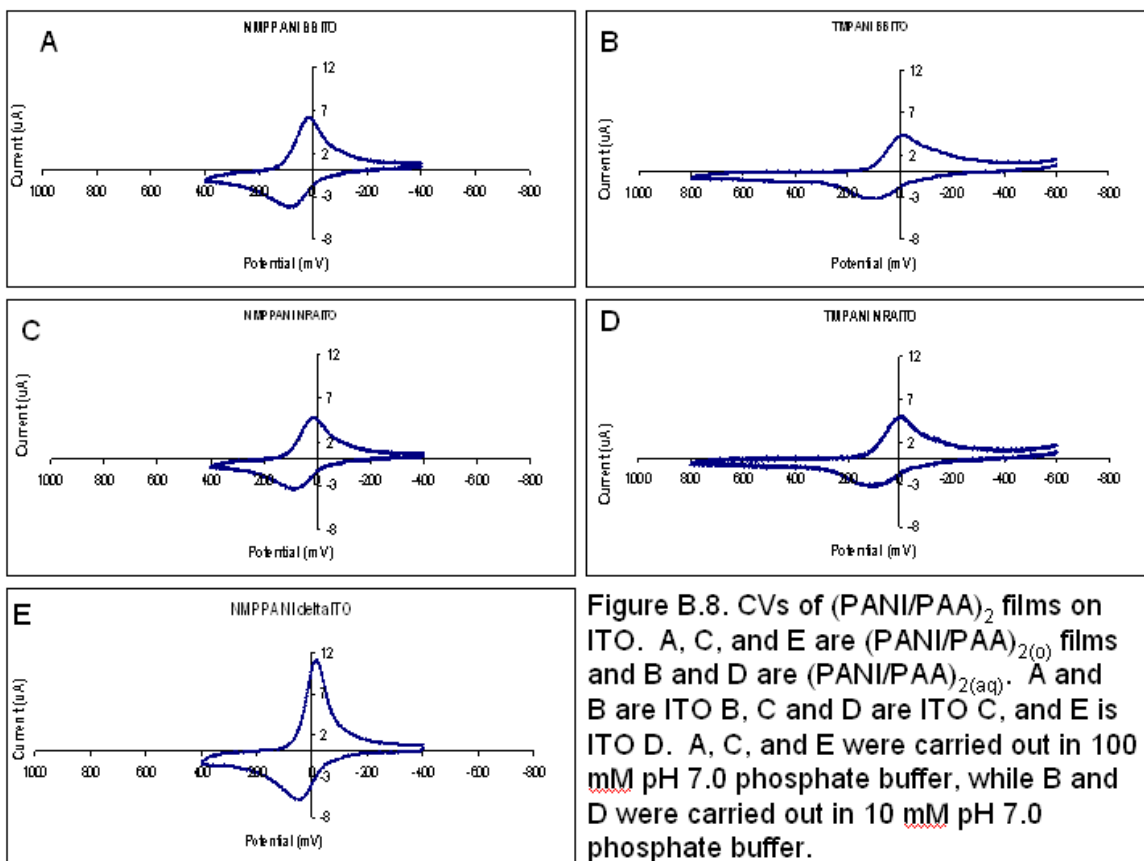


Table B.3. Cyclic voltammograms of ITO/ $(\text{PANI/PAA})_2$.

ITO type	Polymer type	Peak separation (mV)	$E^{0'}$ (mV vs. Ag/AgCl)
B	(o)	71	+50
B	(aq)	121	+46
C	(o)	70	+49
C	(aq)	109	+50
D	(o)	63	+18

The polymer type seems to have a bigger effect on the peak separation than the ITO type. The (aq) polymer preparation leads to larger peak separations than did the (o) polymer preparation. Both types of polymers exhibit quasi-reversible electrochemistry since the peak separations are greater than 59 mV, but the (aq) polymers are even more irreversible. The $E^{o'}$, however, seems to be more affected by the ITO type than the polymer type. ITO type D had a different $E^{o'}$ compared to the other types.

B.3.2.2. pH-response of Polymer Films on ITO

As described in Section B.2.5.1, the potential of ITO/(PANI/PAA)₂ was recorded as a function of time as buffer solutions of differing pH were injected. Figure B.9 has an example of such a plot. The arrows indicate when a buffer of a particular pH was injected. The figure highlights how several minutes were needed for the film in the echem cell to equilibrate with the buffer. Plotting potential as a function of pH yields the data found in Figure B.10 for different ITO types and different polymer preparations. As can be seen by the slopes, the polymer response varies for all films between 40-70 mV/pH. There is change in the response even of the same film when ascending and descending in pH.

It was found that the orientation of the echem cell (film perpendicular or parallel to the ground), the method of rinsing (by hand v. pump, different pumps, different injection speeds, different echem cells, etc.), and the rinse volume could all affect how well the film responded to changes in solution pH (data not shown).

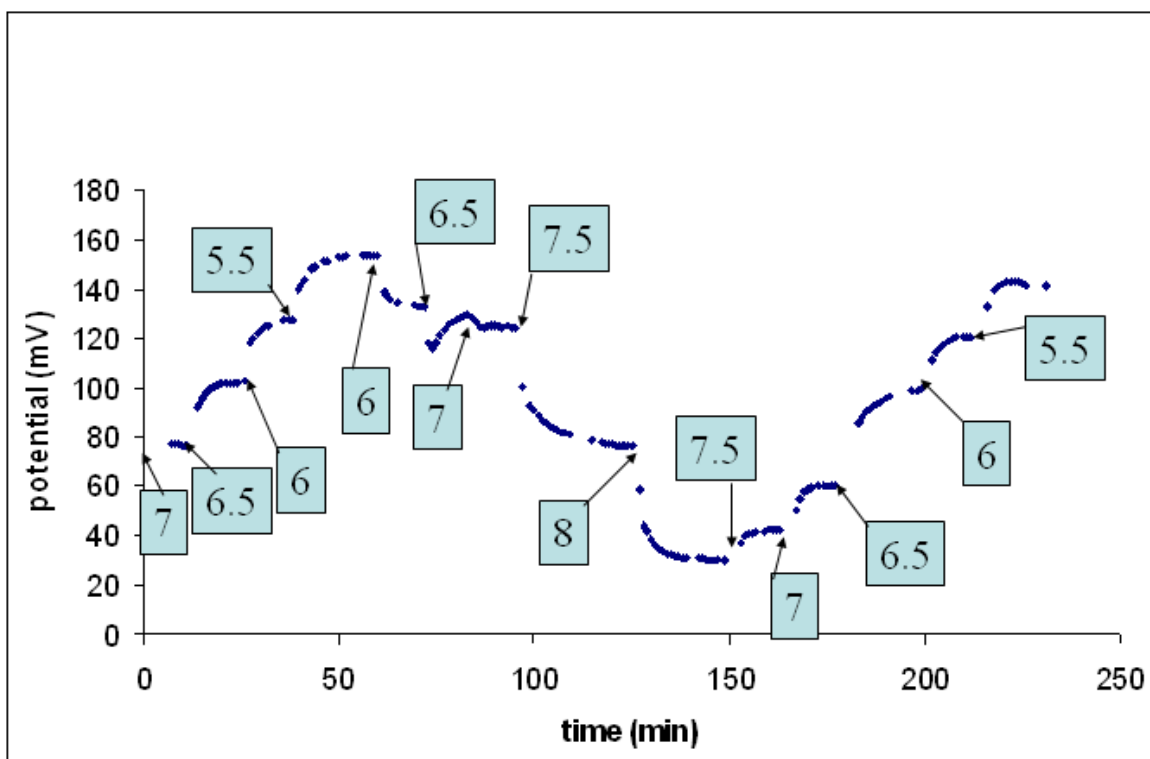
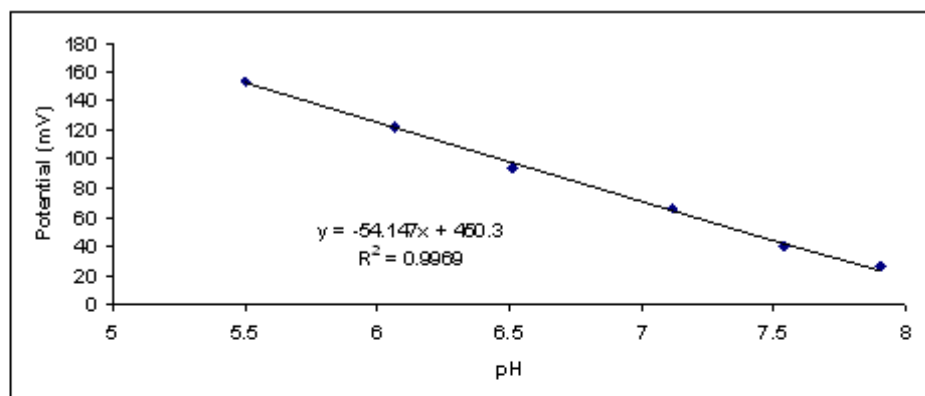
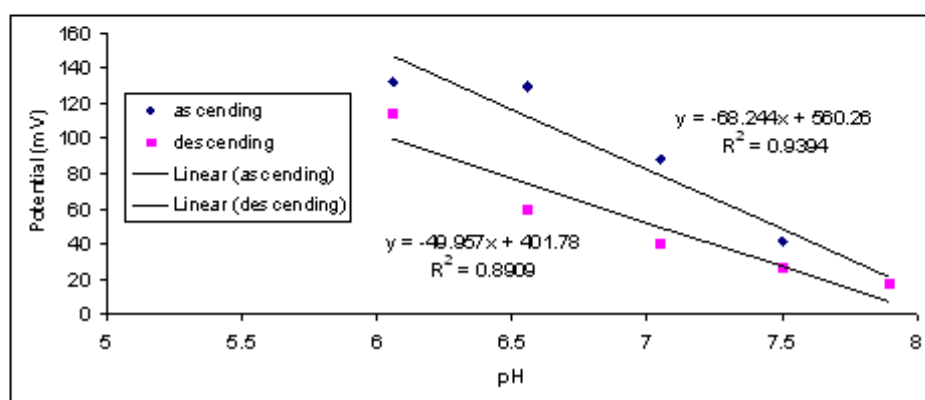


Figure B.9. Plot of potential of $\text{ITO}_C/(\text{PANI/PAA})_{2(o)}$ as a function of time. Arrows indicate when 10 mM phosphate buffer of a particular pH was injected.

A



B



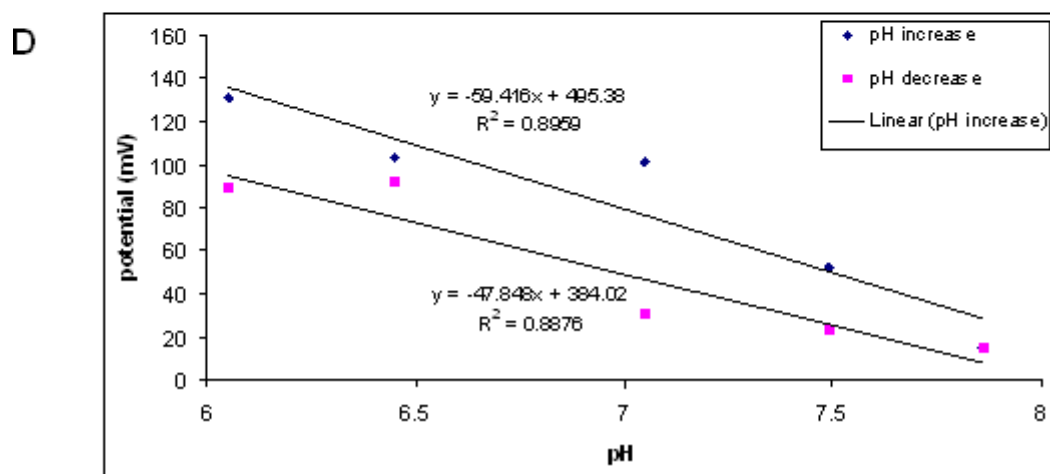
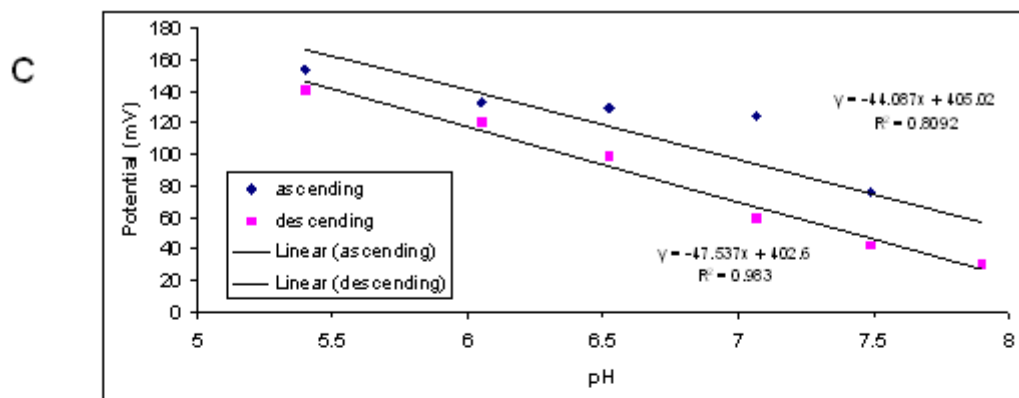


Figure B.10. Potential vs. pH for various ITO types and polymer preparations. A) $\text{ITO}_A/(\text{PANI/PAA})_{2(aq)}$, B) $\text{ITO}_A/(\text{PANI/PAA})_{2(o)}$, C) $\text{ITO}_C/(\text{PANI/PAA})_{2(o)}$, and D) $\text{ITO}_D/(\text{PANI/PAA})_{2(o)}$.

This suggests that there were significant mixing problems in the echem cells used for this experiment.

B.3.3 PSLBs on Polymer Films

The diffusion properties of lipid bilayers on the ITO/(PANI/PAA)₂ surface were investigated with FRAP. The presence of a PSLB was also investigated with fluorescence microscopy and potentiometry.

B.3.3.1 Quantitative FRAP

FRAP was used to determine the diffusion coefficient of PSLBs composed of EggPC with 5 mol% NBD-PC on ITO_A/(PANI/PAA)_{2(aq)}. Examples of FRAP curves for these PSLBs on ITO_A/(PANI/PAA)_{2(aq)} and glass can be found in Figure B.11. ITO_A/(PANI/PAA)_{2(aq)} has a diffusion coefficient of $1 \pm 1 \mu\text{m}^2/\text{s}$ with a percent recovery of $50 \pm 19\%$ ($n = 12$ on 3 separate surfaces). As a comparison, FRAP of EggPC doped with 5 mol% NBD-PC was carried out on detergent-cleaned glass. Detergent-cleaning was carried out by the procedure described in Zhang et al.²⁰⁶ The diffusion coefficient on glass was determined to be $2.69 \pm 0.60 \mu\text{m}^2/\text{s}$ with a recovery of $93.2 \pm 6.4\%$ ($n = 9$ for 3 separate surfaces), which is in agreement with literature.¹¹² It is clear that 1) there is a PSLB on the ITO_A/(PANI/PAA)_{2(aq)} surface and 2) the ITO_A/(PANI/PAA)_{2(aq)} surfaces are variable based on the large standard deviation of the diffusion coefficient. As explained in Ref. 204, this finding agrees with the low rate of success associated with attempting to make a proton-impermeable lipid bilayer and will be described further in the next Section.

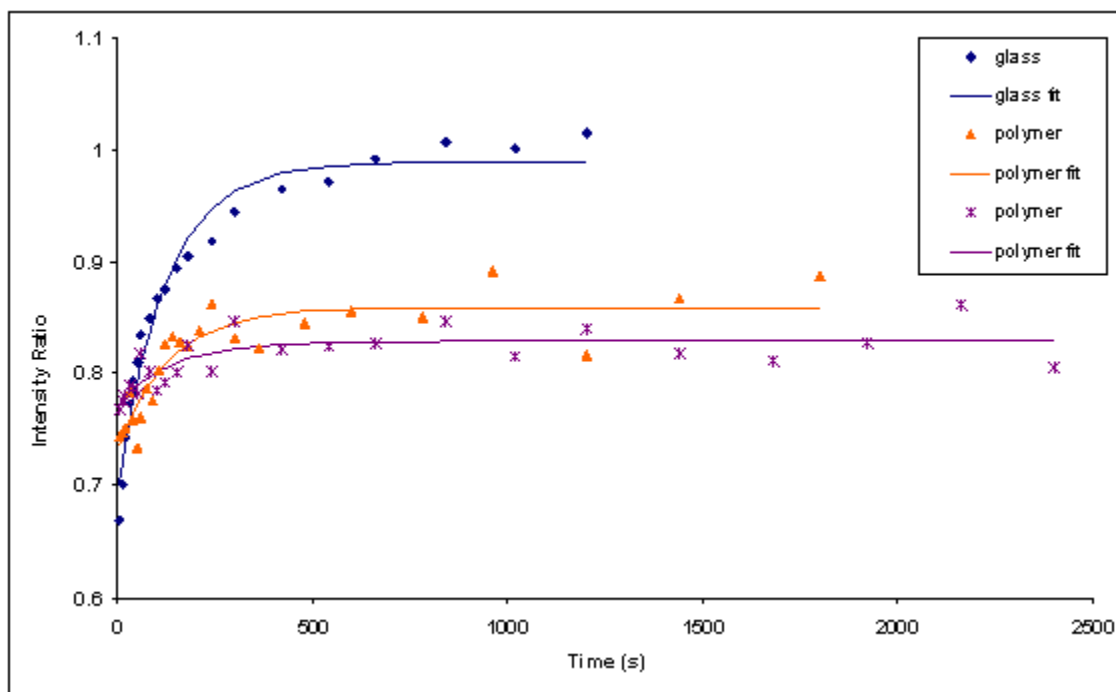


Figure B.11. Quantitative FRAP example for $\text{ITO}_A(\text{PANI/PAA})_{2(\text{aq})}$ and glass with 5 mol % NBD-PC in EggPC (0.5 mg/ml) in pH = 7.0 10 mM phosphate buffer.

It must be noted that only ITO_A/(PANI/PAA)_{2(aq)} was tested with quantitative FRAP. In Section B.3.3.3, qualitative FRAP of other ITO/(PANI/PAA)₂ systems will be described. These other qualitative FRAP experiments led to even less reassuring results.

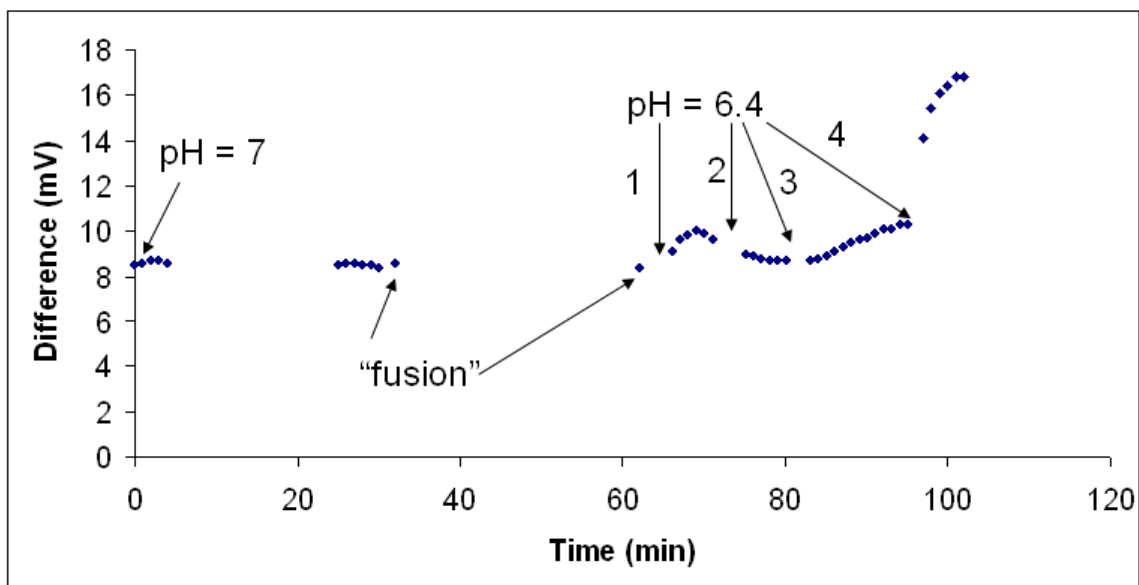
B.3.3.2 Attempted Proton-blocking

Ge et al. and McBee et al. presented data for ITO/(PANI/PAA)₂ films that show potential vs. pH data similar to that found in Section B.3.2.2.²⁰⁰⁻²⁰² Vesicle fusion of a PSLB onto the ITO/(PANI/PAA)₂ surface resulted in films that no longer responded to changes in potential with changing buffer solutions. Injection of a buffer solution of a different pH did not change the potential of the film. In this Appendix, however, unclear results were obtained. Due to the fragility of the PSLB, care had to be taken not to disturb the lipids, so slow injections were needed, but too much caution might result in poor mixing of the solutions in the echem cell as demonstrated in Figure B.12. As shown in the potential difference plot as a function of time in Figure B.12, the difference stayed between 8 and 10 mV until the fastest pump rate was used. After the final pump stage, however, both traces exhibited behavior that suggested failed bilayers, although the larger difference was apparent in the bilayer without EggPC.

B.3.3.3 Qualitative FRAP and Fluorescence Microscopy

Section B.3.3.1 only discussed quantitative FRAP findings for ITO_A/(PANI/PAA)_{2(aq)}. It had been mistakenly assumed that different ITO surfaces would yield similar diffusion results. Years later, this notion was challenged qualitatively.

A



B

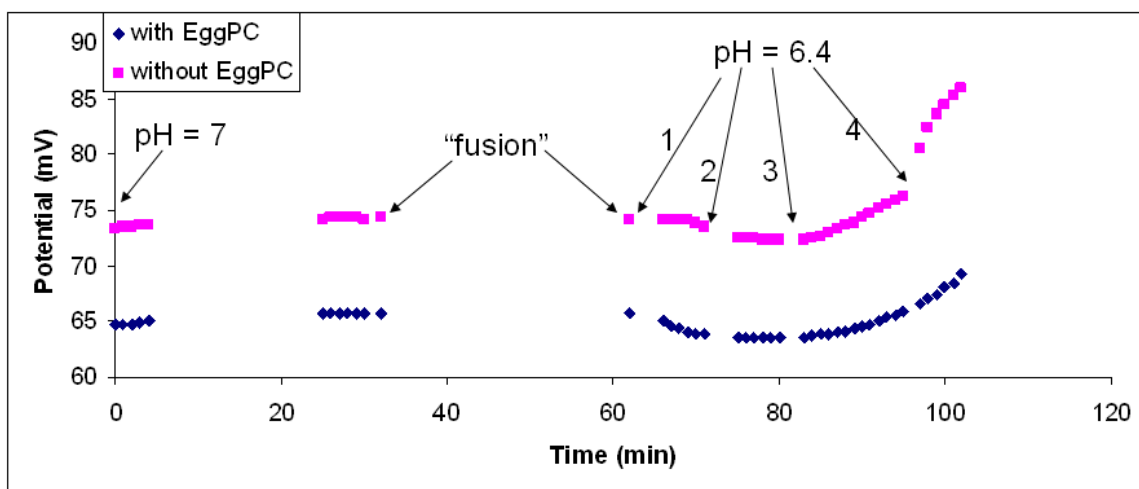


Figure B.12. Potential v. time for $\text{ITO}_D/(\text{PANI}/\text{PAA})_{2(o)}$. 1-4 are increasing pump rates. A) shows the the pink trace minus the blue trace in A), while B) is the potential response vs time.

Figure B.13 contains qualitative FRAP images of EggPC doped with NBD-PC on glass and ITO_D/(PANI/PAA)_{2(o)}. The series of images of the PSLB on glass shows recovery of fluorescence in the photobleached region of the bilayer. ITO_D/(PANI/PAA)_{2(o)}, however, does not show this. In fact, it is difficult to see any photobleaching from the laser (although a 10 s bleach time was used, which is at least 10-fold longer than for glass) for ITO_D/(PANI/PAA)_{2(o)}. NBD-PC is notoriously easy to bleach and both of those samples were run the same day, suggesting that this is not a laser alignment error. This means that the PSLB was not photobleaching or the PSLB was not there.

After many trials, the experiment in Figure B.14 was run: ITO/(PANI/PAA)_(o) with ITO C and D using EggPC and 5 mol% NBD-PC. It must be noted that only 1 PANI and 1 PAA layer were used. With ITO_D, the experiments were tried on multiple spots and different samples on different days. Photobleaching and recovery of a PSLB was never successfully recorded with ITO_D. ITO_C, on the other hand, did exhibit definite photobleaching and slow recovery.

The fraction of a PSLB was estimated using a technique similar to what was described in Cremer et al.²⁰⁷ In short, a PSLB of 1 mol % rhodamine in EggPC was formed on piranha-cleaned glass and scratched with a pipette tip. An image was taken of the glass before fusion and after. The fluorescent image of the scratch and a trace across the scratch are presented in Figure B.15. Unfortunately, many vesicles were adsorbed to the surface in this particular run.

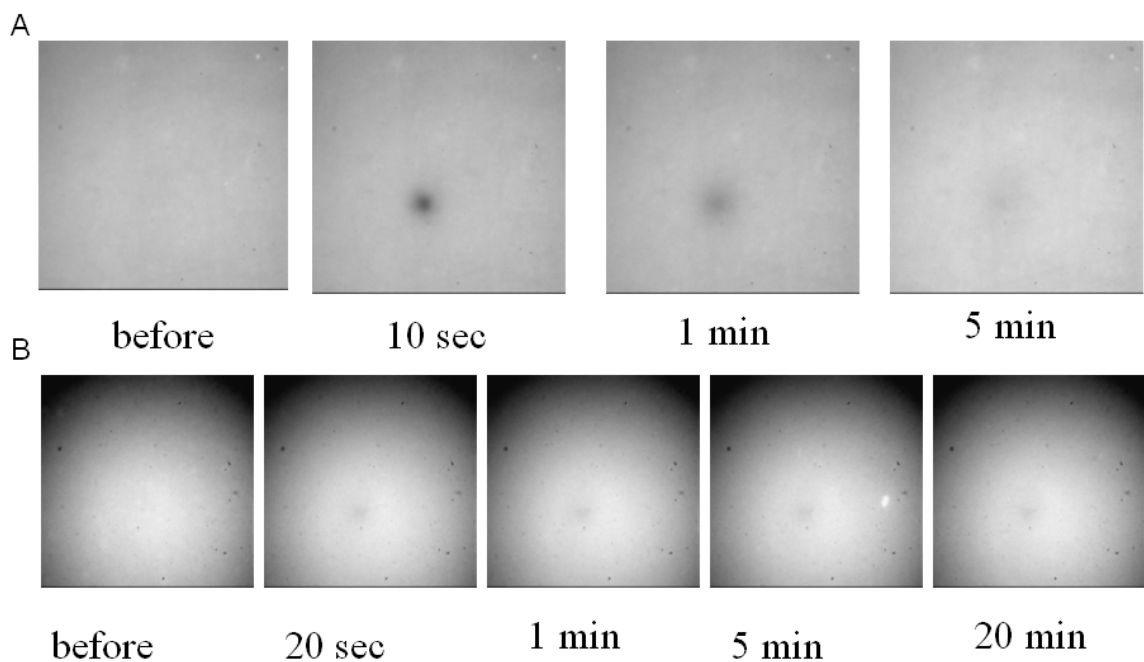


Figure B.13. Qualitative FRAP images of 0.5 mg/ml EggPC with 5 mol% NBD-PC on A) glass and B) $\text{ITO}_D/(\text{PANI/PAA})_{2(o)}$. A <1 s exposure was used to laser bleach A), while a 10 s exposure was used to bleach B).

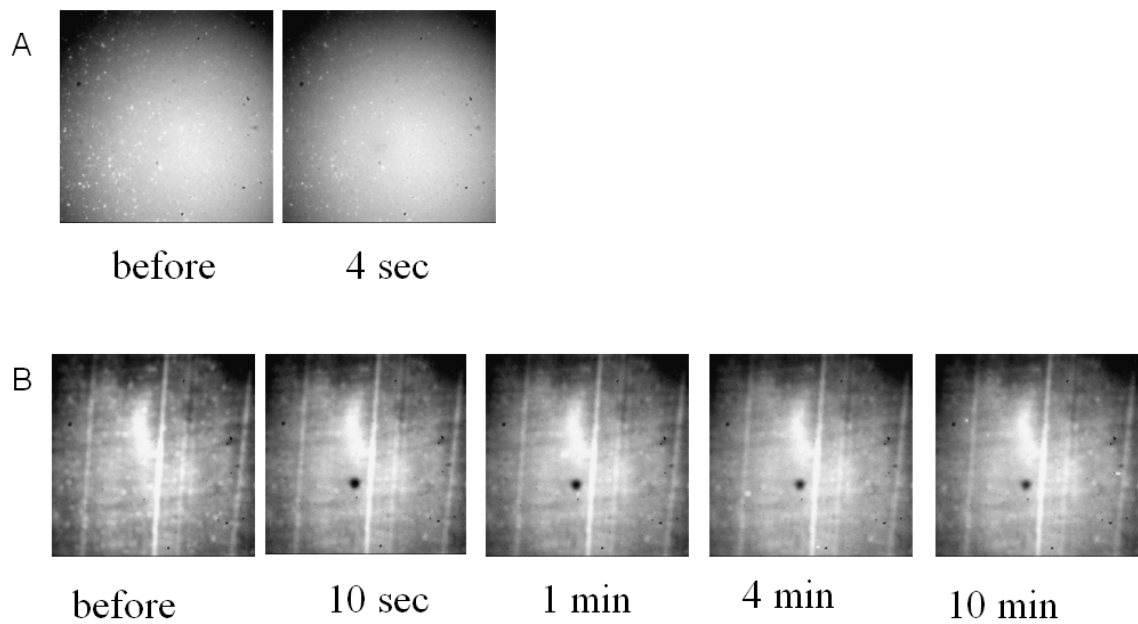


Figure B.14. Qualitative FRAP of 0.5 mg/ml EggPC with 5 mol% NBD-PC on $\text{ITO}/(\text{PANI/PAA})_{(o)}$ (note only one layer of each polymer): A) ITO D, B) ITO C.

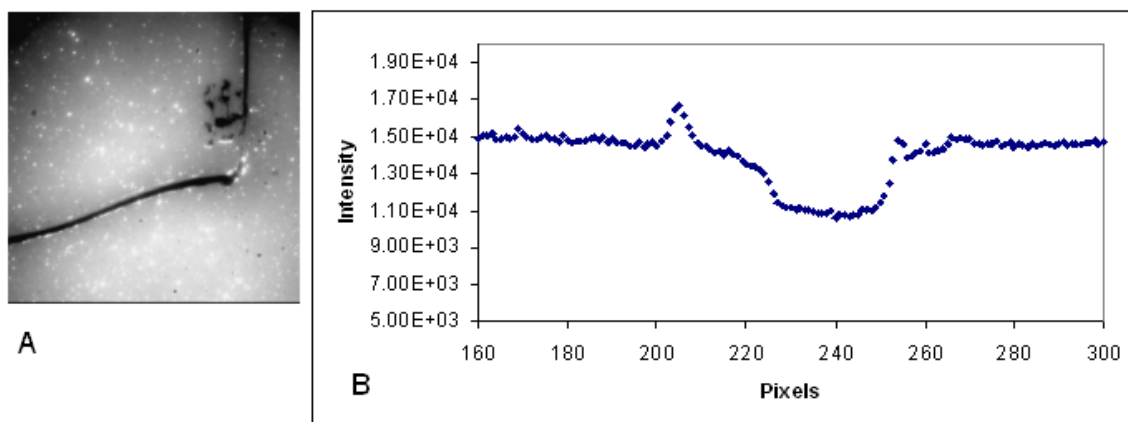


Figure B.15. A) Fluorescence image of glass with a PSLB composed of EggPC doped with 1 mol% rhodamine with a scratch created by dragging a pipette tip lightly across the surface. B) Intensity vs pixel for a line scan across the surface that incorporated the scratch.

It was assumed that the increase in fluorescence intensity before and after vesicle fusion on glass was the result of the formation of a single lipid bilayer on the surface. Then, images before and after vesicle fusion onto ITO_D, ITO_D/PANI_(o) and ITO_D/(PANI/PAA)_(o) were recorded (see Figure B.16 for example of ITO_D/(PANI/PAA)_(o)). The % PSLB was calculated in two ways. First, the average intensity of a clean 10x10 ROI on the bare glass was subtracted from the average intensity of the PSLB on glass in the same ROI. The region chosen lacked vesicles. According to this calculation, a single bilayer under these optical conditions results in an average fluorescence intensity increase of ~14,000. The same ROI was investigated for ITO_D, ITO_D/PANI_(o) and ITO_D/(PANI/PAA)_(o) before and after vesicle fusion, regardless of whether or not there were lots of vesicles in that region. The difference in the pre- and post-vesicle fusion images was divided by 14,000 to get the fraction of PSLB. Table B.4 summarizes the findings (in column “% PSLB (14,000)”).

Another method was also used to calculate the % PSLB. The average intensity of the scratched area in the line scan was subtracted from the average intensity of the regions not scratched (3,700). It was assumed then that an increase in average fluorescence intensity of 3,700 was equal to a single bilayer. The same calculation was done as described above, except that the difference in post- and pre-images was divided by 3,700 to get the PSLB fraction. In this case, the data is in column “% PSLB (3,700)” in Table B.4.

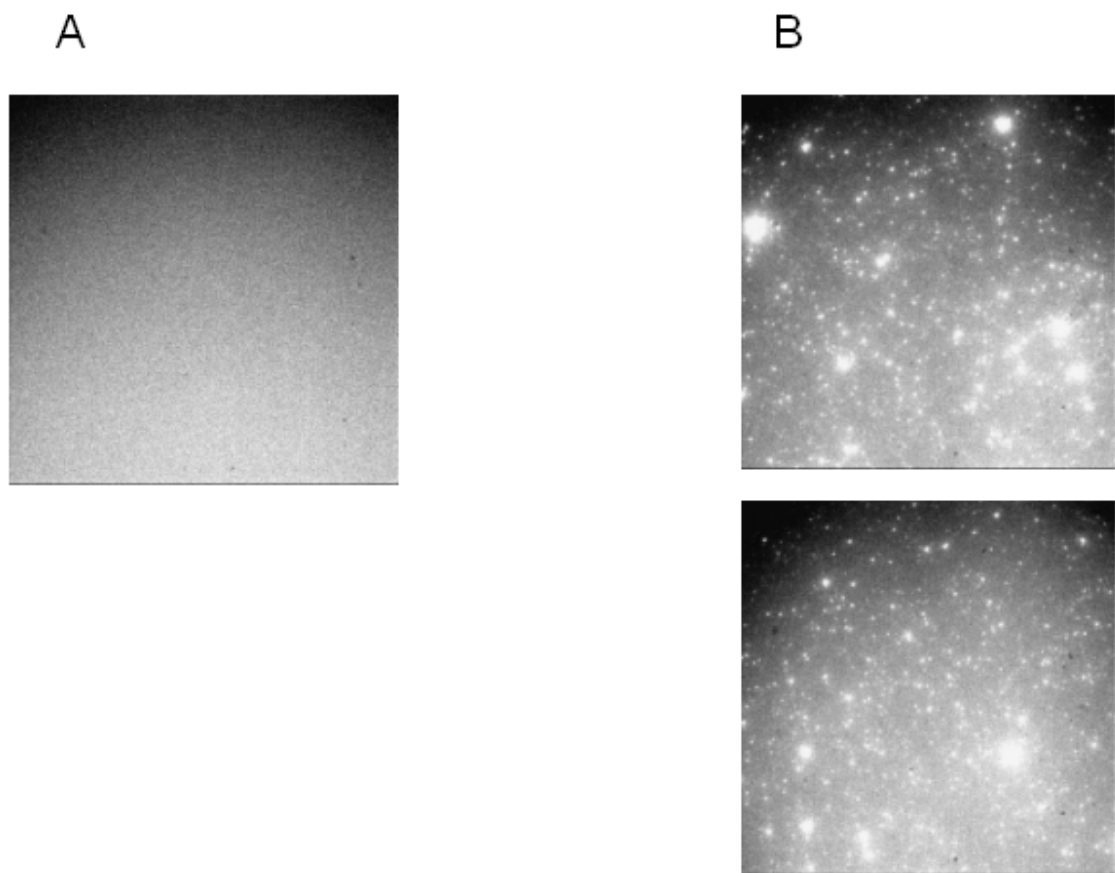


Figure B.16. Fluorescence image of $\text{ITO}_D/(\text{PANI/PAA})_{(o)}$. A) Image before lipid deposition. B) Images after lipid bilayer deposition. Many vesicles are seen on the surface.

Table B.4. Calculation of PSLB % on surfaces.

Surface	% PSLB (14,000)	% PSLB (3,700)
Glass	100% (assumed)	100% (assumed)
ITO_D	2%	5%
$\text{ITO}_D/\text{PANI}_{(o)}$ *	8%	29%
$\text{ITO}_D/(\text{PANI/PAA})_{(o)}$	1%	5%

*ITO was accidentally plasma-cleaned for 32 minutes instead of 15 minutes.

The results in Table B.4 indicate that at most ~30% of a bilayer was formed in any of these cases. It is not expected that a PANI surface, which is hydrophobic, would readily have a lipid bilayer fuse to the surface, so it is particularly puzzling that ITO_D/PANI_(o) displays the largest fraction of a PSLB formed. This may be due to the fact that the ITO piece had accidentally been air plasma-cleaned for over twice as long as in all other cases. Regardless, this data suggests that full bilayers are not forming on these polymer surfaces, which might explain why qualitative FRAP does not show the presence of a diffusing bilayer.

Due to the many mistakes in the fluorescence experiments dealing with PSLB fraction estimation, this work would need to be repeated. However, the tentative fluorescence data along with the qualitative FRAP data suggests that ITO_D does not support full PSLBs when PANI and PAA are adsorbed to the surface. This is in contrast to ITO_A/(PANI/PAA)_{2(aq)}, upon which diffusion coefficients were quantitatively measured.

B.3.4 Attempted Incorporation of C-P-Q into PSLBs on ITO/(PANI/PAA)₂

Repetition of the proton-pumping work of McBee and Ge was attempted using ITO_D before it was known that PSLBs had difficulty fusing onto (PANI/PAA)_{2(o)}, when it was coupled to ITO_D.^{204, 205} This Section will summarize these findings.

The set-up pictured in Figure B.17 was used to shine light onto the PSLB for these experiments. The echem cell was positioned on top of the echem cell holder with the ITO-coated glass on the bottom.

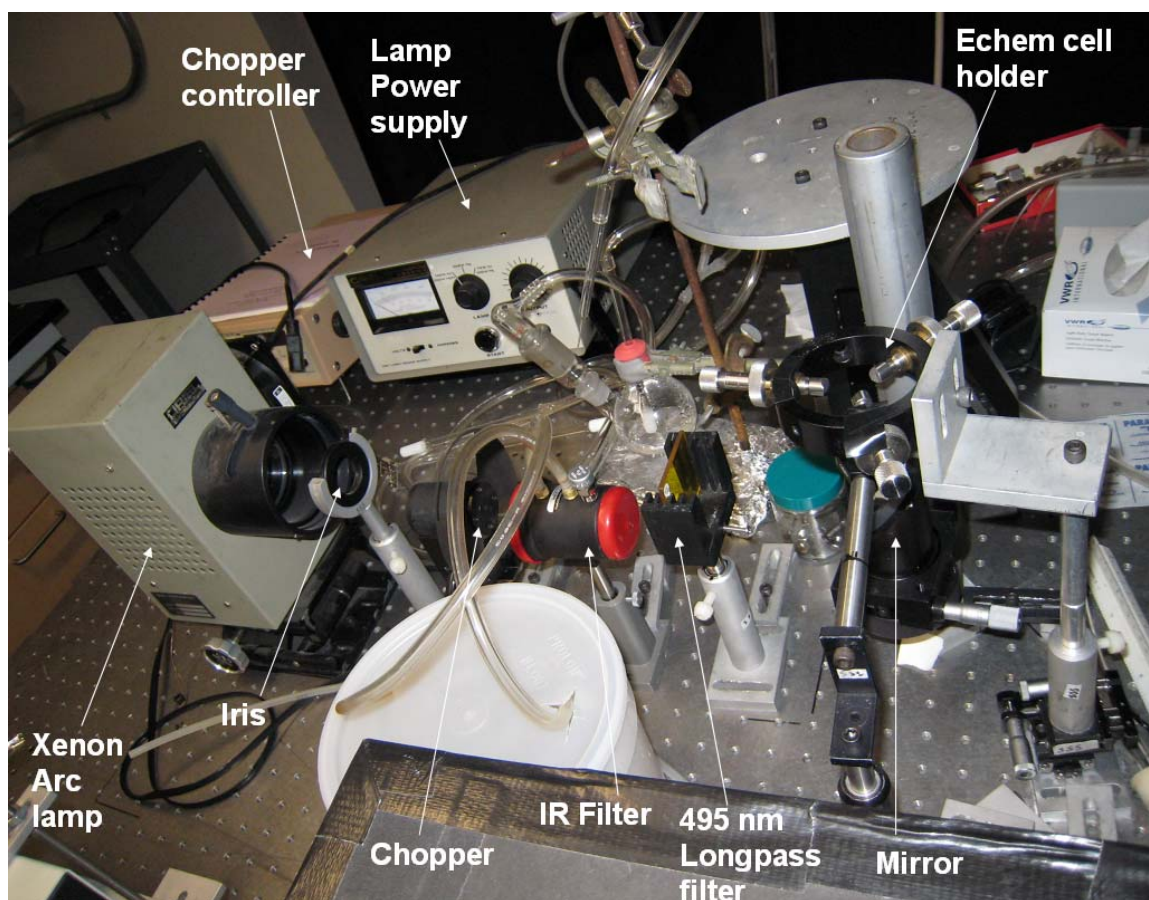


Figure B.17. Proton-pumping set-up.

The chopper was not used in the experiments described below. To very slowly chop the light, a piece of foil was used to cover the port of the XE arc lamp whenever darkness was needed.

The set-up described above was used to investigate how $\text{ITO}_\text{D}/(\text{PANI}/\text{PAA})_{2(\text{o})}$ responded to intense light. The results are shown in Figure B.18. Over the time course of 30 minutes, a slow drift in signal was seen (Figure B.18a). After a PSLB with 2 mol% Q was allegedly fused to the $\text{ITO}_\text{D}/(\text{PANI}/\text{PAA})_{2(\text{o})}$ surface and subjected to 20 s cycles of light and dark, again, only a slow potential drift was seen with time (Figure B.18b). When $\text{ITO}_\text{D}/(\text{PANI}/\text{PAA})_{2(\text{o})}$ had a Q-containing PSLB fused onto the surface and C-P-Q had been introduced into the cell, as described in Ref. 204, there was a small, consistent difference in potential related to whether or not light was shining on the surface (Figure B.18c). This repeatable change in potential was less than 1 mV, but was absent in the previously described controls. An increase in potential when light was impinging on the surface suggests that the pH decreased. If proton-pumping was happening, this is the expected direction of the change. However, because the change was only present in the light, a 'leaky' membrane is suspected. Alternatively, perhaps C-P-Q was adsorbed directly onto the $\text{ITO}/(\text{PANI}/\text{PAA})_2$ film. A control investigating this second possibility was never performed.

Additionally, in repetitions of this experiment, it was found that after disassembling the echem cell after the experiment, an orange color was visible on the tubing side of the echem cell.

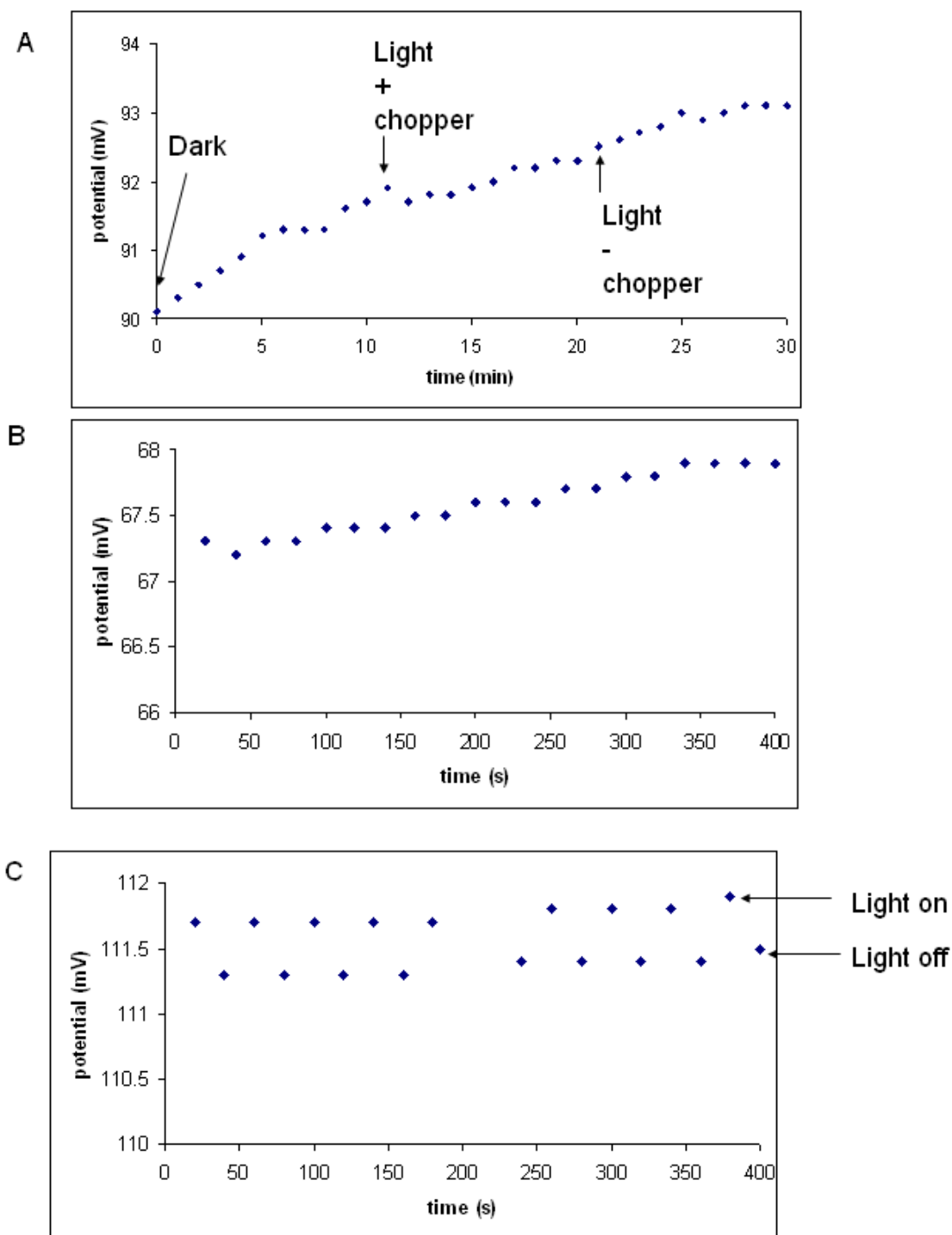


Figure B.18. $\text{ITO}_D/(\text{PANI}/\text{PAA})_{2(o)}$ being exposed to light. A) $\text{ITO}_D/(\text{PANI}/\text{PAA})_{2(o)}$, B) $\text{ITO}_D/(\text{PANI}/\text{PAA})_{2(o)}$ with PSLB and 2 mol% Q being exposed to light for 20 s at a time. C) $\text{ITO}_D/(\text{PANI}/\text{PAA})_{2(o)}$ with PSLB, 2 mol% Q, and C-P-Q being exposed to light for 20 s at a time.

The C-P-Q solution in 10% THF and buffer was orange. This observation suggests that the poor flow qualities of the cell and the slow injection speed may not mix the contents of the entrapped solution in the echem cell very well, in agreement with the findings in Section B.3.2.2.

B.4 Conclusions

The data suggest that the ITO batch matters when a PSLB is being fused to the polymer interface between the lipids and the ITO. Unfortunately, ITO_D was found to be bad for PSLB formation although it had the best surface roughness and electrochemical characteristics. The data supporting this conclusion are outlined below.

B.4.1 ITO Effects

The rms roughnesses of the four ITO types were measured with AFM. Smoother ITO had always been assumed to be better ITO, because it was less likely to create defects in the thin polymer film deposited on top of it. It was found that ITO_A and ITO_D were smoothest and had similar roughness values of 1.5-1.6 nm.

CVs of polymer films on ITO show that ITO_D exhibited the highest current with the most reversible response.

B.4.2 Mixing Difficulties

The design of the flow cell is suspected to have bad mixing properties, which could lead to false positives for blocking bilayers, because the pH of the solution simply had not changed sufficiently with the injection of a new buffer. The presence of an orange hue only near the tubing side of the echem cell interior after C-P-Q injection also suggests poor mixing.

B.4.3 Presence of a Lipid Bilayer

The qualitative FRAP experiments and fluorescence experiments involving ITO_D/(PANI/PAA)_{2(o)} with PSLBs both suggest that there might not be a full PSLB

present when using ITO_D. Quantitative FRAP results of ITO_A/(PANI/PAA)_{2(aq)} imply that PSLBs were forming on that system.

B.4.4 Potential Changes Upon Light Exposure of Full Architecture

Small changes in potential in the expected direction were observed with ITO_D/(PANI/PAA)_{2(o)} with PSLB, Q, and C-P-Q; however, it is suspected that this is a result of ITO_D/(PANI/PAA)_{2(o)} with adsorbed C-P-Q.

APPENDIX C: PROOF OF PERMISSION FOR COPYRIGHTED MATERIAL

Supplier	Elsevier Limited The Boulevard, Langford Lane Kidlington, Oxford, OX5 1GB, UK
Registered Company Number	1982084
Customer name	Kristina Sörös
Customer address	734 E. Roger Rd. #147 Tucson, AZ 85719
License number	2706190245948
License date	Jul 11, 2011
Licensed content publisher	Elsevier
Licensed content publication	Cell
Licensed content title	Molecular Anatomy of a Trafficking Organelle
Licensed content author	Shigeo Takamori, Matthew Holt, Katinka Stenius, Edward A. Lemke, Mads Grønberg, Dietmar Riedel, Henning Urlaub, Stephan Schenck, Britta Brügger, Philippe Ringle, Shirley A. Müller, Burkhard Rammner, Frauke Gräter, et al.
Licensed content date	17 November 2006
Licensed content volume number	127
Licensed content issue number	4
Number of pages	16
Start Page	831
End Page	846
Type of Use	reuse in a thesis/dissertation
Portion	figures/tables/illustrations
Number of figures/tables /illustrations	1
Format	both print and electronic
Are you the author of this Elsevier article?	No
Will you be translating?	No
Order reference number	
Title of your thesis/dissertation	Diffusion coefficients and mechanical properties of polymerizable lipid bilayers
Expected completion date	Jul 2011
Estimated size (number of pages)	300
Elsevier VAT number	GB 494 6272 12
Permissions price	0.00 USD
VAT/Local Sales Tax	0.0 USD / 0.0 GBP
Total	0.00 USD
Terms and Conditions	

Supplier	Elsevier Limited The Boulevard,Langford Lane Kidlington,Oxford,OX5 1GB,UK
Registered Company Number	1982084
Customer name	Kristina S orosz
Customer address	734 E. Roger Rd. #147 Tucson, AZ 85719
License number	2706600802316
License date	Jul 12, 2011
Licensed content publisher	Elsevier
Licensed content publication	Biochimica et Biophysica Acta (BBA) - Reviews on Biomembranes
Licensed content title	Calorimetric and molecular mechanics studies of the thermotropic phase behavior of membrane phospholipids
Licensed content author	Ching-hsien Huang, Shusen Li
Licensed content date	16 November 1999
Licensed content volume number	1422
Licensed content issue number	3
Number of pages	35
Start Page	273
End Page	307
Type of Use	reuse in a thesis/dissertation
Intended publisher of new work	other
Portion	figures/tables/illustrations
Number of figures/tables /illustrations	1
Format	both print and electronic
Are you the author of this Elsevier article?	No
Will you be translating?	No
Order reference number	
Title of your thesis/dissertation	Diffusion coefficients and mechanical properties of polymerizable lipid bilayers
Expected completion date	Jul 2011
Estimated size (number of pages)	300
Elsevier VAT number	GB 494 6272 12
Permissions price	0.00 USD
VAT/Local Sales Tax	0.0 USD / 0.0 GBP
Total	0.00 USD
Terms and Conditions	

REFERENCES

1. Gennis, R. B., *Biomembranes: Molecular Structure and Function*. Springer-Verlag: 1989.
2. Takamori, S.; Holt, M.; Stenius, K.; Lemke, E. A.; Grønborg, M.; Riedel, D.; Urlaub, H.; Schenck, S.; Brügger, B.; Ringler, P.; Müller, S. A.; Rammner, B.; Gräter, F.; Hub, J. S.; De Groot, B. L.; Mieskes, G.; Moriyama, Y.; Klingauf, J.; Grubmüller, H.; Heuser, J.; Wieland, F.; Jahn, R., Molecular Anatomy of a Trafficking Organelle. *Cell* **2006**, 127, (4), 831-846.
3. Yeagle, P. L., *The Structure of Biological Membranes*. 2 ed.; CRC Press: 2005.
4. Barenholz, Y., Cholesterol and other membrane active sterols: from membrane evolution to "rafts". *Progress in lipid research* **2002**, 41, (1), 1-5.
5. Barenholz, Y.; Cevc, G., Structure and properties of membranes. In *Physical Chemistry of Biological Interfaces*, Baszkin, A.; Norde, W., Eds. Marcel Dekker: 2000; pp 171-241.
6. Voet, D.; Voet, J. G., *Biochemistry*. 3 ed.; John Wiley & Sons, Inc.: 2004; Vol. 1.
7. Israelachvili, J., *Intermolecular and Surface Forces*. 2 ed.; Academic Press: 1992.
8. Vaz, W. L. C.; Begley, T. P., Lipid Bilayers: Properties. In *Wiley Encyclopedia of Chemical Biology*, John Wiley & Sons, Inc.: 2007.
9. Brown, M. F., Modulation of rhodopsin function by properties of the membrane bilayer. *Chemistry and Physics of Lipids* **1994**, 73, (1-2), 159-180.
10. Lee, A. G., How lipids affect the activities of integral membrane proteins. *Biochimica et Biophysica Acta (BBA) - Biomembranes* **2004**, 1666, (1-2), 62-87.
11. Powl, A. M.; Lee, A. G.; Owen, P. H., Lipid Effects on Mechanosensitive Channels. In *Current Topics in Membranes*, Academic Press: 2007; Vol. 58, pp 151-178.
12. Destainville, N.; Dumas, F.; Salomé, L., What do diffusion measurements tell us about membrane compartmentalisation? Emergence of the role of interprotein interactions. *Journal of Chemical Biology* **2008**, 1, (1), 37-48.
13. Danelon, C.; Jenke, M. G.; Schreiter, C.; Kim, G. M.; Perez, J.-B.; Santschi, C.; Brügger, J.; Vogel, H., Micro- and Nanostructured Devices for the Investigation

of Biomolecular Interactions. *CHIMIA International Journal for Chemistry* **2006**, 60, 754-760.

14. Hurwitz, N.; Pellegrini-Calace, M.; Jones, D. T., Towards genome-scale structure prediction for transmembrane proteins. *Philosophical Transactions of the Royal Society B: Biological Sciences* **2006**, 361, (1467), 465-475.
15. Howard, A. D.; McAllister, G.; Feighner, S. D.; Liu, Q.; Nargund, R. P.; Van der Ploeg, L. H. T.; Patchett, A. A., Orphan G-protein-coupled receptors and natural ligand discovery. *Trends in Pharmacological Sciences* **2001**, 22, (3), 132-140.
16. Ben, D. D.; Lambertucci, C.; Vittori, S.; Volpini, R.; Cristalli, G., GPCRs as therapeutic targets: A view on adenosine receptors structure and functions, and molecular modeling support. *Journal of the Iranian Chemical Society* **2005**, 2, (3), 176-188.
17. Alvarez-Curto, E.; Pediani, J.; Milligan, G., Applications of fluorescence and bioluminescence resonance energy transfer to drug discovery at G protein coupled receptors. *Analytical and Bioanalytical Chemistry* **2010**, 398, (1), 167-180.
18. Ballesteros, J.; Palczewski, K., G protein-coupled receptor drug discovery: Implications from the crystal structure of rhodopsin. *Current Opinion in Drug Discovery & Development* **2001**, 4, 561-574.
19. Drews, J. r., Drug Discovery: A Historical Perspective. *Science* **2000**, 287, (5460), 1960-1964.
20. Hofmann, K. P.; Scheerer, P.; Hildebrand, P. W.; Choe, H.-W.; Park, J. H.; Heck, M.; Ernst, O. P., A G protein-coupled receptor at work: the rhodopsin model. *Trends in Biochemical Sciences* **2009**, 34, (11), 540-552.
21. Smith, S. O., Structure and activation of the visual pigment rhodopsin. *Annual Review of Biophysics* **2010**, 39, 309-328.
22. Lundbaek, J. A.; Birn, P.; Tape, S. E.; Toombes, G. E. S.; Soegaard, R.; Koeppe, R. E.; Gruner, S. M.; Hansen, A. J.; Andersen, O. S., Capsaicin Regulates Voltage-Dependent Sodium Channels by Altering Lipid Bilayer Elasticity. *Molecular Pharmacology* **2005**, 68, (3), 680-689.
23. Veatch, W. R.; Mathies, R.; Eisenberg, M.; Stryer, L., Simultaneous fluorescence and conductance studies of planar bilayer membranes containing a highly active and fluorescent analog of gramicidin A. *Journal of Molecular Biology* **1975**, 99, (1), 75-92.

24. Wallace, B. A., Gramicidin channels and pores. *Annual Review of Biophysics and Biophysical Chemistry* **1990**, 19, 127-157.
25. Cullis, P. R.; Hope, M. J.; Tilcock, C. P. S., Lipid polymorphism and the roles of lipids in membranes. *Chemistry and Physics of Lipids* **1986**, 40, (2-4), 127-144.
26. Hafez, I. M.; Cullis, P. R., Roles of lipid polymorphism in intracellular delivery. *Advanced Drug Delivery Reviews* **2001**, 47, (2-3), 139-148.
27. Lenaz, G., Membrane fluidity. *NATO ASI series* **1984**, 76, (biomembranes), 111-158.
28. Huang, C.-h.; Li, S., Calorimetric and molecular mechanics studies of the thermotropic phase behavior of membrane phospholipids. *Biochimica et Biophysica Acta (BBA) - Reviews on Biomembranes* **1999**, 1422, (3), 273-307.
29. Sparr, E.; Engstroem, S., Lipid phase behavior: a basis for an understanding of membrane structure and function *Basic and Clinical Dermatology* **2004**, 26, (Skin, hair, and nails), 25-63.
30. Nagle, J. F., Critical role of fluctuations in lipid bilayers In *Phase Transitions in Complex Fluids*, World Scientific: 1998; pp 247-269.
31. Singer, S. J.; Nicolson, G. L., The Fluid Mosaic Model of the Structure of Cell Membranes. *Science* **1972**, 175, (4023), 720-731.
32. Engelman, D. M., Membranes are more mosaic than fluid. *Nature* **2005**, 438, (7068), 578-580.
33. Baker, A.; Saulière, A.; Dumas, F.; Millot, C.; Mazères, S.; Lopez, A.; Salomé, L., Functional membrane diffusion of G-protein coupled receptors. *European Biophysics Journal* **2007**, 36, (8), 849-860.
34. Owen, D. M.; Williamson, D.; Rentero, C.; Gaus, K., Quantitative Microscopy: Protein Dynamics and Membrane Organisation. *Traffic* **2009**, 10, (8), 962-971.
35. Evans, E.; Needham, D., Physical properties of surfactant bilayer membranes: thermal transitions, elasticity, rigidity, cohesion and colloidal interactions. *The Journal of Physical Chemistry* **1987**, 91, (16), 4219-4228.
36. Rawicz, W.; Smith, B. A.; McIntosh, T. J.; Simon, S. A.; Evans, E., Elasticity, Strength, and Water Permeability of Bilayers that Contain Raft Microdomain-Forming Lipids. *Biophysical Journal* **2008**, 94, (12), 4725-4736.

37. Marsh, D., Elastic curvature constants of lipid monolayers and bilayers. *Chemistry and Physics of Lipids* **2006**, 144, (2), 146-159.
38. Hope, M. J.; Bally, M. B.; Mayer, L. D.; Janoff, A. S.; Cullis, P. R., Generation of multilamellar and unilamellar phospholipid vesicles. *Chemistry and Physics of Lipids* **1986**, 40, (2-4), 89-107.
39. Reeves, J. P.; Dowben, R. M., Formation and properties of thin-walled phospholipid vesicles. *Journal of Cellular Physiology* **1969**, 73, (1), 49-60.
40. Castellana, E. T.; Cremer, P. S., Solid supported lipid bilayers: From biophysical studies to sensor design. *Surface Science Reports* **2006**, 61, (10), 429-444.
41. Richter, R. P.; Bérat, R.; Brisson, A. R., Formation of Solid-Supported Lipid Bilayers: An Integrated View. *Langmuir* **2006**, 22, (8), 3497-3505.
42. Sackmann, E., Supported Membranes: Scientific and Practical Applications. *Science* **1996**, 271, (5245), 43-48.
43. Heitz, B. A.; Xu, J.; Jones, I. W.; Keogh, J. P.; Comi, T. J.; Hall, H. K.; Aspinwall, C. A.; Saavedra, S. S., Polymerized Planar Suspended Lipid Bilayers for Single Ion Channel Recordings: Comparison of Several Dienoyl Lipids. *Langmuir* **2011**, 27, (5), 1882-1890.
44. Mey, I.; Stephan, M.; Schmitt, E. K.; Müller, M. M.; Ben Amar, M.; Steinem, C.; Janshoff, A., Local Membrane Mechanics of Pore-Spanning Bilayers. *Journal of the American Chemical Society* **2009**, 131, (20), 7031-7039.
45. Montal, M.; Mueller, P., Formation of Bimolecular Membranes from Lipid Monolayers and a Study of Their Electrical Properties. *Proceedings of the National Academy of Sciences* **1972**, 69, (12), 3561-3566.
46. Mueller, P.; Rudin, D. O.; Ti Tien, H.; Wescott, W. C., Reconstitution of Cell Membrane Structure in vitro and its Transformation into an Excitable System. *Nature* **1962**, 194, (4832), 979-980.
47. Cornell, B. A.; Braach-Maksvytis, V. L. B.; King, L. G.; Osman, P. D. J.; Raguse, B.; Wieczorek, L.; Pace, R. J., A biosensor that uses ion-channel switches. *Nature* **1997**, 387, (6633), 580-583.
48. Danelon, C.; Terrettaz, S.; Guenat, O.; Koudelka, M.; Vogel, H., Probing the function of ionotropic and G protein-coupled receptors in surface-confined membranes. *Methods* **2008**, 46, (2), 104-115.

49. Groves, J. T., *Supported lipid bilayers as mimics for cell surfaces and as tools in biotechnology*. 2006; Vol. 3, p 305-323.
50. Hoffman, T. L.; Canziani, G.; Jia, L.; Rucker, J.; Doms, R. W., A biosensor assay for studying ligand-membrane receptor interactions: Binding of antibodies and HIV-1 Env to chemokine receptors. *Proceedings of the National Academy of Sciences* **2000**, 97, (21), 11215-11220.
51. Im, H.; Wittenberg, N. J.; Lesuffleur, A.; Lindquist, N. C.; Oh, S.-H., Membrane protein biosensing with plasmonic nanopore arrays and pore-spanning lipid membranes. *Chemical Science* **2010**, 1, (6), 688-696.
52. Janshoff, A.; Steinem, C., Transport across artificial membranes—an analytical perspective. *Analytical and Bioanalytical Chemistry* **2006**, 385, (3), 433-451.
53. Reimhult, E.; Kumar, K., Membrane biosensor platforms using nano- and microporous supports. *Trends in Biotechnology* **2008**, 26, (2), 82-89.
54. Stora, T.; Lakey, J. H.; Vogel, H., Ion-Channel Gating in Transmembrane Receptor Proteins: Functional Activity in Tethered Lipid Membranes. *Angewandte Chemie International Edition* **1999**, 38, (3), 389-392.
55. Albertorio, F.; Diaz, A. J.; Yang, T.; Chapa, V. A.; Kataoka, S.; Castellana, E. T.; Cremer, P. S., Fluid and Air-Stable Lipopolymer Membranes for Biosensor Applications. *Langmuir* **2005**, 21, (16), 7476-7482.
56. McBee, T. W.; Saavedra, S. S., Stability of Lipid Films Formed on γ -Aminopropyl Monolayers. *Langmuir* **2005**, 21, (8), 3396-3399.
57. Ross, E. E.; Rozanski, L. J.; Spratt, T.; Liu, S.; O'Brien, D. F.; Saavedra, S. S., Planar Supported Lipid Bilayer Polymers Formed by Vesicle Fusion. 1. Influence of Diene Monomer Structure and Polymerization Method on Film Properties *Langmuir* **2003**, 19, (5), 1752-1765.
58. Joubert, J. R.; Smith, K. A.; Johnson, E.; Keogh, J. P.; Wysocki, V. H.; Gale, B. K.; Conboy, J. C.; Saavedra, S. S., Stable, Ligand-Doped, Poly(bis-SorbPC) Lipid Bilayer Arrays for Protein Binding and Detection. *ACS Applied Materials & Interfaces* **2009**, 1, (6), 1310-1315.
59. Morigaki, K.; Kiyosue, K.; Taguchi, T., Micropatterned Composite Membranes of Polymerized and Fluid Lipid Bilayers. *Langmuir* **2004**, 20, (18), 7729-7735.

60. Okazaki, T.; Inaba, T.; Tatsu, Y.; Tero, R.; Urisu, T.; Morigaki, K., Polymerized Lipid Bilayers on a Solid Substrate: Morphologies and Obstruction of Lateral Diffusion. *Langmuir* **2008**, 25, (1), 345-351.
61. Okazaki, T.; Tatsu, Y.; Morigaki, K., Phase Separation of Lipid Microdomains Controlled by Polymerized Lipid Bilayer Matrices. *Langmuir* **2009**, 26, (6), 4126-4129.
62. Ross, E. E.; Joubert, J. R.; Wysocki, R. J.; Nebesny, K.; Spratt, T.; O'Brien, D. F., Patterned Protein Films on Poly(lipid) Bilayers by Microcontact Printing. *Biomacromolecules* **2006**, 7, (5), 1393-1398.
63. Mueller, A.; O'Brien, D. F., Supramolecular Materials via Polymerization of Mesophases of Hydrated Amphiphiles. *Chemical Reviews* **2002**, 102, (3), 727-758.
64. O'Brien, D. F.; Armitage, B.; Benedicto, A.; Bennett, D. E.; Lamparski, H. G.; Lee, Y.-S.; Srisiri, W.; Sisson, T. M., Polymerization of Preformed Self-Organized Assemblies. *Accounts of Chemical Research* **1998**, 31, (12), 861-868.
65. Zhang, H.; Joubert, J. R.; Saavedra, S. S., Membranes from polymerizable lipids. *Advances in Polymer Science* **2010**, 224, 1-42.
66. Akimoto, A.; Dorn, K.; Gros, L.; Ringsdorf, H.; Schupp, H., Polymer Model Membranes. *Angewandte Chemie International Edition in English* **1981**, 20, (1), 90-91.
67. Johnston, D. S.; McLean, L. R.; Whittam, M. A.; Clark, A. D.; Chapman, D., Spectra and physical properties of liposomes and monolayers of polymerizable phospholipids containing diacetylene groups in one or both acyl chains. *Biochemistry* **1983**, 22, (13), 3194-3202.
68. Kusumi, A.; Singh, M.; Tirrell, D. A.; Oehme, G.; Singh, A.; Samuel, N. K. P.; Hyde, J. S.; Regen, S. L., Dynamic and structural properties of polymerized phosphatidylcholine vesicle membranes. *Journal of the American Chemical Society* **1983**, 105, (10), 2975-2980.
69. Regen, S. L.; Czech, B.; Singh, A., Polymerized vesicles. *Journal of the American Chemical Society* **1980**, 102, (21), 6638-6640.
70. O'Brien, D. F.; Whitesides, T. H.; Klingbiel, R. T., The photopolymerization of lipid-diacetylenes in bimolecular-layer membranes. *Journal of Polymer Science, Polymer Letters Edition* **1981**, 19, (3), 95-101.

71. Conboy, J. C.; Liu, S.; O'Brien, D. F.; Saavedra, S. S., Planar Supported Bilayer Polymers Formed from Bis-Diene Lipids by Langmuir-Blodgett Deposition and UV Irradiation. *Biomacromolecules* **2003**, 4, (3), 841-849.
72. Ross, E. E.; Bondurant, B.; Spratt, T.; Conboy, J. C.; O'Brien, D. F.; Saavedra, S. S., Formation of Self-Assembled, Air-Stable Lipid Bilayer Membranes on Solid Supports. *Langmuir* **2001**, 17, (8), 2305-2307.
73. Ross, E. E.; Spratt, T.; Liu, S.; Rozanski, L. J.; O'Brien, D. F.; Saavedra, S. S., Planar Supported Lipid Bilayer Polymers Formed by Vesicle Fusion. 2. Adsorption of Bovine Serum Albumin *Langmuir* **2003**, 19, (5), 1766-1774.
74. Akama, K.; Yano, Y.; Tokuyama, S.; Hosoi, F.; Omichi, H., [gamma]-Ray irradiation of liposomes of polymerizable phospholipids containing octadeca-2,4-dienoyl groups and characterization of the irradiated liposomes. *Journal of Materials Chemistry* **2000**, 10, (5), 1047-1059.
75. Lamparski, H.; O'Brien, D. F., Two-Dimensional Polymerization of Lipid Bilayers: Degree of Polymerization of Sorbyl Lipids. *Macromolecules* **1995**, 28, (6), 1786-1794.
76. Tsuchida, E.; Hatashita, M.; Makino, C.; Hasegawa, E.; Kimura, N., Polymerization of unsaturated phospholipids as large unilamellar liposomes at low temperature. *Macromolecules* **1992**, 25, (1), 207-212.
77. Heitz, B. A.; Jones, I. W.; Hall, H. K.; Aspinwall, C. A.; Saavedra, S. S., Fractional Polymerization of a Suspended Planar Bilayer Creates a Fluid, Highly Stable Membrane for Ion Channel Recordings. *Journal of the American Chemical Society* **2010**, 132, (20), 7086-7093.
78. Heitz, B. A.; Xu, J.; Hall, H. K.; Aspinwall, C. A.; Saavedra, S. S., Enhanced Long-Term Stability for Single Ion Channel Recordings Using Suspended Poly(lipid) Bilayers. *Journal of the American Chemical Society* **2009**, 131, (19), 6662-6663.
79. Feng, J.; Tseng, P.-Y.; Faucher, K. M.; Orban, J. M.; Sun, X.-L.; Chaikof, E. L., Functional Reconstitution of Thrombomodulin within a Substrate-Supported Membrane-Mimetic Polymer Film. *Langmuir* **2002**, 18, (25), 9907-9913.
80. Shenoy, D. K.; Barger, W. R.; Singh, A.; Panchal, R. G.; Misakian, M.; Stanford, V. M.; Kasianowicz, J. J., Functional Reconstitution of Protein Ion Channels into Planar Polymerizable Phospholipid Membranes. *Nano Letters* **2005**, 5, (6), 1181-1185.

81. Daly, S. M.; Heffernan, L. A.; Barger, W. R.; Shenoy, D. K., Photopolymerization of Mixed Monolayers and Black Lipid Membranes Containing Gramicidin A and Diacetylenic Phospholipids. *Langmuir* **2005**, 22, (3), 1215-1222.
82. Seuring, J.; Reiss, P.; Koert, U.; Agarwal, S., Synthesis, characterization and properties of a new polymerisable surfactant: 12-Methacryloyl dodecylphosphocholine. *Chemistry and Physics of Lipids* **2010**, 163, (4-5), 367-372.
83. Subramaniam, V.; Alves, I. D.; Salgado, G. F. J.; Lau, P.-W.; Wysocki, R. J.; Salamon, Z.; Tollin, G.; Hruby, V. J.; Brown, M. F.; Saavedra, S. S., Rhodopsin Reconstituted into a Planar-Supported Lipid Bilayer Retains Photoactivity after Cross-Linking Polymerization of Lipid Monomers. *Journal of the American Chemical Society* **2005**, 127, (15), 5320-5321.
84. Subramaniam, V.; D'Ambruoso, G. D.; Hall, H. K.; Wysocki, R. J.; Brown, M. F.; Saavedra, S. S., Reconstitution of Rhodopsin into Polymerizable Planar Supported Lipid Bilayers: Influence of Dienoyl Monomer Structure on Photoactivation. *Langmuir* **2008**, 24, (19), 11067-11075.
85. Michel, R.; Subramaniam, V.; McArthur, S. L.; Bondurant, B.; D'Ambruoso, G. D.; Hall, H. K.; Brown, M. F.; Ross, E. E.; Saavedra, S. S.; Castner, D. G., Ultra-High Vacuum Surface Analysis Study of Rhodopsin Incorporation into Supported Lipid Bilayers. *Langmuir* **2008**, 24, (9), 4901-4906.
86. Heitz, B. A. Characterization of novel poly(lipid) BLMs for long-term ion channel scaffolds towards the development of high-throughput screening devices. University of Arizona, Tucson, AZ, 2010.
87. Cafiso, D. S., Alamethicin: a peptide model for voltage gating and protein-membrane interactions. *Annual Review of Biophysics and Biomolecular Structure* **1994**, 23, 141-165.
88. Sansom, M. S. P., Alamethicin and related peptaibols — model ion channels. *European Biophysics Journal* **1993**, 22, (2), 105-124.
89. Baker, A. I.-M.; Saulière, A.; Gaibelet, G.; Lagane, B.; Mazères, S.; Fourage, M.; Bachelier, F.; Salomé, L.; Lopez, A.; Dumas, F., CD4 Interacts Constitutively with Multiple CCR5 at the Plasma Membrane of Living Cells. *Journal of Biological Chemistry* **2007**, 282, (48), 35163-35168.
90. Gaibelet, G.; Planchenault, T.; Mazères, S.; Dumas, F.; Arenzana-Seisdedos, F.; Lopez, A.; Lagane, B.; Bachelier, F., CD4 and CCR5 Constitutively Interact at

the Plasma Membrane of Living Cells. *Journal of Biological Chemistry* **2006**, 281, (49), 37921-37929.

91. Lenaz, G., Lipid fluidity and membrane protein dynamics *Bioscience Reports* **1987**, 7, (11), 823-837.
92. Mullineaux, C. W.; Kirchhoff, H., Role of lipids in the dynamics of thylakoid membranes *Lipids in Photosynthesis: Essential and Regulatory Functions* **2009**, 30, 283-294.
93. Sprague, B. L.; McNally, J. G., FRAP analysis of binding: proper and fitting. *Trends in cell biology* **2005**, 15, (2), 84-91.
94. Wagner, M. L.; Tamm, L. K., Reconstituted Syntaxin1A/SNAP25 Interacts with Negatively Charged Lipids as Measured by Lateral Diffusion in Planar Supported Bilayers. *Biophysical Journal* **2001**, 81, (1), 266-275.
95. Kolchens, S.; Lamparski, H.; O'Brien, D. F., Gelation of two-dimensional assemblies. *Macromolecules* **1993**, 26, (2), 398-400.
96. Longo, M. L.; Waring, A. J.; Gordon, L. M.; Hammer, D. A., Area Expansion and Permeation of Phospholipid Membrane Bilayers by Influenza Fusion Peptides and Melittin. *Langmuir* **1998**, 14, (9), 2385-2395.
97. Perozo, E.; Kloda, A.; Cortes, D. M.; Martinac, B., Physical principles underlying the transduction of bilayer deformation forces during mechanosensitive channel gating. *Nature Structural and Molecular Biology* **2002**, 9, (9), 696-703.
98. Phillips, R.; Ursell, T.; Wiggins, P.; Sens, P., Emerging roles for lipids in shaping membrane-protein function. *Nature* **2009**, 459, (7245), 379-385.
99. Ly, H. V.; Block, D. E.; Longo, M. L., Interfacial Tension Effect of Ethanol on Lipid Bilayer Rigidity, Stability, and Area/Molecule: A Micropipet Aspiration Approach. *Langmuir* **2002**, 18, (23), 8988-8995.
100. Qin, S.-S.; Yu, Z.-W.; Yu, Y.-X., Structural Characterization on the Gel to Liquid-Crystal Phase Transition of Fully Hydrated DSPC and DSPE Bilayers. *The Journal of Physical Chemistry B* **2009**, 113, (23), 8114-8123.
101. Chen, Y.; Lagerholm, B. C.; Yang, B.; Jacobson, K., Methods to measure the lateral diffusion of membrane lipids and proteins. *Methods* **2006**, 39, (2), 147-153.
102. Kovalski, J. M.; Wirth, M. J., Peer Reviewed: Applications of Fluorescence Recovery after Photobleaching. *Analytical Chemistry* **1997**, 69, (19), 600A-605A.

103. Axelrod, D.; Koppel, D. E.; Schlessinger, J.; Elson, E.; Webb, W. W., Mobility measurement by analysis of fluorescence photobleaching recovery kinetics. *Biophysical Journal* **1976**, 16, (9), 1055-1069.
104. Soumpasis, D. M., Theoretical analysis of fluorescence photobleaching recovery experiments. *Biophysical Journal* **1983**, 41, (1), 95-97.
105. Barrow, D. A.; Lentz, B. R., Large vesicle contamination in small, unilamellar vesicles. *Biochimica et Biophysica Acta (BBA) - Biomembranes* **1980**, 597, (1), 92-99.
106. Menger, F. M.; Lee, J.-J.; Aikens, P.; Davis, S., Vesicle size: dependence on experimental parameters. *Journal of Colloid and Interface Science* **1989**, 129, (1), 185-191.
107. Cremer, P. S.; Boxer, S. G., Formation and Spreading of Lipid Bilayers on Planar Glass Supports. *The Journal of Physical Chemistry B* **1999**, 103, (13), 2554-2559.
108. Johnson, S. J.; Bayerl, T. M.; McDermott, D. C.; Adam, G. W.; Rennie, A. R.; Thomas, R. K.; Sackmann, E., Structure of an adsorbed dimyristoylphosphatidylcholine bilayer measured with specular reflection of neutrons. *Biophysical Journal* **1991**, 59, (2), 289-294.
109. Williams, L. M.; Evans, S. D.; Flynn, T. M.; Marsh, A.; Knowles, P. F.; Bushby, R. J.; Boden, N., Kinetics of the Unrolling of Small Unilamellar Phospholipid Vesicles onto Self-Assembled Monolayers. *Langmuir* **1997**, 13, (4), 751-757.
110. Mullineaux, C. W.; Kirchhoff, H., Using fluorescence recovery after photobleaching to measure lipid diffusion in membranes *Methods in Molecular Biology* **2007**, 400, (Methods in Membrane Lipids), 267-275.
111. Endress, E.; Weigelt, S.; Reents, G.; Bayerl, T. M., Derivation of a closed form analytical expression for fluorescence recovery after photo bleaching in the case of continuous bleaching during read out. *Eur. Phys. J. E* **2005**, 16, (1), 81-87.
112. Seu, K. J.; Cambrea, L. R.; Everly, R. M.; Hovis, J. S., Influence of Lipid Chemistry on Membrane Fluidity: Tail and Headgroup Interactions. *Biophysical Journal* **2006**, 91, (10), 3727-3735.
113. Bennun, S. V.; Faller, R.; Longo, M. L., Drying and Rehydration of DLPC/DSPC Symmetric and Asymmetric Supported Lipid Bilayers: a Combined AFM and Fluorescence Microscopy Study. *Langmuir* **2008**, 24, (18), 10371-10381.

114. Smith, E. A.; Coym, J. W.; Cowell, S. M.; Tokimoto, T.; Hruby, V. J.; Yamamura, H. I.; Wirth, M. J., Lipid Bilayers on Polyacrylamide Brushes for Inclusion of Membrane Proteins. *Langmuir* **2005**, 21, (21), 9644-9650.
115. Seu, K. J.; Pandey, A. P.; Haque, F.; Proctor, E. A.; Ribbe, A. E.; Hovis, J. S., Effect of Surface Treatment on Diffusion and Domain Formation in Supported Lipid Bilayers. *Biophysical Journal* **2007**, 92, (7), 2445-2450.
116. Derzko, Z.; Jacobson, K., Comparative lateral diffusion of fluorescent lipid analogs in phospholipid multibilayers. *Biochemistry* **1980**, 19, (26), 6050-6057.
117. Blackburn, F. R.; Wang, C.-Y.; Ediger, M. D., Translational and Rotational Motion of Probes in Supercooled 1,3,5-Tris(naphthyl)benzene. *The Journal of Physical Chemistry* **1996**, 100, (46), 18249-18257.
118. Jourdainne, L.; Lecuyer, S. n.; Arntz, Y.; Picart, C.; Schaaf, P.; Senger, B.; Voegel, J.-C.; Laval, P.; Charitat, T., Dynamics of Poly(l-lysine) in Hyaluronic Acid/Poly(l-lysine) Multilayer Films Studied by Fluorescence Recovery after Pattern Photobleaching. *Langmuir* **2008**, 24, (15), 7842-7847.
119. Tinland, B.; Maret, G.; Rinaudo, M., Reptation in semidilute solutions of wormlike polymers. *Macromolecules* **1990**, 23, (2), 596-602.
120. Sackmann, E.; Egg, P.; Fahn, C.; Bader, H.; Ringsdorf, H.; Schollmeier, M., Compound Membranes of Linearly Polymerized and Cross-Linked Macrolipids with Phospholipids: Preparation, Microstructure and Applications. *Berichte der Bunsengesellschaft für physikalische Chemie* **1985**, 89, (11), 1198-1208.
121. Gaub, H.; Büschl, R.; Ringsdorf, H.; Sackmann, E., Phase transitions, lateral phase separation and microstructure of model membranes composed of a polymerizable two-chain lipid and dimyristoylphosphatidylcholine. *Chemistry and Physics of Lipids* **1985**, 37, (1), 19-43.
122. Gaub, H.; Sackmann, E.; Büschl, R.; Ringsdorf, H., Lateral diffusion and phase separation in two-dimensional solutions of polymerized butadiene lipid in dimyristoylphosphatidylcholine bilayers. A photobleaching and freeze fracture study. *Biophysical Journal* **1984**, 45, (4), 725-731.
123. Fahmy, T.; Wesser, J.; Spiess, H. W., Structure and molecular dynamics of highly mobile polymer membranes. *Die Angewandte Makromolekulare Chemie* **1989**, 166, (1), 39-56.

124. Lamparski, H.; Liman, U.; Barry, J. A.; Frankel, D. A.; Ramaswami, V.; Brown, M. F.; O'Brien, D. F., Photoinduced destabilization of liposomes. *Biochemistry* **1992**, 31, (3), 685-694.
125. Jones, I. W.; Hall Jr, H. K., Demonstration of a convergent approach to UV-polymerizable lipids bisDenPC and bisSorbPC. *Tetrahedron Letters* **2011**, 52, (29), 3699-3701.
126. Liu, S.; Sisson, T. M.; O'Brien, D. F., Synthesis and Polymerization of Heterobifunctional Amphiphiles to Cross-Link Supramolecular Assemblies. *Macromolecules* **2000**, 34, (3), 465-473.
127. Lamparski, H.; Lee, Y. S.; Sells, T. D.; O'Brien, D. F., Thermotropic properties of model membranes composed of polymerizable lipids. 1. Phosphatidylcholines containing terminal acryloyl, methacryloyl, and sorbyl groups. *Journal of the American Chemical Society* **1993**, 115, (18), 8096-8102.
128. Lei, J.; Sisson, T. M.; Lamparski, H. G.; O'Brien, D. F., Two-Dimensional Polymerization of Lipid Bilayers: Effect of Lipid Lateral Diffusion on the Rate and Degree of Polymerization. *Macromolecules* **1998**, 32, (1), 73-78.
129. Liu, S.; O'Brien, D. F., Cross-Linking Polymerization in Two-Dimensional Assemblies: Effect of the Reactive Group Site. *Macromolecules* **1999**, 32, (17), 5519-5524.
130. Ratnayaka, S. N. Formation and characterization of hybrid bilayers and diffusion of cations across liposomal membranes: Studies based on polymerizable lipids. University of Arizona, Tucson, AZ, 2007.
131. <http://www.avantilipids.com/>
132. Scomparin, C.; Lecuyer, S.; Ferreira, M.; Charitat, T.; Tinland, B., Diffusion in supported lipid bilayers: Influence of substrate and preparation technique on the internal dynamics. *Eur. Phys. J. E* **2009**, 28, (2), 211-220.
133. Tinland, B., In Orosz, K. S., Ed. 2011.
134. Bolikal, D.; Regen, S. L., Degree of polymerization of a vesicle membrane. *Macromolecules* **1984**, 17, (6), 1287-1289.
135. Srisiri, W.; Lee, Y.-S.; Sisson, T. M.; Bondurant, B.; O'Brien, D. F., Polymerization of supramolecular assemblies: Comparison of lamellar and inverted hexagonal phases. *Tetrahedron* **1997**, 53, (45), 15397-15414.

136. Lamparski, H. Polymerization in two-dimensional assemblies of sorbyl-containing lipids. University of Arizona, Tucson, AZ, 1993.
137. Saxton, M. J., Lateral diffusion in an archipelago. The effect of mobile obstacles. *Biophysical Journal* **1987**, 52, (6), 989-997.
138. Saxton, M. J., Lateral diffusion in an archipelago. Distance dependence of the diffusion coefficient. *Biophysical Journal* **1989**, 56, (3), 615-622.
139. Saxton, M. J., Lateral diffusion and aggregation. A Monte Carlo study. *Biophysical Journal* **1992**, 61, (1), 119-128.
140. Saxton, M. J., Anomalous diffusion due to obstacles: a Monte Carlo study. *Biophysical Journal* **1994**, 66, (2), 394-401.
141. Almeida, P. F. F.; Vaz, W. L. C.; Thompson, T. E., Lateral diffusion and percolation in two-phase, two-component lipid bilayers. Topology of the solid-phase domains in-plane and across the lipid bilayer. *Biochemistry* **1992**, 31, (31), 7198-7210.
142. Ratto, T. V.; Longo, M. L., Obstructed Diffusion in Phase-Separated Supported Lipid Bilayers: A Combined Atomic Force Microscopy and Fluorescence Recovery after Photobleaching Approach. *Biophysical Journal* **2002**, 83, (6), 3380-3392.
143. Needham, D., In Orosz, K. S., Ed. 2009.
144. Discher, B. M.; Bermudez, H.; Hammer, D. A.; Discher, D. E.; Won, Y.-Y.; Bates, F. S., Cross-linked Polymersome Membranes: Vesicles with Broadly Adjustable Properties. *The Journal of Physical Chemistry B* **2002**, 106, (11), 2848-2854.
145. Discher, B. M.; Won, Y.-Y.; Ege, D. S.; Lee, J. C.-M.; Bates, F. S.; Discher, D. E.; Hammer, D. A., Polymersomes: Tough Vesicles Made from Diblock Copolymers. *Science* **1999**, 284, (5417), 1143-1146.
146. Bermudez, H.; Brannan, A. K.; Hammer, D. A.; Bates, F. S.; Discher, D. E., Molecular Weight Dependence of Polymersome Membrane Structure, Elasticity, and Stability. *Macromolecules* **2002**, 35, (21), 8203-8208.
147. Lee, J. C. M.; Santore, M.; Bates, F. S.; Discher, D. E., From Membranes to Melts, Rouse to Reptation: Diffusion in Polymersome versus Lipid Bilayers. *Macromolecules* **2001**, 35, (2), 323-326.

148. Mabrouk, E.; Cuvelier, D.; Pontani, L.-L.; Xu, B.; Levy, D.; Keller, P.; Brochard-Wyart, F.; Nassoy, P.; Li, M.-H., Formation and material properties of giant liquid crystal polymersomes. *Soft Matter* **2009**, 5, (9), 1870-1878.
149. Kim, D. H.; Needham, D., Lipid bilayers and monolayers: Characterization using micropipette manipulation techniques. In *Encyclopedia of Surface and Colloid Science*, Marcel Dekker: 2002; Vol. 3, pp 3057-3086.
150. Haines, T. H.; Li, W.; Green, M.; Cummins, H. Z., The elasticity of uniform, unilamellar vesicles of acidic phospholipids during osmotic swelling is dominated by the ionic strength of the media. *Biochemistry* **1987**, 26, (17), 5439-5447.
151. Rutkowski, C. A.; Williams, L. M.; Haines, T. H.; Cummins, H. Z., The elasticity of synthetic phospholipid vesicles obtained by photon correlation spectroscopy. *Biochemistry* **1991**, 30, (23), 5688-5696.
152. Pan, J.; Mills, T. T.; Tristram-Nagle, S.; Nagle, J. F., Cholesterol Perturbs Lipid Bilayers Nonuniversally. *Physical Review Letters* **2008**, 100, (19), 198103.
153. Koenig, B. W.; Strey, H. H.; Gawrisch, K., Membrane lateral compressibility determined by NMR and x-ray diffraction: effect of acyl chain polyunsaturation. *Biophysical journal* **1997**, 73, (4), 1954-1966.
154. Dieluweit, S.; Csiszár, A.; Rubner, W.; Fleischhauer, J.; Houben, S.; Merkel, R., Mechanical Properties of Bare and Protein-Coated Giant Unilamellar Phospholipid Vesicles. A Comparative Study of Micropipet Aspiration and Atomic Force Microscopy. *Langmuir* **2010**, 26, (13), 11041-11049.
155. Garcia-Manyes, S.; Sanz, F., Nanomechanics of lipid bilayers by force spectroscopy with AFM: A perspective. *Biochimica et Biophysica Acta (BBA) - Biomembranes* **2010**, 1798, (4), 741-749.
156. Kocun, M.; Mueller, W.; Maskos, M.; Mey, I.; Geil, B.; Steinem, C.; Janshoff, A., Viscoelasticity of pore-spanning polymer membranes derived from giant polymersomes. *Soft Matter* **2010**, 6, (11), 2508-2516.
157. Campillo, C.; Pepin-Donat, B.; Viallat, A., Responsive viscoelastic giant lipid vesicles filled with a poly(N-isopropylacrylamide) artificial cytoskeleton. *Soft Matter* **2007**, 3, (11), 1421-1427.
158. Fa, N.; Lins, L.; Courtoy, P. J.; Dufrêne, Y.; Van Der Smissen, P.; Brasseur, R.; Tyteca, D.; Mingeot-Leclercq, M. P., Decrease of elastic moduli of DOPC bilayers induced by a macrolide antibiotic, azithromycin. *Biochimica et Biophysica Acta (BBA) - Biomembranes* **2007**, 1768, (7), 1830-1838.

159. Ly, H. V.; Longo, M. L., Probing the Interdigitated Phase of a DPPC Lipid Bilayer by Micropipette Aspiration. *Macromolecular Symposia* **2005**, 219, (1), 97-122.
160. Manneville, J. B.; Bassereau, P.; Lévy, D.; Prost, J., Activity of Transmembrane Proteins Induces Magnification of Shape Fluctuations of Lipid Membranes. *Physical Review Letters* **1999**, 82, (21), 4356.
161. Shoemaker, S. D.; Kyle Vanderlick, T., Material Studies of Lipid Vesicles in the L_{α} and L_{α} -Gel Coexistence Regimes. *Biophysical Journal* **2003**, 84, (2), 998-1009.
162. Shoemaker, S. D.; Vanderlick, T. K., Stress-Induced Leakage from Phospholipid Vesicles: Effect of Membrane Composition. *Industrial & Engineering Chemistry Research* **2001**, 41, (3), 324-329.
163. Zhou, Y.; Raphael, R. M., Solution pH Alters Mechanical and Electrical Properties of Phosphatidylcholine Membranes: Relation between Interfacial Electrostatics, Intramembrane Potential, and Bending Elasticity. *Biophysical Journal* **2007**, 92, (7), 2451-2462.
164. Hochmuth, R. M., The micropipet and the mechanical deformation of cells. *Bioengineering Science News* 1991, pp 35-39.
165. Duncan, P. B. Dissolution of two-phase microsystems: Gas and liquid microparticle dissolution and dehydration of biomaterials. Duke University, Durham, NC, 2005.
166. Kim, D. H., Micromanipulation - A practical guide. In.
167. Longo, M. L.; Ly, H. V., Micropipet aspiration for measuring elastic properties of lipid bilayers. *Methods in Molecular Biology* **2007**, 400, 421-437.
168. Kwok, R.; Evans, E., Thermoelasticity of large lecithin bilayer vesicles. *Biophysical Journal* **1981**, 35, (3), 637-652.
169. McIntosh, T. J.; Simon, S. A.; Needham, D.; Huang, C. H., Structure and cohesive properties of sphingomyelin/cholesterol bilayers. *Biochemistry* **1992**, 31, (7), 2012-2020.
170. Zhelev, D. V.; Needham, D.; Hochmuth, R. M., A novel micropipet method for measuring the bending modulus of vesicle membranes. *Biophysical Journal* **1994**, 67, (2), 720-727.

171. Heinrich, V.; Rawicz, W., Automated, High-Resolution Micropipet Aspiration Reveals New Insight into the Physical Properties of Fluid Membranes. *Langmuir* **2005**, 21, (5), 1962-1971.
172. Tierney, K. J.; Block, D. E.; Longo, M. L., Elasticity and Phase Behavior of DPPC Membrane Modulated by Cholesterol, Ergosterol, and Ethanol. *Biophysical Journal* **2005**, 89, (4), 2481-2493.
173. Evans, E.; Rawicz, W., Entropy-driven tension and bending elasticity in condensed-fluid membranes. *Physical Review Letters* **1990**, 64, (17), 2094.
174. Rawicz, W.; Olbrich, K. C.; McIntosh, T.; Needham, D.; Evans, E., Effect of Chain Length and Unsaturation on Elasticity of Lipid Bilayers. *Biophysical Journal* **2000**, 79, (1), 328-339.
175. Evans, E.; Rawicz, W., Elasticity of "Fuzzy" Biomembranes. *Physical Review Letters* **1997**, 79, (12), 2379.
176. Evans, E.; Heinrich, V.; Ludwig, F.; Rawicz, W., Dynamic Tension Spectroscopy and Strength of Biomembranes. *Biophysical Journal* **2003**, 85, (4), 2342-2350.
177. Olbrich, K.; Rawicz, W.; Needham, D.; Evans, E., Water Permeability and Mechanical Strength of Polyunsaturated Lipid Bilayers. *Biophysical Journal* **2000**, 79, (1), 321-327.
178. Melikov, K. C.; Frolov, V. A.; Shcherbakov, A.; Samsonov, A. V.; Chizmadzhev, Y. A.; Chernomordik, L. V., Voltage-Induced Nonconductive Pre-Pores and Metastable Single Pores in Unmodified Planar Lipid Bilayer. *Biophysical Journal* **2001**, 80, (4), 1829-1836.
179. Abiror, I. G.; Arakelyan, V. B.; Chernomordik, L. V.; Chizmadzhev, Y. A.; Pastushenko, V. F.; Tarasevich, M. R., 246 - Electric breakdown of bilayer lipid membranes I. The main experimental facts and their qualitative discussion. *Bioelectrochemistry and Bioenergetics* **1979**, 6, (1), 37-52.
180. Benz, R.; Beckers, F.; Zimmermann, U., Reversible electrical breakdown of lipid bilayer membranes: A charge-pulse relaxation study. *Journal of Membrane Biology* **1979**, 48, (2), 181-204.
181. Genco, I.; Gliozzi, A.; Relini, A.; Robello, M.; Scalas, E., Electroporation in symmetric and asymmetric membranes. *Biochimica et Biophysica Acta (BBA) - Biomembranes* **1993**, 1149, (1), 10-18.

182. Glaser, R. W.; Leikin, S. L.; Chernomordik, L. V.; Pastushenko, V. F.; Sokirko, A. I., Reversible electrical breakdown of lipid bilayers: formation and evolution of pores. *Biochimica et Biophysica Acta (BBA) - Biomembranes* **1988**, 940, (2), 275-287.
183. Wilhelm, C.; Winterhalter, M.; Zimmermann, U.; Benz, R., Kinetics of pore size during irreversible electrical breakdown of lipid bilayer membranes. *Biophysical Journal* **1993**, 64, (1), 121-128.
184. Evans, E.; Florian, L., Dynamic strengths of molecular anchoring and material cohesion in fluid biomembranes. *Journal of Physics: Condensed Matter* **2000**, 12, (8A), A315.
185. Paluwatte Muhandiramlage, T. Preparation and characterization of glucose nanosensors for intracellular applications. University of Arizona, Tucson, AZ, 2010.
186. Needham, D.; Nunn, R. S., Elastic deformation and failure of lipid bilayer membranes containing cholesterol. *Biophysical Journal* **1990**, 58, (4), 997-1009.
187. Bermúdez, H.; Hammer, D. A.; Discher, D. E., Effect of Bilayer Thickness on Membrane Bending Rigidity. *Langmuir* **2003**, 20, (3), 540-543.
188. Subramaniam, V. Preparation and characterization of novel lipid and proteolipid membranes from polymerizable lipids. University of Arizona, Tucson, AZ, 2007.
189. Filippov, A.; Orädd, G.; Lindblom, G., The Effect of Cholesterol on the Lateral Diffusion of Phospholipids in Oriented Bilayers. *Biophysical Journal* **2003**, 84, (5), 3079-3086.
190. Filippov, A.; Orädd, G.; Lindblom, G., Lipid Lateral Diffusion in Ordered and Disordered Phases in Raft Mixtures. *Biophysical Journal* **2004**, 86, (2), 891-896.
191. Lindblom, G.; Orädd, G., Lipid lateral diffusion and membrane heterogeneity. *Biochimica et Biophysica Acta (BBA) - Biomembranes* **2009**, 1788, (1), 234-244.
192. Fahey, P. F.; Webb, W. W., Lateral diffusion in phospholipid bilayer membranes and multilamellar liquid crystals. *Biochemistry* **1978**, 17, (15), 3046-3053.
193. Weiskopf, D.; Schmitt, E. K.; Klühr, M. H.; Dertinger, S. K.; Steinem, C., Micro-BLMs on Highly Ordered Porous Silicon Substrates: Rupture Process and Lateral Mobility. *Langmuir* **2007**, 23, (18), 9134-9139.

194. Helluin, O.; Dugast, J. Y.; Molle, G.; Mackie, A. R.; Ladha, S.; Duclohier, H., Lateral diffusion and conductance properties of a fluorescein-labelled alamethicin in planar lipid bilayers. *Biochimica et Biophysica Acta (BBA) - Biomembranes* **1997**, 1330, (2), 284-292.
195. Ladha, S.; Mackie, A. R.; Harvey, L. J.; Clark, D. C.; Lea, E. J.; Brullemans, M.; Duclohier, H., Lateral diffusion in planar lipid bilayers: a fluorescence recovery after photobleaching investigation of its modulation by lipid composition, cholesterol, or alamethicin content and divalent cations. *Biophysical Journal* **1996**, 71, (3), 1364-1373.
196. Steinberg-Yfrach, G.; Liddell, P. A.; Hung, S.-C.; Moore, A. L.; Gust, D.; Moore, T. A., Conversion of light energy to proton potential in liposomes by artificial photosynthetic reaction centres. *Nature* **1997**, 385, (6613), 239-241.
197. Steinberg-Yfrach, G.; Rigaud, J.-L.; Durantini, E. N.; Moore, A. L.; Gust, D.; Moore, T. A., Light-driven production of ATP catalysed by F₀F₁-ATP synthase in an artificial photosynthetic membrane. *Nature* **1998**, 392, (6675), 479-482.
198. Gust, D.; Moore, T. A.; Moore, A. L., Mimicking bacterial photosynthesis. *Pure and Applied Chemistry* **1998**, 70, (11), 2189-2200.
199. Gust, D.; Moore, T. A.; Moore, A. L., Mimicking Photosynthetic Solar Energy Transduction. *Accounts of Chemical Research* **2000**, 34, (1), 40-48.
200. Ge, C.; Armstrong, N. R.; Saavedra, S. S., pH-Sensing Properties of Poly(aniline) Ultrathin Films Self-Assembled on Indium-Tin Oxide. *Analytical Chemistry* **2007**, 79, (4), 1401-1410.
201. Ge, C.; Doherty III, W. J.; Mendes, S. B.; Armstrong, N. R.; Saavedra, S. S., Voltammetric and waveguide spectroelectrochemical characterization of ultrathin poly(aniline)/poly(acrylic acid) films self-assembled on indium-tin oxide. *Talanta* **2005**, 65, (5), 1126-1131.
202. McBee, T. W.; Wang, L.; Ge, C.; Beam, B. M.; Moore, A. L.; Gust, D.; Moore, T. A.; Armstrong, N. R.; Saavedra, S. S., Characterization of Proton Transport across a Waveguide-Supported Lipid Bilayer. *Journal of the American Chemical Society* **2006**, 128, (7), 2184-2185.
203. Decher, G., Fuzzy Nanoassemblies: Toward Layered Polymeric Multicomposites. *Science* **1997**, 277, (5330), 1232-1237.
204. McBee, T. W., In University of Arizona: Tucson, AZ, 2009.

205. Ge, C. Development of self-assembled conducting polymer ultrathin films and poly(aniline) nanowires/sol-gel composite materials as substrates for planar supported biomimetic artificial photosynthetic systems. University of Arizona, Tucson, AZ, 2006.
206. Zhang, H.; Orosz, K. S.; Takahashi, H.; Saavedra, S. S., Broadband plasmon waveguide resonance spectroscopy for probing biological thin films. *Applied Spectroscopy* **2009**, 63, (9), 1062-1067.
207. White, R. J.; Ervin, E. N.; Yang, T.; Chen, X.; Daniel, S.; Cremer, P. S.; White, H. S., Single Ion-Channel Recordings Using Glass Nanopore Membranes. *Journal of the American Chemical Society* **2007**, 129, (38), 11766-11775.